AD NUMBER

AD445821

NEW LIMITATION CHANGE

TO

Approved for public release, distribution unlimited

FROM

Distribution authorized to U.S. Gov't. agencies and their contractors; Administrative/Operational Use; JUL 1964. Other requests shall be referred to Air Force Office of Scientific Research, Bolling AFB, Washington, DC 20332.

AUTHORITY

Air Force Office of Scientific Research ltr dtd 21 Oct 1968

AD 445821

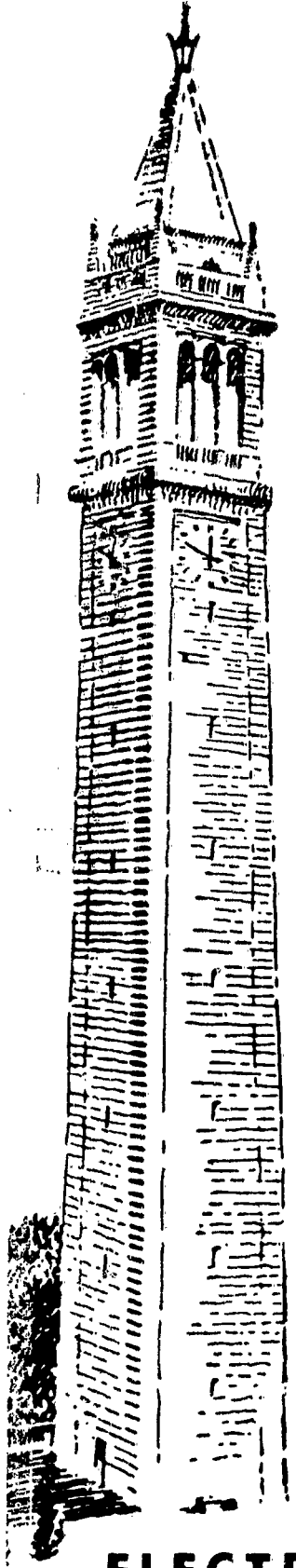

Synthesis of Dual Reflector Antennas

by
Victor Galindo

July 30, 1964

Report No. 64-22
AF-AFOSR 139-63 and 139-64

ELECTRONICS RESEARCH LABORATORY

UNIVERSITY OF CALIFORNIA
BERKELEY, CALIFORNIA

Electronics Research Laboratory
University of California
Berkeley, California
Report No. 64-22

SYNTHESIS OF DUAL REFLECTOR ANTENNAS

by

Victor Galindo

The research reported herein was supported in part by the Joint Services Electronics Program (Air Force Office of Scientific Research, Army Research Office, Office of Naval Research) under Grants AF-AFOSR-139-63.

July 30, 1964

FOREWORD

The author was supported by several individuals and organizations in producing this work and wishes to assign them due credit here. In any case, the entire responsibility for errors herein is that of the author.

Professor W. J. Welch who supervised the entire work is separately acknowledged at the end of the report. The major support was given by the Joint Services Electronics Program under Grants AF-AFOSR-139-63 and 139-64. The original idea for the work in Chapter 1 was suggested by Frank Hennessey of Dalmo Victor Company, Belmont, California. Some of the early work was performed at Dalmo Victor Company. The Computer Center of the University of California contributed considerable time on the IBM-7090. Finally, great appreciation is due Mrs. Hilda Mills and her secretarial staff at Dalmo Victor Company for their preparation of the final manuscript.

ABSTRACT

A synthesis method based on geometrical optics for designing a dual reflector antenna system with an arbitrary phase and amplitude distribution in the aperture of the second reflector is presented. The first reflector may be illuminated by a pattern with an arbitrarily curved phase front. A pair of first order ordinary nonlinear differential equations of the form $dy/dx = f(x, y)$ are developed for the system. Questions concerning uniqueness, existence, and bounds for the solutions are discussed. Calculations and numerical results for the design of a uniform amplitude and phase dual-reflector system are presented.

The diffraction effects of the small reflector are analyzed by the methods of geometrical diffraction. Their effects upon the aperture distribution of the larger reflector are analyzed in detail. Correction for the small reflector diffracted field is obtained partially by an iterative procedure utilizing the above synthesis method. It is shown, although not conclusively, by extensive numerical analysis that complete correction for the diffraction effects is not possible.

TABLE OF CONTENTS

TABLE OF CONTENTS (Cont'd)

GENERAL INTRODUCTION

Conventional dual-reflector antenna systems have been based largely on the Cassegrain parabola-hyperbola design or the Gregorian parabola-ellipse design [1]. Some highly specialized exceptions have also been reported [2]. The designs are all based on the principles of geometrical optics and are limited accordingly. That is, the reflectors must be large and have a large radius of curvature compared to the wavelength in addition to other restrictions.

A generalization of the design techniques for a dual reflector antenna that is also based on geometrical optics and is similarly limited in application is presented in Chapter 1. It has been found that an arbitrary phase and amplitude distribution can be developed in the aperture of the larger reflector of a dual-reflector system with an arbitrarily curved phase front illuminating the smaller reflector. The design procedure is sufficiently general so that many useful variations of the design objectives are clearly possible. For example, the large reflector of the system may be specified to have a circular cross-section and arbitrary phase distribution (uniform,for example) and the appropriate sub-reflector is then found for a given primary radiation pattern.

The methods of geometrical optics which are used for the above synthesis are of the first order from the point of view of the assymptotic solution of Maxwell's equations, which is an expansion in powers of the wavelength. Second and higher order solutions have been obtained for many problems and yield the diffraction effects. A discussion of the assymptotic expansion and the use of higher order terms in the geometrical theory of diffraction is made in Chapter 2. This theory is then used to analyse the diffracted field of the subreflector. The effect of this diffracted field upon the aperture distributio

of the larger reflector is discussed in Chapter 3 in detail, together with a presentation of numerical results illustrating the effects. The importance of higher order terms or the diffracted field due to the larger reflector is generally not nearly as significant as is the diffraction due to the subreflector. In addition, as the subreflector is made smaller in wavelength, diffraction becomes more significant and places a limitation on the minimum size and consequently the minimum blockage the subreflector presents to the main or larger reflector.

An attempt at including the diffracted field in the synthesis procedure and hence correcting for it exactly proved unsuccessful. It appears that in the context of the present formulation a solution for this problem does not exist. The complexity of the problem makes a proof of no existence difficult although this conclusion is strongly implied by the discussion of Chapter 4. Since an exact solution did not appear possible, an attempt at an iterative solution using the synthesis method developed in Chapter 1 was made and is discussed in Chapter 5. The numerical results obtained here tended to support the implications made in Chapter 4 that no exact solution exists. However, the results of the iterative procedure indicated that a reasonable compensation for the diffraction effects can be obtained. Although an approximate theory of diffraction was used in this iterative procedure, the true diffracted field could, in principle, also be used in this method; although perhaps with considerable inconvenience in proportion to the increased accuracy obtainable.

CHAPTER 1

FIRST ORDER DUAL REFLECTOR SYNTHESIS

I. Introduction

In this chapter a method for the synthesis of a dual reflector antenna with an arbitrarily specified phase and amplitude distribution in the aperture of the main reflector is developed. An arbitrary primary source may be used to illuminate the subreflector. The design is based upon geometrical optics. This technique for synthesis is used later to obtain an iterative solution for the reflector shapes which accounts for the diffraction field of the subreflector to some extent.

The synthesis method utilizes the analytical expression of the geometric optics principles together with the geometry for the reflectors illustrated in Figure 1 to develop a pair of first-order nonlinear ordinary differential equations of the form

$$\frac{dy}{dx} = f(x, y) \tag{1}$$

which leads to the cross-sections of each reflector when subject to boundary conditions such as

$$y(x = x_{max}) = 0 . \tag{2}$$

The above differential equation can, in general, be solved readily by high-speed machine computations. A pair of such solutions for a uniform phase and amplitude design is presented.

A desirable feature about the form of the differential solution, Equation (1), is that frequently much information can be predicted about the final solution before a machine computation is attempted. The questions of existence and upper bounds on the size of the reflector ($|y|_{max}$) can be answered by considering little more than the boundary conditions of the problem. If $f(x, y)$ is found in a suitable form, then lower bounds for the radius of curvature of the reflectors can also be found. The procedures for finding the bounds, existence and uniqueness proofs are discussed in Part III and can also be found in the literature on non-linear differential equations (see Reference 8 for example). See also Reference 9 for an alternative formulation of the problem.

The optical principles which are utilized to develop equations of the form given in (1) for the system are the following:

a. Snell's Law[3]. Application of this law at each reflector leads to a form of (1) with f specified in terms of the angular variables shown in Figure 1.

b. Conservation of Energy Flow[4] along the ray trajectories. The requirement that the energy flow be conserved in any solid angle bounded by ray trajectories leads to one equation of constraint for the system.

c. The surfaces of Constant Phase form Normal Surfaces[5] to the ray trajectories, and this normal congruence is maintained after any number of reflections[6] (theorem of Malus). This principle leads to another constraint for the system.

It can be shown that all these principles are not independent (References 2 - 6). Hence we will not need to use the expression for Snell's law

at reflector #2 (Equation 5). The optical principles together with the geometrical bounds of the system and the primary pattern and the phase and amplitude distribution in the large reflector define a unique optical system (sometimes equivalent alternative systems exist, as with the Cassegrain and Gregorian systems).

The design method is described for surfaces of revolution, in particular, although the antenna design method can be readily extended to include doubly curved surfaces where the surface coordinates are separable, and possibly also under other special conditions (see Reference 10). When the curvature in one plane is specified for the dual-reflector system, the design procedure for the curvature in the perpendicular plane can be the same as reported herein with an extension similar to that made by Dunbar [7] for a single doubly curved reflector.

II. Analytic Expressions of Optical Principles and Formal Solution*

The principles stated earlier can be expressed as the following basic equations from which the solution is developed.

Snell's law at reflector #1 leads to (see Figure 2)

$$\frac{dy_1}{dx_1} = \tan\left[\frac{\theta_1 - \theta_2(x_1, y_1, x_2, y_2)}{2}\right] \tag{3}$$

where

$$\theta_2 = \arctan\left(\frac{x_2 - x_1}{\alpha+\beta+y_2-y_1}\right) \tag{4}$$

---

* The solution presented in this part and much of the remainder of this chapter is published in Reference 11.

The quantities $\alpha(\theta_1)$ and $\beta(\theta_1)$ are prescribed such that $\alpha(\theta_1)+\beta(\theta_1)$ = given constant (see Figure 1). The intersection of a primary field ray with the y_1 axis determines $\alpha(\theta_1)$ and $\beta(\theta_1)$. The rays are found from the known or given form of the primary field.

Snell's law at reflector #2 leads to (see Figure 3)

$$\frac{dy_2}{dx_2} = -\tan\left[\frac{\theta_2 - \theta_3}{2}\right] \tag{5}$$

where

$$\theta_3 = \arctan\left(\frac{x_2' - x_2}{y_2}\right) \tag{6}$$

The conservation of energy principle is expressed differentially as

$$I_1(\theta_1)\sin\theta_1\left(\frac{d\theta_1}{dx_2'}\right) = I_{3p}(x_2')\,x_2' \tag{7}$$

The quantity $I_1(\theta_1)$ is the power density of the primary illumination. The quantity $I_{3a}(x'_2)$ is the power density flow normal to the aperture of reflector #2 (y_2=0). It is chosen arbitrarily except for the required normalization:

$$\int_{\theta_{1\,min}}^{\theta_{1\,max}} I_1(\theta_1)\sin\theta_1\,d\theta_1 = \int_{x'_{2min}}^{x'_{2max}} I_{3p}(x_2')\,x_2'\,dx_2' \tag{8}$$

The phase at the aperture can be assigned arbitrarily as $C_p(x_2')$. The path length from the primary illumination is given by

$$C_p(x_2') = r_1(\theta_1, y_1) + \rho_2(\theta_1, y_1, x_2, y_2) + \rho_3(x_2, y_2, x_2') + C_{p0}(\theta_1) \tag{9}$$

The quantity $C_{p_0}(\theta_1)$ is defined by the primary illumination as illustrated in Figure 4. An arbitrary primary illumination $\left[I_1(\theta_1)\right]$ phase front is chosen as a reference. The aperture phase $C_p(x_2')$ must be defined with respect to this reference. The remaining quantities in Equation (9) are easily found as

$$r_1 = \left[\beta(\theta_1) - y_1\right] \sec \theta_1, \tag{10}$$

$$\rho_2 = \sqrt{(x_2 - x_1)^2 + (\alpha + \beta + y_2 - y_1)^2} \tag{11}$$

and

$$\rho_3 = \sqrt{(x_2' - x_2)^2 + y_2^2} = \frac{y_2}{\sqrt{1 - \left(\frac{dC_p}{dx_2'}\right)^2}} . \tag{12}$$

The right-hand side of Equation (12) is found by expressing the theorem of Malus from the diagram of Figure 3 as

$$\frac{dC_p}{dx_2'} = \sin \theta_3 . \tag{13}$$

Since $C_p(x_2')$ is assumed given, then $\theta_3(x_2')$ is thus determined directly.

We will now choose as a single independent variable the quantity x_2'. The remaining dependent variables will be considered functions of x_2'. We will then derive the two differential equations

$$\frac{d\theta_1}{dx_2'} = f_{\theta_1}(\theta_1; x_2') \tag{14}$$

and

$$\frac{dy_1}{dx_2'} = f_{y_1}(\theta_1, y_1; x_2') . \tag{15}$$

Upon solving these equations all the remaining dependent variables can be immediately found as functions of x_2'. Although the choice of x_2' as the independent variable and θ_1 and y_1 for the differential equations is somewhat arbitrary, this choice does allow all the following expressions (f_{θ_1}, f_y; etc.) to be found in explicit form. An equivalent formulation in terms of $dy_1/dx_1 = f_1(x_1, y_1)$ and $dy_2/dx_2 = f_2(x_2; y_2)$ can also be found (see Reference 9).

The quantity $d\theta_1/dx_2'$ is found directly from Equation (7) as

$$\frac{d\theta_1}{dx_2'} = f_{\theta_1}(\theta_1; x_2') = \frac{I_{3p}(x_2')\, x_2'}{I_1(\theta_1) \sin\theta_1} . \tag{16}$$

This equation can be solved immediately (by numerical methods) subject to the appropriate boundary conditions (see Figure 1 and Reference 8 for example). If $I_1(\theta_1) \sin\theta_1$ and $I_{3p}(x_2')\, x_2'$ are integrable then we can solve (16) very easily as

$$\int_{\theta_{1\,\min}}^{\theta_1} I_1(\theta_1) \sin\theta_1 \, d\theta_1 = P_1(\theta_1) = \int_{x_{2\,\min}}^{x_2'} I_{3p}(x_2')\, x_2' \, dx_2' = P_{3a}(x_2'). \tag{17}$$

This integral solution will be of especial value if we can find $\theta_1(x_2')$ explicitly from (17). Otherwise it appears just as well to solve (16) since the numerical solution can be used simultaneously to solve (15). That is, the solutions of (14) and (15) can be set up on the same computor program.

Before finding dy_1/dx_2' explicitly we will find dx_1/dx_2' as a function of $(\theta_1, y_1, dy_1/dx_2'; x_2')$, $x_1(\theta_1, y_1)$, $x_2(\theta_1, y_1; x_2')$, and $y_2(\theta_1, y_1; x_2')$ explicitly. Upon finding dy_1/dx_2' we will then have obtained a complete solution for the system.

From the diagrams of reflector #1 it is seen directly that

$$x_1 = x_1(\theta_1, y_1) = \left[\beta(\theta_1) - y_1\right] \tan\theta_1. \tag{18}$$

To find $dx_1/dx_2' \left(\theta_1, y_1, dy_1/dx_2'; x_2'\right)$ we use

$$\frac{dx_1}{dx_2'} = \frac{\partial x_1}{\partial \theta_1}\frac{d\theta_1}{dx_2'} + \frac{\partial x_1}{\partial y_1}\frac{dy_1}{dx_2'} \tag{19}$$

with

$$\frac{\partial x_1}{\partial \theta_1} = \beta_{\theta_1} \tan\theta_1 + (\beta - y_1)\sec^2\theta_1 \tag{20}$$

where $\beta_{\theta_1} = d\beta/d\theta_1$, and

$$\frac{\partial x_1}{\partial y_1} = -\tan\theta_1. \tag{21}$$

We can find $y_2(\theta_1, y_1; x_2')$ and $x_2(\theta_1, y_1; x_2')$ explicitly by solving Equations (9) and (13) simultaneously. This gives

$$y_2 = y_2(\theta_1, y_1; x_2') = -\frac{\left[(x_1 - x_2')^2 + (\alpha+\beta-y_1)^2 - B^2\right]}{2\left[(\alpha+\beta-y_1) + \dfrac{\dfrac{dC_p}{dx_2'}(x_1 - x_2') + B}{\sqrt{1-\left(\dfrac{dC_p}{dx_2'}\right)^2}}\right]} \tag{22}$$

and

$$x_2 = x_2\left(\theta_1, y_1; x_2'\right) = x_2' + \frac{\left[\left(x_1 - x_2'\right)^2 + \left(\alpha+\beta - y_1\right)^2 - B^2\right]}{2\left[\left(x_1 - x_2'\right) + \frac{\left(\alpha+\beta - y_1\right)\sqrt{1 - \left(\frac{dC_p}{dx_2'}\right)^2} + B}{\left(\frac{dC_p}{dx_2'}\right)}\right]} \tag{23}$$

with

$$B = C_p - (\beta - y_1)\sec\theta_1 - C_{p_0}(\theta_1). \tag{24}$$

Now from Equations(3) and (4) we obtain

$$\frac{dy_1}{dx_2'} = f_1(\theta_1, y_1; x_2')\ \frac{dx_1}{dx_2'} \tag{25}$$

where

$$f_1(\theta_1, y_1; x_2') = \tan\left[\frac{\theta_1 - \arctan\left(\frac{x_2 - x_1}{\alpha+\beta+y_2 - y_1}\right)}{2}\right]. \tag{26}$$

With Equations (18) - (24) substituted into Equations (25) and (26) we obtain explicitly

$$\frac{dy_1}{dx_2'} = f_{y_1}(\theta_1, y_1; x_2') = \frac{\left[\beta_{\theta_1}\tan\theta_1 + (\beta - y_1)\sec^2\theta_1\right] f_{\theta_1} f_1}{(1 + \tan\theta_1 f_1)}. \tag{27}$$

Upon solving (27) for $y_1(x_2')$ and either (16) or (17) for $\theta_1(x_2')$, then all the remaining dependent variables, θ_2, x_1, y_2, and x_2 can be found also as functions of x_2' by application of Equations (4), (18), (22), and (23) respectively.

III. Existence, Bounds and Uniqueness

For the purpose of determining existence and uniqueness of the solution and obtaining bounds for y_1 and y_2, it is convenient to use the form of the equations given in (3) and (5) (see also Reference 9). For any specific synthesis problem, it is frequently possible to estimate bounds for the solutions $y_1(x_1)$ and $y_2(x_2)$ in addition to predicting uniqueness merely by using the forms given in (3) and (5). The methods for employing this useful property are easily seen from a study of the theory of these equations such as given in Reference 8. Some discussion of this is given in Appendix I.

IV. Uniform Phase and Amplitude Examples

The solution for the dual-reflector system which will produce a uniform phase and amplitude distribution in the aperture of reflector #2 is found for a primary illumination $I_1(\theta_1) = \cos^n \theta_1$. It is assumed that the primary phase front is circular with center location given by the constants α and β. In this case we will take the phase center of primary radiation as the phase reference for the system so that $C_{p_0}(\theta_1) = 0$. The aperture amplitude distribution will be given by $I_{3p}(x_2') =$ constant found from (8). The aperture phase distribution $C_p(x_2')$ is also given as a constant which is determined from (9) and the boundary conditions. We may note immediatel that in this case

$$\left[\theta_3 = 0 \text{ and } x_2' = x_2\right] \quad . \tag{28}$$

The boundary conditions will be chosen so that

$$\theta_{1\,min} = x'_{2\,min} = x_{2\,min} = 0.$$

Four more independent boundary conditions are available. We will choose

$$x_{2\,max},\ x_{1\,max},\ \theta_{1\,max},\ \text{and}\ \alpha.$$

The remaining conditions are found from Figure 1 as

$$\left\{ \begin{array}{l} \beta = \dfrac{x_{1\,max}}{\tan \theta_{1\,max}} \\ \\ \theta_{2\,max} = \arctan \left[\dfrac{x_{2\,max} - x_{1\,max}}{\alpha + \beta} \right] \\ \\ C_p(x'_2) = \left(\dfrac{\beta}{\cos \theta_{1\,max}} \right) + \left(\dfrac{\alpha + \beta}{\cos \theta_{2\,max}} \right) \end{array} \right\} \qquad (29)$$

Since the overall scale of the structure is arbitrary, the value of $x_{2\,max}$ will be chosen as either

a. $x_{2\,max} = +1$, which leads to a convex type of solution for reflector #1 $\left[y_1(x_1) \right]$

or

b. $x_{2\,max} = -1$, which leads to a concave type of solution for reflector #1.

In this example we find that Equation (17) is integrable and that $\theta_1(x'_2) = \theta_1(x_2)$ can be found explicitly as

$$\theta_1 = \arccos\left(\sqrt[n+1]{1 - M x_2^2}\right) \tag{30}$$

with

$$M = 1 - \cos^{n+1}\theta_{1\,max}. \tag{31}$$

From Equation (22), with $dC_p/dx_2' = \sin\theta_3 = 0$ and $C_{p_0}(\theta_1) = 0$, we obtain

$$y_2 = y_2(\theta_1, y_1; x_2') = \frac{(C_p - r_1)^2 - (x_2' - x_1)^2 - (\alpha+\beta - y_1)^2}{2(\alpha+\beta - y_1 + C_p - r_1)} \tag{32}$$

where r_1 is given by (10).

It is now possible to construct the function (Equation 27)

$$\frac{dy_1}{dx_2'} = f_{y_1}(\theta_1, y_1; x_2') = f_{y_1}(y_1; x_2') \tag{33}$$

explicitly and solve for y_1, x_1, y_2, and x_2 as functions of x_2'.

It should be mentioned that the alternative solution discussed previously in terms of $dy_1/dx_1 = f_1(x_1, y_1)$ and $dy_2/dx_2 = f_2(x_2, y_2)$ leads in the present example to explicit equations for $f_1(x_1, y_1)$ and $f_2(x_2, y_2)$ (see Reference 9).

Numerical computations were made for the following special case:

$$n = 16,\ x_{1\,max} = 0.1,\ \alpha = 0,\ \text{and}\ \theta_{1\,max} = 30°.$$

The values chosen are reasonably practical:

$$\cos^{16} \theta_{1\,max} \approx \frac{1}{10} \; (-10 \text{ db})$$

and

$$\left| \frac{x_{1\,max}}{x_{2\,max}} \right|^2 = 0.01 \text{ or } 1\% \text{ optical blockage by}$$

reflector #1.

The results for the convex (Cassegrain type) solution are depicted in Figure 5. A parabola, matched at two points, is drawn for comparison with reflector #2. The results for the concave (Gregorian type) solution are depicted in Figure 6. In both cases, a numerical and graphical check of the results indicate that the solutions conform to the optical constaints as required. The smoothness of the contours (large radii of curvature) indicate that the optical design will be a useful one in this case.

CHAPTER 1

REFERENCES

1. P. Hannon, "Microwave Antennas Derived from the Cassegrain Telescope", IRE Trans. PGAP., Vol. AP-9, pp. 140-153; March 1961

2. S. Silver, "Microwave Antenna Theory and Design", McGraw-Hill Book Co., New York, Sec. 13.9; 1949

3. _____, Sec. 4.8.

4. _____, Sec. 4.4.

5. _____, Sec. 4.2.

6. _____, Sec. 4.9.

7. A. S. Dunbar, "Calculation of Doubly Curved Reflectors for Shaped Beams", IRE Proc., Vol. 36, pp. 1289-1296; October 1948

8. H. T. Davis, "Introduction to Non-Linear Differential and Integral Equations", U. S. Atomic Energy Commission, pp. 88-93; September 1960.

9. V. Galindo, "Design of Dual Reflector Antennas with Arbitrary Phase and Amplitude Distributions", PTGAP International Symposium Proceedings, pp. 91-95; July 1963.

10. B. Ye Kimber, "On Two Reflector Antennas", Radio Engineering and Electronic Physics, No. 6, pp. 914-921; June 1962. (Scripta Technica Translations, Inc.)

11. V. Galindo, "Design of Dual Reflector Antennas with Arbitrary Phase and Amplitude Distributions", to be published in IEEE Trans., PTGAP; July 1964.

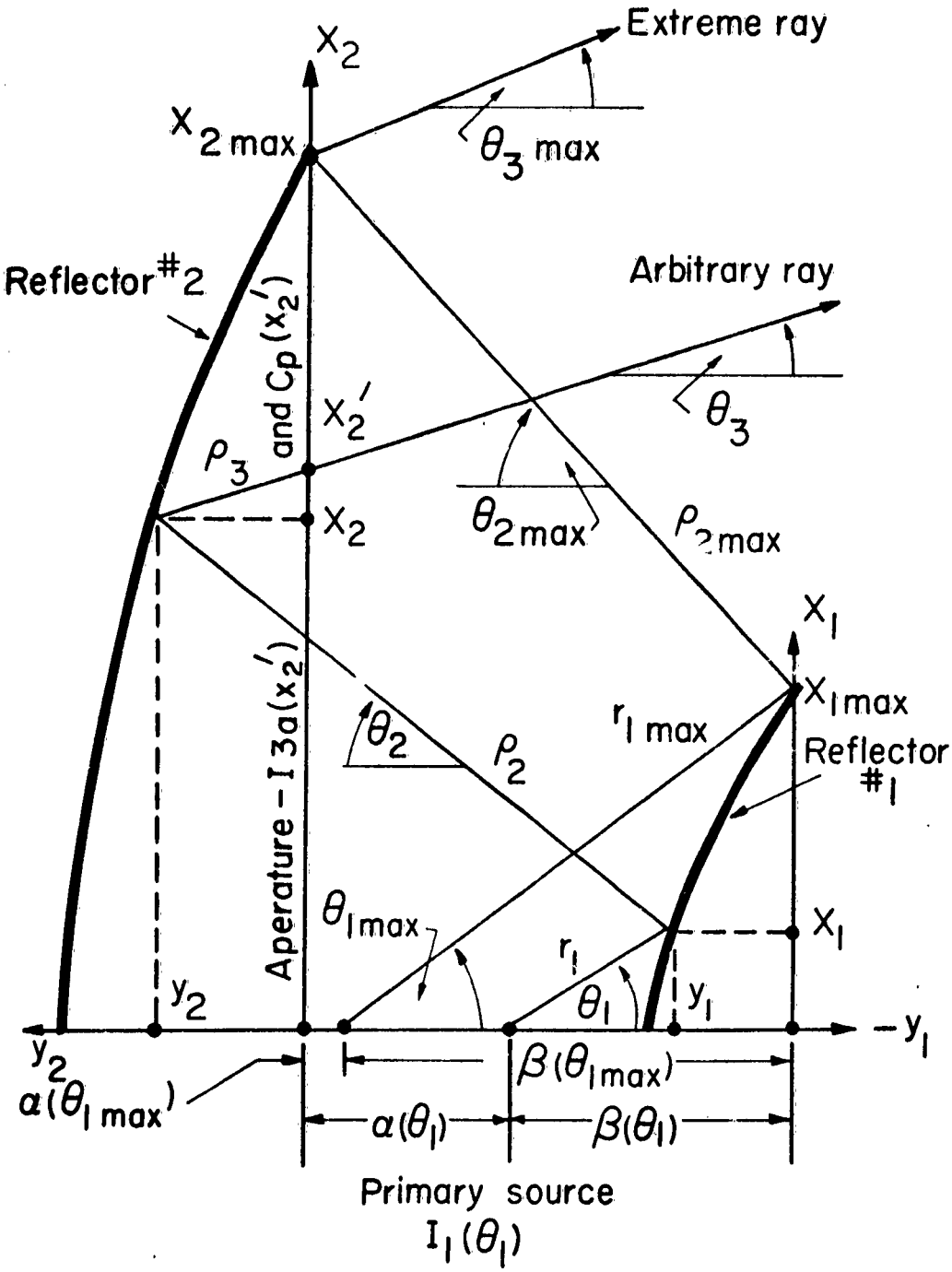

Fig. 1 Dual reflector system cross-section.

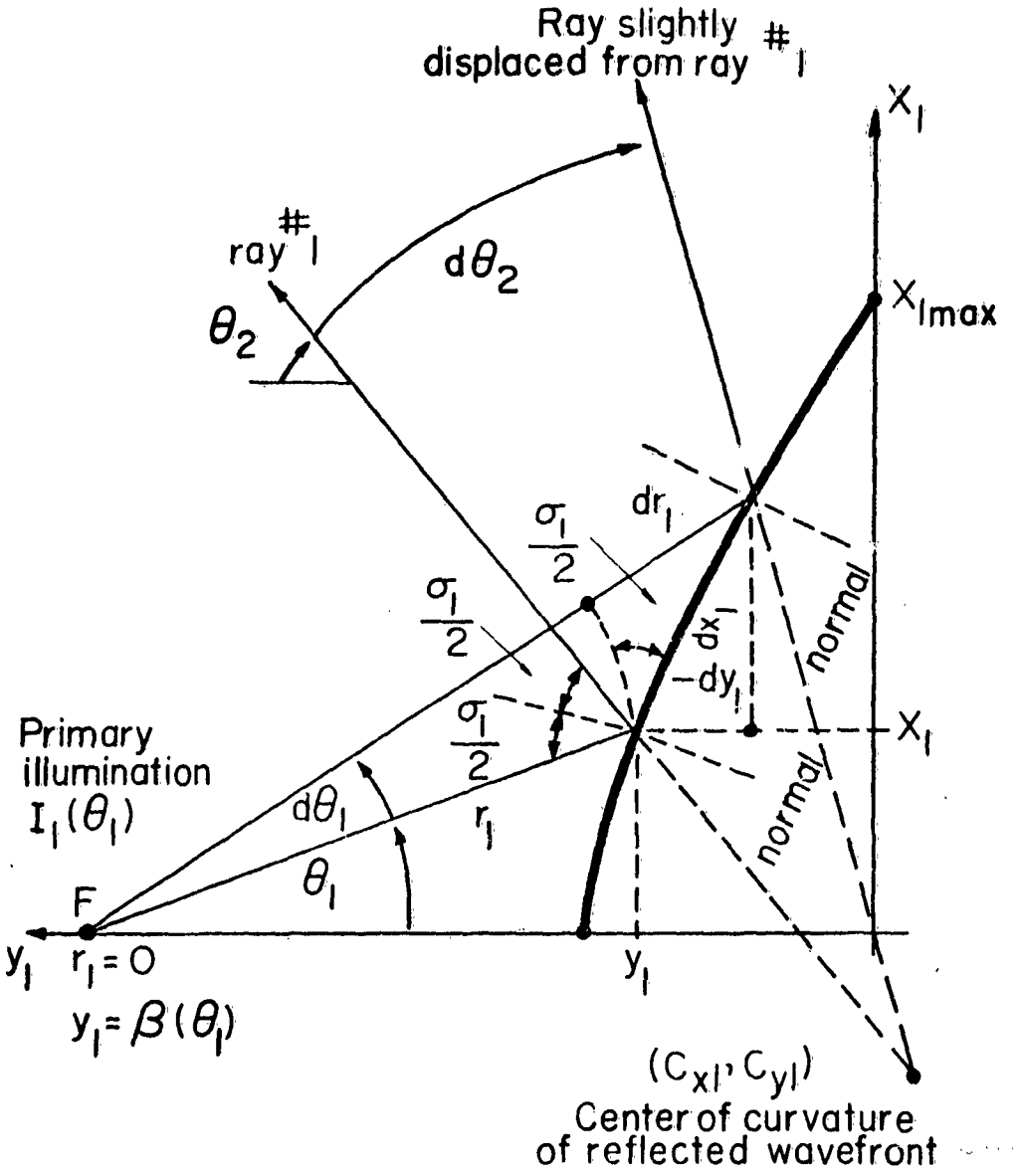

Fig. 2. Geometry at reflector #1.

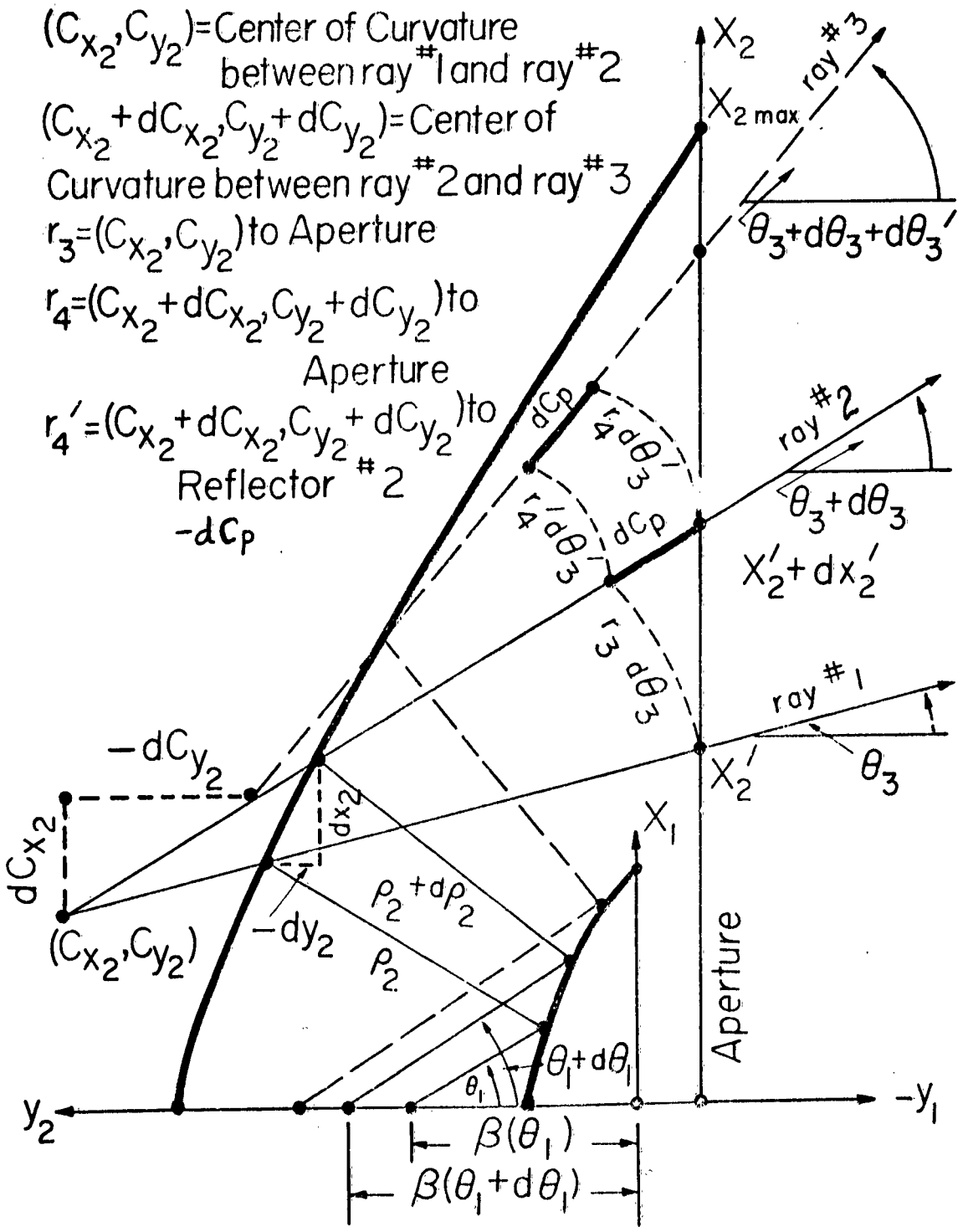

Fig. 3. Phase rate of change along aperture.
Detail at reflector #2.

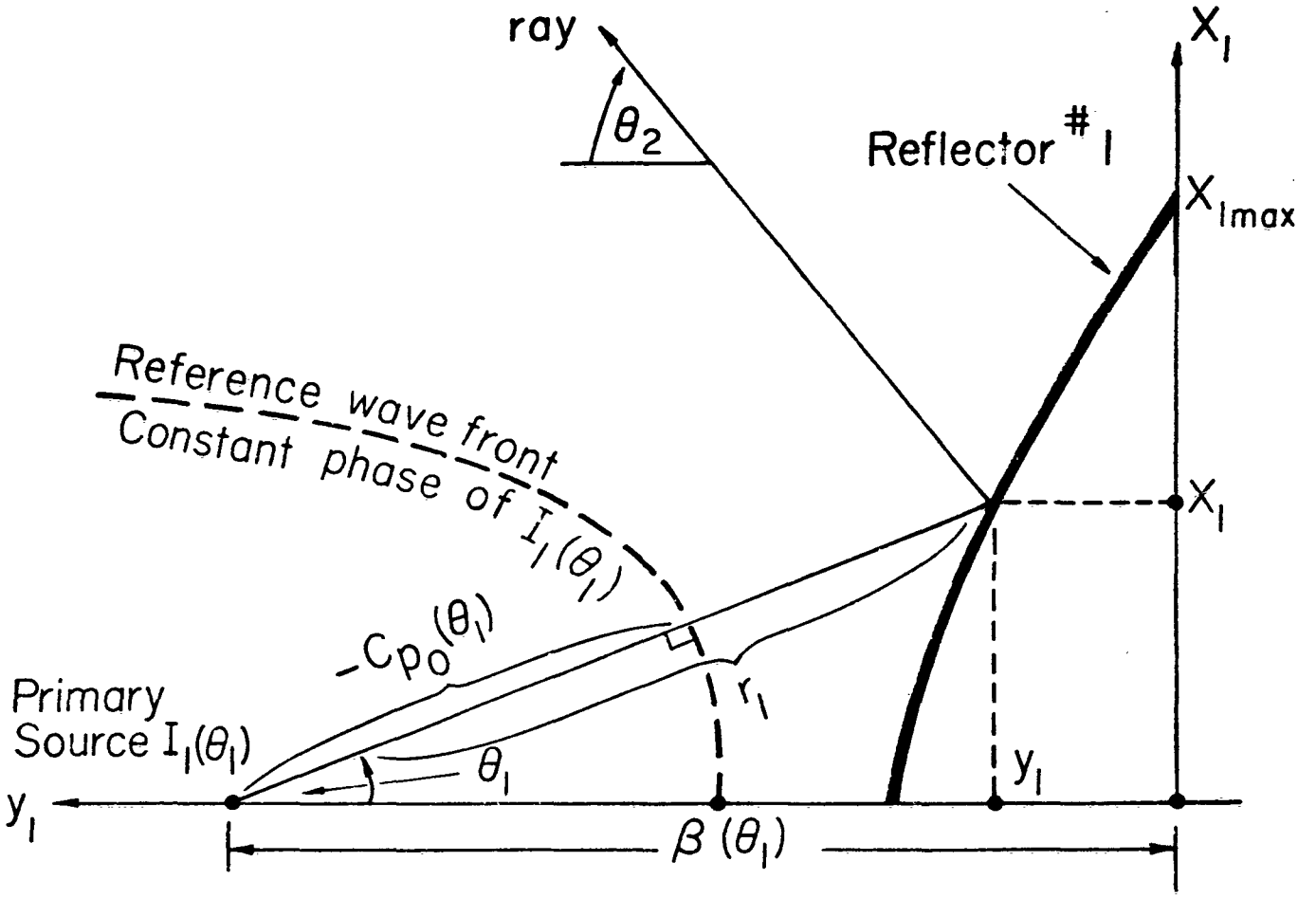

Fig. 4. Constant phase front reference of $I_1(\theta_1)$.

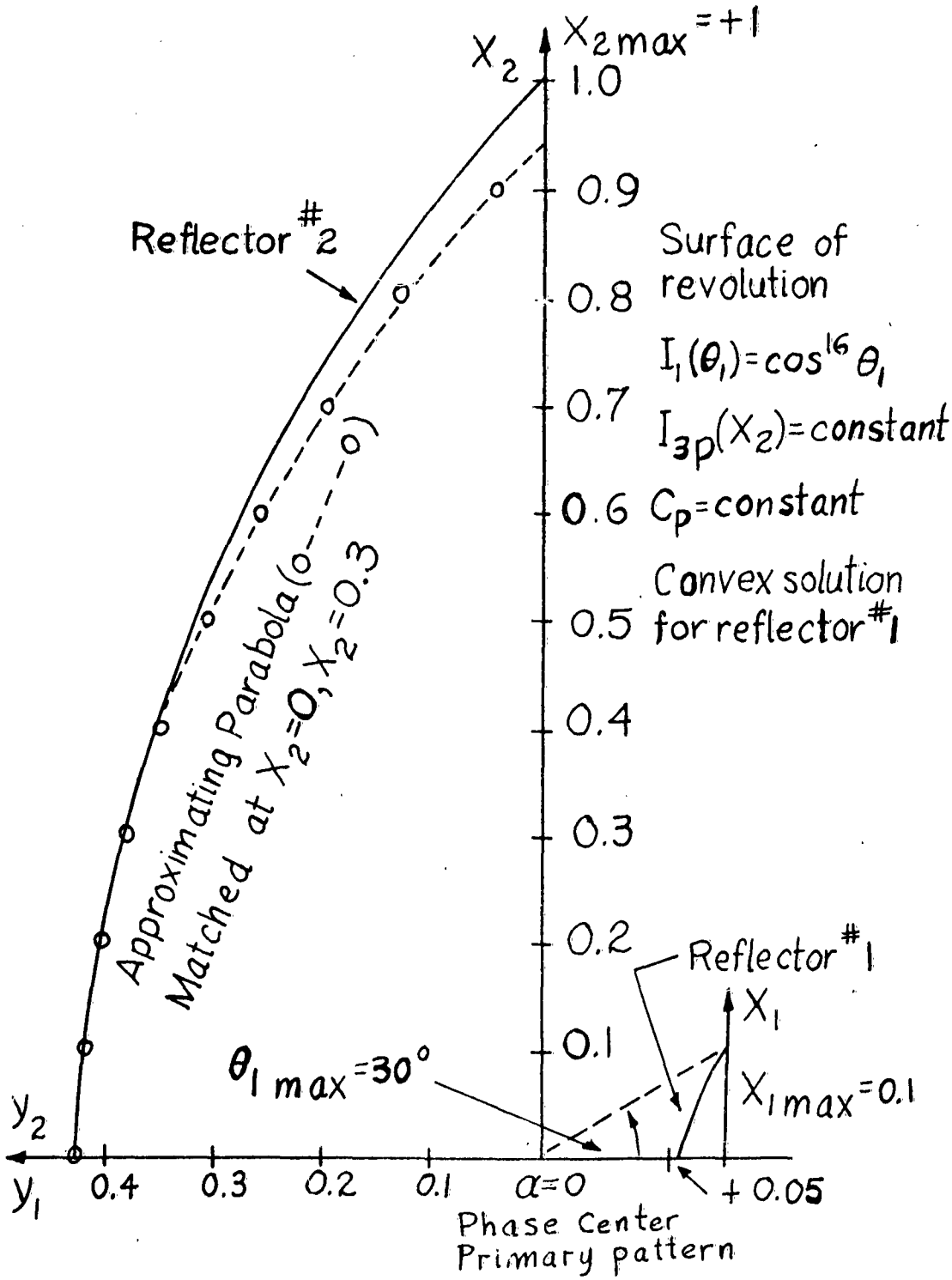

Fig. 5. Dual reflector, uniform phase-amplitude, convex solution.

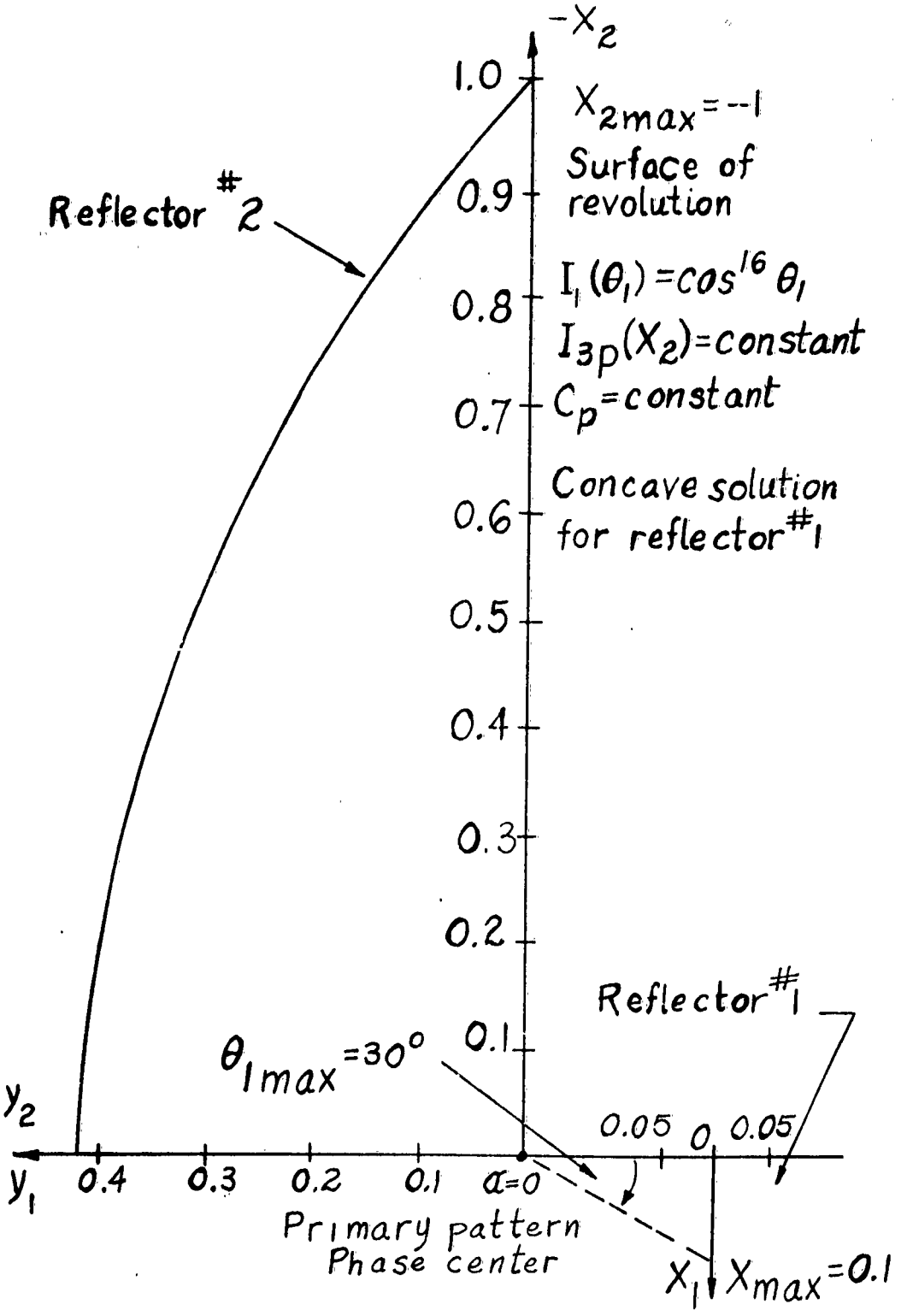

Fig. 6. Dual reflector, uniform phase-amplitude, concave solution.

CHAPTER 2

THE SYNTHESIS PROBLEM AND THE LUNEBERG-KLINE EXPANSION

I. Introduction

The synthesis method developed in Chapter 1 was based on the principles of geometrical optics. Although these principles were discovered independent of electromagnetic theory, they may be derived from Maxwell's equations. For the design of optical instruments which operate at wavelengths measured in angstroms, the connection with Maxwell's equations if often unimportant. At radio and microwave frequencies where the wavelength becomes significantly large, the connection of geometrical optics to Maxwell's equations is important, for it allows us to determine how accurate the geometrical optics approximation is and how, if possible, geometrical optics designs may be improved.

For example, the geometrical optics field scattered from the subreflector of our dual reflector system will have, in general, a sharp cutoff at the shadow boundary as is illustrated below (a). For subreflectors many wavelenths in diameter, the scattered field observed appears to have just such a sharp discontinuity. When the subreflector is of the order of 7 or 8 wavelengths and less, significant changes in the true scattered field from the geometrical optics field may be noticed. Diffraction effects become significant and one observes a scattered field such as is illustrated below in (b). In addition to the ripple that is noticeable, a large change in the amplitude is observable at the shadow boundary. A detailed discussion and analysis of this diffraction effect will be made in later chapters.

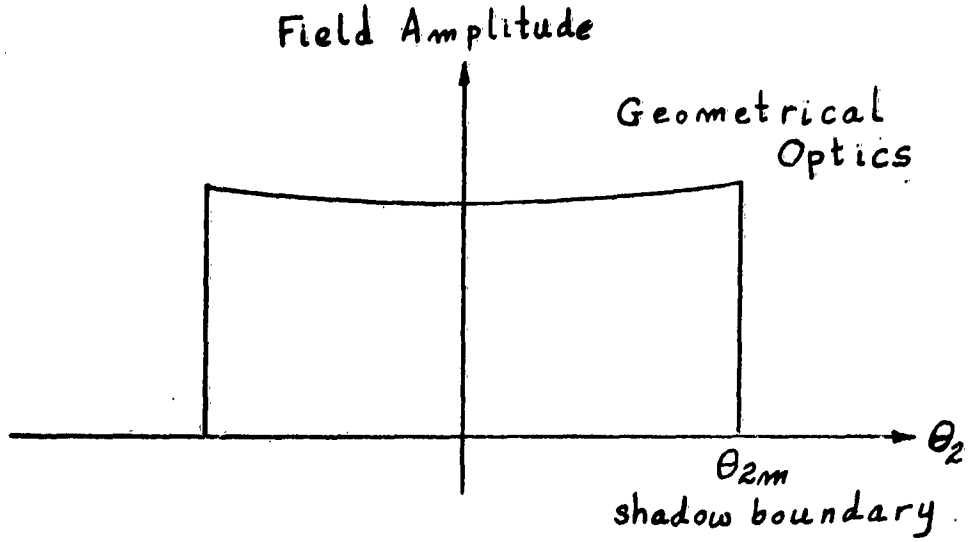
Field Amplitude
Geometrical Optics
θ_2
θ_{2m}
shadow boundary

(a)

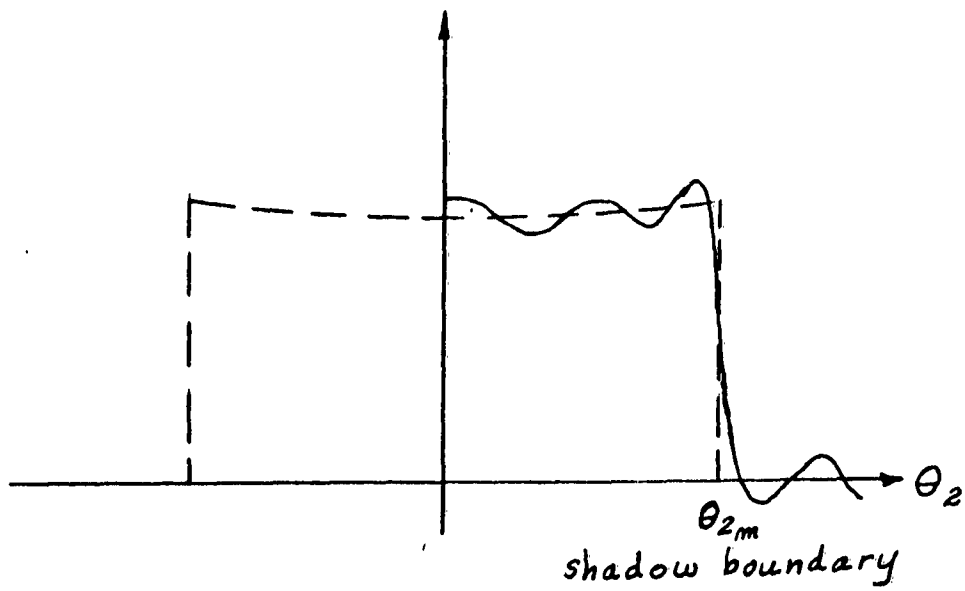
θ_2
θ_{2m}
shadow boundary

(b)

Another consideration that is necessary at larger wavelengths is the effect of a small radius of curvature for a reflecting surface. That is, we would like to know what radius of curvature, in wavelengths, is necessary for geometrical optics to be a valid approximation to electromagnetic theory. Although this problem cannot be solved exactly for most practical cases, considerable insight into the effects of diffraction and small radii of curvature can be obtained by deriving the principles of geometrical optics from Maxwell's equations. There have been many such derivations[1,2], but the most satisfactory appears to be that developed by Luneberg and Kline[3] in the form of an asymptotic solution to Maxwell's equations. This expansion in inverse powers of $k(2\pi/\lambda$ where λ = wavelength) is shown to have as its first term the geometrical optics field. Hence geometrical optics may be referred to as a first order solution to Maxwell's equations.

Strictly speaking, under certain conditions, the higher order terms of the Luneberg-Kline expansion satisfy the geometrical optics principles also. The important condition is the usual far field assumption that the fields are considered only at a great distance from their sources. Hence the primary source field in the synthesis problem may be represented exactly by geometrical optics if the far field is considered or if the subreflector lies in the far zone of the primary source.

An additional reason for discussing the Luneberg-Kline expansion is its similarity to the asymptotic expansion of the Sommerfeld solution to

the half-plane problem. The higher order terms of the asymptotic solution to the half-plane problem describe the sharp edge diffracted field. The second term provides an accurate description of the far zone diffracted field. One distinction between the Luneberg-Kline expansion and the asymptotic expansion of the half-plane solution is that the latter is in powers of $k^{-\frac{n}{2}}$.

In general it is not possible to obtain an asymptotic solution to a diffraction problem in powers of k^{-n} where n is an integer unless certain conditions are satisfied. The original paper by Kline[3] derives and explains these conditions quantitatively. In essence, these conditions require the diffracting obstacle to have a convex curvature and to cast no optical shadows when illuminated by the incident field. A surface that is concave at any point may cause reflected rays to cross at a caustic. The asymptotic expansions do not exist on the caustics of a field defined by a ray system. A particular expansion may however be valid away from a caustic. It can be shown [14] that more terms of the expansion are generally necessary, however, to evaluate the field nearer to the caustic. Away from the caustics, then, the field diffracted from a surface which casts no shadow boundaries may be expressed as an asymptotic expansion in k^{-n}. Such surfaces may be infinite paraboloids and hyperboloids[5,6].

When the diffracting surface casts a shadow boundary it is still usually possible to express the solution in terms of an asymptotic expansion with the distinction that non-integer powers of k must frequently be used [13,15,16]. As was mentioned earlier, the exact half-plane solution

may be expanded in powers $k^{\frac{\eta}{2}}$ where η is an integer. Unfortunately, in most of these cases the expansions are known only after the exact solution is found. Nevertheless, it should be noted that all the expansions have the same first term, the geometrical optics solution. Hence the field diffracted from the reflectors considered in this work will always consist in part of the surface reflected field given by geometrical optics.

The Sommerfeld half-plane solution suggests that a substantial part of the diffracted field in our problem is due to edge currents near the knife edge of the reflector. These currents, as will be shown in the next chapter, give rise to a field which is of higher order in powers of $1/k$ than the geometrical optics field. In problems for which the solution is not known apriori it has been possible to obtain excellent results for the diffracted field by clever use of the edge current concept [7, 9, 10, 11]. Application of this approximation will be made for the subreflector diffracted field in the next chapter.

When the reflecting surface is curved two additional considerations are important. The first concerns the possible excitation of a surface diffracted wave by rays incident tangentially to the surface[5]. In the subreflector problem this is possible due to secondary edge diffracted rays enamating from the edge current. Their effect is estimated and shown to be small in the next chapter. An additional consideration is the accuracy of the geometrical optics field when the reflecting surface has a small radius of curvature.

This last question is too difficult to answer in a precise and conclusive manner. For example, it has been shown that the geometrical optics solution is an exact solution to the vector electromagnetic diffraction problem of a plane wave incident on an infinite paraboloid of revolution[6]. This solution is exact and independent of the paraboloid curvature at the apex. This result is unusual, however, and in fact, peculiarly enough, does not apply to the equivalent acoustic problem. In general, when the radius of curvature of the reflecting surface is larger, then fewer terms of the expansions in powers of k^{-n} are needed. This has been shown in a number of cases investigated by Keller, Lewis, and Seckler[5]. They apply the Luneberg-Kline expansion in analyses of parabolas and hyperbolas of revolution and also of cylindrical shape. The solutions for these cases are generally difficult to interpret since the geometrical parameters describing these shapes (radius of curvature, focal length, etc.) do not enter into the expansions in a reasonably simple way. The application of the expansion to reflection from a circular cylinder allows a direct interpretation of the effect of surface curvature on the convergence of the expansion. As discussed earlier, the application to this problem is approximate and does neglect diffraction due to shadowing, etc. This example is presented after the theory is developed in a more quantitative manner next.

II. The Luneberg-Kline Expansion and Geometrical Optics

We will assume a time harmonic $e^{-i\omega t}$ dependence and suppress this factor. Our notation will follow those of Keller[5] and Schensted[6] which are the same if we set $\vec{V}_n/(i2\pi)^n = \vec{E}_n$. We have three sets of waves; the primary wave $\vec{U}_1$ incident on reflector #1, the secondary wave $\vec{U}_2$ incident on reflector #2, and the tertiary wave $\vec{U}_3$ passing outward through the aperture. We synthesize for a given $\vec{U}_3$ tangential in the aperture with $\vec{U}_1$ specified arbitrarily. The vector $\vec{U}$ is the electric vector with an $e^{-i\omega t}$ time factor suppressed.

The Luneberg-Kline asymptotic expansions for the fields are

$$\vec{U}_1 = \left[\sum_o \vec{V}_{1n}/(ik)^n\right] e^{ikC_{p1}} \quad \left(C_{p1} = s_1 + C_{po}\right) \tag{1}$$

$$\vec{U}_2 = \left[\sum_o \vec{V}_{2n}/(ik)^n\right] e^{ikC_{p2}} \quad \left(C_{p2} = s_2 + r_1 + C_{po}\right) \tag{2}$$

$$\vec{U}_3 = \left[\sum_o \vec{V}_{3n}/(ik)^n\right] e^{ikC_{p3}} \quad \left(C_{p3} = s_3 + \rho_2 + r_1 + C_{po}\right) \tag{3}$$

The notation is the same as that used previously except that s_j is the distance from the Y-axis for $j = 1$, the distance from reflector #1 for $j = 2$, and the distance from reflector #2 for $j = 3$, in each case along the ray which is normal to the optical phase fronts defined by

$$C_{pj} = \text{constant}. \tag{4}$$

In order to have (1), (2), and (3) satisfy Maxwell's equations we first insert them into the homogeneous vector wave equation

$$(\nabla^2 + k^2)\ \vec{U}_j = 0$$

and set to zero the coefficients of like powers of k^{-n}. This leads to a recurrence relation

$$\frac{d\vec{\mathcal{V}}_n}{d\mathcal{A}} + \frac{1}{2}\vec{\mathcal{V}}_n \nabla^2 C_p = -\frac{1}{2}\nabla^2 \mathcal{V}_{n-1} \tag{5}$$

where $\vec{\mathcal{V}}_{-1} \equiv 0$.

The divergence condition ($\nabla \cdot \vec{U} = 0$) gives

$$\nabla C_p \cdot \vec{\mathcal{V}}_n = -\nabla \cdot \vec{\mathcal{V}}_{n-1}. \tag{6}$$

The boundary condition on a perfectly conducting reflector surface defined by the unit normal $\hat{n}$ gives

$$\hat{n} \times \vec{\mathcal{V}}_n = 0 \tag{7}$$

Finally, from the wave equation we also obtain the eikonal equation of geometrical optics

$$\left|\nabla C_p\right|^2 = 1 \tag{8}$$

(The subscripts j have been dropped from (5) through (8)). Hence (1) through (3) satisfy

$$\left.\begin{aligned} &\left(\nabla^2 + k^2\right)\vec{U} = 0 \\ &\nabla\cdot\vec{U} = 0 \\ &\text{and } \hat{n}\times\vec{U} = 0 \end{aligned}\right\} \qquad (9)$$

if (5) through (8) are satisfied.

Equation (8) implies that there is a system of rays which form orthogonal trajectories to the wavefronts C_p = constant. This wavefront is a true wavefront for the first term, $\vec{V}_0$, of the expansion. It is generally not a true phase or wave front for the field when more terms are used.

Equation (5) is a first order ordinary differential equation in the orthogonal coordinate system defined by the ray trajectories and phase fronts. This equation permits us to relate the field at one point of a ray, $\vec{V}_n(s_0)$ to the field at another point, $\vec{V}_n(s)$, when the behavior between s and s_0 is known for the $\vec{V}_{n-1}$ term. This equation describes the flow of energy along a tube of rays[2]. The $\nabla^2\vec{V}_{n-1}$ term is a measure of the diffusion of energy between adjacent tubes of rays. Energy flow is confined within a tube of rays when $\nabla^2\vec{V}_{n-1} = 0$. This is true for the $n = 0$ or geometrical optics term.

Finally, equation (6) is of very great significance insofar as it helps to describe the vector nature of the field. We may write (6) as

$$\nabla C_p\cdot\vec{V}_n = V_{ns} = -\nabla\cdot\vec{V}_{n-1}\,.$$

That is, the longitudal component of $\vec{v}_n$, along s, is given by

$$-\nabla \cdot \vec{v}_{n-1} .$$

Hence $\vec{v}_0$ is always normal to the ray since $\vec{v}_{0s} = 0$.

At first order, $n = 0$, equations (5) through (7) become

$$\frac{d\vec{v}_0}{ds} + \frac{1}{2}\vec{v}_0 \left(\nabla^2 C_p \right) = 0 \tag{10}$$

$$\nabla C_p \cdot \vec{v}_0 = 0. \tag{11}$$

$$\hat{n} \times \vec{v}_0 = 0. \tag{12}$$

Equations (8), (10), (11), and (12) are the usual geometrical optics laws.

III. Example of the Effect of Surface Curvature on the Accuracy of Geometrical Optics Reflection

Geometrical optics principles clearly do not account for the diffraction effects at a knife edge. One may consider the radius of curvature at such an edge as being zero (or the Gaussian curvature as being infinite). It is well known that geometrical optics does give good results for the fields scattered from large flat or nearly flat reflectors. Hence one may state that if the radius of curvature of the reflecting surface is large then geometrical optics or the first term of the asymptotic expansion of the field gives an accurate result for the field. In this section we wish to give some insight into the problem of just how large in wavelengths the radius of curvature of the reflector surface must be in order for geometrical optics to give accurate results.

In the introduction to this chapter, it was mentioned that a specific answer to this question cannot be given since, for example, the geometrical optics solution is exact for the infinite paraboloid[5, 6]. A number of different problems have been analyzed by Keller, Lewis, and Seckler[5] by use of the Luneberg-Kline expansion wherein the convergence properties of the k^{-n} series is illustrated. In many of their problems the k^{-n} expansion is in fact a true asymptotic solution since no shadow boundaries, caustics, etc., exist in the problem. The convergence dependence on curvature is best illustrated however by applying the Luneberg-Kline expansion to scattering from a metal circular cylinder. The application is approximate since diffraction effects exist here and are neglected; nevertheless, the problem is illustrative since the radius of curvature

of the scatterer is a constant and the convergence dependence on this radius is easily discernible. Furthermore, away from the shadow boundary and shadow region the expansion is correct.

For the sake of brevity, the complete details of the derivation of this solution are not presented here. A complete derivation is given by Keller et al[5]. In essence, the geometrical optics solution is found by direct application of the stated principles and the higher order terms are then found from the geometrical optics solution by application of the recurrence relation discussed earlier.

A plane wave, $U_i = e^{ikx}$ is incident upon a perfectly conducting right circular cylinder from the left as illustrated below (c). The cylinder radius is b_o. The electric field is oriented parallel to the cylinder axis so that the total field $E_z = U_t = 0$ on the cylinder. The incident field rays are parallel to the x-axis. The reflected wavefront is not circular (except, as always, it is very nearly so in the far zone). The reflected rays and phase fronts form an orthogonal coordinate system. The rays are tangential to the caustic curve which is defined by

$$\mathcal{A}_0 = \frac{b_o}{2} \sin(\beta/2) \qquad (13)$$

where $\mathcal{A}_0$ is the distance from the caustic to the reflector surface.

The solution for the scattered field is obtained in a non-orthogonal coordinate system wherein a point is defined by $(\mathcal{A}, \beta)$. The distance $\mathcal{A}$

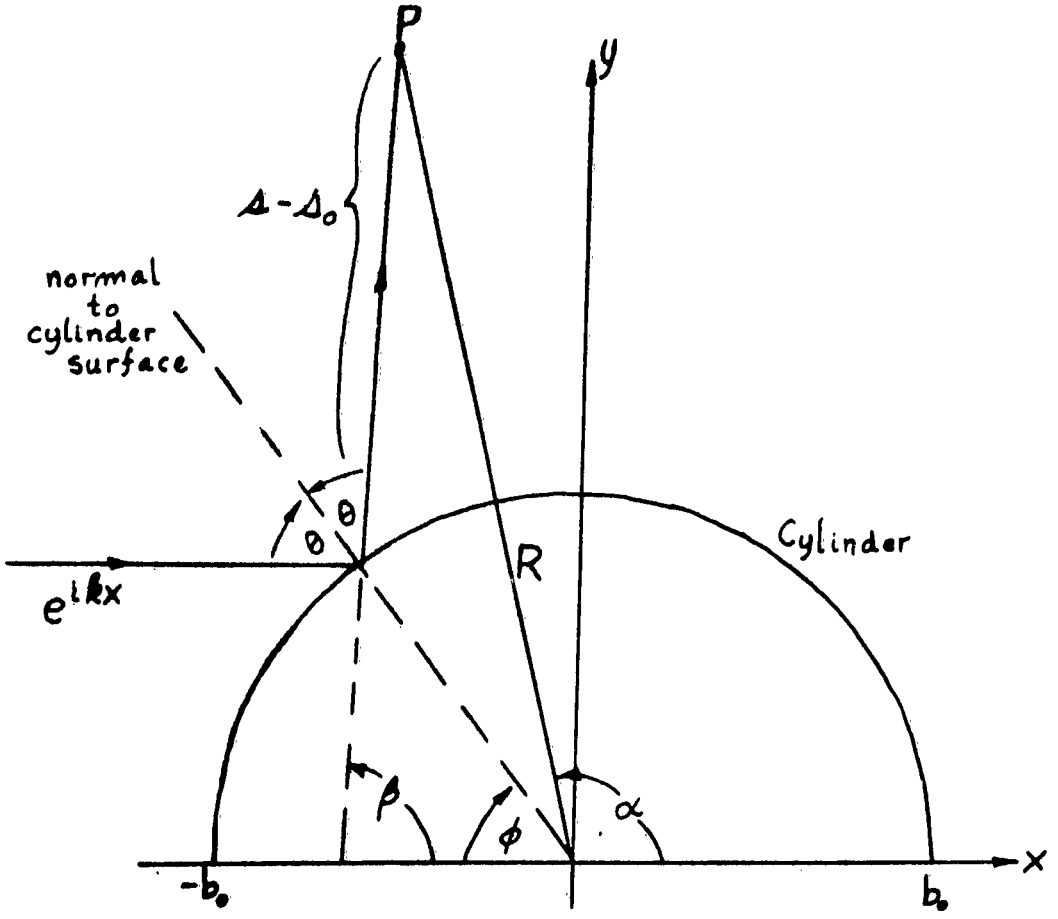
P
y
$s - s_0$
normal
to
cylinder
surface
θ
θ
R
Cylinder
e^{ikx}
β
φ
α
x
$-b_0$
b_0

(c)

i" that taken along a reflected ray from the caustic to the point of observation P. The angle β is that made by the reflected ray and positive X-axis. The solution for the reflected or scattered field is the Luneberg-Kline expansion

$$U = \frac{1}{2}\sqrt{\left(\frac{b_o}{s}\right)\sin\left(\frac{\beta}{2}\right)}\; e^{ik\left(s - \frac{3}{2}\sin\frac{\beta}{2}\right)} \cdot \sum_{n=0}^{\infty}\sum_{j=0}^{3n}\sum_{t=0}^{n} a_{jtn}\left(16ib_o k \sin\frac{\beta}{2}\right)^{-n}\left(\frac{b_o}{2}\right)^{j}\left(\sin\frac{\beta}{2}\right)^{j-2t} \cdot \tag{14}$$

The expansion is found by application of the recursion formula to the geometrical optics solution. The a_{jtn} coefficients are independent of b_o, s, and β and are given by the recursion relations

$$\begin{aligned} a_{jtn} = j^{-1}\Big[& (2j + 4t + 2n - 3)(6j - 4t - 2n - 1)\Big]a_{j-1,t,n-1} \\ & + (2j - 4t + 2n + 5)(2j - 4t - 2n + 3)a_{j-1,t-1,n-1} \\ & + \Big[24(j-1)(j-2t-n) - 6\Big]a_{j-2,t,n-1} \\ & + 12(1 - j)(2j - 4t - 2n + 3)\, a_{j-2,t-1,n-1} \\ & + 9\,(2j - 5)(1 - 2j)\, a_{j-3,t,n-1} \\ & + 9\,(2j - 5)(2j - 1)a_{j-3,t-1,n-1} \end{aligned} \tag{15}$$

and

$$a_{otn} = -\sum_{j=1}^{3n} a_{jtn} \tag{16}$$

and

$$a_{ooo} = -2 . \tag{17}$$

First of all, it should be noticed that the asymptotic solution (14) blows up at the shadow boundary $\beta = 0$ as may be expected. Away from the shadow boundary, $\beta > 0$, we wish to investigate the convergence properties of the expansion with respect to the radius of curvature b_o. Except for the $(b_o/\rho)^j$ factor, b_o occurs only together with k as a factor $(1/b_o k)^n$. In general we are interested in the field far away from the reflecting surface where $\rho \gg b_o$. In that circumstance we may consider only the far field solution j = 0 and make the approximation

$$U \sim \frac{1}{2}\sqrt{\left|\frac{b_o}{\rho}\right| \sin\frac{\beta}{2}}\; e^{ik(\rho - \frac{3}{2}\sin\frac{\beta}{2})} \cdot \sum_{n=0}^{\infty}\sum_{t=0}^{n} a_{otn} \tag{18}$$

$$\cdot (16ib_o k \sin\tfrac{\beta}{2})^{-n} (\sin\tfrac{\beta}{2})^{-2t} .$$

In this important case we note that the geometrical optics solution in the far field,

$$U_o \sim -\sqrt{\left|\frac{b_o}{\rho}\right| \sin\frac{\beta}{2}}\; e^{ik(\rho - \frac{3}{2}\sin\frac{\beta}{2})} , \tag{19}$$

is accurate uniformly in β ($\beta > 0$) so long as $(k\, b_o)$ is large. The percentage error in this specific case is $\sim \left[100/(16 b_o k \sin\tfrac{\beta}{2})\right]\%$

when the effect of only the second term is considered. Note that the error increases nearer to the shadow boundary $\beta = 0$.

This example illustrates, quantitatively for this case only, that the geometrical optics solution is more accurate for reflecting obstacles with larger radii of curvature. As a crude measure of the accuracy of the geometrical optics solution to an arbitrary reflection problem we may use the factor $(1/kb_o)$ as the approximate order of magnitude of the second term in the asumptotic expansion. We may regard b_o as the local radius of curva ture of the reflecting surface and the accuracy thus obtained will, roughly, apply to the field reflected from that portion of the surface. This confirms what is known generally through experience. It is expected that k and b_o should occur together since any other result would contradict the fact that it is the size of b_o as measured in units of wavelength only that is significant. That result may be expected generally.

CHAPTER 3

REFERENCES

1. S. Silver, "Microwave Antenna Theory and Design", McGraw Hill Book Co., New York, N.Y.

2. F.G. Friedlander, "Geometrical Optics and Maxwell's Equations", Proc. Cambridge Phil. Soc., Vol. 43, Pt. 2, pp 284-286; 1946

3. M. Kline, "An Asymptotic Solution of Maxwell's Equations", Communications on Pure and Applied Mathematics", Vol. IV, No. 2-3. pp. 225-263; August 1951

4. M. Kline, "Asymptotic Solutions of Maxwell's Equations Involving Fractional Powers of Frequency", Comm. on Pure and Applied Mathematics, Vol. 7, pp 595-614; November 1955

5. J.B. Keller et al, "Asymptotic Solution of Some Diffraction Problems", Research Report No. EM-81, Inst. of Mathematical Sciences, Div. of E.M. Rsch., New York University; 1955

6. C. E. Schensted, "Electromagnetic and Acoustic Scattering By a Semi-Infinite Body of Revolution", Journal of Applied Physics, Vol. 26, No. 3, pp 306-308; March 1955

7. A.D. Jacobson, "Luneberg-Kline Analysis of Scattering from a Sinusoidal Dielectric Interface", IRE Transactions on Antennas and Propagation, Vol. AP-10, No. 6; November 1962

8. A.J. Sommerfeld, Optics, Academic Press, New York, N.Y.; 1954

9. J.B. Keller, "Geometrical Theory of Diffraction", Research Report No. EM-175, Courant Institute of Mathematical Sciences, Div. of E.M. Research; April 1962

10. R.F. Millar, "An Approximate Theory of the Diffraction of an Electromagnetic Wave By an Aperture in a Plane Screen", Part C of the Proceedings of the IRE; October 1955.

11. W. J. Welch, "Diffraction of Obliquely Incident Plane Waves by a Circular Aperture", Thesis, Master of Science, University of California, Berkeley, California, Electrical Engineering Department

12. W. Braunbek, "Diffraction of an Electromagnetic Plane Wave by a Funnel-Shaped Screen", IRE Trans. on Antennas and Propagation, pp. 571-577, Vol. AP-7, Special Supplement; December 1959

13. A. Erdelyi," Asymptotic Expansions", Dover Publications, New York, N. Y.; 1956

14. I. Kay, "Fields in the Neighborhood of a Caustic", Research Report No. EM-138, N. Y. U. Inst. of Mathematical Sciences, Divn. of E. M. Research; September 1959

15. F. G. Friedlander and J. B. Keller, "Asymptitic Expansions of Solutions of $(\nabla^2 + k^2 u) = 0$", Comm. on Pure and Applied Math., Vol. VIII, pp. 387-394, 1955.

16. M. Kline, "Asymptitic Solution of Linear Hyperbolic Partial Differential Equations, "Journal of Rational Mech. and Analysis, Vol, 3, No. 3, May 1954, pp. 315-342. Also in a report by N. Y. U. Inst. of Math., EM-48.

CHAPTER 3

THE EDGE DIFFRACTED FIELD

I Introduction

A consideration of great importance in any dual reflector system is the extent and effect of the diffracted field scattered from the smaller or subreflector. The geometrical optics field scattered from the subreflector is the field that is considered in the synthesis method developed in Chapter 1. From the discussion in Chapter 2, it is clear that this field is of first order with respect to the Luneberg-Kline series field description. The remaining terms or the diffracted field scattered from this reflector may or may not be of great consequence depending upon the radius of curvature and overall size of this reflector in wavelengths. A smaller sub-reflector will have a scattered field which is more different from the geometrical optics field. This is expected from experience and is borne out in the numerical results presented later.

In general it is important to have as small a sub-reflector as possible. Besides the obvious mechanical reasons of weight support, etc., (which are of very great practical significance) the blockage of the main reflector by the smaller one reduces the overall gain and raises the sidelobes of the tertiary pattern. The diffracted field of the larger main reflector is generally negligible in the vicinity of the aperture of this reflector. That is, geometrical optics is very accurate for a very large reflector. The far field of the main reflector aperture distribution is usually determined by a Kirchhoff[1] integration over the aperture which accounts for diffraction effects with reasonable accuracy. For

a uniform aperture phase distribution the far zone field is a purely diffraction determined field.

We will use the term "Kirchhoff integration" rather frequently in what follows so that a brief definition of this term is in order. The definition given by Baker and Copson[1] is interpreted broadly here. Their definition applies more directly to diffraction through a hole in a screen rather than from a metal scatterer. If E_i, H_i is the field incident upon the aperture and generated by the sources in free space (no screen or scatterers present), then a Kirchhoff integration would assume that E_i, H_i is the total field in the aperture, and the tangential field on the screen is zero. Strictly speaking, neither assumption is true. For scattering from a metal scatterer, we will interpret a Kirchhoff integration as follows:

If E_i, H_i is the field incident upon the scatterer, we assume that the current distribution on the scatterer surface is given by $2\,\hat{n} \times H_i$ where $\hat{n}$ is normal to the surface. Those portions of the surface which are shadowed by the scatterer are assumed to have zero current. The assumptions made here are similar to those made for the hole in a screen problem and are similarly approximate. An integration of these approximate surface currents to obtain the scattered field will be termed a Kirchhoff integration

The purpose of this chapter will be first to determine the diffraction field of the subreflector. In addition we will determine the actual error in aperture phase and amplitude caused by this second order effect. In subsequent chapters, we will discuss various efforts to correct the

diffraction field effects in the main reflector aperture and numerical results will be presented.

An exact determination of the field scattered from reflector shapes that are used in practice is not possible in general except for the flat circular disk[2]. A Kirchhoff integration over the subreflector surface such as that made by Rusch[3] has several disadvantages. The accuracy for very small reflectors (less than 4 λ in diameter) is questionable. The analysis requires laborious numerical computations. The entire reflector shape is required. This is so since this analysis yields the first order geometrical optics field and the diffracted field in the same computation.

The diffraction field is primarily an edge phenomenon caused and determined by the abrupt discontinuity of the reflector surface and the actual edge shape (knife edge, rolled edge, wedge or square, etc.). Hence many very successful diffraction theories have been developed which depend upon only the shape, position, and slope of the edge of the scatterer. Although such edge shapes as the wedge[4,5] or cylindrically tipped edge[6] could be treated we will confine ourselves to the most simple subreflector edge, the knife edge. In particular, we will apply the geometrical theory of diffraction as developed by Keller[7]. As discussed in Chapter 2, this theory is based on the Sommerfeld half-plane solution[8]. Other methods[9,10,11] which are similar have been based on the same solution and have yielded very satisfactory results as determined experimentally[10,12]. The geometrical theory of diffraction[7] is somewhat simpler to apply, and yields very accurate results for reflectors of the order of one wavelength or greater in diameter.

It should be emphasized that the exactness of the solutions for the diffracted field found in this chapter is of no great importance to the general conclusions which may be drawn from the numerical results presented later in this chapter. The edge diffracted fields found in this chapter will, however, be very accurate in general if the primary source amplitude and phase does not vary rapidly near the edge. The edge diffraction theory is based on an assumption that locally, very close to the edge, the physical situation resembles the half-plane problem of Sommerfeld.

The edge diffracted field has a non-circular phase front. Opposite edges of the subreflector as shown in Figure 1 are illuminated symmetrically by the primary source. According to the theory of geometrical diffraction each edge contributes to the total field only in the plane normal to the edges and containing the axis of the system. Since each edge is a directional source oriented in different directions, there can be no fixed phase center for the combination[13]. An equivalent geometrical optics description of this field will therefore require the generality used in the description of the primary source in Chapter 1.

The descriptive geometrical parameters are illustrated in Figure 2. Since it will be convenient later to add the primary and edge fields at the aperture, the particular edge field ray intersecting the primary field ray at the aperture is illustrated in the Figure. $J_e(\gamma_2)$ is the angular power density of the diffracted field in the same units as $I_1(\theta_1)$. $I_{3_e}(X_2')$ is the aperture power flow density normal to the aperture. The edge field ray intersects the y axes at a distance $d_e(\gamma_2)$ from the aperture. Not illustrated in Figure 2 is the reference wavefront

$C_{e_o}(\gamma_2)$ which serves the same purpose for this field description that $C_{p_o}(\theta_1)$ served for the description of the primary source field. The quantity $C_e(\gamma_2)$ is defined as the aperture phase given by $\rho_4 + \rho_5 + C_{e_o}$. Our objective in this chapter is to find the values of these parameters for various frequencies and reflector systems.

II. Edge Diffracted Fields and Sources

We propose to define precisely what is meant by an edge diffracted field or an edge source in this section. This will be done by describing the Sommerfeld solution to the half-plane problem in detail.

Consider the diagram on the following page which is a cross-section of the semi-infinite or half-plane located at $\phi = 0$. We assume a plane wave is incident on the half-plane at an angle α. The incidence is normal in the sense that there is no z-dependence, the plane wave travels in the plane of the diagram. The polarization is either normal or parallel to the edge.

The diagram is divided into three regions, I, II, and III by boundaries G_r and G_i and the half-plane. The boundaries G_r and G_i are the geometrical optics shadow boundaries. Region I contains the incident and reflected geometrical optics fields, Region II contains only the incident geometrical optics field, and Region III is a shadow region, being optically dark. If we subtract these fields, the geometrical optics fields, from the total field solution, there will remain what is referred to as the edge diffracted field. If we examine this edge diffracted field near the

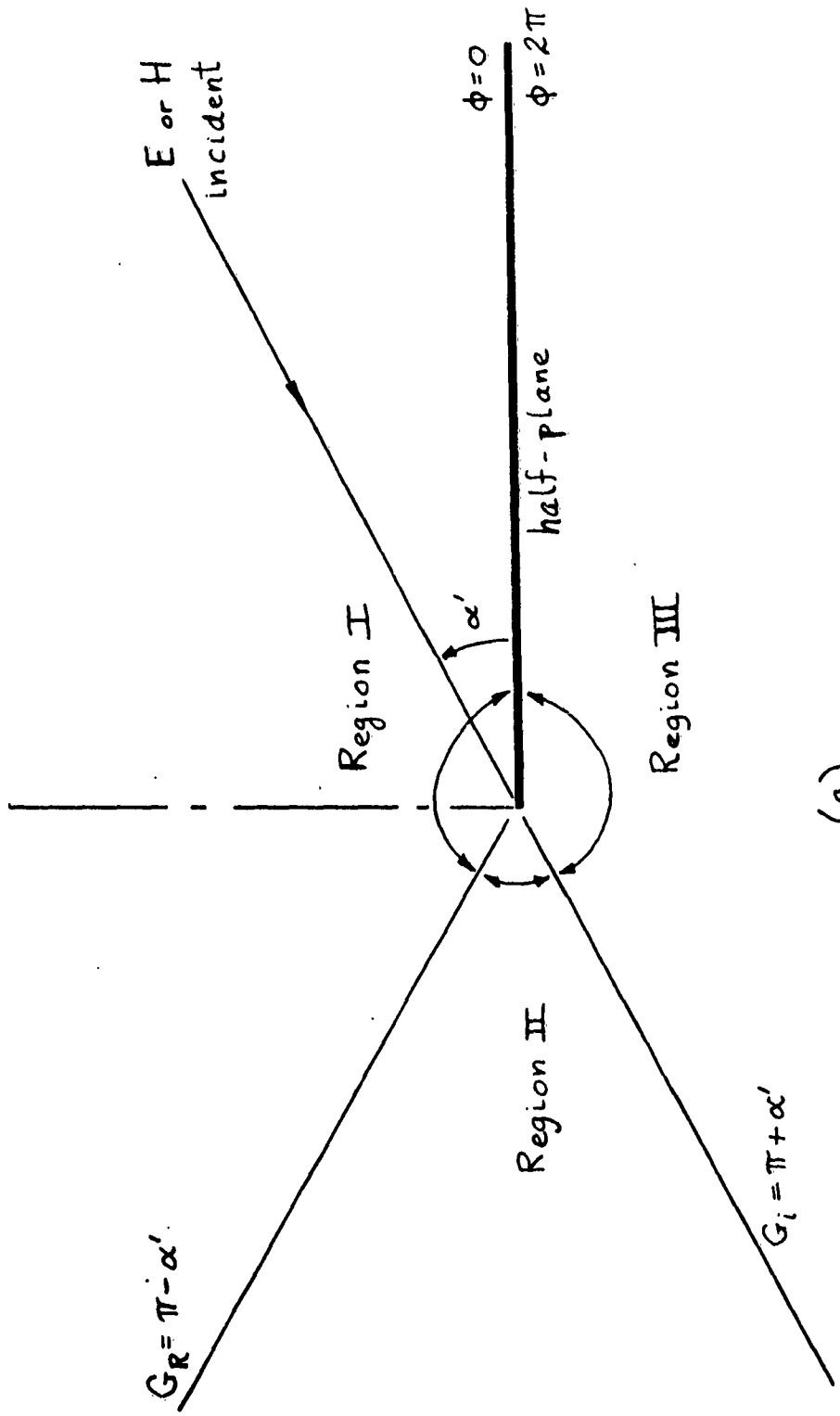
E or H
incident
φ=0
φ=2π
half-plane
Region I
α'
Region III
Region II
$G_R = \pi - \alpha'$
$G_i = \pi + \alpha'$

(a)

edge and on the surface we find an associated current distribution on the half-plane that decays rapidly away from the edge. In fact, in the far zone of the edge diffracted field, when $1/\sqrt{kr} \ll r$ (r = distance from the edge), the energy all appears to flow from the edge itself. That is, the edge is the center of phase of the far edge diffracted field. Hence Keller, in his geometrical theory of diffraction is able to represent this diffraction by rays emanating from the edge itself.

We must note that the geometrical optics representation of the far zone edge diffracted field is not a geometrical optics field. The geometrical optics field is that first term of the asymptotic expansion in inverse powers of k where k is allowed to approach an infinite value. As we will see shortly, the far field term of the edge field is a $1/\sqrt{kr}$ term (k and r always occur together in this dimensionless problem). Hence the edge field becomes zero for $k \to \infty$, except at the shadow boundaries where the asymptotic expansion does not converge. However, the $1/\sqrt{kr}$ term in this problem is the first correction to the geometrical optics field. It is the second term of an asymptotic expansion in $k^{-\frac{n}{2}}$ of the exact field, the first term being the geometrical optics field.

Letting U_o be either the electric or magnetic field depending upon whether E or H is oriented parallel to the edge, we express the incident plane wave by

$$U_o = e^{-ikr\cos(\phi-\alpha')} \quad (e^{-iwt} \text{ suppressed}). \qquad (1)$$

If U is the scattered E or H field, as appropriate, then the solution[8]

can be expressed asymptotically (first two terms only) inside Regions I, II, or III, as

$$U_I = e^{-ikr\cos(\phi-\alpha')} \pm e^{-ikr\cos(\phi+\alpha')} - \frac{1+i}{4\sqrt{\pi kr}} e^{ikr}\left[\sec\left(\frac{\phi-\alpha'}{2}\right) \pm \sec\left(\frac{\phi+\alpha'}{2}\right)\right], \tag{2}$$

$$U_{II} = e^{-ikr\cos(\phi-\alpha')} - \frac{1+i}{4\sqrt{\pi kr}} e^{ikr}\left[\sec\left(\frac{\phi-\alpha'}{2}\right) \pm \sec\left(\frac{\phi+\alpha'}{2}\right)\right], \tag{3}$$

and

$$U_{III} = -\frac{1+i}{4\sqrt{\pi kr}} e^{ikr}\left[\sec\left(\frac{\phi-\alpha'}{2}\right) \pm \sec\left(\frac{\phi+\alpha'}{2}\right)\right]. \tag{4}$$

It is clear from the above equations that the asymptotic solution blows up at the shadow boundaries given by $\phi = \pi \pm \alpha'$. The negative and plus signs are used accordingly as

$$\left\{\begin{array}{l} - \quad \text{when } U = E_z \text{ (parallel to edge)} \\ + \quad \text{when } U = H_z \text{ (parallel to edge).} \end{array}\right\} \tag{5}$$

If we subtract the geometrical optics field from the above equations, we are left with the edge diffracted field which is expressed identically in all regions, excluding the shadow boundaries, as

$$U_e = -\frac{(1+i)}{4\sqrt{\pi kr}} e^{ikr}\left[\sec\left(\frac{\phi-\alpha'}{2}\right) \pm \sec\left(\frac{\phi+\alpha'}{2}\right)\right]. \tag{6}$$

These expressions, (2) through (6), are valid to second order in the asymptotic expansion of the exact solution for the diffracted field and for

$$0 \leq \phi < 2\pi \quad \text{exclusive of} \quad \phi = G_r,\ G_i \,. \tag{7}$$

The accuracy of these equations, for a given (kr), is poorer near $\phi = G_r$ and $\phi = G_i$, since, of course, the convergence of the asymptotic expansion is more slow closer to G_r and G_i. Near the shadow boundaries G_r and G_i we must use the exact expression for U. We will give this expression only for the field near G_r and in Region I, since this is the region which concerns us in the synthesis problem. With δ defined as the angle away from $\phi = G_r$ in a negative ϕ direction, we have

$$U_e(\phi \lesseqgtr G_r) = -\left(\pm 1/2\, e^{ikr\cos\delta}\right) \tag{8}$$

$$\pm \frac{(1-i)}{2} e^{ikr\cos\delta} \int_0^2 \sqrt{\frac{kr}{\pi}}\, \sin(\delta/2)\; e^{i\frac{\pi}{2}\tau^2}\, d\tau$$

$$- \frac{(1+i)\; e^{ikr}}{4\sqrt{\pi kr}\, \sin(\alpha' + \delta/2)}$$

where $\delta = \pi - \alpha' - \phi$ and the integral in (8) is the complex Fresnel integral which is well tabulated.[14]

We may note in (6) that the phase center of this edge diffracted field

is at $r = 0$ (i.e., the phase of this function is a constant independent of ϕ), and the energy radiated appears to flow from this point.

Now in order to obtain an approximate solution to problems more complex than that of the half-plane, many other analysts have used the above Sommerfeld solution as the basis for their approximations. In all cases they assume that the knife edge of their diffracting obstacle is locally straight and that the conductor is locally flat. Braunbek[9], is analyzing the flat circular disk, assumed that the currents near the edge of the disk were the same as those for the half-plane (decaying as $(r)^{-1/2}$ away from the edge) and integrated the contributions of such currents along the edge contour to obtain the diffracted field. Millar[10] and Clemmow[11] analyzed the diffraction from an artibrarily shaped aperture in a plane conducting screen when a plane wave is normally incident upon the screen from one side. They assumed that a fictitious filamentary edge current exists along the aperture edge. This current is assumed to radiate the same field pattern as the extended current that Braunbek assumed, when the Braunbek field is evaluated in the far zone $\left[(kr)^{-1/2} << 1 \right]$. Despite this latter assumption, Millar and Clemmow obtained excellent results even up to the aperture. In fact their results are excellent even for apertures on the order of a wavelength in diameter (see the experimental results of Welch[12]).

Keller, in his theory of geometrical diffraction[7] from knife edges, also uses the Sommerfeld edge diffraction solution. However, he does not sum the contributions from all parts of the edge. The edge current at a given point on the edge contributes to the radiated field only in

the plane normal to the edge at that point. This method assumes that the same fictitious current filament exists along the edge that Millar and Clemmow assume.

In the formulation for the edge source which will follow, we will use the method of Keller. His far field results for the slit in a plane (analogous to our cylindrical problem) and also for the circular aperture in a conducting plane (analogous to our axially symmetric problem) are excellent even for slit widths and aperture radii of the order of one wavelength. In the slit problem, the edge is, of course, straight (as in our cylindrical problem). In Keller's problems, as in those of Millar and Welch, the edge is part of a flat conducting screen. Braunbek[16], however, also analyzed the problem of diffraction by a plane wave incident upon a semi-infinite truncated funnel. He also used the Sommerfeld half-plane solution as the basis for his approximation in this problem. In this case, the edge is part of a curved surface. The principle effect of the curved surface is not in altering the basic nature of the edge currents, but in altering their orientation in space and in altering the surface reflected geometrical optics field. These changes are considered in the analysis made here.

An additional assumption made in the analysis is that the field incident on the edge is locally a plane wave. This assumption is, or course, consistent with the other assumptions that the edge and screen are locally straight and flat.

III. The Edge Diffracted Field

Under the assumptions of symmetry which we have made, the present formulation will in general apply for either the cylindrical or rotationally symmetric system. The differences are minor, so we will discuss only the somewhat more practical rotationally or axially symmetric case.

A. Combining the Edge Fields from Opposite Edges

The plane of incidence of the field incident on the edge is normal to the plane containing the tangent to the edge. In this plane we have, according to Keller, radially directed rays emanating from the point caustic at the edge as illustrated on the following page. The ϕ-dependence of this distribution is given by equations (6) or (8). The angle α' can be determined, since the slope of the reflector at the edge and the angle of incidence of the primary source are given boundary conditions of the synthesis problem: $\theta_{1\,max}$, and $\left(\frac{dy_1}{dx_1}\right)_{max} = \tan 1/2\left[\theta_{1_{max}} - \theta_{2\,max}\right]$.

There are two edge sources radiating fields that must be summed in order to determine $J_e(\gamma_2)$, $C_{e_o}(\gamma_2)$, and $d_e(\gamma_2)$. These sources lie at opposite edges of the reflector in the plane containing the axis of the axially symmetric system. Each source contributes to the field at the point P as illustrated in the diagram following (c).

The field radiated from edge No. 1 will be designated $\mathcal{N}_{e_1}(r_1, \phi_1)$. This field is constructed of three factors. The first

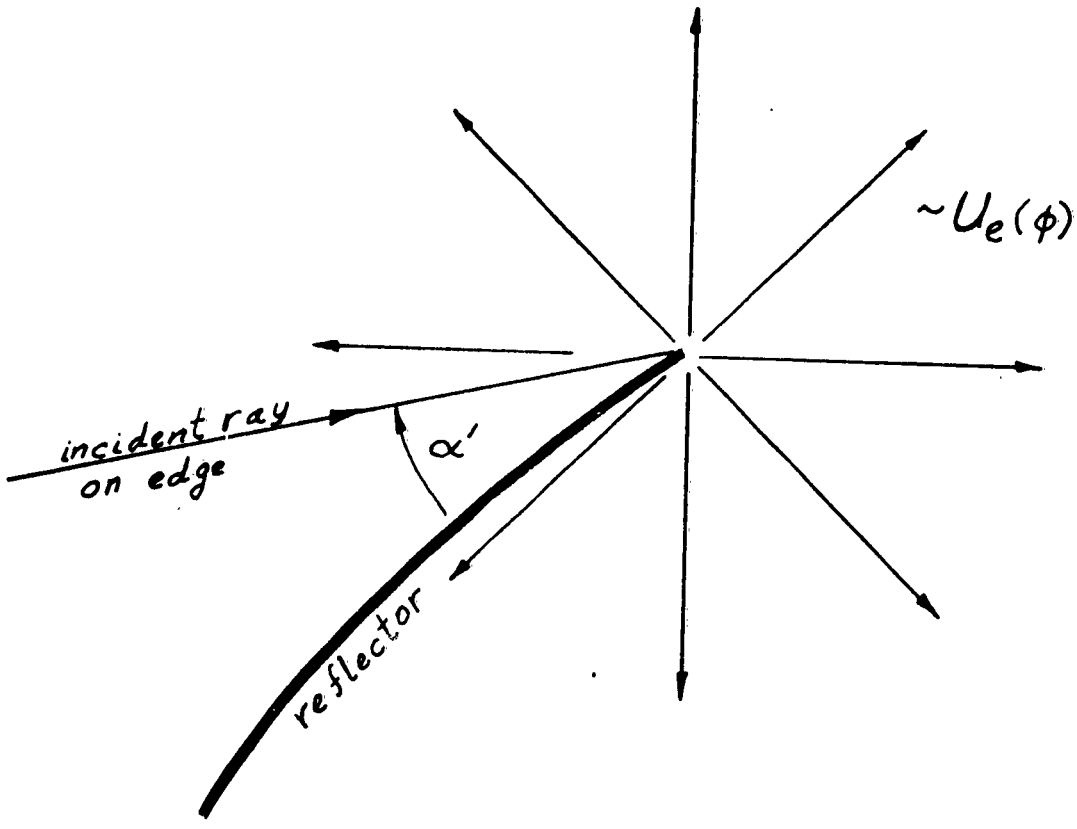

(b)

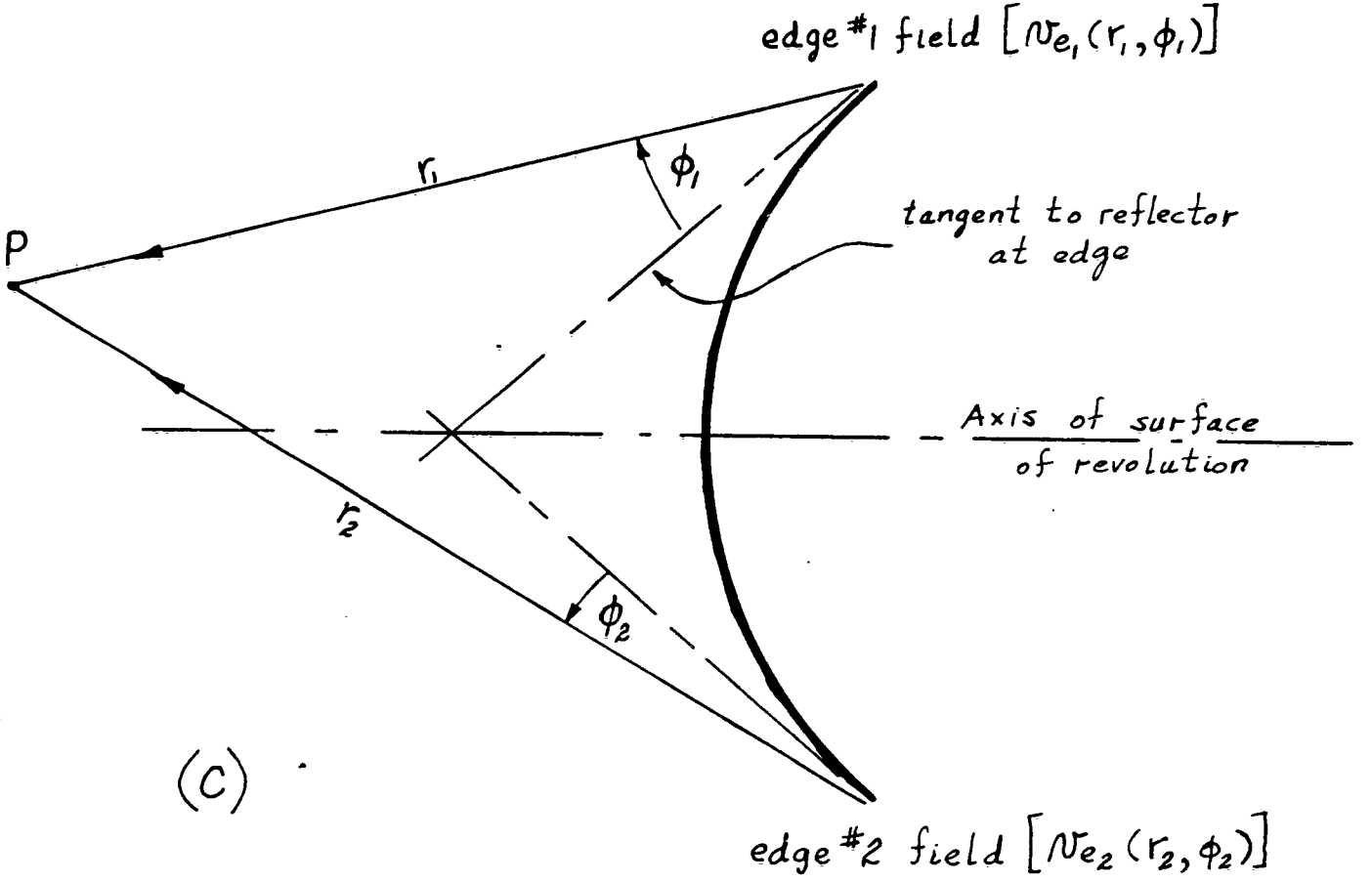
edge #1 field $[\mathcal{N}_{e_1}(r_1, \phi_1)]$
r_1
ϕ_1
P
tangent to reflector at edge
Axis of surface of revolution
r_2
ϕ_2
(C)
edge #2 field $[\mathcal{N}_{e_2}(r_2, \phi_2)]$

is given by equations (6), (7) and (8) except that for the axially symmetric case the curvature $(kr)^{-1/2}$ in formulas (6) through (8) becomes the Gaussian curvature when P is in the far zone field of the edges*. We designate this factor as $U_{e_1}(r_1, \phi_1)$. In this expression we will write $\mathscr{L}_1' = \mathscr{L}'$, since it is clear that the angle of incidence is the same for both edges. The field U_{e_1} is the edge field for an incident wave of unit amplitude and zero phase at the edge. The amplitude and phase of the incident wave at both edges is the same (polarization neglected for the moment) and given by the boundary conditions and the given primary source field. We find the amplitude and phase of the wave incident at the edges as follows:

The primary source electric field evaluated on reflector No. 1 is given by (for the preferred polarization component)

$$E_1 = G_1 e^{ik\left[r_1 + C_{p_o}(\theta_1)\right]} \mathscr{L}_1(\theta_1)$$

where G_1 is a factor proportional to the Gaussian curvature. Consider the diagram following (d).

At the reflector edge we have

$$\mathscr{L}_{1_m} = \mathscr{L}_1(\theta_{1_m}) = \sqrt{I_1(\theta_{1_m})} \tag{9}$$

The curvature of the wavefront at the reflector depends on

---

* See Appendix II or Reference 7. See also equation (24b).

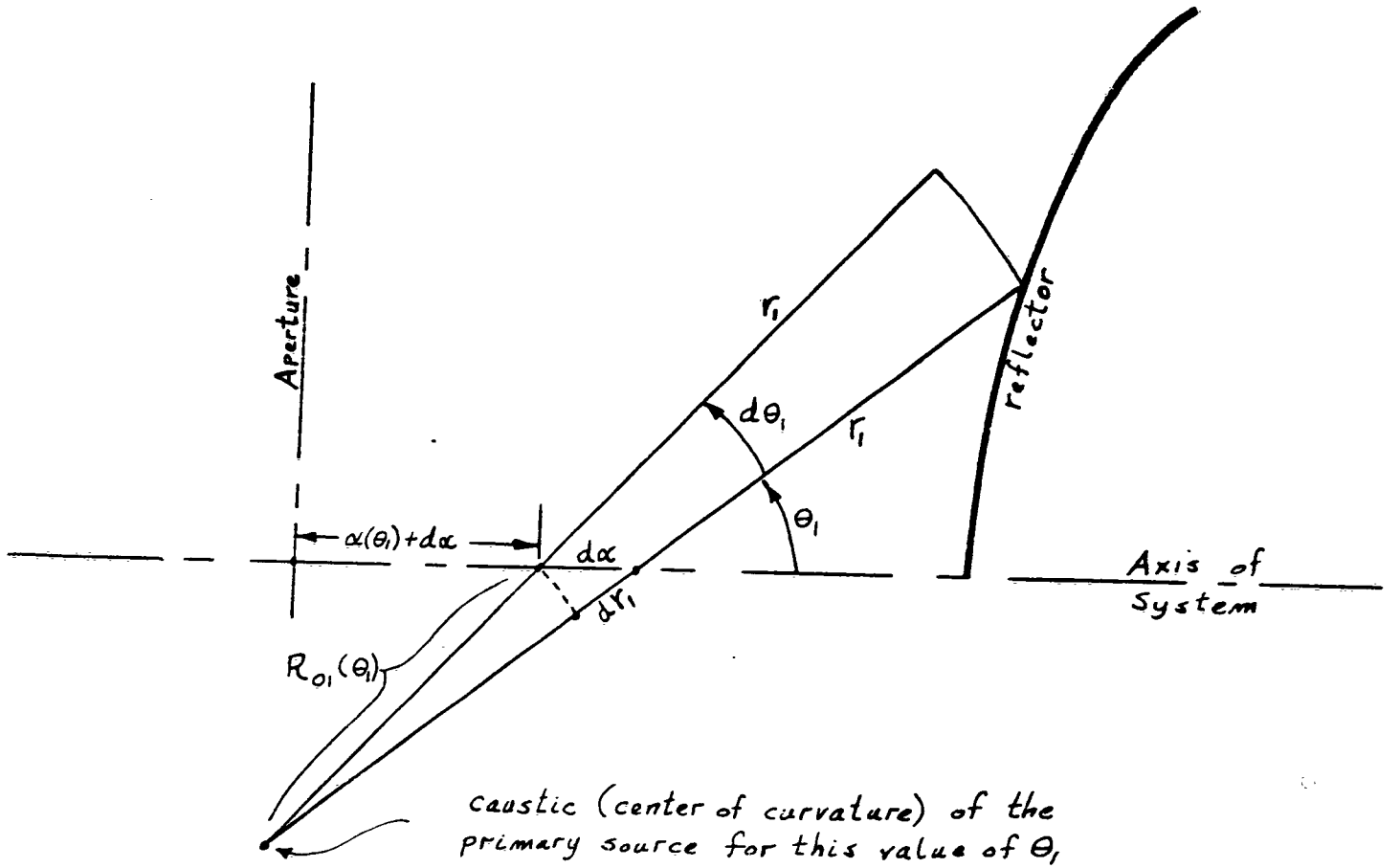
Aperture
r_1
$d\theta_1$
r_1
reflector
$\alpha(\theta_1)+d\alpha$
$d\alpha$
θ_1
Axis of System
dr_1
$R_{01}(\theta_1)$
caustic (center of curvature) of the primary source for this value of θ_1

(d)

$R_{o_1}(\theta_1)$ and $r_1(\theta_1)$. From the diagram we find that

$$R_{o_1} = -\left(\frac{d\alpha}{d\theta_1}\right) \sin\theta_1, \text{ and } R_{o_{1m}} = -\left(\frac{d\alpha}{d\theta_1}\right)_m \sin\theta_{1_m}. \quad (9a)$$

The radius of curvature in the plane of the above diagram is then

$$R_1 = R_{o_1} + r_1, \text{ and } R_{1_m} = R_{o_{1m}} + r_{1m} \text{ at the edge.} \quad (9b)$$

Hence we find for G_1 at the edge

$$G_{1m}^{-1} = \sqrt{(kR_{1m})(k r_{1m})}\ ^*$$

The phase of the incident primary field at the edges is given by

$$e^{ik\left[r_{1_{max}} + C_{po}(\theta_{1_{max}})\right]} \equiv e^{ik\psi_m} \quad (10)$$

Hence the edge diffracted field at edge No. 1 is given by

$$\mathcal{N}_{e_1}(r_1, \phi_1) = \mathcal{A}_{1_m} G_{1_m} U_{e_1}(r_1, \phi_1)\, e^{ik\psi_m} \quad (11)$$

and similarly the edge diffracted field at edge No. 2 is given by

$$\mathcal{N}_{e_2}(r_2, \phi_2) = \mathcal{B}_{1_m} G_{1_m} U_{e_2}(r_2, \phi_2)\, e^{ik\psi_m} \quad (12)$$

---

* Note that G_1 is not the complete formula for the Gaussian curvature for the primary field. The Gaussian curvature is given by

$G_{A_1} = \left[(k R_1)(k r_1 \sin\theta_1)\right]^{-1/2}$. See Appendix II for G_{A_e}, the Gaussian curvature for the edge field, which is obtained similarly.

The edge diffracted field at P is (r_1 and $r_2 >> 2\ X_{1\ max}$)

$$U_e = U_{e_1}(r_1, \phi_1) \pm U_{e_2}(r_2, \phi_2). \tag{13}$$

Whether the plus or minus sign in (13) is used depends on the vector symmetry of the problem. In the acoustic case we always use the plus sign. In the cylindrical case we generally would use the plus sign also. In the axially symmetric case, when the incident vector field on the edges is polarized identically with respect to the edge for all rotation angles (vector symmetry) then we must use the minus sign. When the incident field is linearly polarized in the axial case (E-field in same absolute direction everywhere) we must perform an averaging of the fields around the edges such as was performed by Rusch[3]. How this may be done will be discussed subsequently. For the axially symmetric case near the axis we cannot use (13) accurately, since the axis is a caustic of the system. A caustic approximation will be presented shortly and is discussed in Appendix II.

Our next steps should be to first let P become far from the edges, i.e., let $(k r_1)^{-1} >> 1$ and $(k r_2)^{-1} >> 1$ (this is actually implied already when we assume r_1 and $r_2 >> 2\ X_{1_m}$). This is consistent with geometrical optics approximations. To determine $J_e(\gamma_2)$, $C_{e_o}(\gamma_2)$, and $d_e(\gamma_2)$ we must first determine the phase contours of the far field. This will complete the determination of the edge field. Before proceeding to determine these quantities we should, however, clarify three important details about the expressions for U_{e_1} and U_{e_2}. The

first concerns the precise form of U_e when the indicent plane wave polarization is neither normal nor parallel to the plane of incidence. The second question concerns the precise value of ϕ near G_r, the shadow boundary, at which point equation (6) must be replaced by (8). The third question concerns the manner in which the caustic axis for the axial system will be accounted for.

B. Polarization at an Angle γ with Respect to the Edge

In order to resolve the question concerning the incident polarization, let us define

$$A = -\frac{(1+i)}{4\sqrt{\pi}} G_{A_e} e^{ikr} \left[\sec\left(\frac{\phi - \alpha'}{2}\right)\right] \text{and} \quad (14)$$

$$B = -\frac{(1+i)}{4\sqrt{\pi}} G_{A_e} e^{ikr} \left[\sec\left(\frac{\phi + \alpha'}{2}\right)\right] \quad (15)$$

when ϕ is not near G_r, and

$$B = -\frac{(1+i)}{4\sqrt{\pi}} G_{A_e} e^{ikr} \left[\sqrt{2\pi}\, G_{A_e}^{-1} e^{-ikr(1+\cos[\phi+\alpha']\,)} \cdot e^{i\frac{3\pi}{4}} \cdot \left\{\sqrt{2}\, e^{-i\frac{\pi}{4}} \int_0^{\frac{2}{\sqrt{\pi}} G_{A_e}^{-1} \cos\left(\frac{\phi+\alpha'}{2}\right)} \exp\left(i\frac{\pi}{2}\tau^2\right) d\tau - 1\right\}\right] \quad (15a)$$

when ϕ is near G_r.

The quantity G_{A_e} is the appropriate "curvature" for the system as explained in Appendix II, where

$$G_{A_e} = 1/(kr \sin^{1/2} |\Gamma_2|) \quad \text{(in the far zone away from } |\Gamma_2| = 0)^* \tag{14a}$$

The angle Γ_2 is the angle from the horizontal defined in equations (26) and (27). See also Figure 1 of this chapter. The validity of (15a) when $G_{A_e} = 1/(kr \sin^{1/2} |\Gamma_2|)$ is justified by the asymptotic form for (15a) (see Sommerfeld[8]) in a three dimensional system. Equations (14), (15), and (15a) are identical with (6) and (8) when G_{A_e} is accounted for.

When the incident electric vector is polarized parallel to the edge we have

$$U_e = U_{e_{11}} = A - B \tag{16}$$

and when the electric vector is polarized normal to the edge we have

$$U_e = U_{e_\perp} = A + B \tag{17}$$

Now let the incident electric vector be polarized at an angle with respect to the edge. Then we find

$$U_{e_{11}} = (\cos\gamma)(A + B) \quad \text{and} \tag{18}$$

$$U_{e_\perp} = (\sin\gamma)(A + B). \tag{19}$$

---

* See Appendix II.

Hence we see that the edge diffracted field polarization does not remain fixed for all ϕ. In this event we will consider the field component that is normal to the γ-direction along a ray as a cross-polarized component which must be accounted for. The desired component in the γ-direction is found from

$$U_{e_{11}} \cos\gamma = U_{e_{11}\gamma} = \cos^2\gamma\ (A - B)$$

and $$U_{e_\perp} \sin\gamma = U_{e_\perp\gamma} = \sin^2\gamma\ (A + B)$$

so that

$$U_e = U_{e_{11}\gamma} + U_{e_\perp\gamma} = A - B\ (\cos 2\gamma) \qquad (20)^*$$

When the polarization is either normal or parallel to the edge, there is no cross-polarized edge field. It is clear that in case the preferred polarization is, for example, right circularly polarized, then a "cross-polarized" left circular component will exist in the edge diffracted fiends. (Note: If a right circular wave is incident on the edge, then the principle polarization reflected is left circular as it is for reflection from any conducting surface. This fact was taken into account in the previous statement.)

Equation (20) is suggestive of an "averaging" method which can be used when the incident polarization is not rotationally symmetric or, in other words, those cases where $\gamma = \gamma(\theta)$ and θ is the angle of rotation about the axis of the axially symmetric system. For example, if the incident wave on the subreflector

---

* See equation (20a) which follows (24),which follows.

is linearly polarized, that is $\gamma = \theta$, then we may use as an

<u>average edge field</u>

$$U_e = A,$$

for on the average we do have $\gamma = \pi/4$ and $\gamma = 3\pi/4$ for the top and bottom halves of the reflector. When using $U_e = A$ we would also use

$$\mathcal{N}_e = \mathcal{N}_{e_1} + \mathcal{N}_{e_2}$$

from equation (13), and hence would not get a zero on the axis or caustic from this equation.

C. <u>Field Near the Shadow Boundary $\phi = G_r$</u>

We will determine a value of $\phi \lesssim G_r$ at which we will exchange (15) for (15a) in evaluating the field. This value is somewhat arbitrary and is chosen for analytical convenience and for reasonable approximation. Before considering this question further, it will be necessary to decide upon a value of r at which to evaluate B when $\phi = \pi - \alpha'$.

At $\phi = \pi - \alpha'$, the value of B at the aperture is given for $r = \rho_{2_{max}} = \rho_{2m}$. Since the main reflector is in the far zone of the subreflector, the r dependence of equation (15a) is given essentially by the factor

$$- \frac{(1+i)}{4\sqrt{\pi}} G_{A_e} e^{ikr}$$

when $\phi \lesssim (\pi - \alpha') = G_r$ (see the asymptotic expansion of Sommerfeld[8]). Hence for our purposes we may use

$$B = -\frac{(1+i)}{4\sqrt{\pi}} G_{Ae} e^{ikr} \left[\sqrt{2\pi}\, G_{Ae}^{-1}(\rho_{2m})\, e^{-ik\rho_{2m}\left[1+\cos(\theta+\alpha')\right]}\, e^{i\frac{3\pi}{4}} \cdot \left\{ \sqrt{2}\, e^{-i\frac{\pi}{4}} \int_0^{\frac{2}{\sqrt{\pi}} G_{Ae}^{-1}(\rho_{2m})\cos\left(\frac{\phi+\alpha'}{2}\right)} \exp\left(i\frac{\pi}{2}\tau^2\right) d\tau - 1 \right\} \right], \tag{15b}$$

where

$$G_{Ae}^{-1}(\rho_{2m}) = \sqrt{k^2 \rho_{2m}^2 \sin\left|\theta_{2m}\right|} \tag{15c}$$

and

$$\left|\Gamma_{2m}\right| \approx \left|\theta_{2m}\right| \quad \text{(See Appendix II).} \tag{15d}$$

Our problem now is to connect equations (15) and (15b). The best way to connect these equations would probably be to find two values of ϕ for which they are equal in amplitude and in phase. In this way we could maintain the continuity of both the amplitude and phase of the edge field. Connecting the amplitude as indicated in the diagram following (e) would in principle be simple, although connecting the phase may lead to some difficulties. Whereas the range $\phi_r \leq \phi \leq G_r$ is small for the amplitude connection, it may be large for the phase connection. For the sake of simplicity in analysis and because the range $\phi_r \leq \phi \leq G_r$ will be small, we will use instead a somewhat simpler connection. For the phase of B in the region $\phi_r \leq \phi \leq G_r$ we will use the phase of equation (15). This phase is constant over the entire range $0 \leq \phi \leq G_r$. This is justified because the region $\phi_r \leq \phi \leq G_r$ is very small;

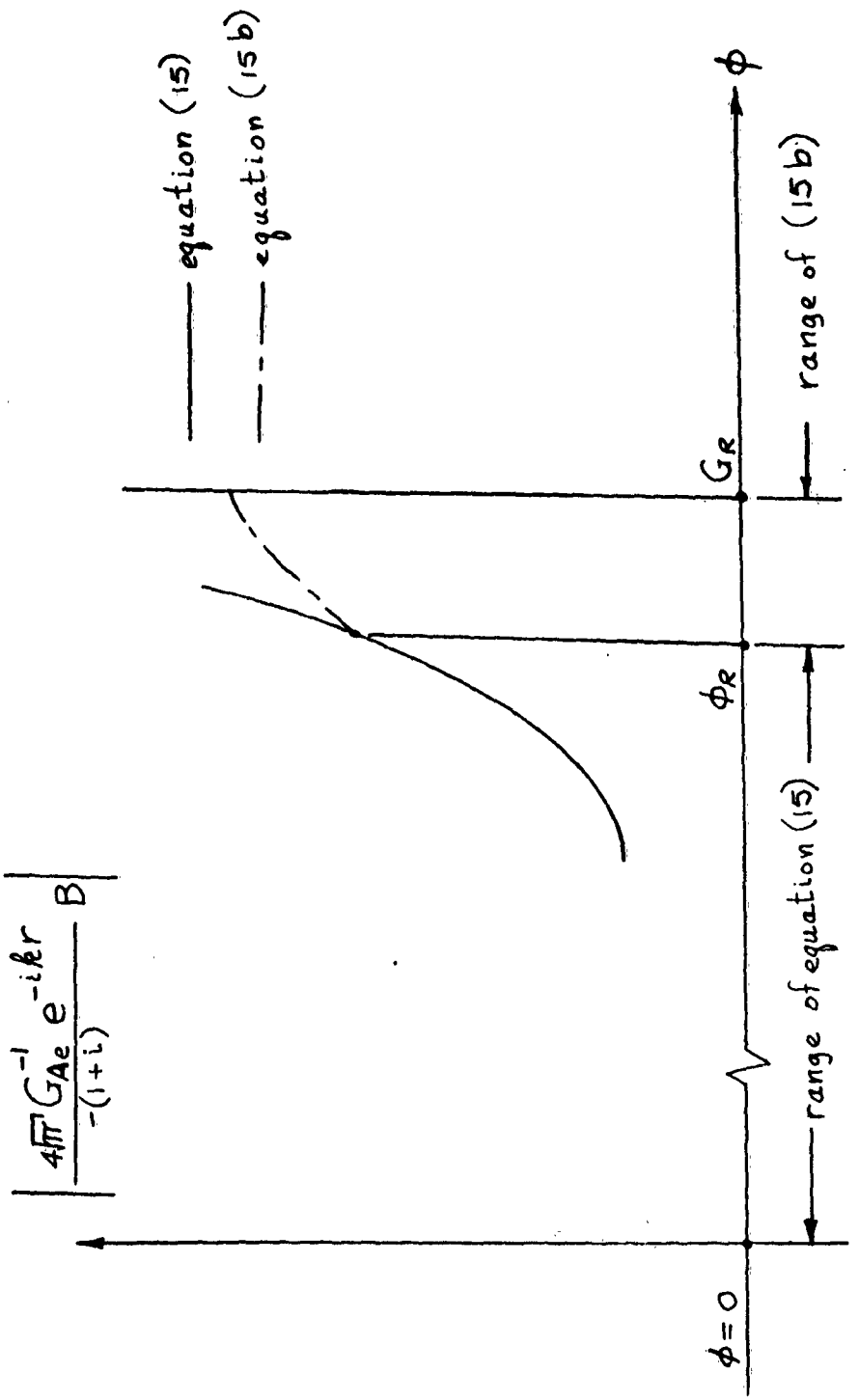
$\left| \frac{4\pi G_{Ae}^{-1} e^{-ikr}}{-(1+i)} B \right|$
equation (15)
equation (15b)
ϕ
G_R
ϕ_R
range of (15b)
range of equation (15)
$\phi = 0$

(e)

usually less than 1° or 2°. Hence

$$\left[\text{phase of } B\right] = \left(-\frac{3\pi}{4} + kr\right) \text{ for } (0 \leq \phi \leq G_r). \tag{21}$$

We will connect the amplitude by assuming that the amplitude is constant in the region $\phi_r \leq \phi \leq G_r$ and is given by equation (15b) evaluated at $\phi = G_r$. The value of ϕ_r is determined by finding the intersection as shown in the diagram on the following page (f). If we evaluate the value of (15b) at $\phi = G_r$ (the integral term vanishes at $\phi = G_r$ when r is finite) and set the amplitude of this value equal to the amplitude of equation (15) we find

$$\phi_r = -\alpha' + 2 \operatorname{arcsec}\left[\sqrt{2\pi}\, k \rho_{2m} \sin^{1/2} |\phi_{2m}|\right], \tag{22}$$

and the magnitude of B in the range $\phi_r \leq \phi \leq G_r$ given by

$$|B| = \left| -\frac{(1+i)}{4\sqrt{\pi}} G_{Ae} e^{ikr} \left\{\sqrt{2\pi}\, G_{Ae}^{-1}(\rho_{2m})\right\} \right| \text{ for } (\phi_r \leq \phi \leq G_r). \tag{23}$$

In summary then, we may state that U_e is given by (20) where A is given by (14) and B is given by

$$B = \begin{cases} \left[-\frac{(1+i)}{4\sqrt{\pi}} G_{Ae} e^{ikr}\right] \cdot \left[\sec\left(\frac{\phi + \alpha'}{2}\right)\right] & \text{for } (0 \leq \phi \leq \phi_r) \\ \left[-\frac{(1+i)}{4\sqrt{\pi}} G_{Ae} e^{ikr}\right] \cdot \left[\sqrt{2\pi}\, G_{Ae}^{-1}(\rho_{2m})\right] & \text{for } (\phi_r \leq \phi \leq G_r) \end{cases} \tag{24}$$

where ϕ_r is given by (22).

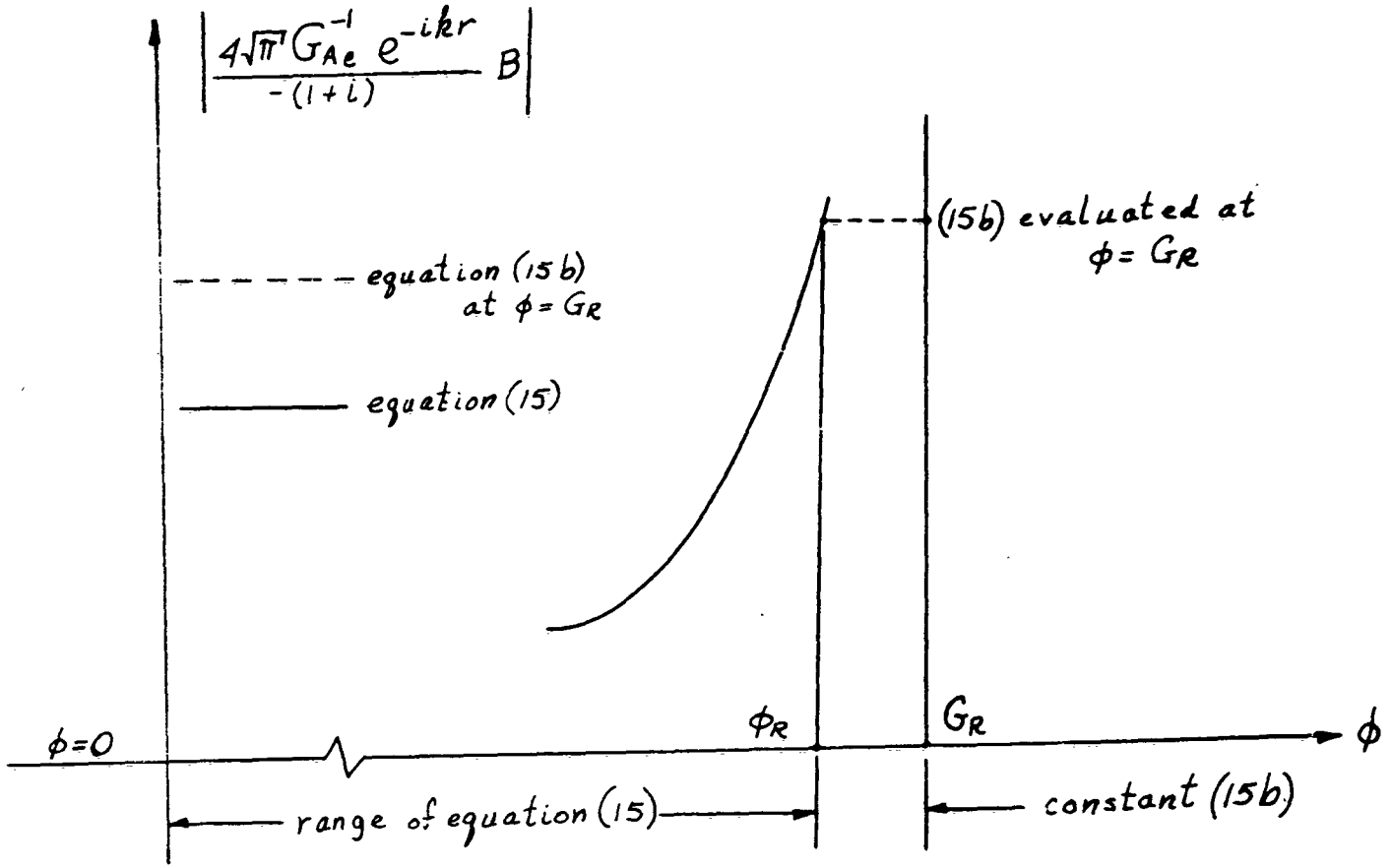
$\left|\frac{4\sqrt{\pi}\,G_{Ae}^{-1}\,e^{-ikr}}{-(1+i)}\,B\right|$
(15b) evaluated at $\phi = G_R$
equation (15b) at $\phi = G_R$
equation (15)
$\phi = 0$
ϕ_R
G_R
ϕ
range of equation (15)
constant (15b)

(f)

Before proceeding to determine $J_e(\gamma_2)$, $d_e(\gamma_2)$, and $C_{eo}(\gamma_2)$, two additional points concerning the range of ϕ for equation (20) (and the above equations for A and B) should be mentioned. As was indicated in equation (7), we require

$$0 \leq \phi < 2\pi \tag{7}$$

Because of the fact that ϕ is divided by two in the equations, the solutions are not periodic in 2π, but rather over 4π. Hence we shall define

$$U_e \equiv 0 \quad \text{unless } (0 \leq \phi < 2\pi). \tag{20a}$$

Taking account of (20a) may become important, for example, if the subreflector is very curved at the edge and the ray from edge No. 2 in the direction of θ_{2max} (toward X_{2m} of reflector No. 2) is blocked or shadowed. In this event the value of ϕ for this ray from edge No. 2 will be negative and (20a) would indicate that $U_e = 0$ as desired.

D. Value of G_{Ae}

Equation (24) specifies two separate ranges of values over which two different equations for B are valid. There are two possible expressions for G_{Ae} depending upon whether $\Gamma_2 = 0$ or not (i.e., Γ_2 is near the caustic at $\Gamma_2 = 0$) and whether we are considering the top edge (U_{e_1}) or bottom edge (U_{e_2}).

We have in general that $G_{Ae}^{-1} \approx \sqrt{(kr)/(kr \sin \Gamma_2 \pm k X_{1m})}$ where the + sign is for U_{e_1} and the - sign is for U_{e_2}.

For $\left|\sin \Gamma_2\right| >> \left| X_{1m}/r \right|$ we have $G_{Ae}^{-1} \simeq kr \sin^{1/2}\left|\Gamma_2\right|$ as the far zone approximation off the caustic. Near the caustic for any finite r we should use

$$G_{Ae}^{-1} = kr \sqrt{\left|\sin \Gamma_2 \pm (X_{1m}/r\right|} \quad .$$

In the vicinity of $\Gamma_2 \approx 0$ we have as an approximation for $r = r_c \approx (\alpha+\beta) + y_3$. An estimate for r_c may be taken as

$$r_c = \rho_{2m} \quad . \tag{24a}$$

More suitable estimates may be made for specific problems.

When $\Gamma_2 = 0$, G_{Ae}^{-1} has the same value for the top and bottom edges (U_{e1} and U_{e2}). Away from $\Gamma_2 = 0$ when $\left|\sin \Gamma_2\right| >> \left|X_{1m}/r_c\right|$, the value of G_{Ae}^{-1} is again independent of the edge designation. As an approximation in the small angular sector near the caustic, we will take

$$G_{Ae}^{-1} = kr \sqrt{\sin \left|\Gamma_2\right| + \left(\frac{X_{1m}}{r_c}\right)} \qquad (0 \leq \left|\Gamma_2\right| \leq \left|\Gamma_{2m}\right|) \tag{24b}$$

for both edges and thus simplify our computations considerably. For the case of vector symmetry, this will give $N_e = 0$ (see equation (13)) for $\Gamma_2 = 0$ which is correct so the error will be over a small angular region comprising a very small solid angle. This is explained further in Appendix II. We choose the + sign in equation (24b) to avoid the infinity which would occur with the - sign when the field of edge No. 2 is evaluated near $\Gamma_2 = 0$.

E. The Total Edge Field

In order to compute the actual edge diffracted field in the far zone of the two edges combined, we let $P \to \infty$ and hence rays r_1 and r_2 to point P from each edge become parallel. We designate their common angle with the y_1 axis as Γ_2. In accordance with Figure 1 and with reference to the distance R from the origin, we have

$$r_1 = R - X_{1m} \sin \Gamma_2 \tag{25}$$

and

$$r_2 = R + X_{1m} \sin \Gamma_2. \tag{25a}$$

Equations (25) and (25a) are used to replace r_1 and r_2 only in the phase factor e^{ikr} indicated in the expressions for U_{e1} and U_{e2} which are obtained from (14) and (24). The r term in the equations for G_{Ae}, equations (24a) and (24b), are replaced by

$$r_1 \approx r_2 \approx R \tag{25b}$$

in accordance with the customary far field assumptions.

From Figure 1 we also readily find

$$\phi_1 = \frac{\pi}{2} + \Gamma_2 + \left(\frac{\theta_{1m} - \theta_{2m}}{2}\right) \tag{26}$$

$$\phi_2 = \frac{\pi}{2} - \Gamma_2 + \left(\frac{\theta_{1m} - \theta_{2m}}{2}\right) \quad \text{and} \tag{27}$$

$$\alpha' = \frac{\pi}{2} - \left(\frac{\theta_{1m} + \theta_{2m}}{2}\right). \tag{28}$$

With (25) through (28) substituted into the expressions for A and B in (14) and (24) we obtain

$$A_1 = \left[-\frac{(1+i)G_{Ae}e^{ikr}}{4\sqrt{\pi}} \right] e^{-ikX_{1m}\sin\Gamma_2} \left[\sec\left(\frac{\Gamma_2 + \theta_{1m}}{2}\right) \right] \tag{29}$$

$$A_2 = \left[-\frac{(1+i)G_{Ae}e^{ikr}}{4\sqrt{\pi}} \right] e^{+ikX_{1m}\sin\Gamma_2} \left[\sec\left(\frac{\Gamma_2 - \theta_{1m}}{2}\right) \right] \tag{30}$$

$$\begin{cases} B_1 = \left[-\dfrac{(1+i)G_{Ae}e^{ikr}}{4\sqrt{\pi}} \right] e^{-ikX_{1m}\sin\Gamma_2} \left[-\csc\left(\dfrac{\Gamma_2 - \theta_{2m}}{2}\right) \right] & (31) \\ \qquad \text{for } (0 \lesseqgtr \phi_1 \lesseqgtr \phi_r) \\ B_2 = \left[-\dfrac{(1+i)G_{Ae}e^{ikr}}{4\sqrt{\pi}} \right] e^{+ikX_{1m}\sin\Gamma_2} \left[\csc\left(\dfrac{\Gamma_2 + \theta_{2m}}{2}\right) \right] & (32) \\ \qquad \text{for } (0 \lesseqgtr \phi_2 \lesseqgtr \phi_r) \end{cases}$$

and

$$\begin{cases} B_1 = \left[-\dfrac{(1+i)G_{Ae}e^{ikr}}{4\pi} \right] e^{-ikX_{1m}\sin\Gamma_2} \left[\sqrt{2\pi}\, G^{-1}(\rho_{2m}) \right] & (31a) \\ \qquad \text{for } (\phi_r \lesseqgtr \phi_1 \lesseqgtr G_r) \\ B_2 = \left[-\dfrac{(1+i)G_{Ae}e^{ikr}}{4\pi} \right] e^{+ikX_{1m}\sin\Gamma_2} \left[\sqrt{2\pi}\, G^{-1}(\rho_{2m}) \right] & (32a) \\ \qquad \text{for } (\phi_r \lesseqgtr \phi_2 \lesseqgtr G_r) \end{cases}$$

From equations (11), (12) and (20) we get

$U_{e1} = A_1 - B_1 \cos 2\gamma$, and $U_{e2} = A_2 - B_2 \cos 2\gamma$ or

$$\nu_{e1} = \left[-\frac{(1+i)\alpha_{1m}G_{1m}G_{Ae}e^{ik(R+\psi_m)}}{4\sqrt{\pi}} \right] e^{-ikX_{1m}\sin\Gamma_2} \left[\sec\left(\frac{\Gamma_2 + \theta_{1m}}{2}\right) + \csc\left(\frac{\Gamma_2 - \theta_{2m}}{2}\right)\cos 2\gamma \right] \tag{33}$$

$$\text{for } (0 \lesseqgtr \phi_1 \lesseqgtr \phi_r)$$

$$V_{e_2} = \left[\frac{-(1+i)\delta_{1m} G_{1m} G_{Ae}}{4\sqrt{\pi}}\right] e^{ik(R+\psi_m)} e^{+ikX_{1m}\sin\Gamma_2} \left[\sec\left(\frac{\Gamma_2 - \theta_{1m}}{2}\right) - \csc\left(\frac{\Gamma_2 + \theta_{2m}}{2}\right)\cos 2\gamma\right] \quad (34)$$

$$\text{for } (0 \lesseqgtr \phi_2 \lesseqgtr \phi_r)$$

$$V_{e_1} = \left[\frac{-(1+i)\delta_{1m} G_{1m} G_{Ae}}{4\sqrt{\pi}}\right] e^{ik(R+\psi_m)} e^{-ikX_{1m}\sin\Gamma_2} \left[\sec\left(\frac{\Gamma_2 + \theta_{1m}}{2}\right) - \sqrt{2\pi}\, G^{-1}(\rho_{2m})\cos 2\gamma\right] \quad (33a)$$

$$\text{for } (\phi_r \lesseqgtr \phi_1 \lesseqgtr G_r)$$

$$V_{e_2} = \left[\frac{-(1+i)\delta_{1m} G_{1m} G_{Ae}}{4\sqrt{\pi}}\right] e^{ik(R+\psi_m)} e^{+ikX_{1m}\sin\Gamma_2} \left[\sec\left(\frac{\Gamma_2 - \theta_{1m}}{2}\right) - \sqrt{2\pi}\, G^{-1}(\rho_{2m})\cos 2\gamma\right] \quad (34a)$$

$$\text{for } (\phi_r \lesseqgtr \phi_2 \lesseqgtr G_r).$$

For the sake of convenience in future manipulations, we define from equations (33) and (34),

$$Z_1 = \left[\sec\left(\frac{\Gamma_2 + \theta_{1m}}{2}\right) + \csc\left(\frac{\Gamma_2 - \theta_{2m}}{2}\right)\cos 2\gamma\right] \text{ for } (0 \lesseqgtr \phi_1 \lesseqgtr \phi_r) \quad (35)$$

$$Z_2 = \left[\sec\left(\frac{\Gamma_2 - \theta_{1m}}{2}\right) - \csc\left(\frac{\Gamma_2 + \theta_{2m}}{2}\right)\cos 2\gamma\right] \text{ for } (0 \lesseqgtr \phi_2 \lesseqgtr \phi_r) \quad (36)$$

$$Z_1 = \left[\sec\left(\frac{\Gamma_2 + \theta_{1m}}{2}\right) - \sqrt{2\pi}\, G_{Ae}^{-1}(\rho_{2m})\cos 2\gamma\right] \text{ for } (\phi_r \lesseqgtr \phi_1 \lesseqgtr G_r) \quad (35a)$$

$$Z_2 = \left[\sec\left(\frac{\Gamma_2 - \theta_{1m}}{2}\right) - \sqrt{2\pi}\, G_{Ae}^{-1}(\rho_{2m})\cos 2\gamma\right] \text{ for } (\phi_r \lesseqgtr \phi_2 \lesseqgtr G_r). \quad (36a)$$

Note that Z_1 is the field contribution from edge No. 1 and that

Γ_2 is the field contribution from edge No. 2. A common factor from each of these contributions is omitted as may be seen in equation (37) below.

From equation (13) we get for the edge diffracted field subject to the conditions of symmetry specified earlier, the result

$$\mathcal{V}_e = \mathcal{V}_{e_1} \pm \mathcal{V}_{e_2} = \left[\frac{-(1+i)\,g_{1m} G_{1m}\, G_{Ae}\, e^{ik(R + \psi_m)}}{4\sqrt{\pi}} \right] \tag{37}$$

$$\cdot \left[(Z_1 \pm Z_2) \cos(k X_{1m} \sin\Gamma_2) + i\,(-Z_1 \pm Z_2) \sin(k X_{1m} \sin\Gamma_2) \right]$$

where the appropriate values of Z_1 and Z_2 are to be used from equations (35), (35a), (36), and (36a) depending on the values of ϕ_1 and ϕ_2.

The edge diffracted field given by (37) is complex and no fixed phase center exists for this field. Hence the phase contours are not circles. Therefore $\Gamma_2 \neq \gamma_2$. From (37) we can derive $\Gamma_2(\gamma_2)$, $d_e(\gamma_2)$, and $C_{e_o}(\gamma_2)$. The value of $g'_e(\Gamma_2)$* or $J'_e(\Gamma_2)$ can be found directly from (37). When $\Gamma_2(\gamma_2)$ is found subsequently, then we can obtain $g_e(\gamma_2)$ or $J_e(\gamma_2)$. As will be made more evident shortly, we cannot obtain $J_e(\gamma_2)$ from $J'_e(\Gamma_2)$ simply by substituting $\Gamma_2(\gamma_2)$ for Γ_2. The transformation is more complex.

---

* $g'_e = \sqrt{J'_e}$ and $g_e = \sqrt{J_e}$.

F. $J_e'(\Gamma_2)$

We will obtain $J_e'(\Gamma_2) = \mathcal{J}_e'^2(\Gamma_2)$ directly from (37). There is some arbitrariness in this determination depending on our definition of $I_1(\theta_1) = \mathcal{J}_1^2(\theta_1)$ from the given primary field. We have assumed, however, that the primary field is obtained by:

$$E_1(\theta_1) = G_1 \exp\left(ik\left[r_1 + C_{p_o}(\theta_1)\right]\right)\mathcal{J}_1(\theta_1) = \frac{e^{ik(r_1 + C_{p_o})}}{\sqrt{kR_1\, kr_1}}\mathcal{J}_1 \quad (38)$$

With this definition of $\mathcal{J}_1(\theta_1)$ we factor $1/kR$ and obtain from equation (37),

$$J_e^1(\Gamma_2) = \left(\frac{1}{8\pi}\right) G_e^2 I_{lm} G_{lm}^2 \left[(Z_1 \pm Z_2)^2 \cos^2(k X_{lm} \sin\Gamma_2) + (-Z_1 \pm Z_2)^2 \sin^2(k X_{lm} \sin\Gamma_2)\right] \quad (39)$$

where

$$G_e^2 = 1/(\sin|\Gamma_2| + X_{lm}/r_c). \quad (39a)$$

As we expect, this power flow is of a higher order in $1/k$ than the primary field.

G. Reference Wavefront of the Edge Field - $R(\Gamma_2)$

We desire to find the reference phase contour curve given by $R(\Gamma_2)$. As pointed out earlier, the curves of constant phase are not circles for the edge field. We will choose there, a particular curve given by the phase being set equal to zero for equation (37). Although any phase value is adequate, the value zero is the reference contour for which the distance from the curve to the y_1 axis, along a normal to the curve, is equal to $-C_{e_o}(\gamma_2)$.

the reference phase.

To simplify the notation, the following substitutions are made:

$$\xi \equiv k X_{1m} \sin \Gamma_2 \tag{40}$$

$$\mathcal{J} \equiv k (R + \psi_m) + \pi/4 \tag{40a}$$

$$Y_1 \equiv Z_1 \pm Z_2, \quad Y_2 = - Z_1 \pm Z_2. \tag{40b}$$

Equation (37) may then be written as

$$\mathcal{N}_e = \frac{\mathcal{D}_{1m} G_{1m} G_{Ae} \sqrt{2}}{4\sqrt{\pi}} \left[\left\{ Y_1 \cos \mathcal{J} \cos \xi - Y_2 \sin \mathcal{J} \sin \xi \right\} + i \left\{ Y_1 \sin \mathcal{J} \cos \xi + Y_2 \sin \xi \cos \mathcal{J} \right\} \right].$$

Note from the above equation that the phase distribution of $\mathcal{N}_e$ is determined in large measure by the relative magnitude of Y_1 and Y_2; the sum and the difference of the edge field contributions from each edge.

The phase of $\mathcal{N}_e$ is equal to zero* if

$$Y_1 \sin \mathcal{J} \cos \xi + Y_2 \sin \xi \cos \mathcal{J} = 0$$

Hence we obtain

$$\mathcal{J} = - \arctan \left(\frac{Y_2}{Y_1} \tan \xi \right)$$

or

---

* Actually zero or 180°. The following additional condition is required for zero degrees: $\left[Y_1 \cos \mathcal{J} \cos \xi - Y_2 \sin \mathcal{J} \sin \xi \right] > 0$.

$$R = R(\Gamma_2) = -\psi_m - \frac{\pi}{4k} - \left(\frac{1}{k}\right) \arctan\left(\frac{Y_2}{Y_1} \tan \xi\right). \tag{41}$$

(A convenient branch for ψ_m should be chosen, although this can be seen to be arbitrary. Once ψ_m is chosen it is generally preferable to maintain $R(\Gamma_2)$ continuous by the appropriate branch choice in (41). It is important, however, that the branch choice for ψ_m be chosen so that R is far from the caustic of the field; near ρ_{2m} would be a good choice for example).

H. The Transformation Function $\Gamma_2(\gamma_2)$

The transformation function $\Gamma_2(\gamma_2)$ can be obtained from the phase contour $R(\Gamma_2)$ given by (41). We need $\Gamma_2(\gamma_2)$ in order to obtain $J_e(\gamma_2)$, $d_e(\gamma_2)$, and $C_{e_o}(\gamma_2)$.

From the diagram following (g), we note that

$$\Gamma_2 = \frac{\pi}{2} - \Delta_2 \quad \text{and} \quad \tan \Delta_2 = \operatorname{ctn} \Gamma_2 \tag{42}$$

$$\eta = \gamma_2. \tag{42a}$$

If $y_1(x_1)$ is the rectangular equation for the curve $R(\Gamma_2)$, then

$$\left.\begin{aligned} dy_1 &= dR \sin \Delta_2 + R \cos \Delta_2 \, d\Delta_2, \\ dx_1 &= dR \cos \Delta_2 - R \sin \Delta_2 \, d\Delta_2, \text{ and} \end{aligned}\right\} \tag{42b}$$

$$\frac{dy_1}{dx_1} = \tan(\pi - \eta) = -\tan \eta. \tag{42c}$$

Equations (42) through (42c) yield for $\gamma_2(\Gamma_2)$

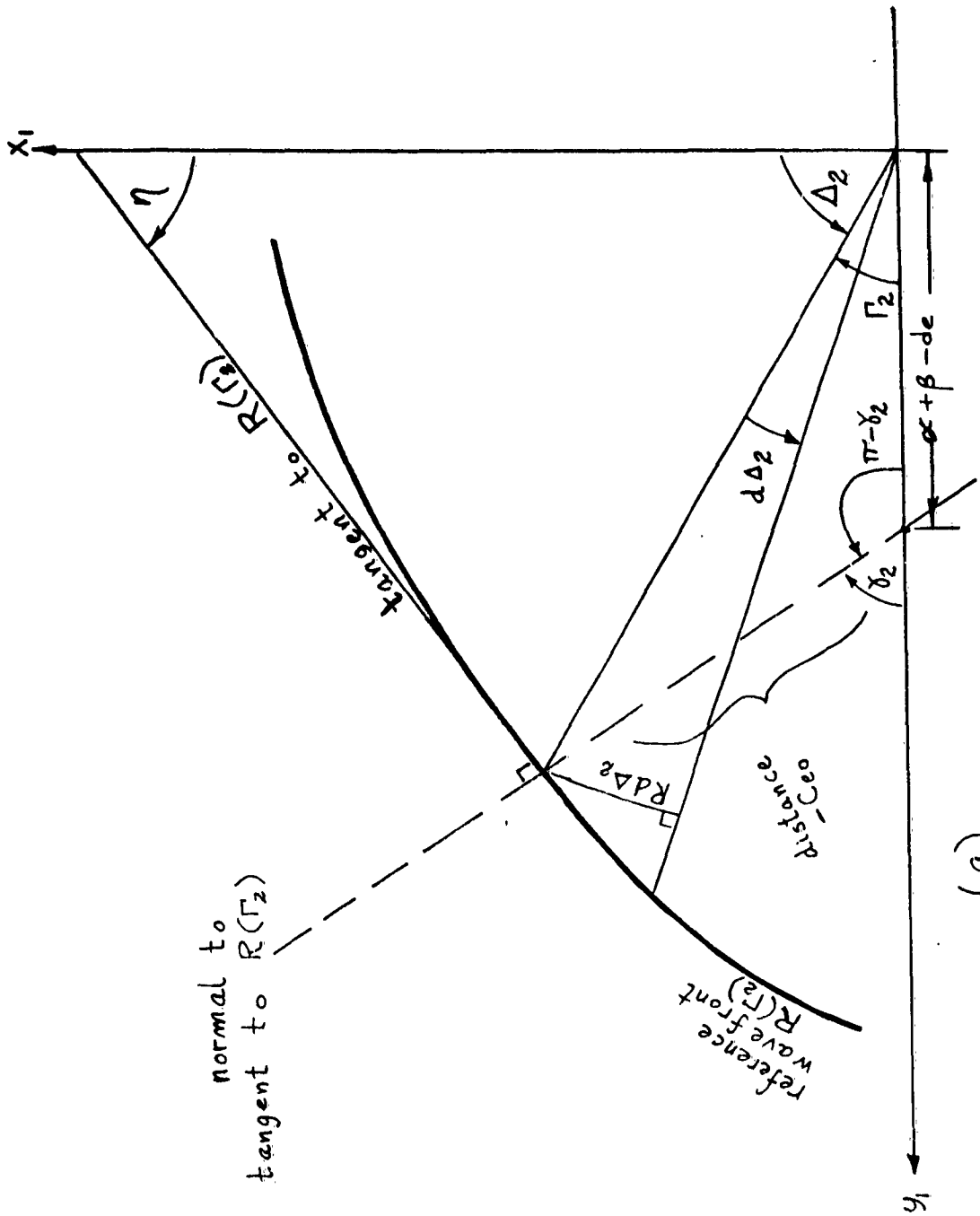
x_1
y_1
η
$R(\Gamma_1)$
tangent to
$R(\Gamma_1)$
Δ_2
Γ_2
$d\Delta_2$
$\pi-\gamma_2$
$\alpha+\beta-d\epsilon$
γ_2
$Rd\Delta_2$
distance
normal to
tangent to $R(\Gamma_2)$
reference
wave front
$R(\Gamma_2)$

(g)

$$\tan \gamma_2 = \frac{\tan \Gamma_2 - \frac{1}{R}\left(\frac{dR}{d\Gamma_2}\right)}{1 + (\tan \Gamma_2)\frac{1}{R}\left(\frac{dR}{d\Gamma_2}\right)} \tag{43}$$

which gives, numerically, the result

$$\Gamma_2 = \Gamma_2 (\gamma_2) \tag{43a}$$

In order to evaluate (43) we find

$$\frac{dR}{d\Gamma_2} = \frac{-1}{k(1 + [Y_2^2/Y_1^2]\tan^2\xi)} \cdot \left\{ \frac{-Y_1' Y_2 \tan\xi}{Y_2^2} + \frac{Y_2' \tan\xi}{Y_1} + \frac{Y_2 \sec^2\xi\, \xi'}{Y_1} \right\} \tag{44}$$

where the prime denotes differentiation with respect to Γ_2.

I. The Reference Phase Functions de and Ce_o

The reference quantities $d_e(\gamma_2)$ and $Ce_o(\gamma_2)$ can also be obtained from a knowledge of $R(\Gamma_2)$, equation (41). If we refer to the figure in part H above and apply the law of sines to the diagram we obtain first

$$\frac{R}{\sin(\pi - \gamma_2)} = \frac{[(\alpha+\beta) - d_e]}{\sin[\pi - (\pi - \gamma_2) - \Gamma_2]} .$$

Note that $(\alpha+\beta)$ is a given constant for the reflector system. From the above equation we obtain

$$d_e = (\alpha+\beta) + \left[\frac{\sin(\gamma_2 + \Gamma_2)}{\sin \gamma_2}\right] R \tag{45}$$

where R is given by (41).

If we apply the law of sines a second time to the same figure we obtain

$$\frac{R}{\sin(\pi - \gamma_2)} = \frac{-C_{e_o}}{\sin \Gamma_2}$$

which gives

$$C_{e_o} = -\left[\frac{\sin(\Gamma_2)}{\sin(\gamma_2)}\right] R \quad . \tag{46}$$

In both equations (45) and (46) for d_e and C_{e_o} we note that in order to obtain $d_e(\gamma_2)$ and $C_{e_o}(\gamma_2)$, we must first solve equation (43) numerically for $\gamma_2(\Gamma_2)$.

J. $\underline{J_e(\gamma_2)}$

Having found $J_e'(\Gamma_2)$, equation (39), and $\gamma(\Gamma_2)$, equation (43), we are prepared to determine $J_e(\gamma_2)$.

First we will explain why $J_e(\gamma_2) \neq J_e'(\Gamma_2(\gamma_2))$. The quantities J_e and J_e' represent power flows per unit solid angle. At a point on the wavefront given by the values Γ_2 and $R(\Gamma_2)$, J_e' (evaluated at this value of Γ_2) gives the value of the power flow through a solid angle

$$\left[\sin \Gamma_2 \; d \; \Gamma_2 \; d \; \theta\right] \quad .$$

Here we have $d\theta$ as the angle of rotation about the axis of the system. At the same point, the same power flows through a different solid angle given by

$$\left[\sin \gamma_2 \; d \; \gamma_2 \; d \; \theta\right] \quad .$$

J_e designates the power flow per unit solid angle referring to this latter angle. This is evident from the diagram (h) on the following page.

Since the total power flow through both solid angles is the same we have

$$J_e'(\Gamma_2)\ \sin\Gamma_2\ d\Gamma_2 = J_e(\gamma_2)\ \sin\gamma_2\ d\gamma_2$$

or

$$J_e(\gamma_2) = \frac{\sin\Gamma_2}{\sin\gamma_2}\left\{1\Big/\left(\frac{d\gamma_2}{d\Gamma_2}\right)\right\} J_e'(\Gamma_2) \quad . \qquad (47)$$

With considerable manipulation,

$$\frac{d\gamma_2}{d\Gamma_2} = f(\gamma_2) \qquad (48)$$

can be evaluated directly from (43).

With $d_e(\gamma_2)$, $C_{e_o}(\gamma_2)$, and $J_e(\gamma_2)$ determined from equations (45), (46), and (47) together with the auxiliary equation (43) for $\gamma_2(\Gamma_2)$ we have obtained the complete edge field in a form which will allow us to compute the edge field distribution in the aperture of the main reflector after reflection from this reflector.

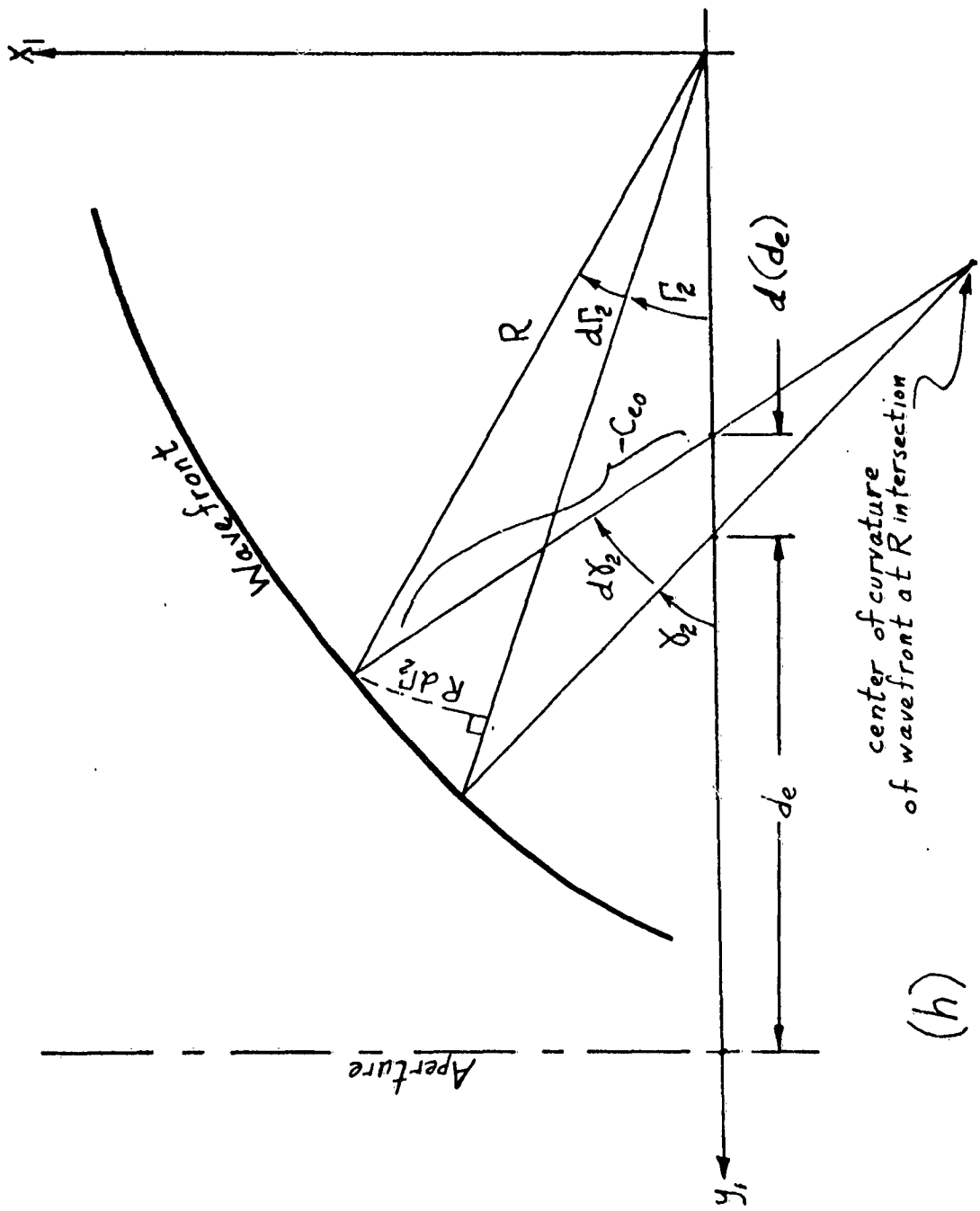
x1
y1
Wavefront
Aperture
R
dΓ2
Γ2
d(de)
-ce0
dδ2
δ2
R dΓ2
de
center of curvature
of wavefront at R intersection

(h)

IV. Computed Edge Diffracted Field Results

In this section the results of numerical computations for the edge diffracted field will be presented and briefly discussed. The computations presented here will not include the edge field scattered from the main reflector into the aperture. The presentation of those results is deferred until the next section.

The results presented here include the diffracted fields for subreflectors of various sizes in wavelengths and for various reflector shapes. They are plotted and illustrated as a function of Γ_2 from 0° to 180°. Between about 170° to 180° the results are in error. The oscillations are 180° out of phase with the true oscillations of the field. This is a computational error not due to the edge diffraction theory. The average field in this area (averaged over the oscillations) is, however, correct, so this portion of the plots was included in any case. Hence we will observe the back radiated field away from the main reflector in addition to the field incident on the main reflector.

It should be stressed that the geometrical optics field has been subtracted from the total field scattered from the reflector. Only the diffracted or second order field is considered.

A large number of input parameters or boundary conditions are necessary for each computation of a curve. Most of these parameters remain fixed for most of the curves computed. It will be far simpler and clutter the graphs much less if a set of standard values for these parameters is adopted and only deviations from this set of values is

mentioned on the graph and in the ensuing discussion. A similar procedure is followed in the next section and later chapters, so we will refer to the following parameters as Standard Set No. 1, and present these values in the following table:

STANDARD SET NO. 1

SYSTEM = Axially symmetric

$\theta_{1m} = 30°$

$X_{1m} = +1.00$

$\nu = \alpha + \beta = \sqrt{3}$

$X_{2m} = +10.0$

α = constant = 0

$I_1(\theta_1) = \cos^{16}\theta_1$ so $I_1(\theta_{1m}) \approx 1/10$

SIGNEG = ± 1 for respectively cancellation or addition of the edge field from each edge at the center ($\Gamma_2 = 0$). It will be chosen as +1 for addition as the standard edge.

γ = polarization angle with respect to the ege. It is chosen as 0° for the standard value.

A. Diffraction of Flat Discs and Strips

The edge diffracted field of a plane wave incident on a flat conducting strip or disk is of no direct interest to the designer of dual reflector systems, but does serve the purpose here of checking our computational procedure against previously computed

work[7] and also checking the theoretical accuracy of this method of computing the diffracted field.

Keller[7] computed the diffracted field of a plane wave incident on a conducting screen with a strip aperture and circular aperture. The results depicted in Figures 3, 4 and 5 are for the diffracted field of a plane wave on a conducting strip and circular disk, the complementary screens[15]. By Babinet's principle the results are equivalent with the principle exception being that the backscattered field in one system is equal to the forward scattered field in the other. (The polarizations must also be altered, but this makes little difference for these cases). Hence Keller[7] presents his results for the forward scattered field only and these compare very well with our backscattered fields (Γ_2 = 0° to 90°) depicted in Figures 3, 4 and 5. In addition the results depicted in these figures extend the published results of Keller to the region $90° \leq \Gamma_2 \leq 180°$.

For the case of the metalic strip with k = 8, Figure 3, the depicted results compare very accurately with the theoretically exact results published by Karp and Russek[17]. This is significant since the Kirchhoff theory[1] predicts substantially different results. The Kirchhoff theory predicts zeros in the field whereas the Keller theory predicts non-zero minima in approximately the same angular regions. The Kirchhoff theory predicts a fixed phase center at the center of the aperture, whereas the edge diffracted field as mentioned earlier does not have a fixed center of curvature for the phase front. This example is important for

our purposes because it demonstrates the breakdown of the Kirchhoff theory for small apertures or reflectors ($k = 8$ implies a diameter or slit width of approximately 1.6 wavelengths) and at the same time illustrates the success of the edge diffraction theory. Since we wish to examine the diffraction effects for small reflectors of this order (two or more wavelengths) in diameter the distinction between the theories is critical.

For larger diameter reflectors and for curved reflectors the two theories, the Kirchhoff and edge diffraction theories, agree well as will be demonstrated in the next part (B). However, it must be remembered that the edge diffraction theory begins to fail badly when the amplitude of the incident wave varies very rapidly near the edge. For example, if the incident wave has a zero at the edge, then the edge diffraction theory gives a zero diffracted field which is, of course, wrong. The Kirchhoff theory gives essentially the same answer for the diffracted field whether the field varies rapidly or slowly near the edge. That is, its solution is not critically dependent on the edge condition.

With regard to Figure 5, those readers who compare that figure with the same case illustrated in Reference 7 will note some small differences. These may be attributed to the difficulty in setting up the computor program for a plane wave incident on a flat reflector in the axially symmetric case. The program was designed for the input parameters of more practical dual reflector designs such as those parameters in Standard Set No. 1 and

large changes in the program were not warranted to merely correct small deficiencies in one curve.

B. Edge Diffracted Fields from a Hyperboloid (for comparison with the Kirchhoff theory and experiment)

The edge diffracted field of a conducting hyperboloid of revolution is presented in Figures 6, 7, 8 and 9 for hyperboloids of diameter 8λ and 16λ. The 8λ results in Figure 6 are for $\phi = 0$ (H-plane cut), and the 16λ results in Figures 7, 8 and 9 are for $\phi = \pi/2$ (E-plane cut). The three Figures 7, 8 and 9 present varying degrees of detail for the 16λ results.

These results are intended for comparison with the results that Rusch obtained by Kirchhoff integration and also with the experimental results that Rusch has obtained[18]. (Rusch presented similar results in Reference 3). The agreement between the results of the two theories is generally good, both theories predicting the same major characteristics of ripple and high back lobe ($\Gamma_2 > 120°$) as do the experimental results also. For those readers making an actual comparison between the results, it should be noted that Rusch presents his results with the geometrical optics field included as is characteristic for results obtained by Kirchhoff integration.

It might be added that Figure 6 through 9 (and later results) are the first results obtained by edge diffraction theory for curved reflectors known to the author and, hence, these results do extend

the known usefulness of the theory.

One important result seen in the figures is that the forward diffracted field ($\Gamma_2 > 90°$) is as large as or greater than the field diffracted toward the main reflector ($\Gamma_2 < 90°$). The forward diffracted field is, however, spread out over the angular regions depicted in the graphs, whereas dual reflector systems designed for high gain (easily better than 99% of all such antennas) will focus the energy diffracted into the main reflector and hence increase its significance in the main lobe area of the tertiary pattern. The forward scattered field contributes to the overall system sidelobes.

C. Edge Diffracted Fields as a Function of Frequency

Consideration of the edge diffracted field as a function of frequency or k is of great importance to this general study. One of the objectives as explained earlier was to examine the possibility of using a smaller than usual subreflector for the dual reflector system in order to reduce blockage by the subreflector. In addition, a general understanding of diffraction effects for any size reflector is of great importance.

With the above considerations in mind a study of the edge field as a function of k was made and is presented in Figures 10 through 24. In addition to plotting $J_e'(\Gamma_2)$ for Γ_2 from 0° to 180°, several auxiliary studies of other parameters were also made and presented among these figures. Except where it is

(x_1, y_1) origin (Γ_2). For $R \to \infty$ it is apparent that $\gamma_2 \to \Gamma_2$. In other words, as explained earlier, the wavefront appears more spherical. We are concerned, however, about the non-circularity of the wavefront near the main reflector, and Figures 13 and 14 show how the ray directions discussed above compare in this region for $k = 2\pi$ and $k = 6\pi$. In both cases, we find that $\gamma_2 \sim \Gamma_2$ over the major portion of the 180° range. Later we will find it extremely valuable to make the approximation that $\gamma_2 = \Gamma_2$ for computational purposes. This approximation will be most necessary near $\Gamma_2 \sim 80°$ where $x_2' \sim x_{2m}$, since this is the general area where the edge field has the largest effect in the main reflector aperture. It is seen from Figures 13 and 14 that the approximation $\gamma_2 \sim \Gamma_2$ is excellent in this region.

We now turn to a consideration of $J_\epsilon'(\Gamma_2)$ as a function of frequency k. It is clear from the previous discussion that $J_e'(\Gamma_2)$ will differ little in any important respect from $J_e(\gamma_2)$. The results of this study are plotted in Figures 15 through 19 for $k = 2\pi$, 4π, 6π, 8π, and 20π, respectively. For our purposes in this section, the two characteristics to take note of are:

1) The average amplitude away from the shadow boundaries diminishes as $1/k$ with k.

2) The interference effect between opposite edges becomes larger in amplitude and more rapidly oscillatory as k increases.

From the point of view that we would like to eventually deform

the reflector shapes to compensate for the edge field, the first fact aids us and the second fact helps to defeat this purpose. It is impractical to attempt to correct a rapidly oscillating field by optical techniques. However, as we will see later, the field is usually, if not always, negligible in those regions where it oscillates.

D. Effect of Reflector Shape and Field Symmetry

Before proceeding to compute the actual aperture edge field, it will be interesting to study the effect on the edge field distribution of varying the primary field symmetry and the subreflector shape.

We will vary the primary field symmetry by varying the relative phase of the top and bottom edge sources. That is, we will let SIGNEG = -1 instead of +1, as in Standard Set No. 1. This type of primary field symmetry occurs quite often,—almost enough to justify a complete set of numerical data for this case. For the most significant example, we refer to the circularly polarized primary distributions. In addition, monopulse or tracking feeds have this symmetry. As indicated in Figure 20, however, the only significant difference between the field of this symmetry and the former is that a zero exists at $\Gamma_2 = 0°$. The remaining general characteristics are the same except that the oscillations are essentially 180° out of phase.

We have already observed the differences between the edge field of a flat reflector and a curved reflector. The differences were

significant. In Figures 21 through 24 we have plotted the edge diffracted field as we varied x_{2m}, keeping all other parameters fixed. This change of x_{2m} in effect changes the "tilt" of the subreflector edges. Referring to Figure 1, this change is manifested by a change in ψ. As x_{2m} increases, ψ decreases. Therefore, the angular position of the shadow boundary changes. Of course, the first order optics field also changes. On Figures 21 through 24, the position of the shadow boundary is indicated by an arrow. The change in position of the shadow boundary and the edge field is very small over a range of x_{2m} from x_{2m} = 10 to x_{2m} = 40. This range covers a majority of practical cases and allows us to draw the conclusion that the choice of x_{2m}/x_{1m} = 10 for Standard Set No. 1 is sufficiently general for practical purposes.

V. The Edge Field Aperture Effects

In this section we will investigate the direct effect of the edge diffracted field in the main reflector aperture. The edge field is reflected by the main reflector into the aperture wherein its amplitude per unit area will be determined. To assess the importance of the aperture edge field, we must, of course, compare it to $\mathcal{J}_{3p}$ or I_{3p}, the aperture field generated by the primary source.

We will find that the edge field is quite significant for subreflector diameters of less than six wavelengths and of diminishing significance for greater diameters. These results are in substantial agreement

with those found from general engineering practice over the years. Without presenting any statistics to document this statement, we will nevertheless state that the vast majority of dual reflector systems have subreflectors greater than, usually much greater than, five wavelengths in diameter. The results of this section it is hoped will clarify in a quantitative way the reason for the five wavelength diameter minimum that appears in standard engineering practice.

In order to calculate the aperture edge field and tertiary field ($\mathcal{J}_{3p}$ or I_{3p}) in both amplitude and phase, we must choose a particular reflector system. As was pointed out earlier, the particular system chosen will have little effect on the substance of the results. We will choose, therefore, a Cassegrain system with the Standard Set No. 1 parameters as the boundary conditions for most calculations. A parabola-hyperbola system is much easier to handle analytically than the dual reflector designs found in Chapter 1, since we can obtain closed form expressions for the surface contours of the parabola-hyperbola system. Furthermore, to date, this system is the most common system used in practice.

In this section, specifically, we will first define the parabola-hyperbola system and find I_{3p} and C_p (C_p = constant for a Cassegrain or Gregorian system; see Chapter 1 for example). We will then determine the aperture edge field and present extensive numerical calculations.

A. The Cassegrain System and the Aperture Field Due to the Primary Source

The main reflector of the Cassegrain system is depicted in the

sketch following (i) and defined by the quadratic equation

$$\left.\begin{aligned} x_2^2 &= -4f_2\, y_2 + x_{2m}^2 \\ \text{or} \\ y_2 &= (x_{2m}^2 / 4f_2) - (1/4f_2)\, x_2^2 = a + b\, x_2^2. \end{aligned}\right\} \qquad (49)$$

The quantity f_2 is the focal length. The focus depicted below will be a focal point, of course, for the hyperbola subreflector also. The slope at any point on the main reflector is given by

$$dy_2 / dx_2 = 2b\, x_2 = -(1/2f_2)\, x_2 \ . \qquad (50)$$

The focal length is found from defined parameters as

$$f_2 = 1/2 \left(\mathcal{V} + p_1 + \sqrt{(\mathcal{V} + p_1)^2 + x_{2m}^2} \right) \qquad (51)$$

where we define

$$\mathcal{V} = \alpha + \beta = \beta = \text{constant} \ (\alpha \equiv 0). \qquad (51a)$$

(See equation (58) for the definition of $p_1 = f_1 - k_1$.)

The hyperbola geometry is depicted in the sketch (j) following sketch (i). With f_1, the distance between hyperbola focii, determined from the given parameters by

$$f_1 = \mathcal{V}/2 \left(\frac{x_{2m}}{x_{2m} - x_{1m}} \right) \qquad (52)$$

and the distance k_1 in the sketch found as

$$k_1 = \mathcal{V} - f_1, \qquad (53)$$

we define

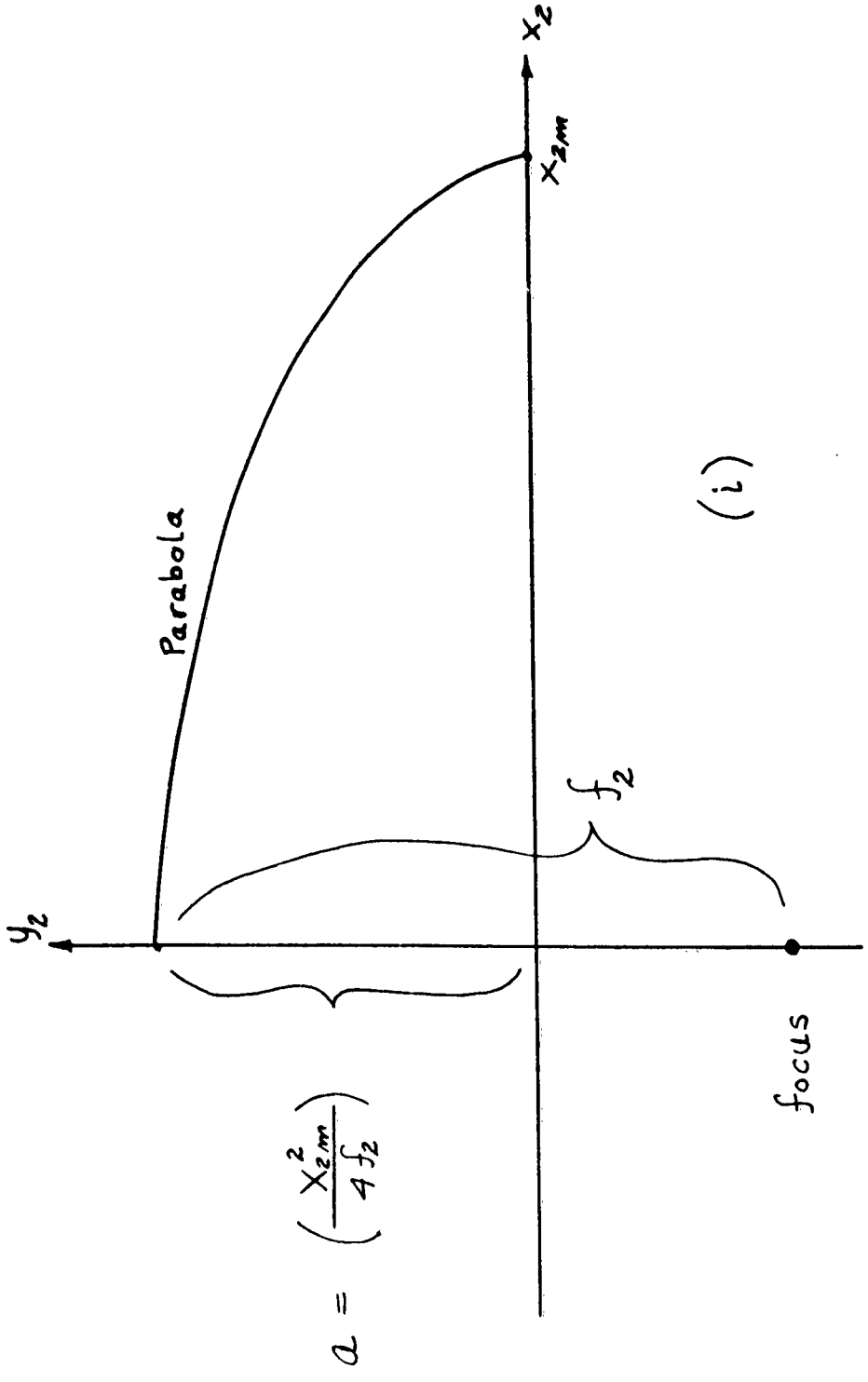

(i)

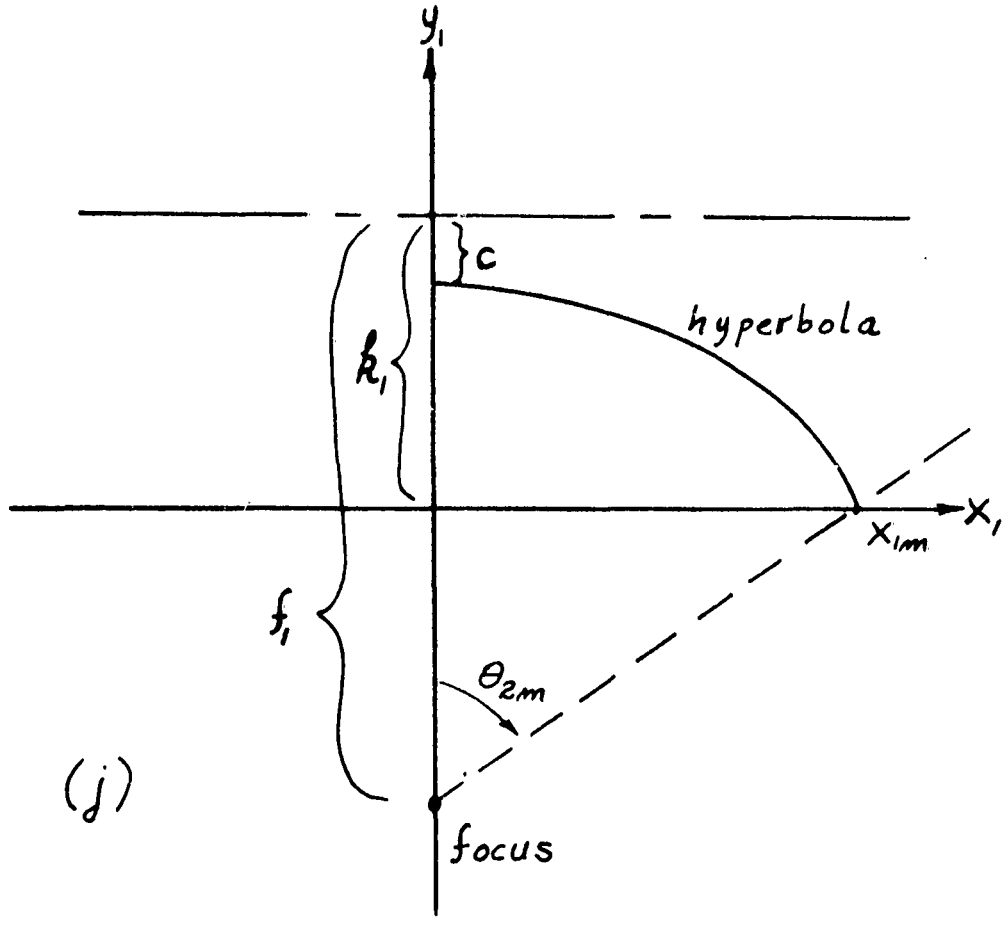

(j)

$$\left.\begin{aligned} k_k &= (k_1^2 + x_{1m}^2 + f_1^2)/2 \\ c^2 &= k_k - \sqrt{k_k^2 - k_1^2 f_1^2} \end{aligned}\right\} \tag{54}$$

and

$$d^2 = f_1^2 - c^2 \tag{55}$$

and obtain the equation for the hyperbola surface as

$$x_1 = \pm \sqrt{\frac{d^2}{c_2} (y_1 - k_1)^2 - d^2} \tag{56}$$

or

$$y_1 = k_1 \pm \sqrt{c^2 + \frac{c^2}{d^2} x_1^2} \quad . \tag{57}$$

The sketch (k) given on the following page of the parabola and hyperbola together illustrates the composite system. Note that $\alpha = 0$ for this system. This system is precisely graphed in Figure 25. This system gives a focal length over diameter ratio for the parabola of a little greater than 0.3, a common ratio found in practice.

With k_1 defined for the hyperbola, we can define and compute

$$p_1 = f_1 - k_1. \tag{58}$$

The maximum value of y_1 in this system is easily found as

$$y_{mx} = k_1 - c. \tag{59}$$

Before proceeding to determine the tertiary field, it will be interesting to find the secondary field or the geometrical optics

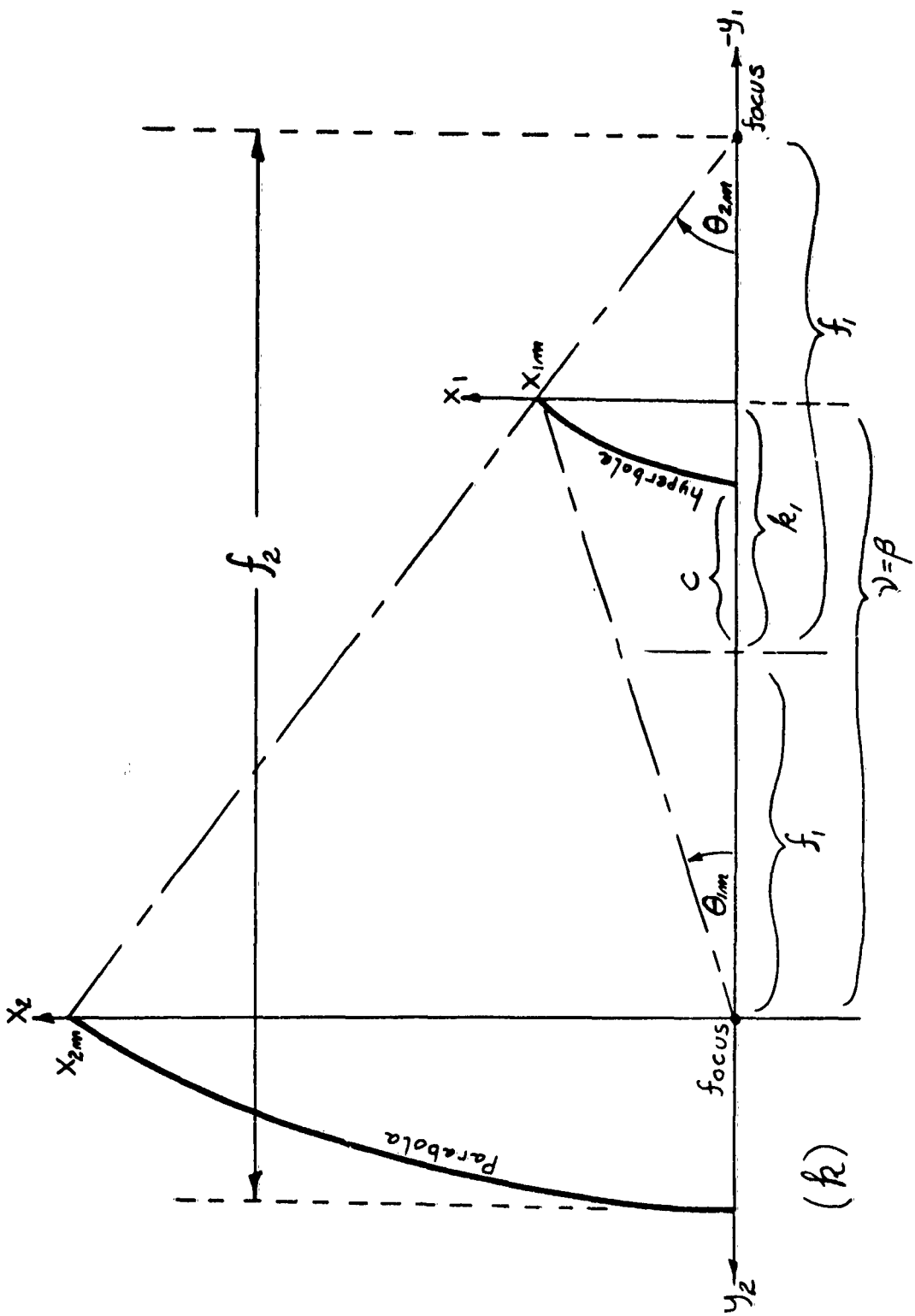
$-y_1$
focus
θ_{2m}
f_1
x_1
x_{1m}
hyperbole
k_1
c
$\gamma=\beta$
f_2
θ_{1m}
f_1
x_2
x_{2m}
focus
parabola
y_2

(h)

field reflected by the hyperbola. We will compute this numerically for the standard primary field $I_1(\theta_1) = \cos^{16}\theta_1$. The actual numerical computations are made by assigning a value to y_1 and computing x_1 from (56). We then find

$$\theta_1 = \arctan\left(\frac{x_1}{\nu + y_1}\right) \tag{60}$$

and

$$\theta_2 = \arctan\left(\frac{x_1}{y_1 + p_1}\right). \tag{61}$$

We now need $\frac{d\theta_1}{d\theta_2}$ in order to evaluate $I_{2_p}(\theta_2)$ from $I_1(\theta_1)$ by application of the energy conservation principle. This derivative is obtained by first finding

$$\frac{dx_1}{dy_1} = \left(\frac{d^2}{c^2}\right)\left(\frac{y_1 - k_1}{x_1}\right), \tag{62}$$

$$\frac{d\theta_1}{dy_1} = \cos^2\theta_1\left[\frac{1}{(\nu - y_1)}\frac{dx_1}{dy_1} + \frac{x_1}{(\nu - y_1)^2}\right], \tag{63}$$

and

$$\frac{d\theta_2}{dy_1} = \cos^2\theta_2\left[\frac{1}{(y_1 + p_1)}\frac{dx_1}{dy_1} - \frac{x_1}{(y_1 + p_1)^2}\right], \tag{64}$$

so that

$$\frac{d\theta_1}{d\theta_2} = \left(\frac{d\theta_1}{dy_1}\right) \Big/ \left(\frac{d\theta_2}{dy_1}\right). \tag{65}$$

With (72) we apply the conservation of energy principle and find

$$I_{2_p}(\theta_2) = \left(\frac{\sin\theta_1}{\sin\theta_2}\right)\left(\frac{d\theta_1}{d\theta_2}\right) I_1(\theta_1). \tag{66}$$

The numerical results for Standard Set No. 1 parameters are depicted in Figure 26.

We now wish to obtain the tertiary field I_{3p}. This can be obtained from $I_{2p}(\theta_2)$ which is already determined by (66) if we find the derivative $(d\theta_2/dx_2^1)$ and apply the conservation of energy rule between the two fields. In the parabola-hyperbola system, we should note that

$$x_2 = x_2^1 . \tag{67}$$

We will allow x_2^1 to be the independent variable and assign its value first and then determine y_1. With y_1 determined, we may find I_{2p} as previously shown.

Given x_2^1 we find from (49) and (50) the values of y_2 and dy_2/dx_2 respectively. Then

$$\tan\theta_2 = \left(x_2/(y_2 + \nu + p_1)\right) \tag{68}$$

is found. We solve (56) and (57) simultaneously to obtain $y_1\,(\tan\theta_2)$ given by

$$y_1 = y_q \pm \sqrt{y_q^2 - y_{q_1}} , \tag{69}$$

$$y_q = (k_1 d^2 + p_1 c^2 \tan^2\theta^2)/(d^2 - c^2 \tan^2\theta_2), \tag{70}$$

and

$$y_{q_1} = (d^2 k_1^2 - c^2 d^2 - p_1^2 c^2 \tan^2\theta_2)\Big/(d^2 - c^2\tan^2\theta_2). \tag{71}$$

In (69) we use the + sign if $(y_{qn}/y_{qd}) \gtrless 0$ and the - sign otherwise, where

$$y_{qn} = k_1^2 d^2 + p_1 c^2 \tan^2\theta_2$$

and

$$y_{qd} = d^2 - c^2 \tan^2 \theta_2$$

If y_{qd} is approximately zero, then use

$$y_1 = (1/2)\,(y_{q1n} / y_{qn})$$

where

$$y_{q1n} = d^2 k_1^2 - c^2 d^2 - p_1^2 c^2 \tan^2 \theta_2 .$$

Having found y_1 we obtain I_{2p} as discussed already. We still need $dx_2^1/d\theta_2 = dx_2/d\theta_2$ to obtain the tertiary field. From (76) we obtain this value as

$$\frac{d\theta_2}{dx_2} = \frac{\cos^2 \theta_2}{(y_2 + \nu + p_1)} \left[1 - \tan \theta_2 \left(\frac{dy_2}{dx_2}\right)\right] . \qquad (72)$$

By applying the conservation of energy principle

$$I_{2p}(\theta_2) \sin \theta_2 \, d\theta_2 = I_{3p}(x_2) \, x_2 \, dx_2 \qquad (73)$$

we obtain

$$I_{3p}(x_2) = I_{2p}(\theta_2) \left(\frac{\sin \theta_2}{x_2}\right) \left(\frac{d\theta_2}{dx_2}\right) \qquad (74)$$

The primary field aperture phase, C_p, is constant and may be obtained, <u>as a check</u>, by

$$C_p = r_1 + \rho_2 + \rho_3 + C_{po} \qquad (75)$$

where

$$r_1 = x_1/\sin \theta_1 , \qquad (76)$$

$$\rho_2 = (x_2 - x_1)/\sin\theta_2, \tag{77}$$

$$\rho_3 = y_2, \tag{78}$$

and $C_{po} = 0$ by definition.

Numerical results are depicted together with results for the aperture edge field to be discussed next.

B. Edge Field in the Aperture

We now wish to determine the edge field amplitude and phase (I_{3e} or ϑ_{3e} and C_e) in the main reflector aperture. We will determine I_{3e} and C_e at $x_2' \doteq x_2$, the same point for which I_{3p} and C_p were determined. This will facilitate the complex addition of the two fields in the aperture which will be made in Chapter 5.

It will simplify the computations considerably if we assume that $\Gamma_2 \approx \gamma_2$ or that the true ray normal to the reference phase front of the edge diffracted field is in the same direction as the ray through the (x_1, y_1) origin. The justification for this approximation in terms of its accuracy was presented earlier in Figures 13 and 14. It should be noted that we will use the true phase of the edge field at the given point on the wavefront. It is only the direction of the ray through the reference wavefront which is approximated.

The projection of the approximate edge field ray as it is reflected

from the main reflector into the aperture at the point x_2' is illustrated in the diagram (1) on the following page. Note the difference between this diagram and Figure 2, where the ray is in the γ_2 direction. The ray reflected from the main reflector is in the γ_3 direction. The point of incidence of the edge field ray on the main reflector is designated (x_3, y_3) in the same reference system as (x_2, y_2). A detailed drawing of this ray and reflector structure, to scale, is shown in Figure 27. The equations for the main reflector shape and slope in terms of (x_3, y_3) is the same, of course, as that given in equations (49) and (50) for the (x_2, y_2) system,

$$x_3 = + \sqrt{- 4f_2 y_3 + x_{2m}^2} \quad , \tag{79}$$

$$y_3 = \left(\frac{x_{2m}^2}{4f_2}\right) - \left(\frac{1}{4f_2}\right) x_3^2 \quad , \tag{80}$$

and

$$\frac{dy_3}{dx_3} = - \left(\frac{1}{2f_2}\right) x_3 \quad . \tag{81}$$

Given the value of the independent variable $x_2' = x_2$ we would like to find Γ_2 directly. It is difficult to do this directly so we will find x_2' when given Γ_2. From the geometry we have

$$\tan \Gamma_2 = x_3/(y_3 + \nu) \tag{82}$$

from which, when solved simultaneously with (80), we obtain

$$x_3 = - 2f_2 \operatorname{ctn} \Gamma_2 + \sqrt{4 \operatorname{ctn}^2 \Gamma_2 f_2^2 + 4f_2 \nu + x_{2m}^2} \, . \tag{83}$$

The values of y_3 and dy_3/dx_3 are then found from (88) and (81).

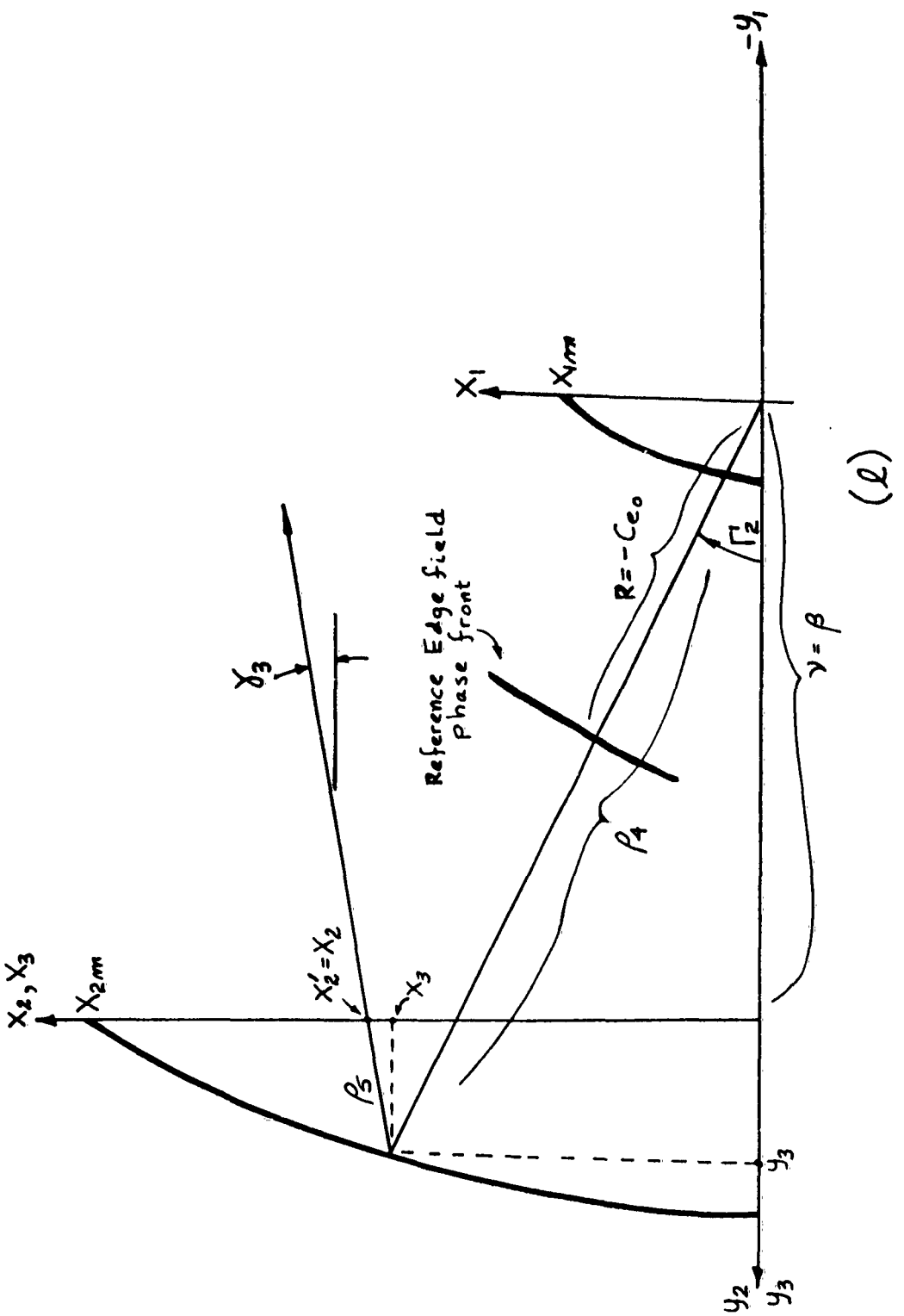
x_2, x_3
x_{2m}
$x_2' = x_2$
x_3
γ_3
ρ_5
y_3
y_2
y_3
Reference Edge field
phase front
ρ_4
$R = -Ce_0$
Γ_2
$\gamma = \beta$
x_1
x_{1m}
$-y_1$
(2)

With Snell's law at the point (x_3, y_3) expressed as

$$dy_3/dx_3 = -\tan\left(\frac{\Gamma_2 - \gamma_3}{2}\right) \tag{84}$$

and (84) and (81) solved simultaneously, we obtain

$$\gamma_3 = \Gamma_2 - 2 \arctan (x_3/2f_2). \tag{85}$$

From (85) and the geometry we then readily obtain

$$x_2 = x_2' = x_3 + y_3 \tan \gamma_3. \tag{86}$$

Now given $x_2' = x_2$ we may solve for Γ_2 by solving the transcendental equations for Γ_2, (81) through (86). This is not very difficult, since $\Gamma_2 (x_2')$ is a monotonic function.

We now need $dx_2/d\Gamma_2$ in order to find I_{3e} by application of the conservation of energy principle to J_e or J_e' (note that the assumption that $\gamma_2 \sim \Gamma_2$ implies also that $J_e \sim J_e'$). This value is found by differentiation of previous results as

$$\frac{dx_2}{d\Gamma_2} = \frac{dx_3}{d\Gamma_2} + \left(\frac{dy_3}{dx_3}\right)\left(\frac{dx_3}{d\Gamma_2} \tan \gamma_3\right) + y_3 \sec^2 \gamma_3 \left(\frac{d\gamma_3}{d\Gamma_2}\right) \tag{87}$$

where

$$\frac{d\gamma_3}{d\Gamma_2} = 1 - \left(\cos^2 \left(\frac{\Gamma_2 - \gamma_3}{2}\right)/ f_2\right) \frac{dx_3}{d\Gamma_2} \tag{88}$$

and

$$\frac{dx_3}{d\Gamma_2} = 2f_2 \csc^2 \Gamma_2 \left[x_3 \Big/ \sqrt{4 \operatorname{ctn}^2 \Gamma_2 f_2^2 + 4f_2 \nu + x_{2m}^2} \right]. \quad (89)$$

Applying the conservation of energy principle, we obtain finally that

$$I_{3e} = \left[J_e^1 \Big/ \left(\frac{dx_2}{d\Gamma_2}\right) \right] \cdot \left(\frac{\sin \Gamma_2}{x_2}\right) . \quad (90)$$

In order to determine the edge field phase, C_e, at the same point in the aperture we find

$$\rho_4 = x_3 \csc \Gamma_2, \quad (91)$$

$$\rho_5 = (x_2 - x_3) \csc (\gamma_3), \quad (92)$$

and finally

$$C_e = \rho_4 + \rho_5 - R. \quad (93)$$

Note that $C_{eo} \sim -R$ according to the approximation $\gamma_2 \sim \Gamma_2$.

In Chapter 5 we will use the synthesis method of Chapter 1 in an attempt to correct the aperture edge field effect. In order to carry out the synthesis, it will be remembered that the derivative of the desired aperture phase distribution must be found. For the work in Chapter 5, we will need, therefore, to find $\frac{dC_e}{dx_2} = \frac{dC_e}{dx_2}$. By the theorum of Malus, we find directly that

$$d\,C_e/dx_2 = \sin \gamma_3 \tag{94}$$

where γ_3 is given by (85).

C. Aperture Edge Field Computations

Aperture edge field computations of $\mathcal{J}_{3e}$ and C_e were made for a wide range of frequencies, for normal and parallel polarizations ($\gamma = \pi/2$ and $\gamma = 0°$), and for even and odd symmetry of the primary field (SIGNEG = +1 and -1) incident on the subreflector. These results will be presented graphically and briefly discussed in this part. Unless it is specifically stated otherwise, the Standard Set No. 1 parameters introduced earlier may be assumed.

Figures 28 through 29 illustrate the edge field amplitude, $\mathcal{J}_{3e}$, contribution to the aperture field in comparison with the primary source contribution, $\mathcal{J}_{3p}$, for frequencies $k = 2\pi$, 4π, 6π, 8π, 10π, 16π, and 20π. The primary source contribution does not change with frequency, of course. The important general characteristics of the edge field contribution are the same for all frequencies, and as will be seen subsequently, for different polarizations (γ) and symmetries (SIGNEG). The characteristics are:

1) A large lobe exists near the outer periphery of the main reflector. Although we would expect this lobe to be centered around x_{2m} we find that it is shifted towards a value of x_2 slightly less than x_{2m}. This shift may be accounted for in part by the approximation

$\Gamma_2 \sim \gamma_2$ (see Figures 13 and 14). Some of the shift is due, however, to a change in the amplitude distribution caused by reflection from the main reflector. For a smaller value of k or a wider edge diffraction lobe, this shift is less important, since it is approximately the same for all values of k considered. The amplitude in this diffraction lobe region has been calculated with the shadow boundary correction discussed earlier in this chapter and should be reasonably reliable. This contribution is of major importance and will be discussed further later.

2) Away from the shadow boundary lobe, the field decays rapidly, the rate of decay increasing with frequency. In the shadow boundary lobe region and in this decay region, there is no interference effect between opposite edges of the subreflector. The top edge field dominates in this region. It is possible, however, to include some contribution from the bottom edge despite the optical blocking of the curved surface of the subreflector. The inclusion of surface diffracted rays is discussed by Keller[7]. However, for this polarization ($\gamma = 0$), the transition to the region where interference between edges takes place is so smooth that it is clear that the present theory is adequate. For the other polarization

($\gamma = \pi/2$) we will see shortly that a discontinuity does exist in this transition, but the discontinuity is of no qualitative significance.

3) In the region where the fields of the two edges interfere and oscillations do take place ($\sim x_2' \leq 6$) the field amplitude levels off, but at a rather low level ($\sim$ -20 db) with respect to the shadow boundary lobe and $\mathcal{D}_{3p}$. This is significant since there is very little possiblity that the rapid oscillations in this region could be corrected by optical techniques (i.e., reshaping the reflector surfaces). However, the low amplitude for all frequencies in this region makes a correction of this effect unnecessary.

From the figures, then, it is clear that the only significant contribution of the edge diffracted field is the shadow boundary lobe where the amplitude is of the same order as the primary source contribution. Actually, this contribution is even more significant than is apparent from the figures. First of all, the area subtended by the small radial segment of the shadow boundary lobe is quite large, since this effect is at the outer edge of the main reflector. Secondly and even more significant is the fact that this contribution to the total aperture distribution is usually $\sim$180° out of phase with the rest of the aperture field. This effect, which is demonstrated quite clearly in Chapter 5, is particularly important with regard to the gain of the antenna. Furthermore, it is not possible to simply change the value of β

in a new parabola-hyperbola antenna system in order to cause the edge field to add in phase instead of out of phase at the aperture. It is reasonably clear from Figure 2 that changing the boundary conditions does not alter the relative phase between these two fields (note that only the top edge makes a contribution to the shadow boundary lobe). What is actually required to make the edge field contribution such that the resultant aperture phase distribution is approximately uniform is to alter, fundamentally, the reflector contours. This is done in Chapter 5 with some success.

Let us examine a little more closely the origin and character of the shadow boundary lobe. In the brief succession of diagrams (m) is depicted the degree of approximation obtainable with larger and larger subreflectors of the desired geometrical optics pattern (the dashed line). This is similar to using more and more terms of a Fourier series to approximate a square wave. The difference between the two curves at the vertical edge of the dashed curve is the shadow boundary lobe. In general the amplitude at this point does not vary, but the steepness of the approximating curve does , and hence the width of the shadow boundary lobe also does vary in the same manner with increasing k. This is the calculated result illustrated in the figures.

For $k = 2\pi$ we find that the shadow boundary lobe is significant for approximately $9 \leq x_2^1 \leq 10$ and hence 10% of the radius or approximately 20% of the area of the aperture since the lobe is near the outer periphery. Since this lobe is out of phase with

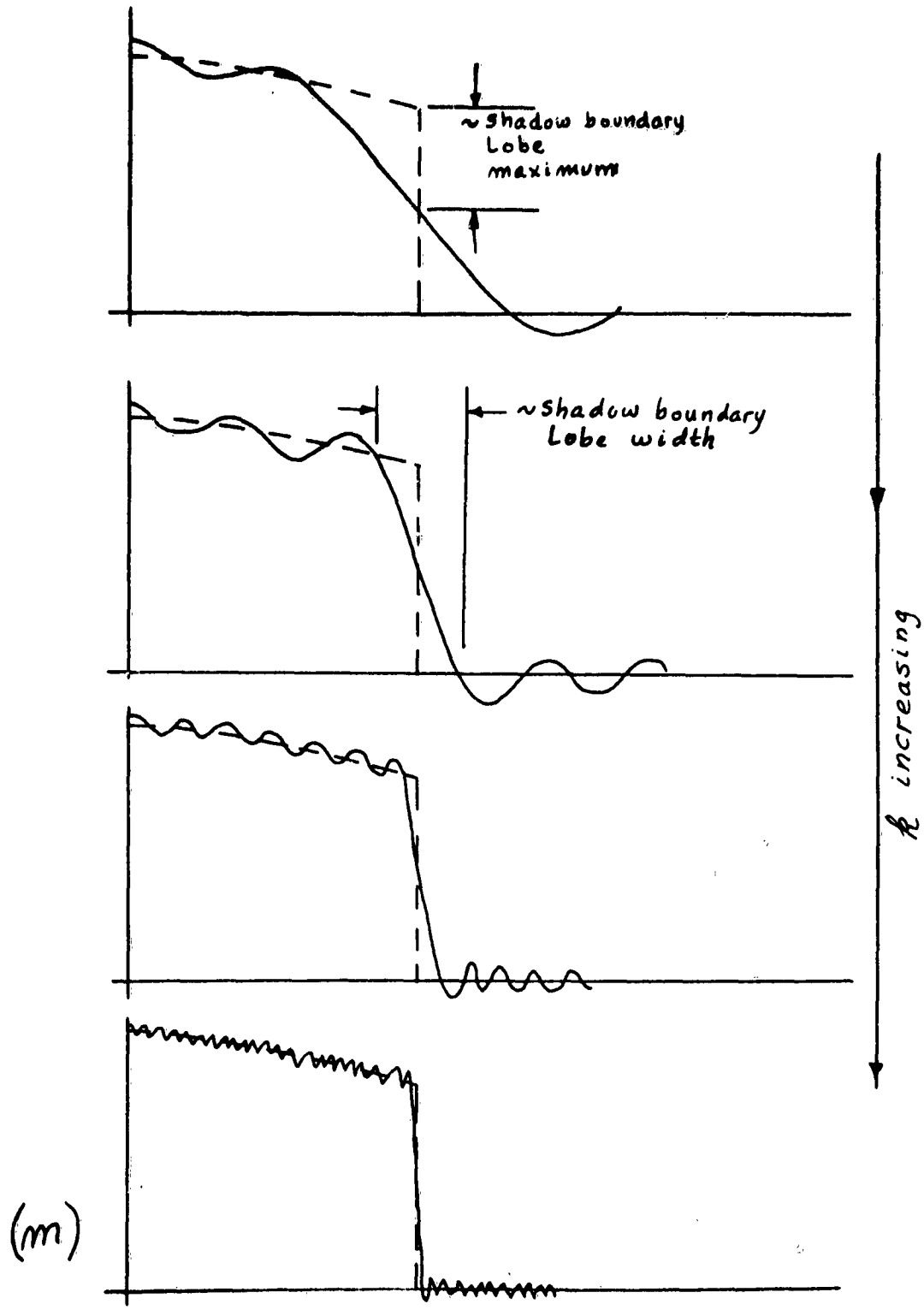
~Shadow boundary
Lobe
maximum
~Shadow boundary
Lobe width
ℓ increasing
(m)

the rest of the aperture, the net reduction of anticipated gain for the antenna may be as great as 40%, surely an intolerable figure in practice. For the case of $k = 6\pi$, we obtain a similar figure of about 15% net reduction in possible gain. Even if these figures were 30% and 10%, qualitatively, the significance is apparent. A subreflector of about 6λ in diameter ($k = 6\pi$) is the minimum tolerable size that can be used in practice. This, as was mentioned earlier, agrees with generally accepted standards found in practice. For much larger subreflectors, the effect becomes progressively less significant as may be expected.

In Figures 31 through 36 are illustrated the edge field phase distributions in the aperture, C_e, for $k = 2\pi$, 4π, 6π, and 8π. Figures 31 and 32 illustrate the same distribution, $k = 2\pi$, but in Figure 31 the various braches of C_e are connected to illustrate the continuous distribution. The various branches are presented segmented in most of the other illustrations. The change in branch for C_e arises from the branch choice of the arctangent in equation (41) for R. Since

$$C_e = \rho_4 + \rho_5 - R$$

this branch choice is reflected in the results for C_e also.

Each branch in the phase curves for C_e represent another lobe of oscillation in the amplitude $\mathcal{D}_{3e}$. Hence, for higher values of k there are more oscillations or lobes and more branch segments in the curves for C_e. If the phase front of the edge

field were perfectly circular with the center of curvature at the focal point of the main reflector parabola, then the phase curves for C_e , when they were connected continuously as illustrated in Figure 31, would appear as shown in the diagram (n). They would be perfectly formed squared steps of π radians or $\lambda/2$ height. The step jumps would occur at zeros of $\mathcal{J}_{3e}$. For a slightly non-circular edge diffracted field from the subreflector or one with the center of curvature not at the focal point of the parabola, the resulting distribution might appear as shown in the diagram (o). In this case the amplitude $\mathcal{J}_{3e}$ does not have zeros and the steps of C_e are not clearly delineated as before. An excellent example of C_e for this case is illustrated in Figure 48. The less circular the edge field diffracted wavefront becomes the smoother the curves for C_e become.

In Figures 37 through 39 are illustrated the aperture edge fields, $\mathcal{J}_{3e}$, when the polarization incident on the edge of the subreflector is normal to the subreflector edge ($\gamma = \pi/2$). This may be interpreted alternatively as an E-plane cut whereas when $\gamma = 0$, the fields then are in the H-plane (planes parallel to electric, E, or magnetic, H, fields). The oscillations in the region where the top and bottom edge fields interfere ($x_2^1 \lesssim 6$) are considerably greater than for the $\gamma = 0$ case. While they are still small compared to the shadow boundary lobe, they are not entirely insignificant, especially for the lower frequencies, $k = 2\pi$ and 4π. At around $x_2^1 = 7.7$, we find a discontinuity in the field that is due to the sudden introduction of edge source No. 2 (the bottom edge) into the computations. At this point, the surface of the

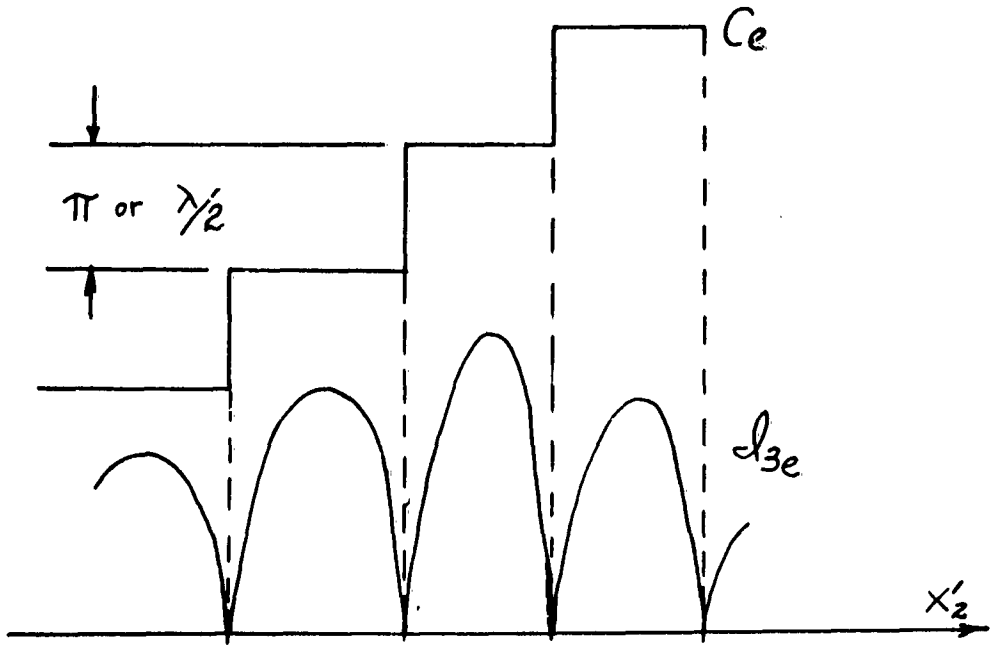

(n)

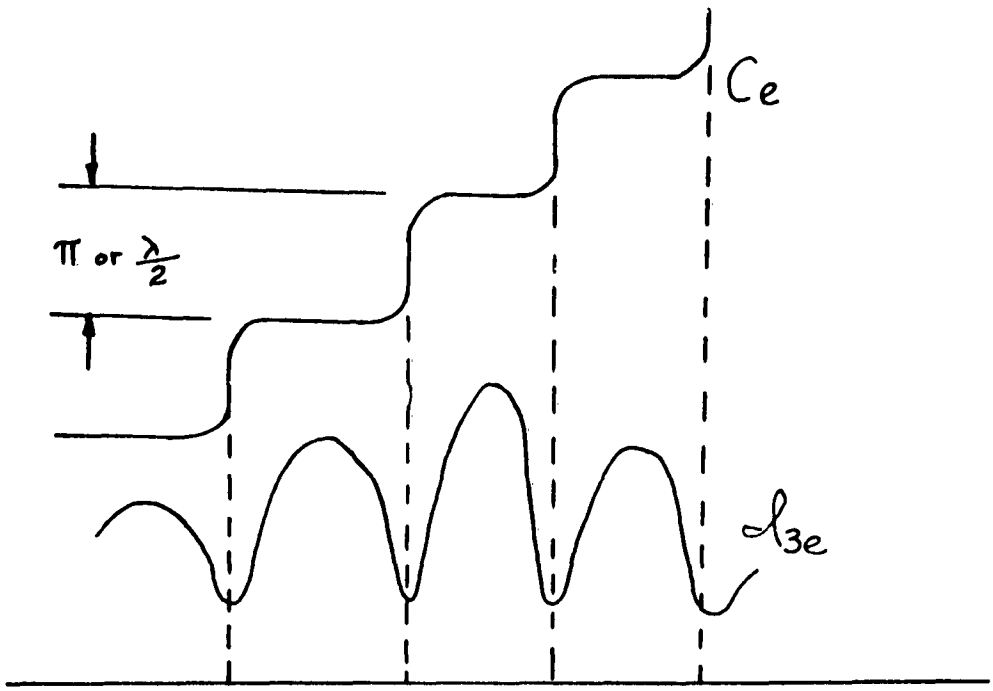

(o)

subreflector no longer optically blocks the rays from edge No. 2 and the interference between edges commences for x_2' less than this value. As mentioned earlier, the creeping or surface wave[7] that can be excited by the edge diffracted field and "seen" around the curved surface of the reflector is much more significant for this polarization. While such a correction to the computed values would give a more continuous transition at this point ($x_2' \sim 7.7$), this effect is not considered very important for the purposes of this work. The effect is interesting, however, and indicative of the general validity of Keller's theory[7] when properly interpreted.

In Figures 40 through 42, the edge field phase in the aperture, C_e, is illustrated for $k = 2\pi$, 4π, and 6π with $\gamma = \pi/2$. Note that this phase distribution is more sharply stepped than the equivalent $\gamma = 0$ case. As discussed earlier, this result is consistant with the lobe structure found for ϑ_{3e} when $\gamma = \pi/2$ as compared to that for $\gamma = 0$ and implies that a more spherical wavefront for the edge diffracted field exists here.

Figures 43 through 48 illustrate the amplitude and phase for the case when odd symmetry (SIGNEG = -1) exists in the primary source distribution. Both polarizations, $\gamma = 0$ and $\pi/2$, were used in computations for $k = 6\pi$. There is no difference of any consequence for the SIGNEG = -1 case relative to the SIGNEG = +1 case. A zero for ϑ_{3e} exists at $x_2' = 0$ for SIGNEG = -1 whereas a maximum exists at this point for SIGNEG = +1, but this expected result of the symmetry is of no important consequence. The

same differences between the $\gamma = 0$ and $\gamma = \pi/2$ cases exist for SIGNEG = -1 as do for SIGNEG = +1. This is true for both the phase and amplitude results as is clearly evident from the figures. No deviation of these results need be expected for other values of k.

CHAPTER 3

REFERENCES

1. B. B. Baker and E. T. Copson, "The Mathematical Theory of Huygens' Principle," 2nd Edition, Oxford Press, London, Great Britain; see Chapter II in particular.

2. Meixner and Andrejewski, Amn. der Physik, Volume 7; 1950

3. W. V. T. Rusch, "Scattering from a Hyperboloidal Reflector in a Cassegrainian Feed System," IEEE Transactions on Antennas and Propagation; July, 1963, pp 414-421

4. F. Oberhettinger, "Diffraction of Waves by a Wedge," Comm. on Pure and Applied Mathematics, Volume 7, August, 1954, pp 551-563

5. J. B. Keller, A. Blank, "Diffraction and Reflection of Pulses by Wedges and Corners," Comm. on Pure and Applied Mathematics, Volume 4; 1951, p. 75

6. S. Karp, "Diffraction by a Tipped Wedge with Application to Blunt Edges," Research Report No. E.M.-52, New York University, Mathematics Research Group; May, 1953

7. J. B. Keller, "Geometrical Theory of Diffraction," Research Report No. E.M.-175, New York University, Courant Institute of Mathematics Sciences, Division of E.M. Research; April, 1962

8. A. Sommerfeld, Optics, Academic Press, New York, New York

9. W. Braunbek, Ann. Phys., 6, 53; 1949

10. R. F. Millar, "An Approximate Theory of the Diffraction of an Electromagnetic Wave by an Aperture in a Plane Screen," Part C of the Proc. of the IEE; October, 1955

11. P. C. Clemmow, "Edge Currents in Diffraction Theory," IRE Transactions on Antennas and Propagation, Volume AP-4; July, 1956, p. 282

12. W. J. Welch, "Diffraction of Obliquely Incident Plane Waves by a Circular Aperture," Master of Science Thesis, Electrical Engineering Department, University of California at Berkeley.

13. J. Ruze, "Phase Centers and Phase Patterns," Proceedings of the Northeast Electronics Research and Engineering Meeting, November 5, 1963

14. E. Jahnke, F. Emde, "Tables of Functions," 4th Edition, Dover Publications, New York, New York; 1945

15. R. E. Collin, "Field Theory of Guided Waves," McGraw-Hill Book Company; 1960, pp 29-34

16. W. Braunbek, "Diffraction of an Electromagnetic Wave by a Funnel-Shaped Screen," IRE Transactions on Antennas and Propagation, Volume AP-7, Special Supplement; December, 1959, pp 571-577

17. S. N. Karp and A. Russek, J. Applied Physics, 27, 886 (1956)

18. W. V. T. Rusch, "Scattering from a Hyperboloidal Reflector," Technical Report No. 32-283, Jet Propulsion Laboratory, California Institute of Technology, Pasadena, California; July 2, 1962

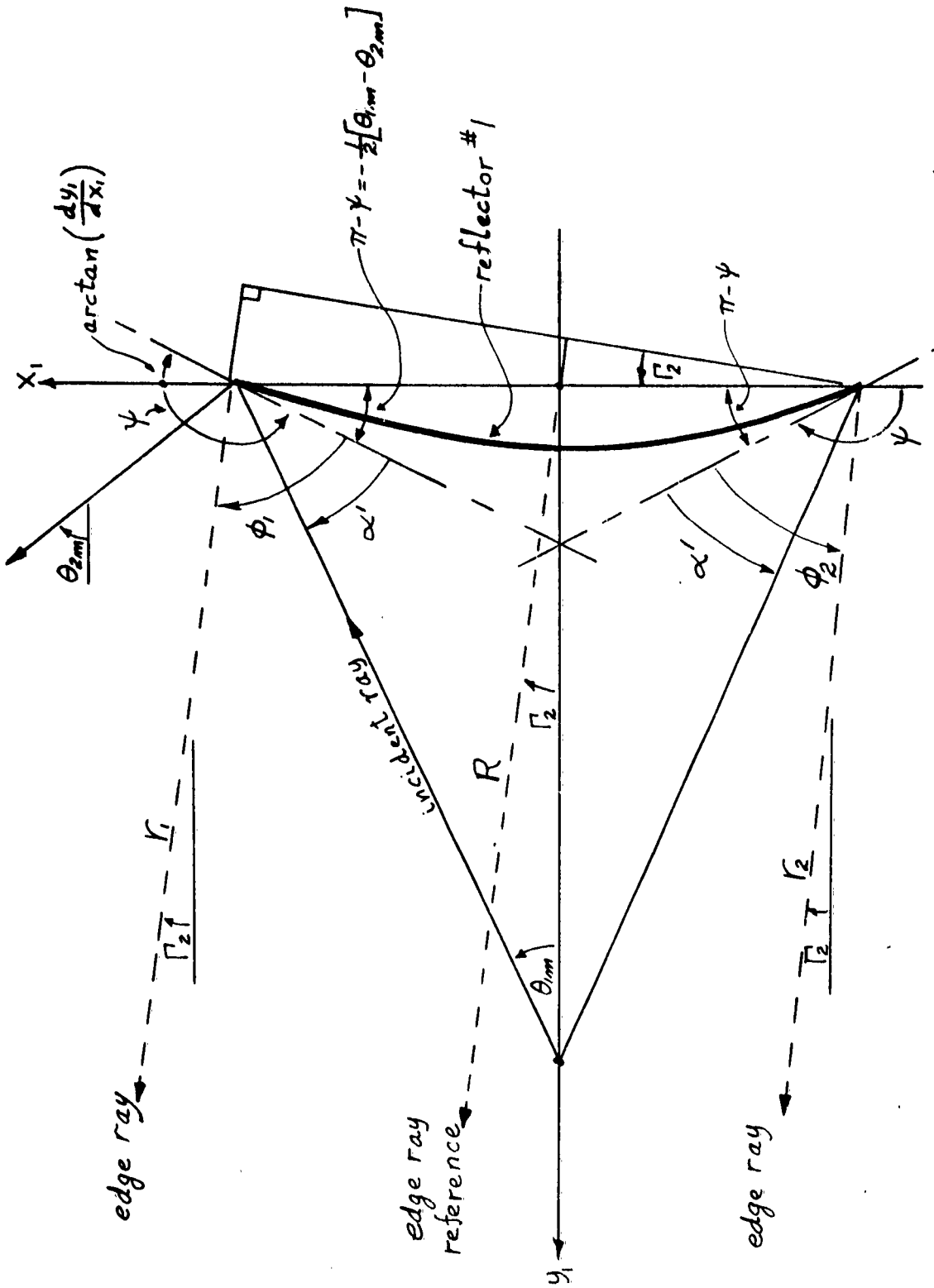

Fig. 1. Edge diffraction geometry at reflector #1.

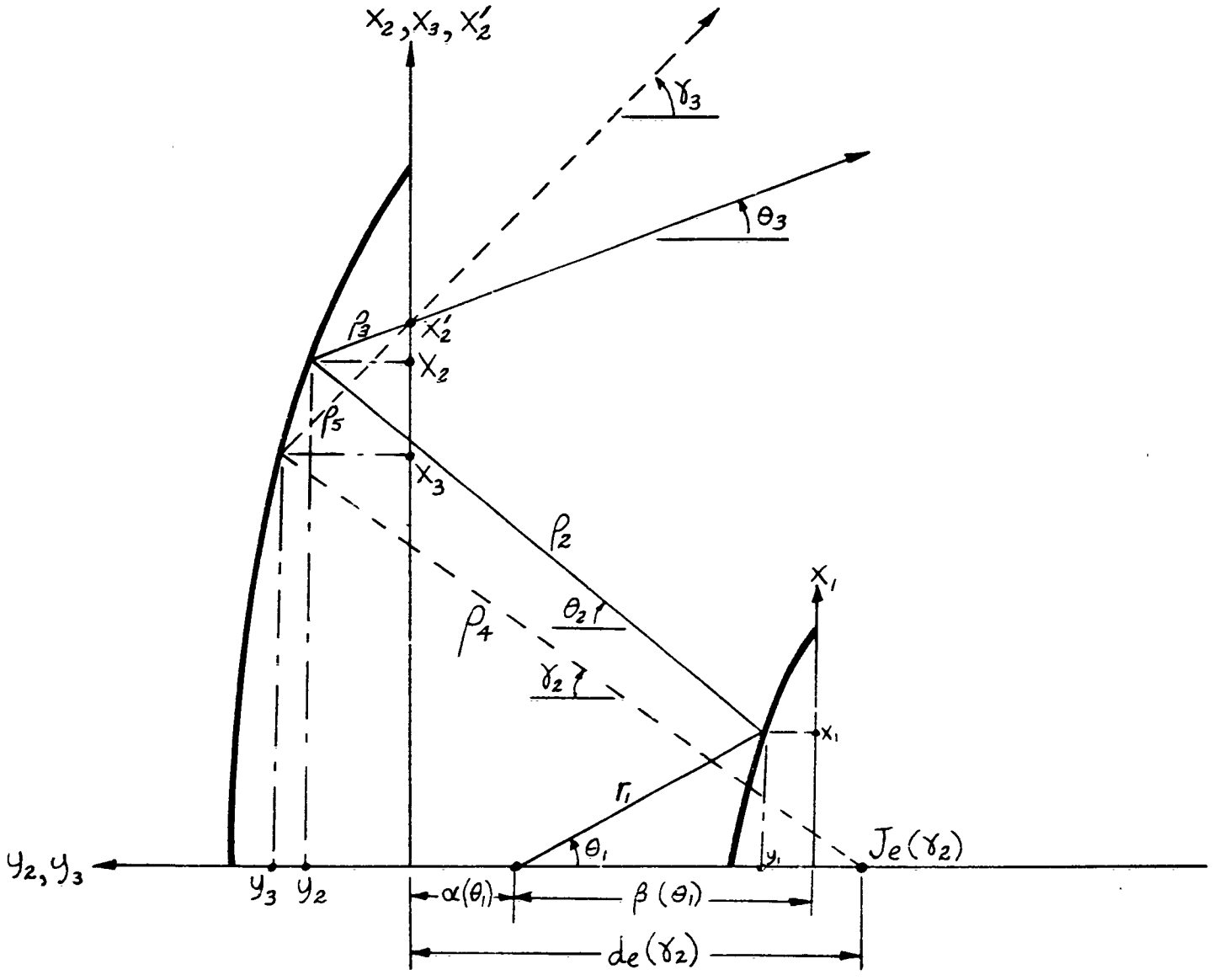

Fig. 2. Edge diffracted field geometry.

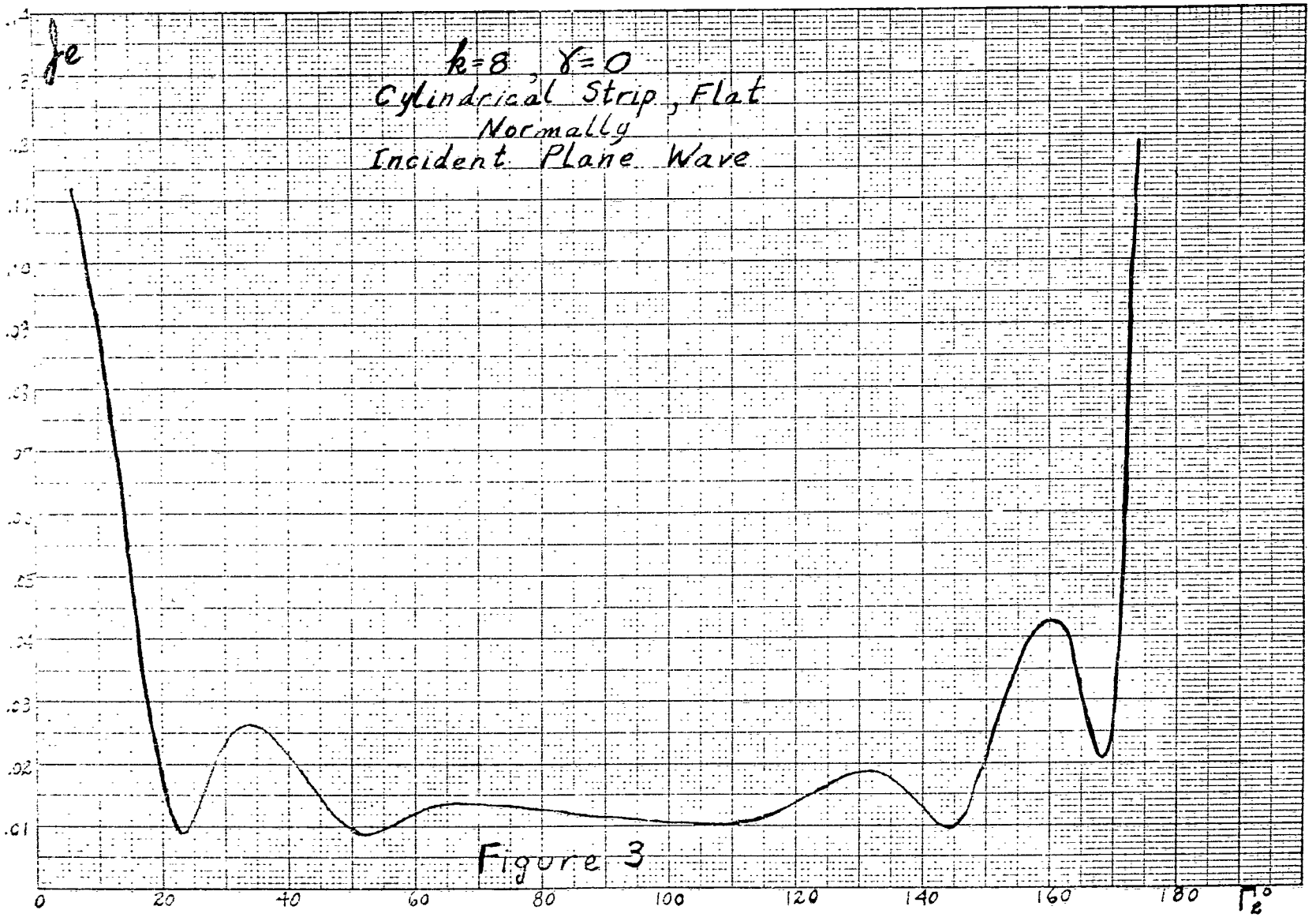
f_e
$k=8$, $\gamma=0$
Cylindrical Strip, Flat
Normally
Incident Plane Wave
.1
.09
.08
.07
.06
.05
.04
.03
.02
.01
0
20
40
60
80
100
120
140
160
180
$\Gamma_e°$

Figure 3

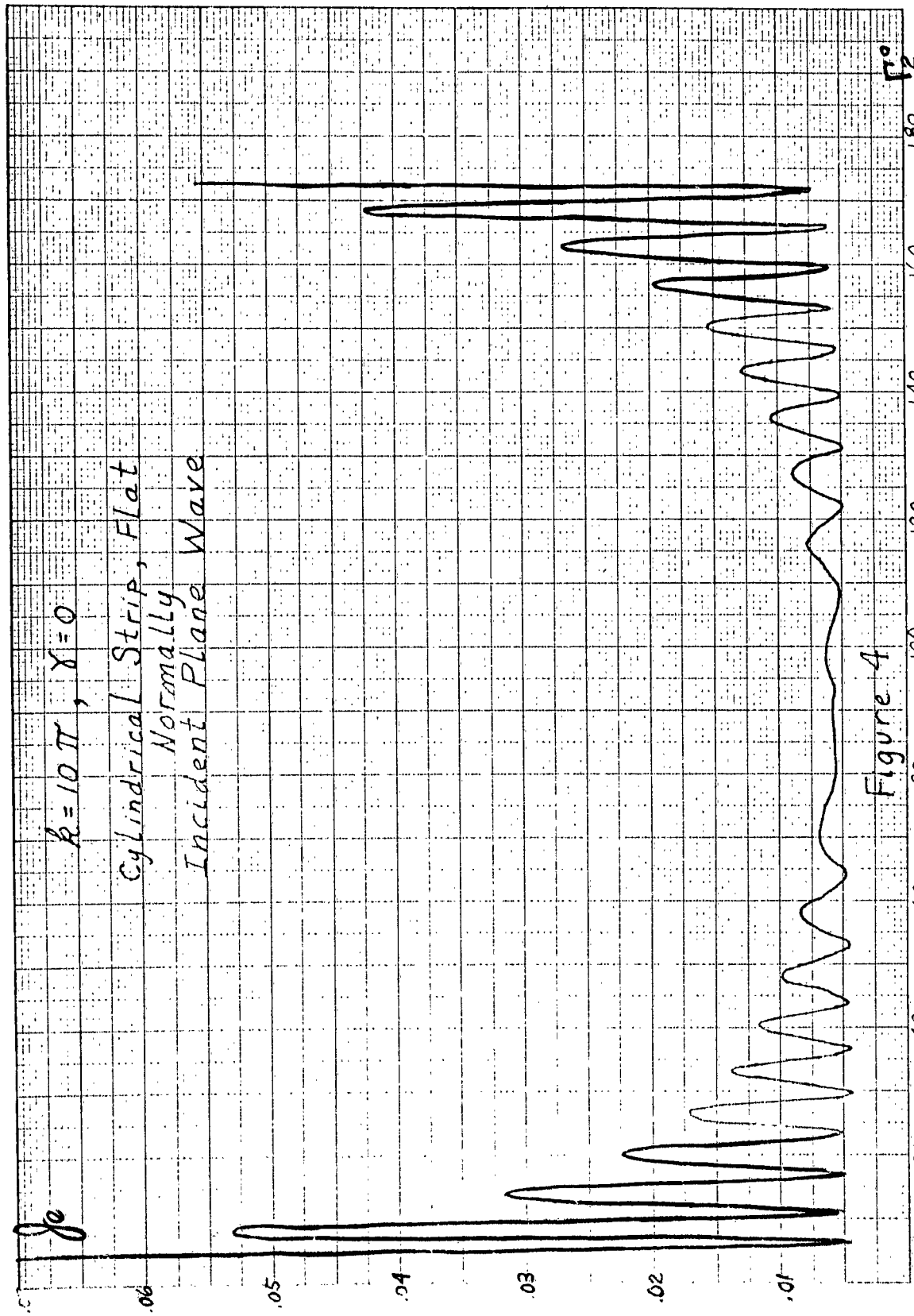
f_e
$k = 10\pi$, $\gamma = 0$
Cylindrical Strip, Flat
Normally
Incident Plane Wave
.06
.05
.04
.03
.02
.01
0
20
40
60
80
100
120
140
160
180
Γ^2

Figure 4

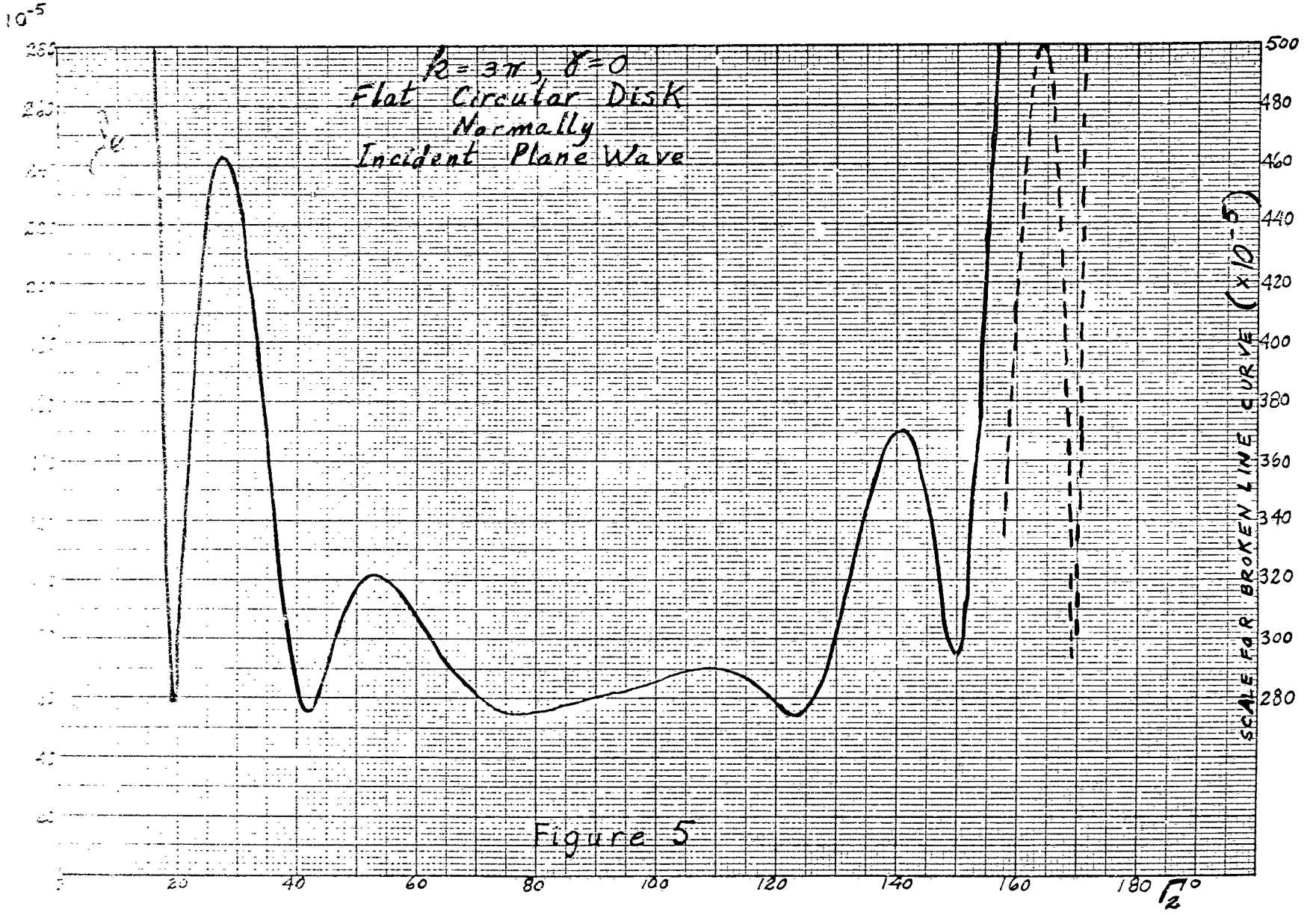
10^{-5}
$k = 3\pi$, $\gamma = 0$
Flat Circular Disk
Normally
Incident Plane Wave
σ_e
SCALE FOR BROKEN LINE CURVE ($\times 10^{-5}$)
500
480
460
440
420
400
380
360
340
320
300
280
20
40
60
80
100
120
140
160
180
Γ_2°

Figure 5

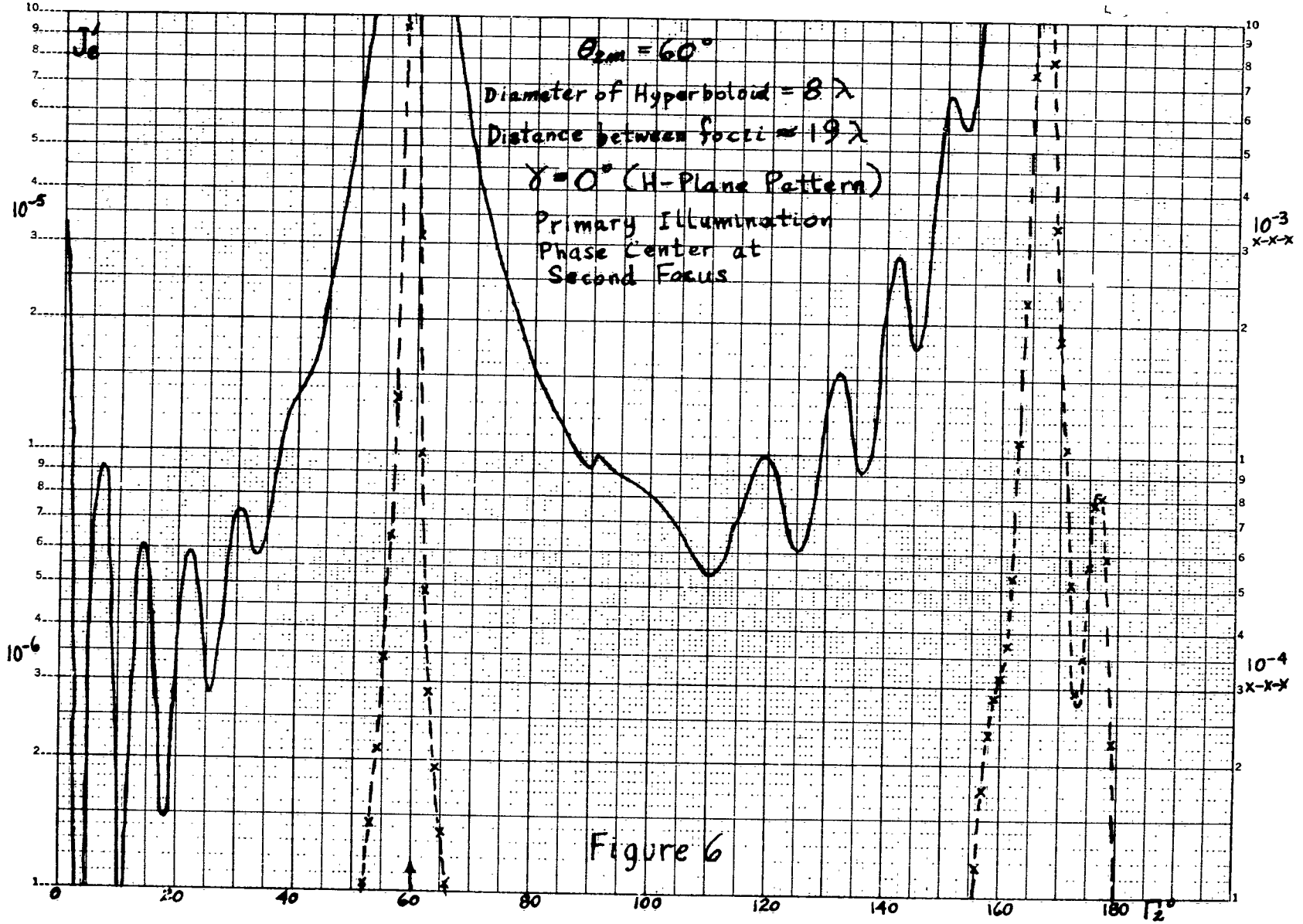
K·Σ SEMI-LOGARITHMIC 359-64
KEUFFEL & ESSER CO.
2 CYCLES X 200 DIVISIONS
J_θ
$\theta_{2m} = 60°$
Diameter of Hyperboloid = 8 λ
Distance between foci = 19 λ
γ = 0° (H-Plane Pattern)
Primary Illumination
Phase Center at
Second Focus
10^{-5}
10^{-6}
10^{-3}
10^{-4}
0
20
40
60
80
100
120
140
160
180
$\theta_2°$

Figure 6

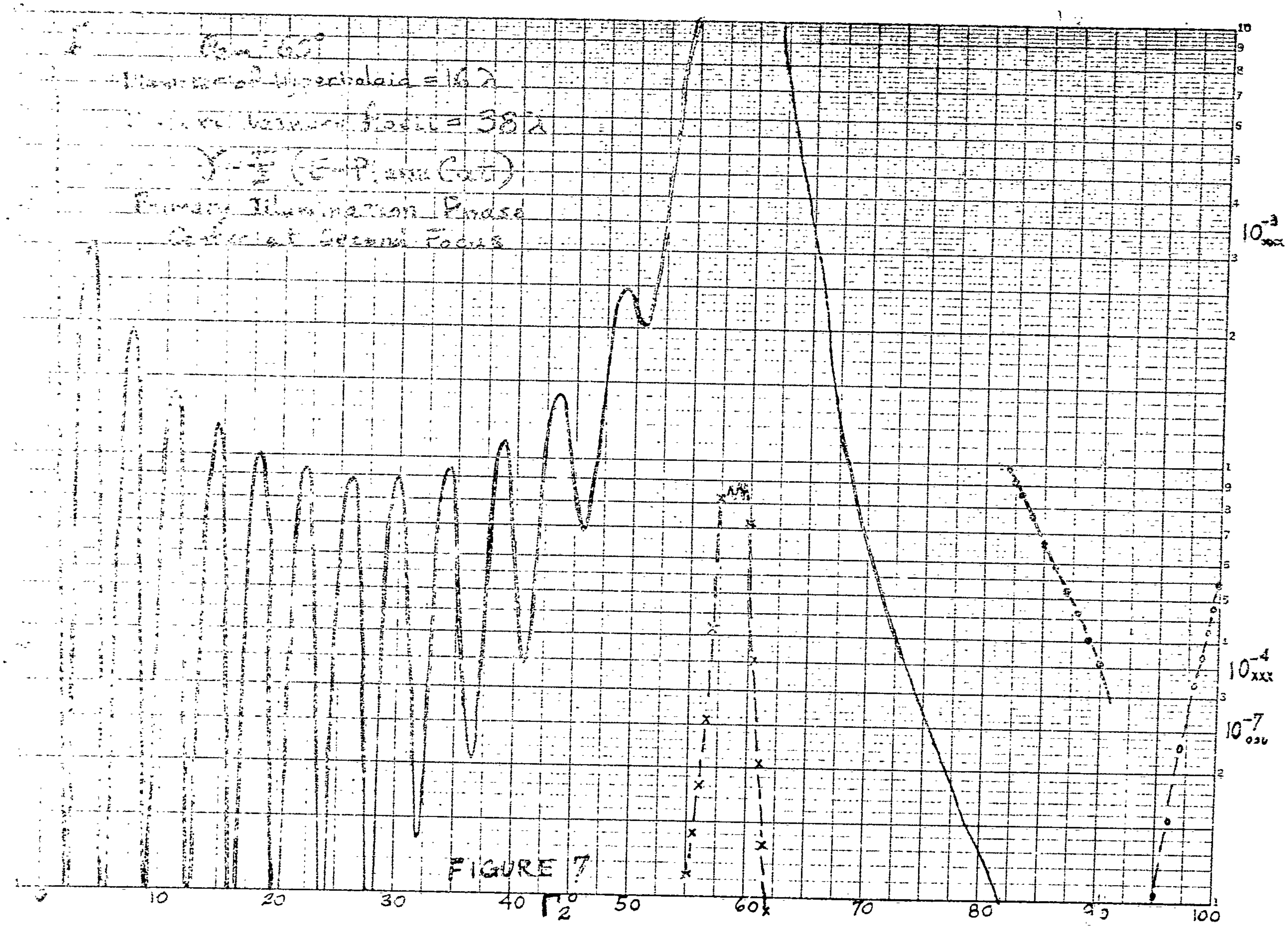
Primary Illumination Phase
10^{-3}
10^{-4}
10^{-7}
0
10
20
30
40
50
60
70
80
90
100
Γ_2°

FIGURE 7

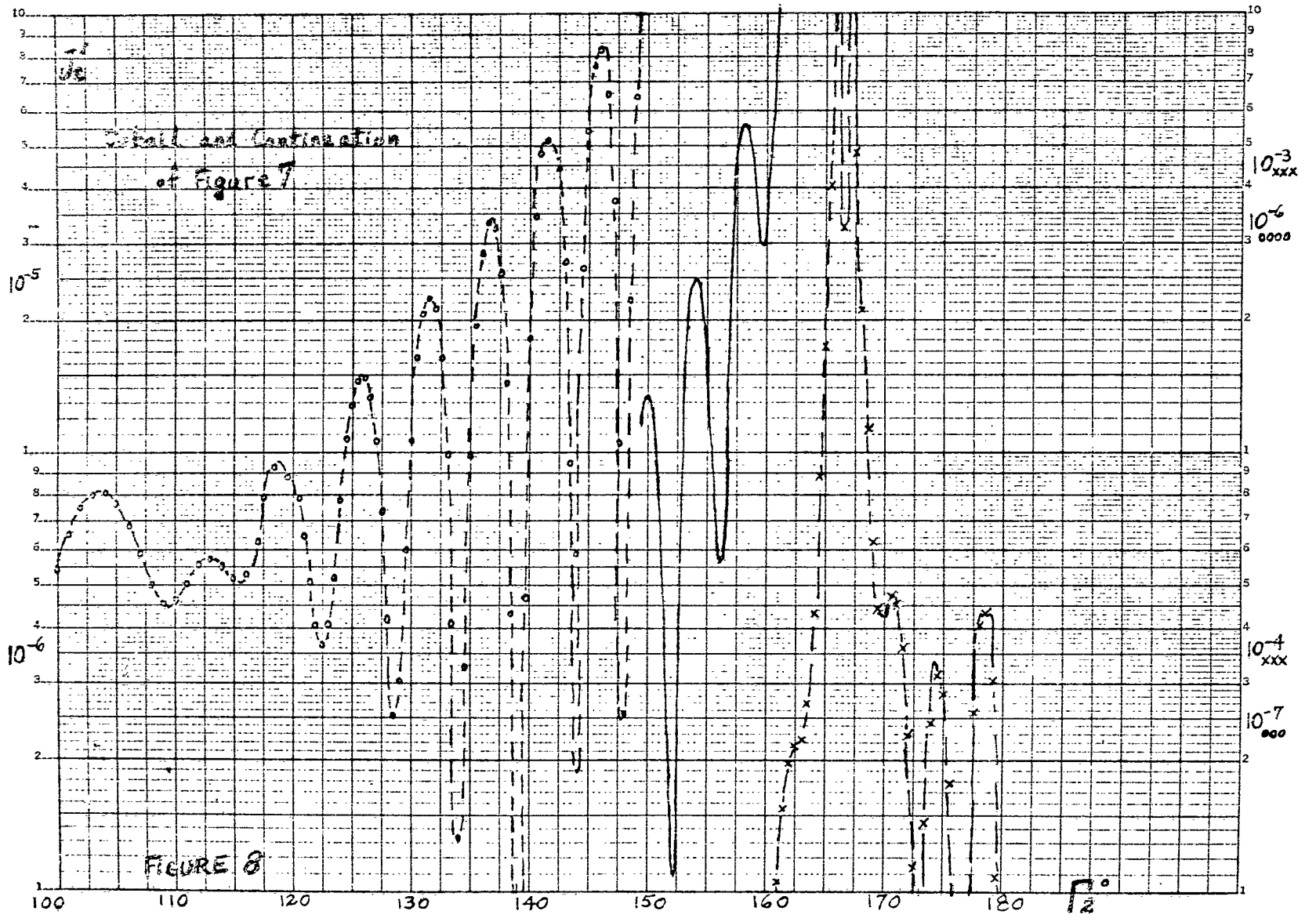
Detail and Continuation of Figure 7
10^{-5}
10^{-6}
10^{-3}
10^{-6}
10^{-4}
10^{-7}
100
110
120
130
140
150
160
170
180
Γ^2

FIGURE 8

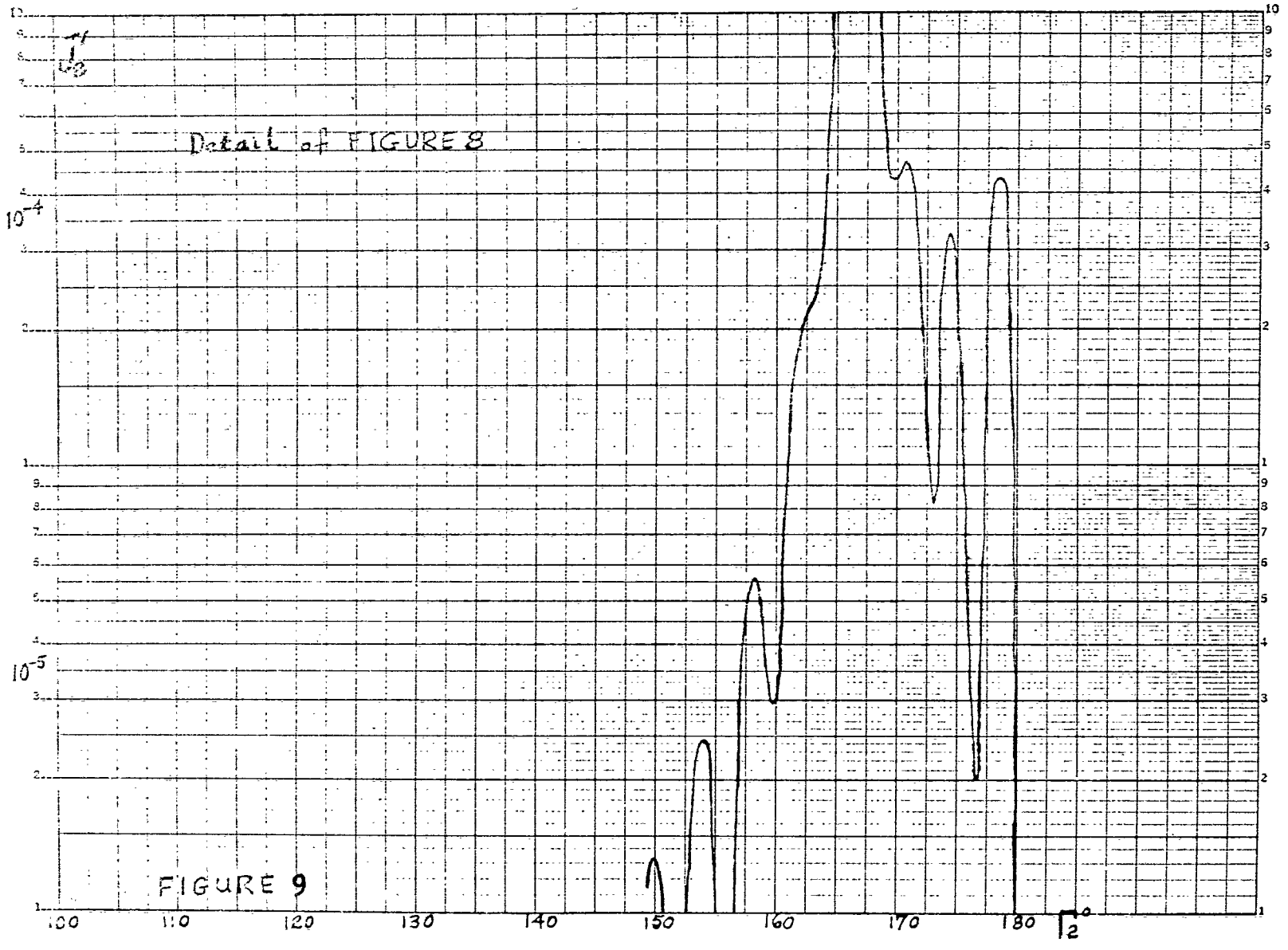
Detail of FIGURE 8
10^{-4}
10^{-5}
100
110
120
130
140
150
160
170
180
Γ_2

FIGURE 9

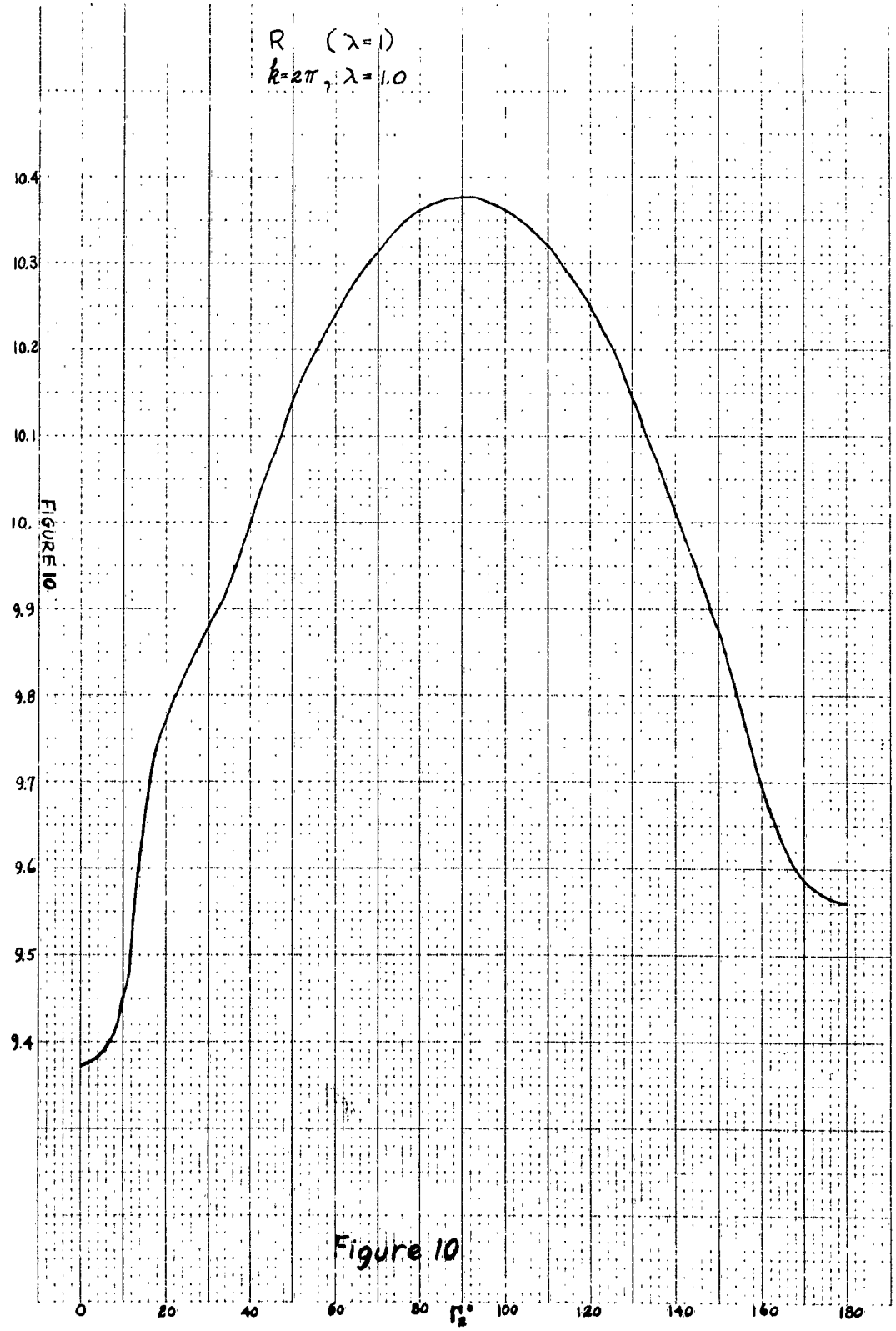
R (λ=1)
k=2π, λ=1.0
10.4
10.3
10.2
10.1
10.
9.9
9.8
9.7
9.6
9.5
9.4
FIGURE 10
0
20
40
60
80
100
120
140
160
180
Γ₂°

Figure 10

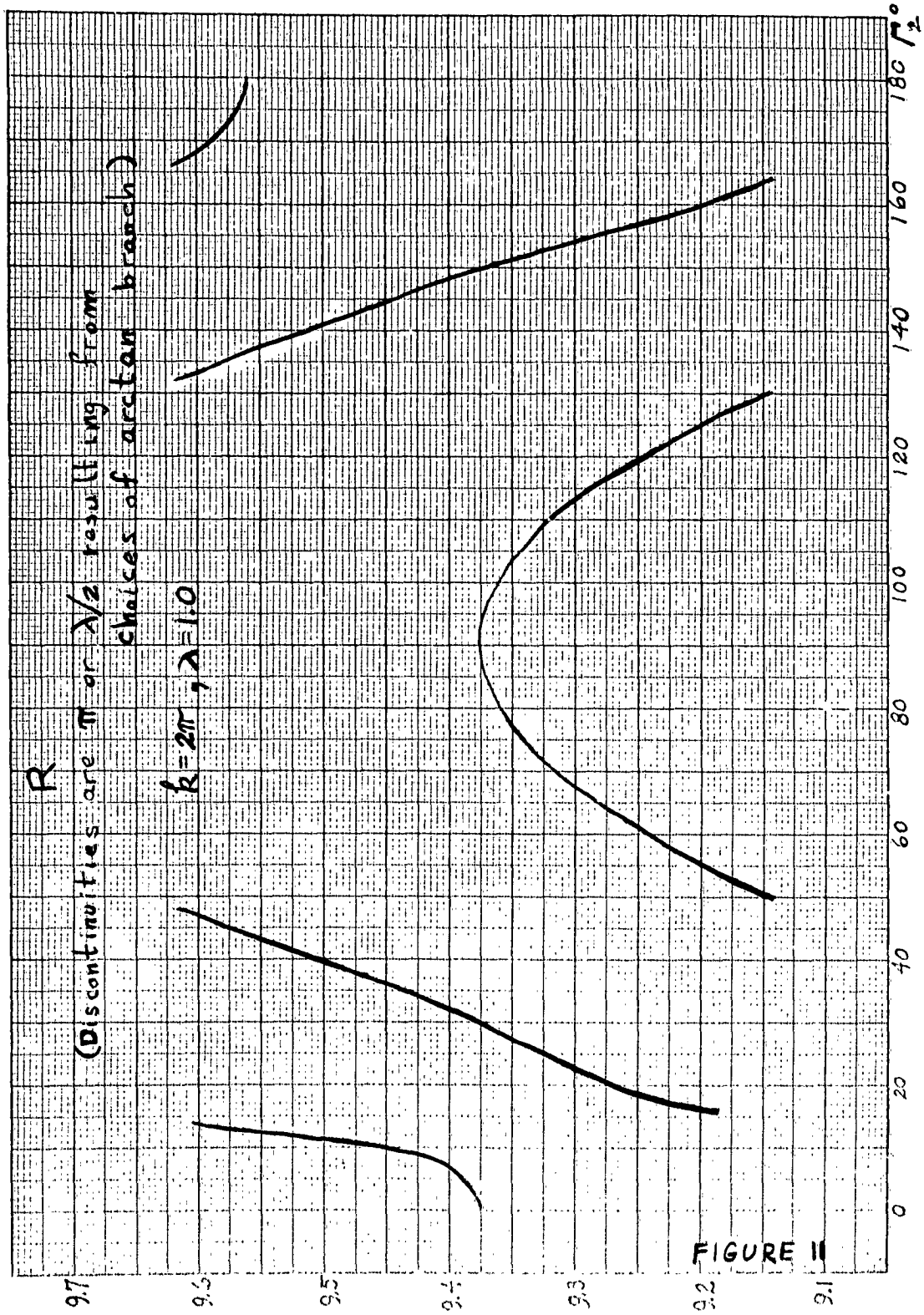
R
(Discontinuities are π or $\lambda/2$ resulting from choices of arctan branch.)
$k = 2\pi$, $\lambda = 1.0$
9.7
9.5
9.3
9.1
0
20
40
60
80
100
120
140
160
180
$\Gamma_2°$

FIGURE 11

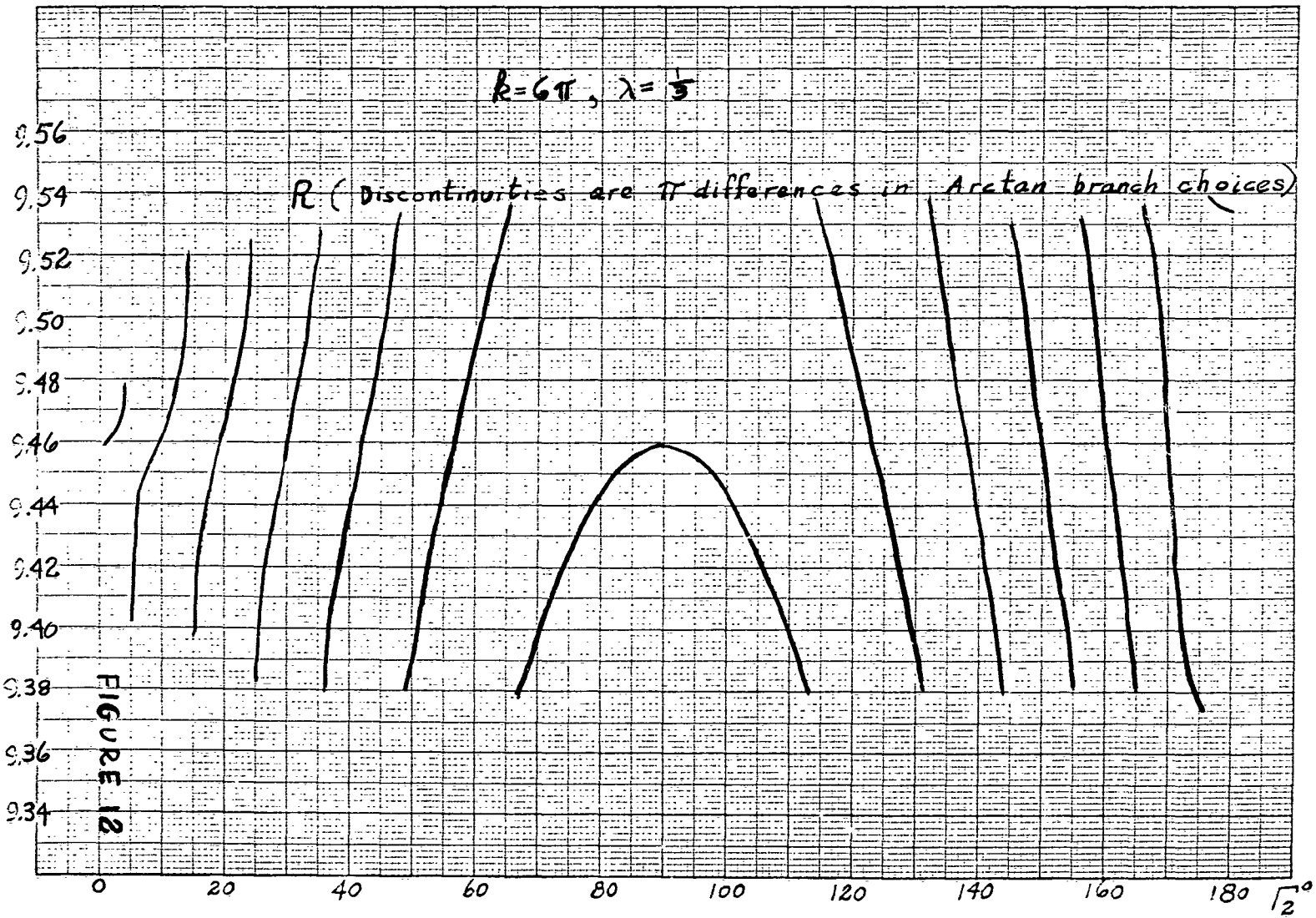
$k = 6\pi$, $\lambda = \frac{1}{3}$
R (Discontinuities are π differences in Arctan branch choices)
9.56
9.54
9.52
9.50
9.48
9.46
9.44
9.42
9.40
9.38
9.36
9.34
0
20
40
60
80
100
120
140
160
180
Γ_2°

FIGURE 12

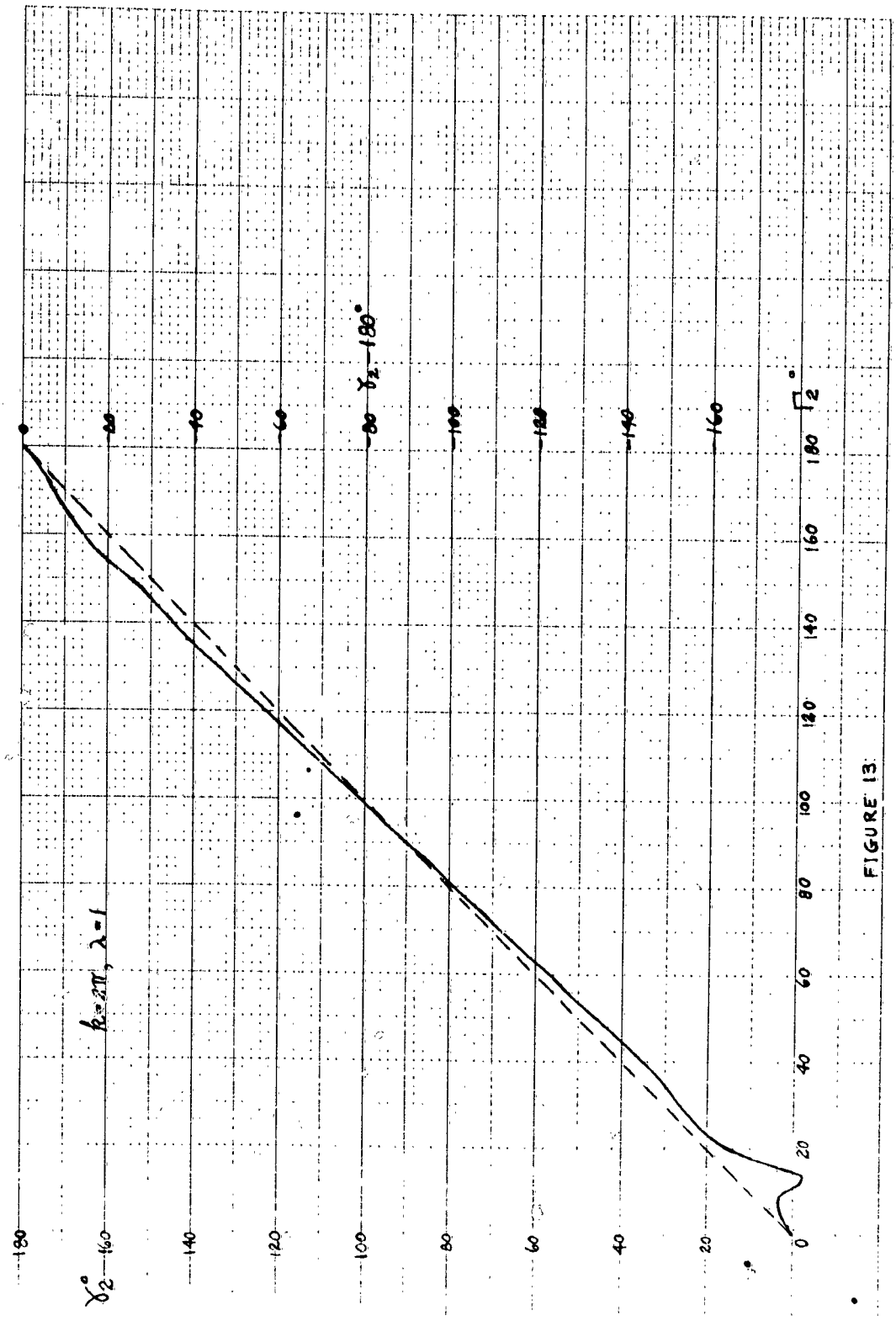
γ_2°
$k=2\pi,\ \lambda=1$
$\gamma_2=180^\circ$
θ_2
180
160
140
120
100
80
60
40
20
0
20
40
60
80
100
120
140
160
180

FIGURE 13

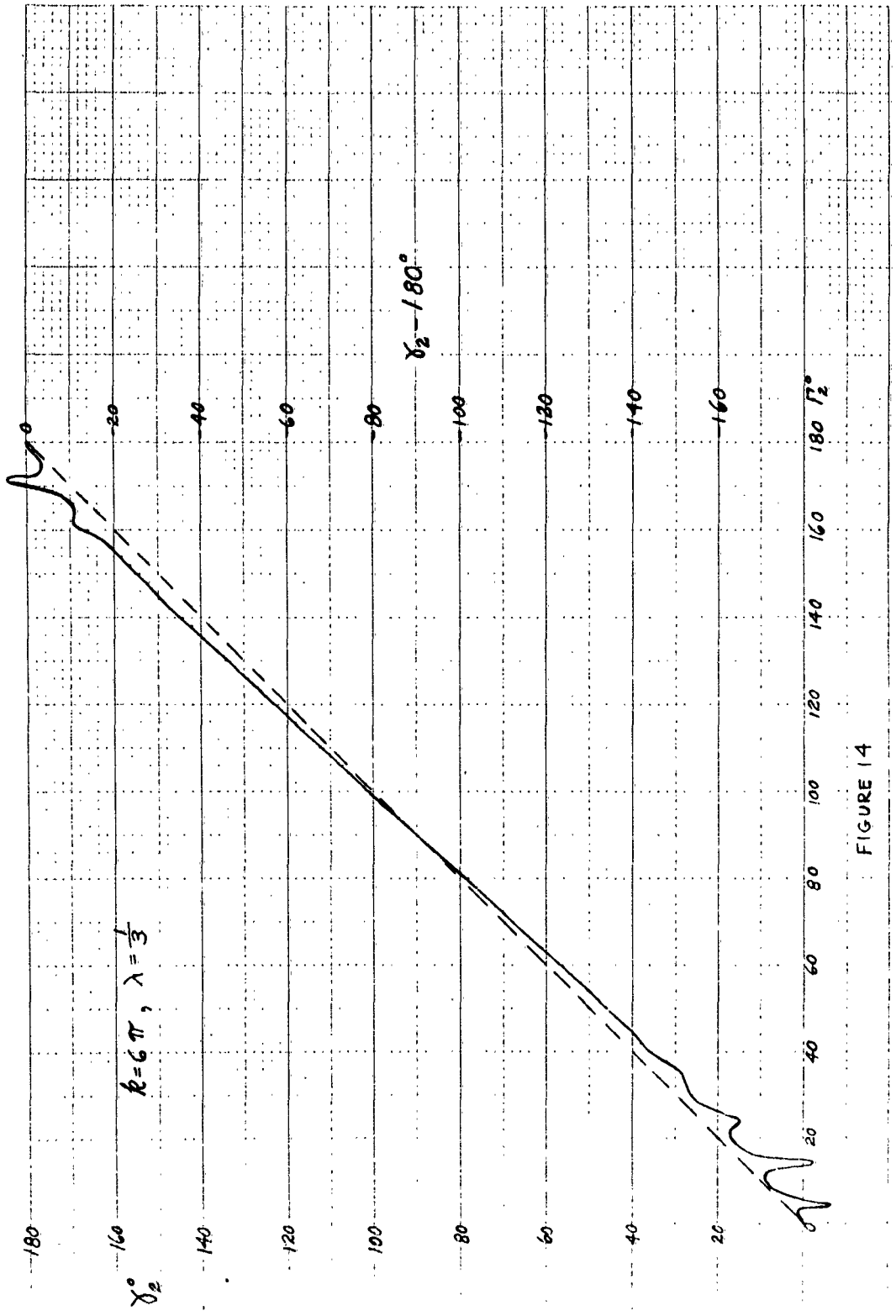

FIGURE 14

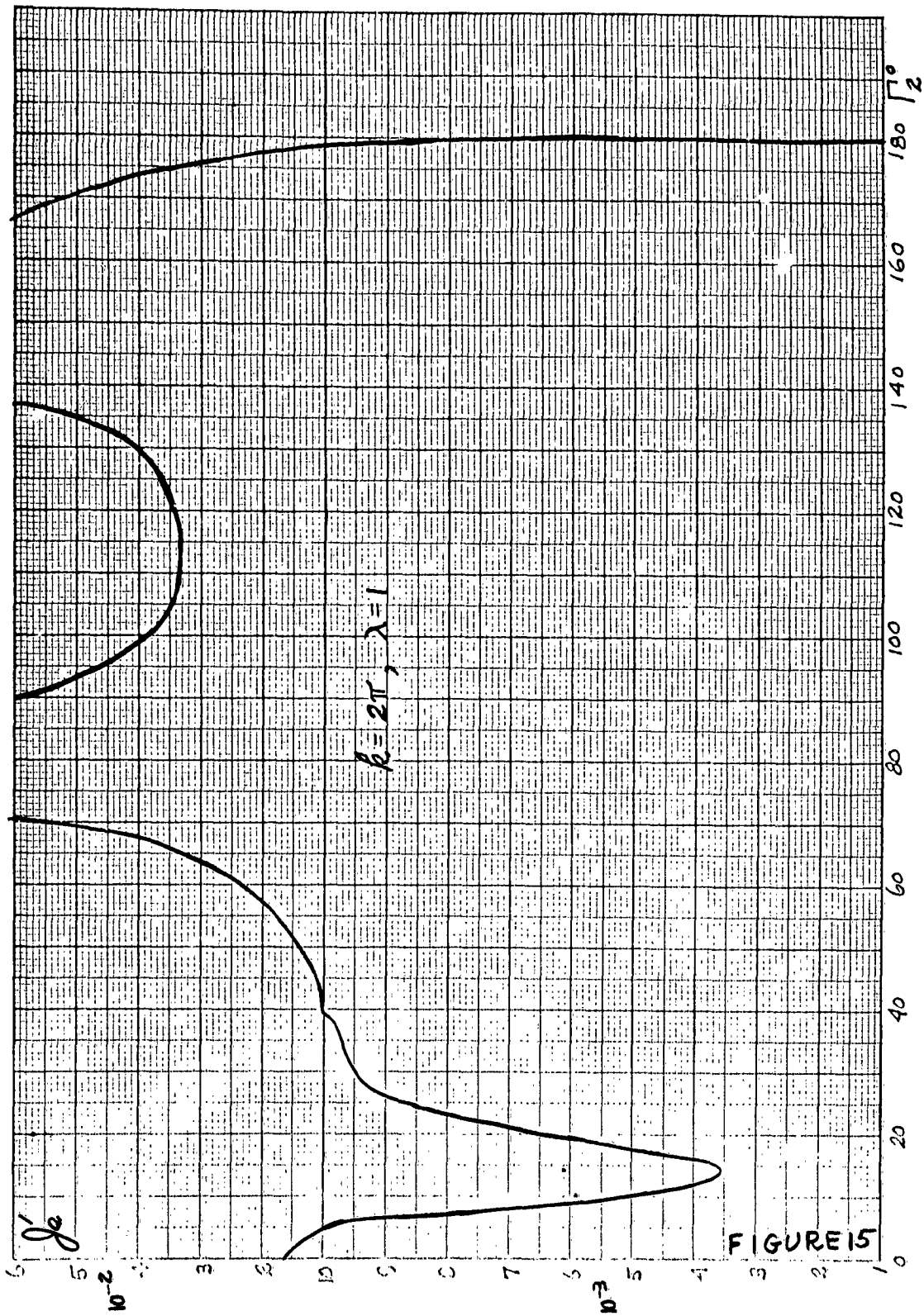
$\beta = 2\pi$, $\lambda = 1$
g'_e
Γ_2°
0
20
40
60
80
100
120
140
160
180
10^{-2}
10^{-3}

FIGURE 15

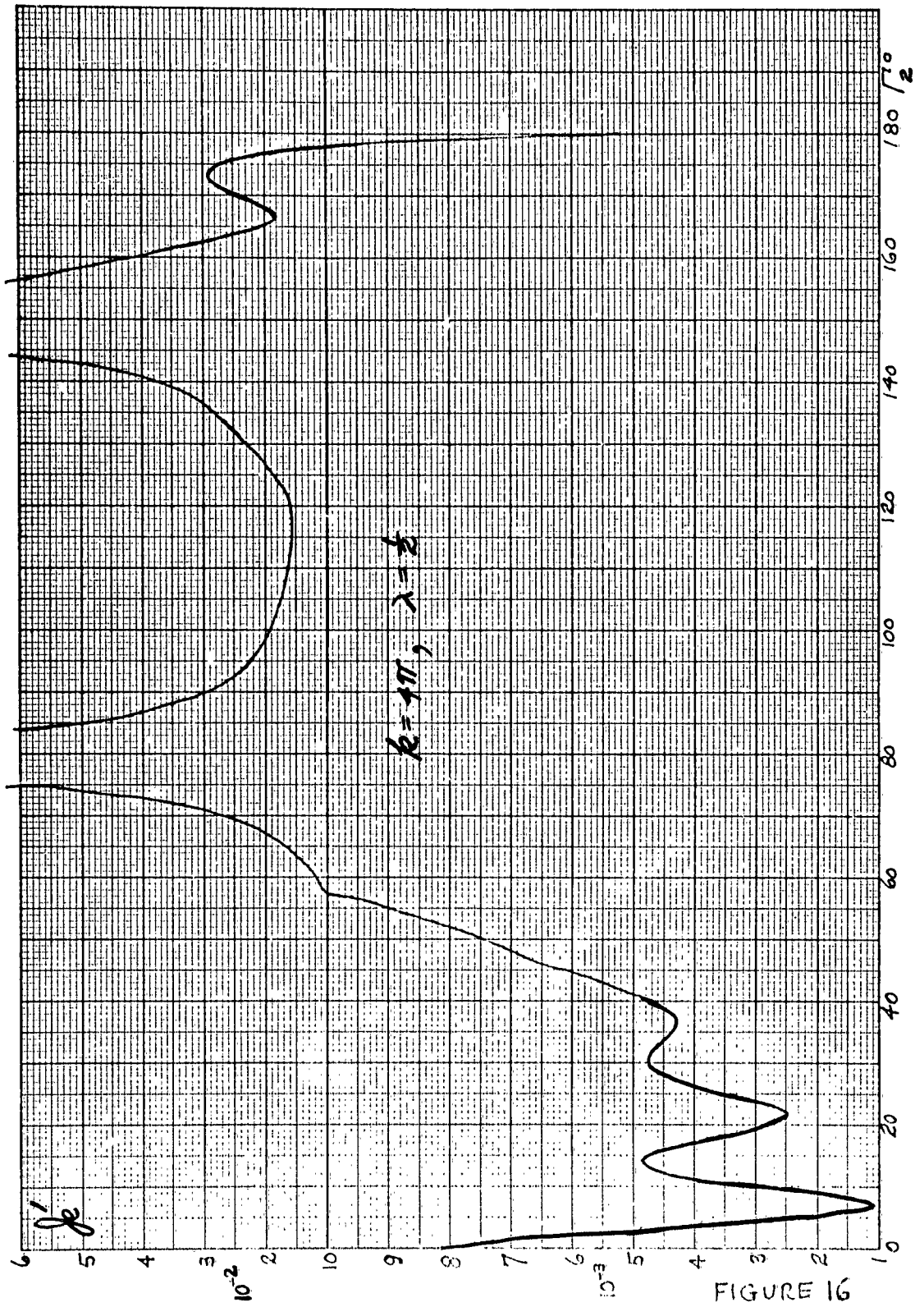

FIGURE 16

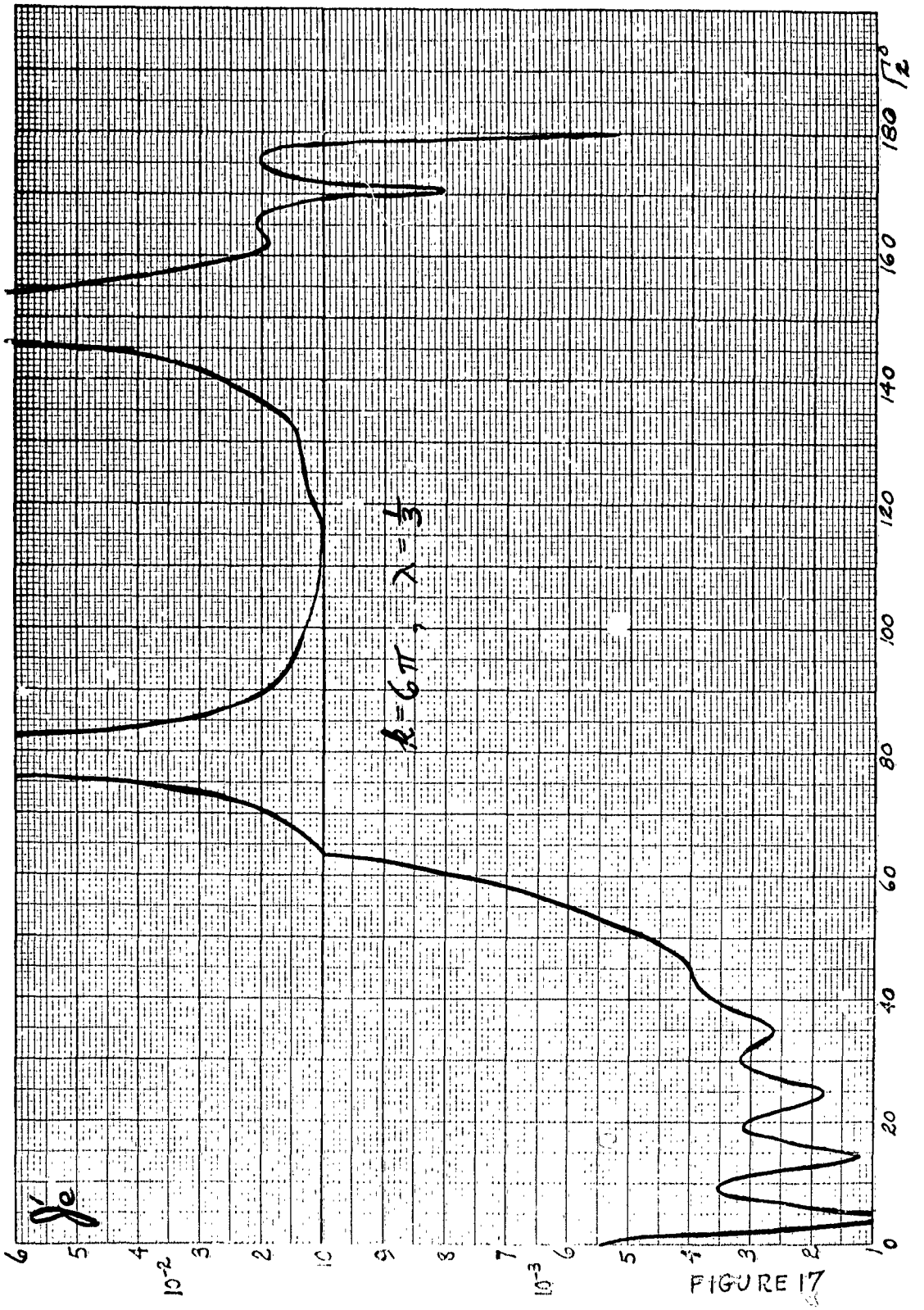
$k = 6\pi$, $\lambda = \frac{1}{3}$
q_e
10^{-2}
10^{-3}
Γ_2^0
0
20
40
60
80
100
120
140
160
180

FIGURE 17

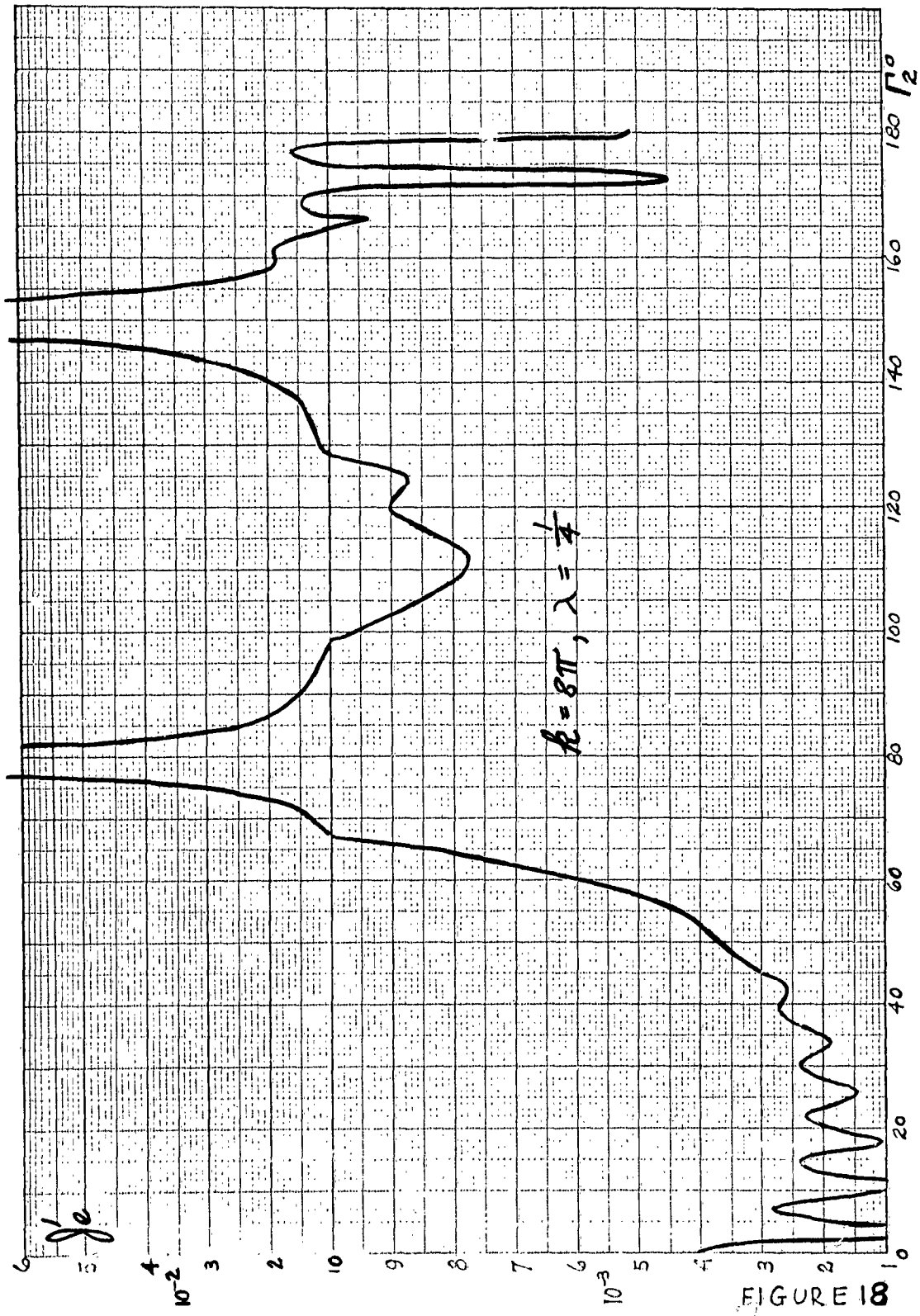
$\beta = 8\pi$, $\lambda = \frac{1}{4}$
γ_e
10^{-2}
10^{-3}
Γ_2^0
0
20
40
60
80
100
120
140
160
180

FIGURE 18

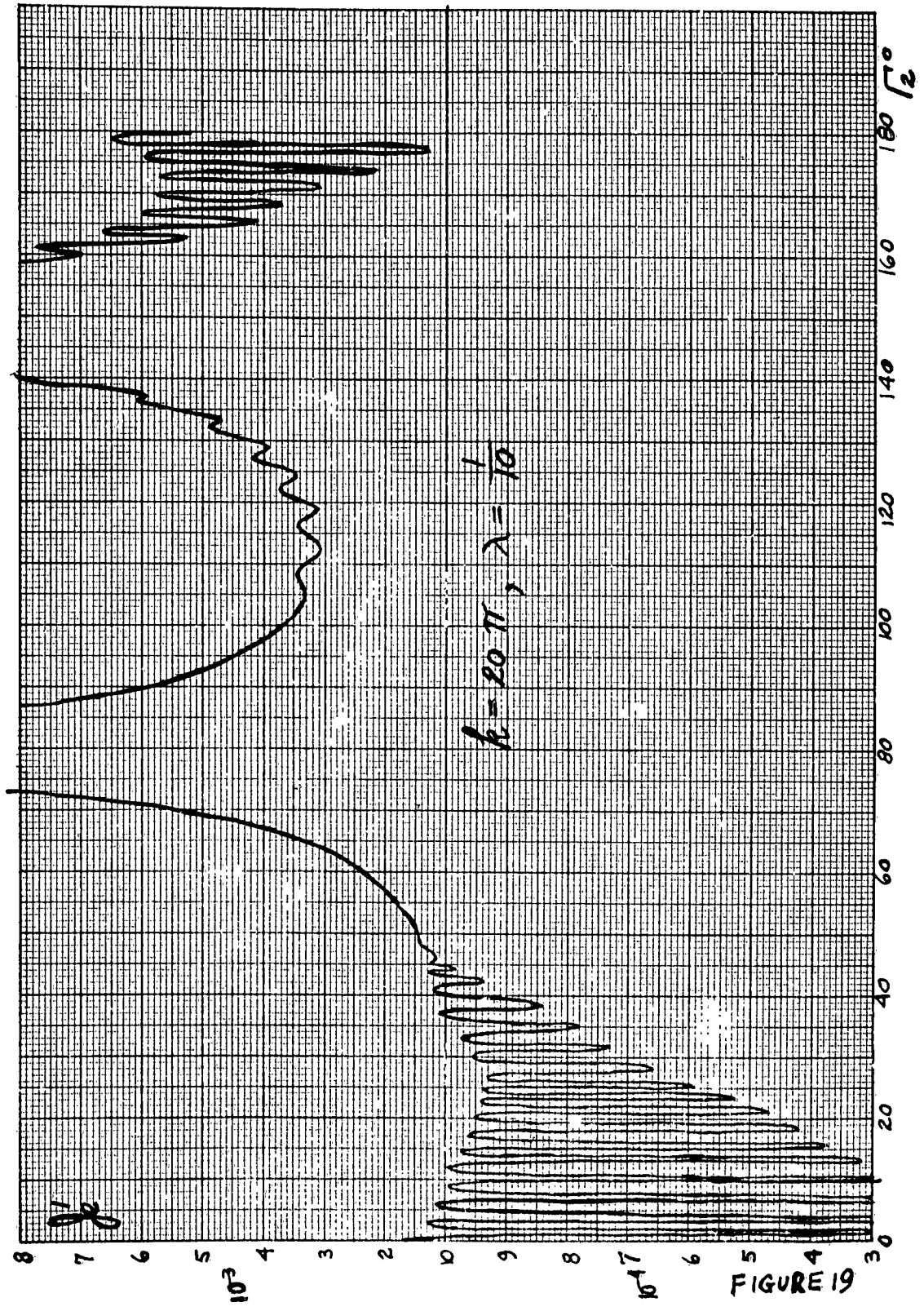
$k = 20\pi$, $\lambda = \frac{1}{10}$
Γ_2°
0
20
40
60
80
100
120
140
160
180
10^{-3}
10^{-7}

FIGURE 19

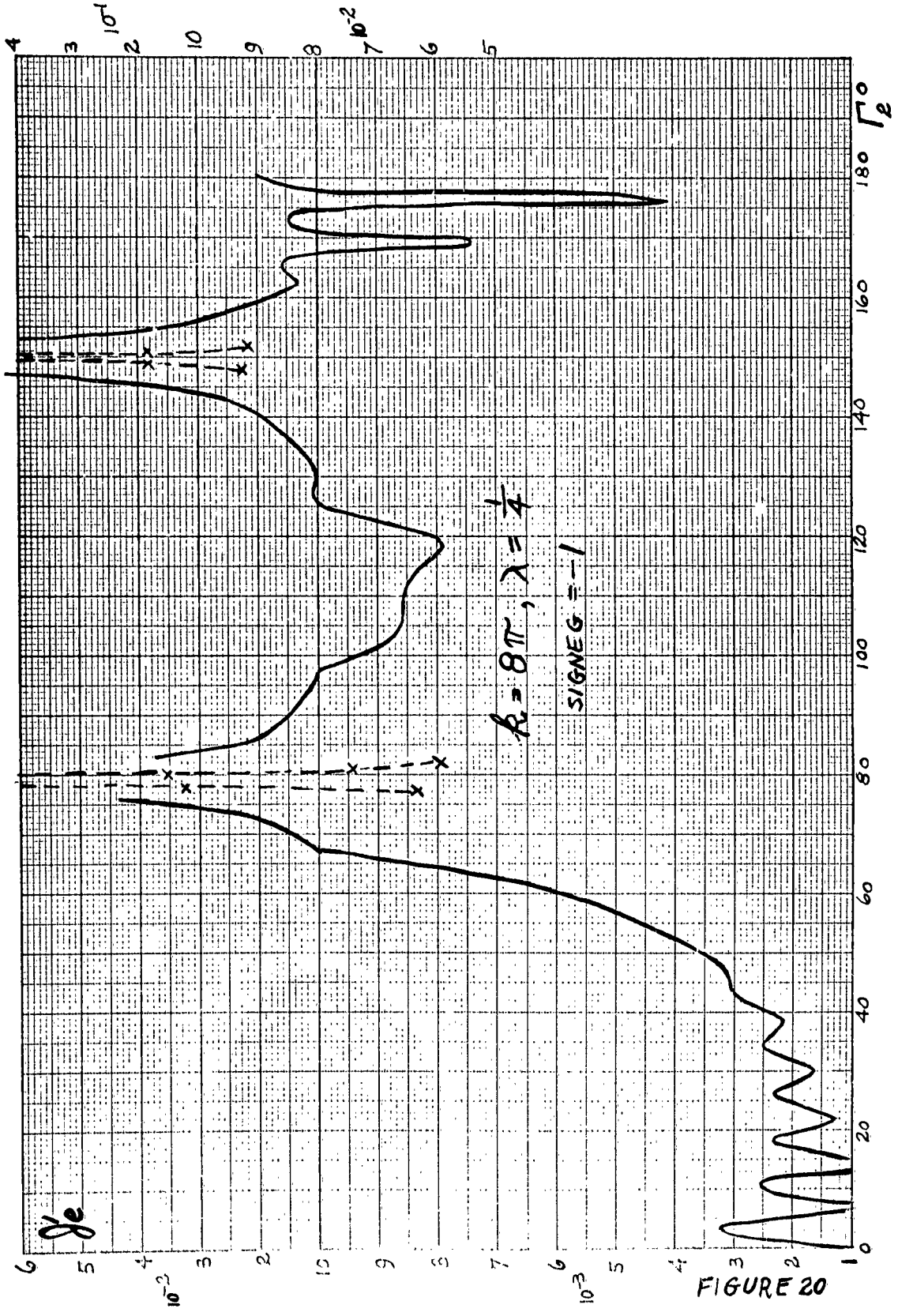

FIGURE 20

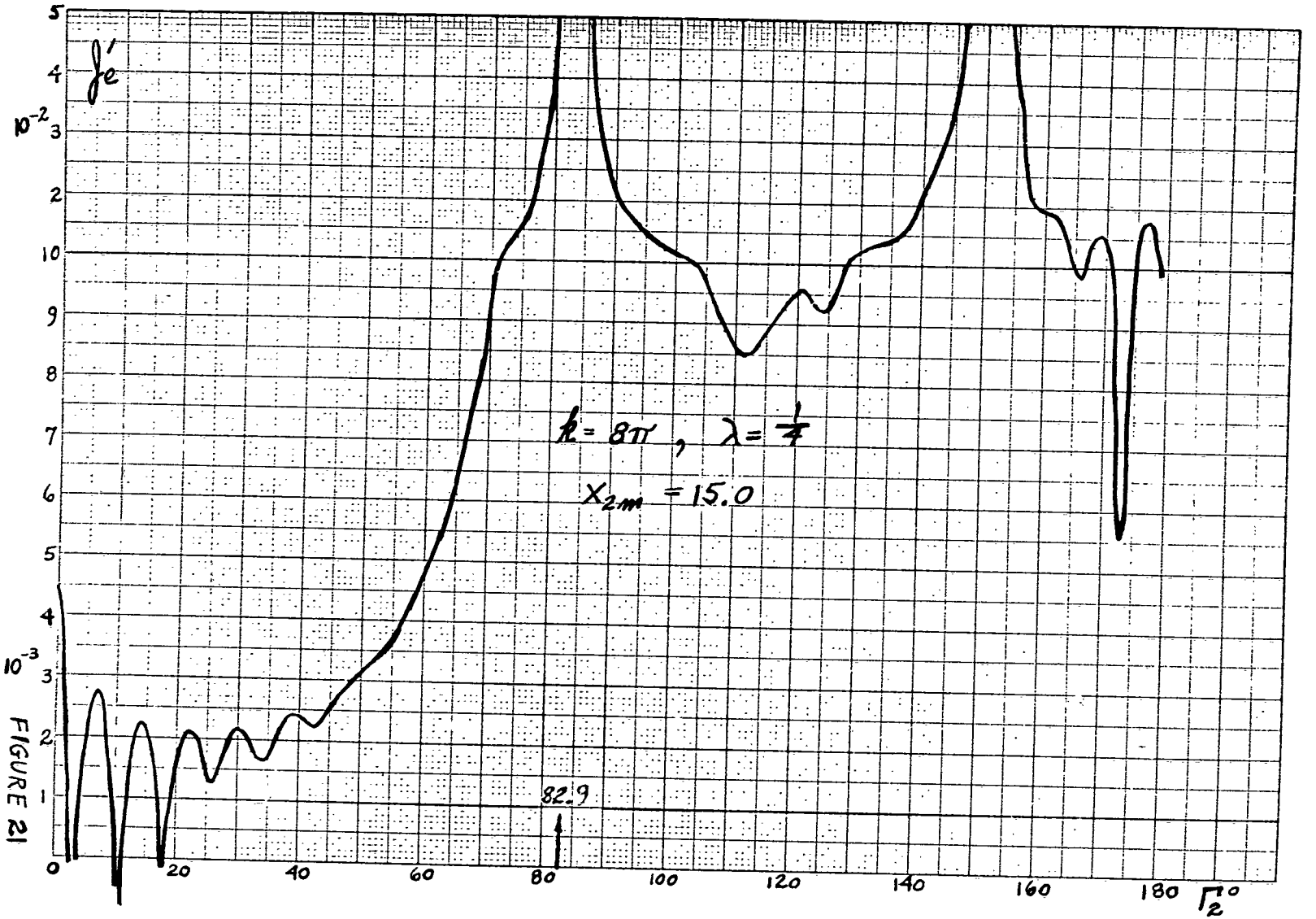
j'_e
10^{-2}
5
4
3
2
10
9
8
7
6
5
4
10^{-3}
3
2
1
0
20
40
60
80
100
120
140
160
180
Γ_2^0
82.9
$k = 8\pi$, $\lambda = \frac{1}{4}$
$X_{2m} = 15.0$

FIGURE 21

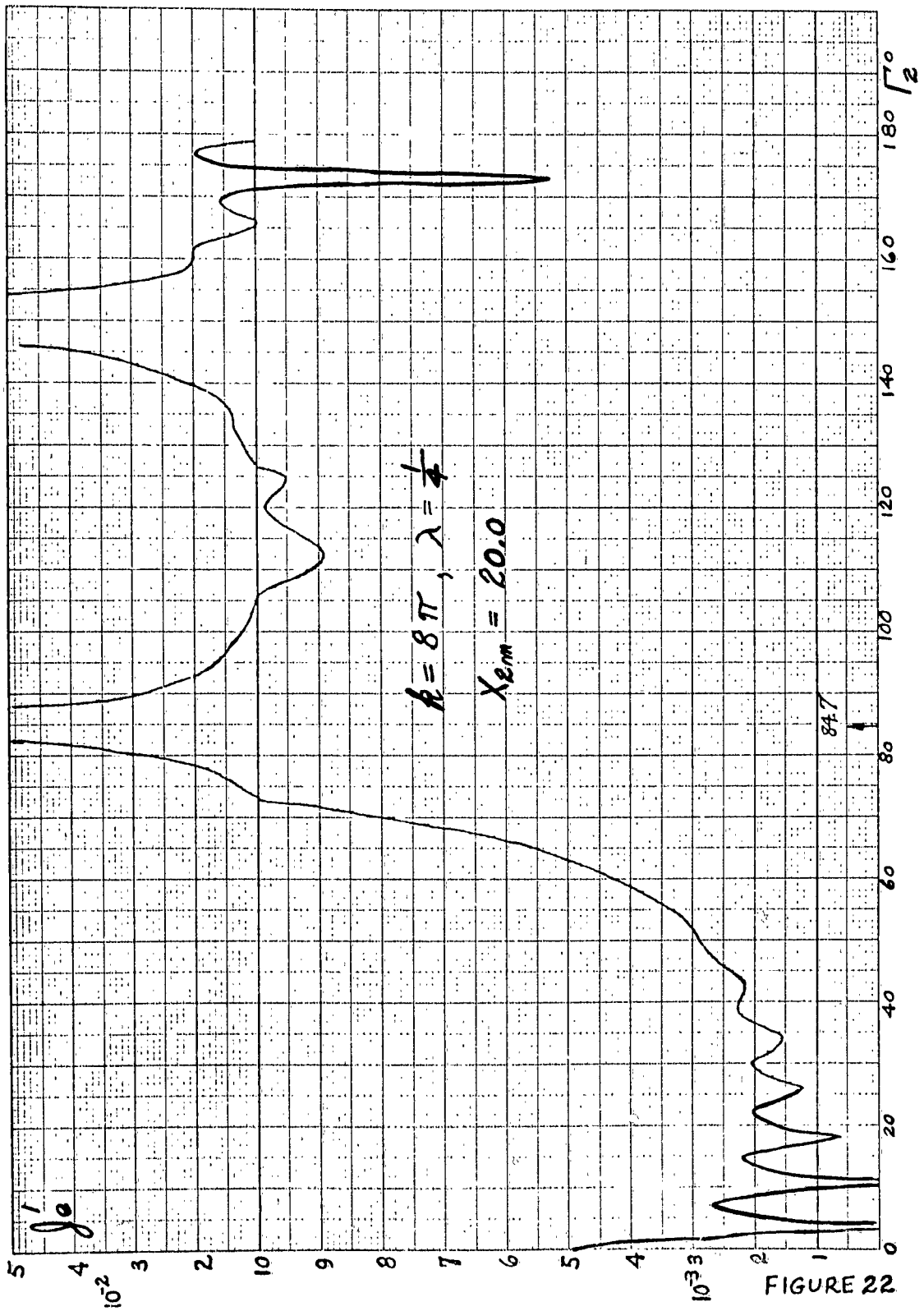
I_{θ}
10^{-2}
10^{-3}
$k = 8\pi$, $\lambda = \frac{1}{4}$
$X_{em} = 20.0$
84.7
Γ_2°
0
20
40
60
80
100
120
140
160
180

FIGURE 22

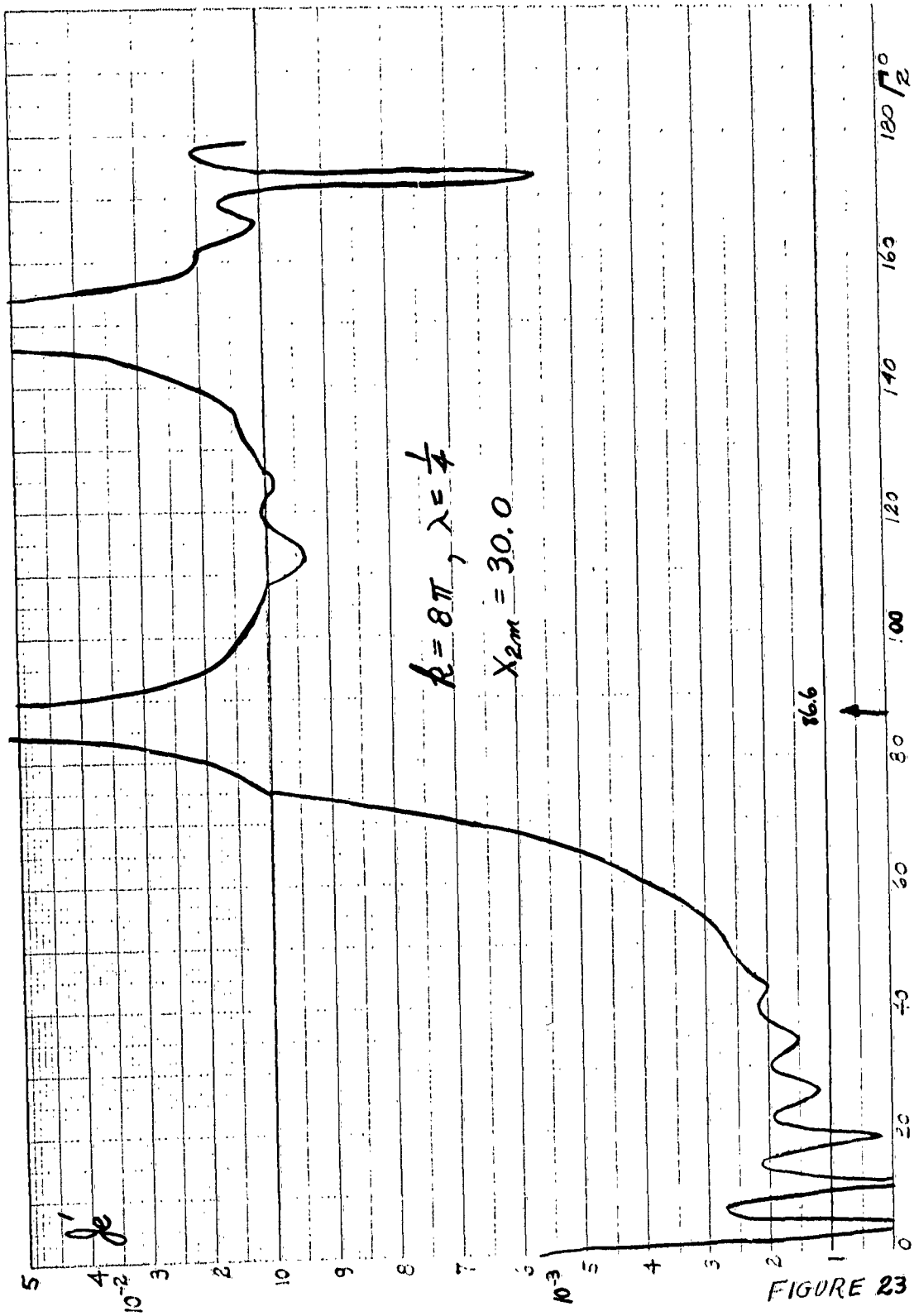
$k = 8\pi$, $\lambda = \frac{1}{4}$
$X_{2m} = 30.0$
86.6
I'_{ge}
10^{-2}
10^{-3}
θ_2
0
20
40
60
80
100
120
140
160
180

FIGURE 23

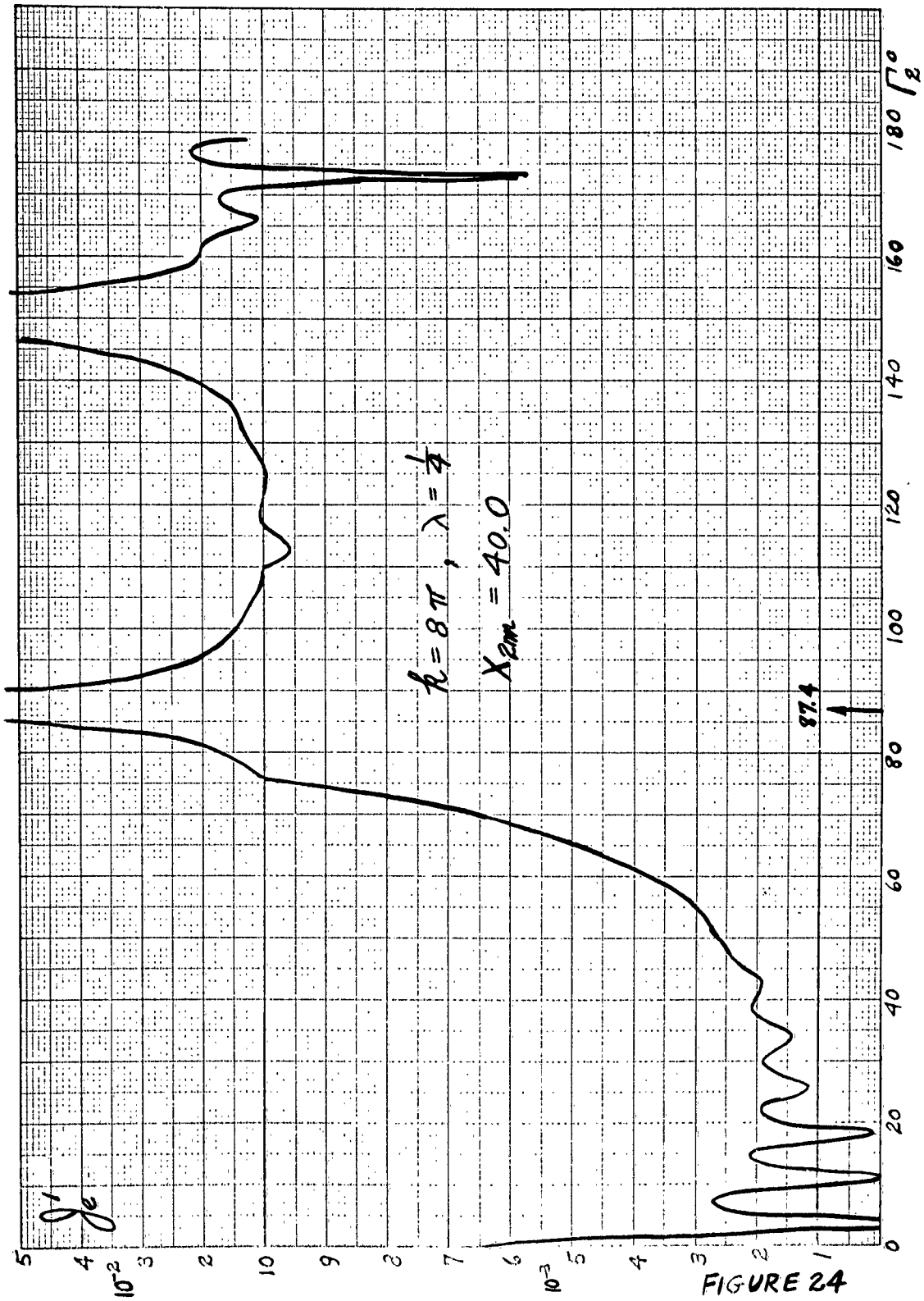
g'_e
10^{-2}
10^{-3}
$k = 8\pi$, $\lambda = \frac{1}{4}$
$X_{2m} = 40.0$
87.4
Γ_2^0
0
20
40
60
80
100
120
140
160
180

FIGURE 24

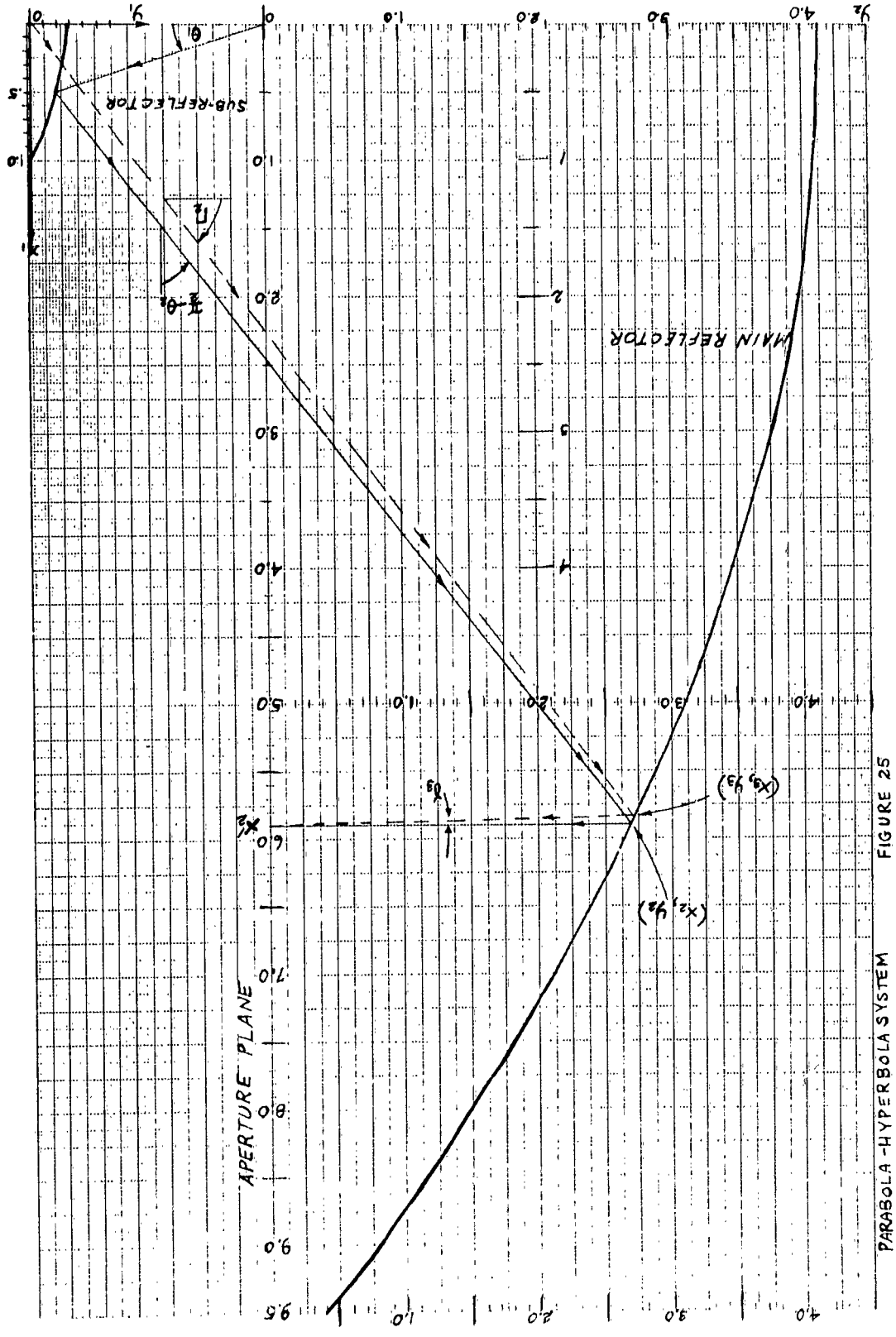

PARABOLA-HYPERBOLA SYSTEM FIGURE 25

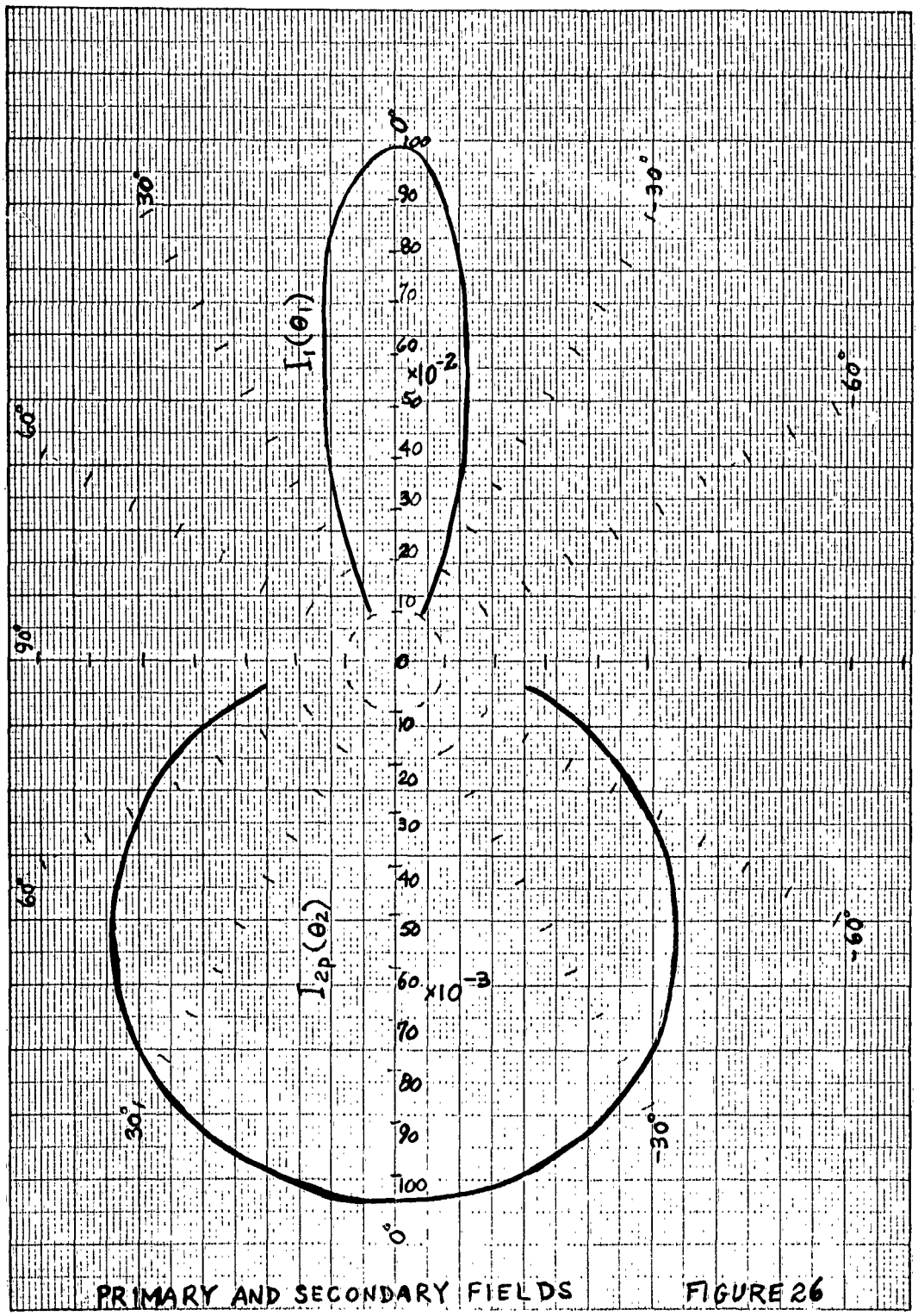

PRIMARY AND SECONDARY FIELDS FIGURE 26

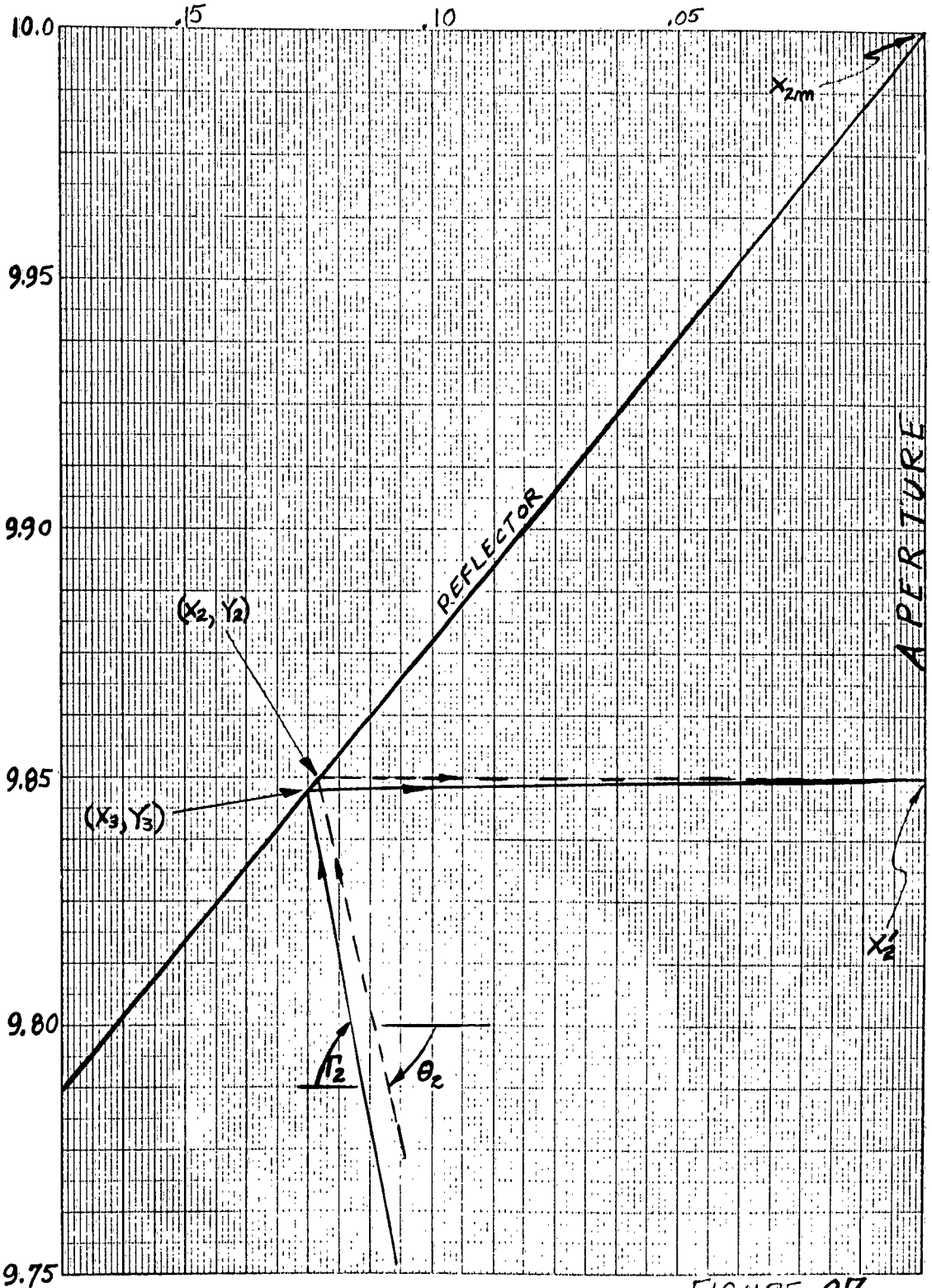
10.0
9.95
9.90
9.85
9.80
9.75
.15
.10
.05
x_{2m}
REFLECTOR
APERTURE
(x_2, y_2)
(x_3, y_3)
x_2'
r_2
θ_2

FIGURE 27

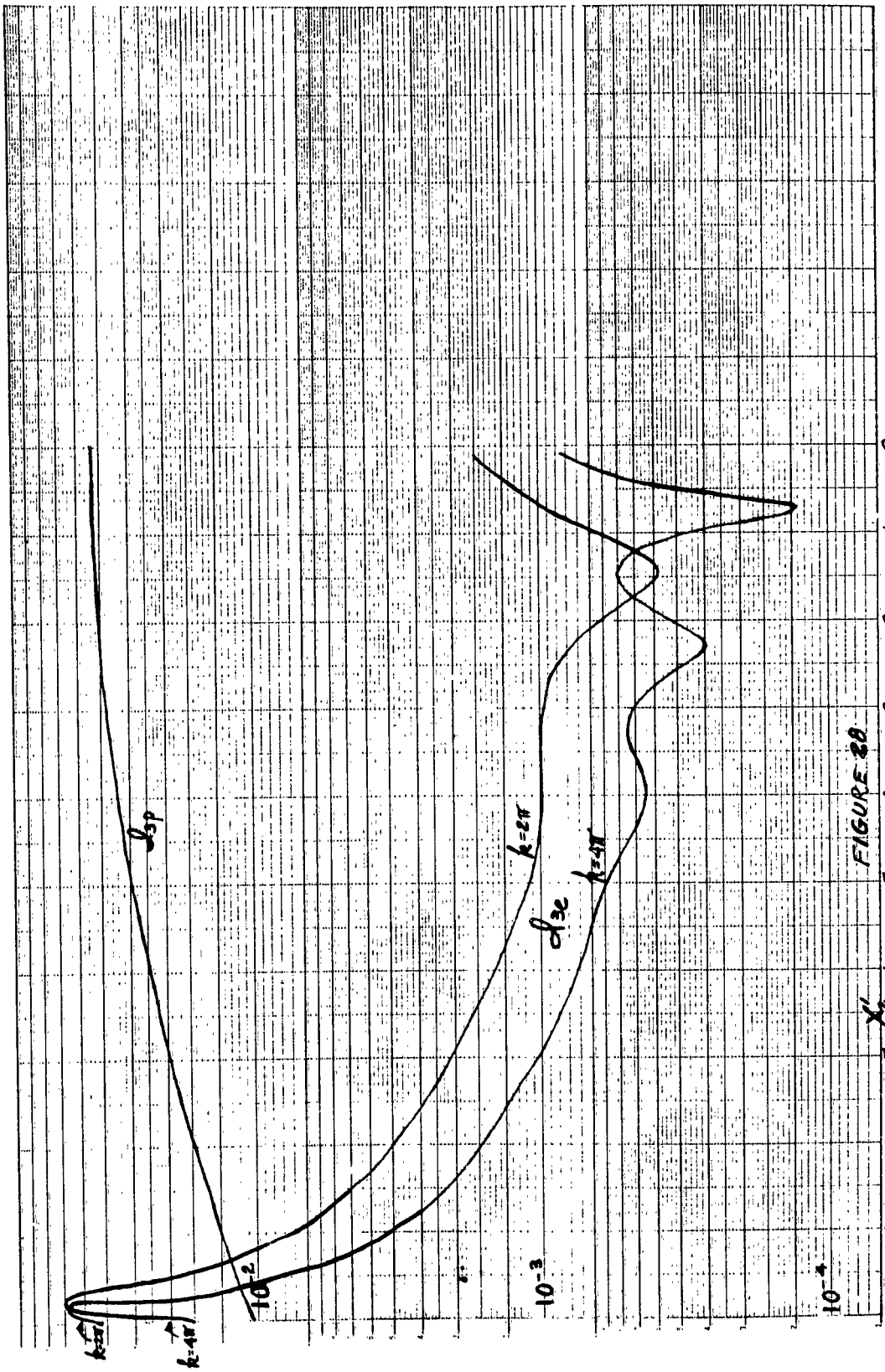

FIGURE 20

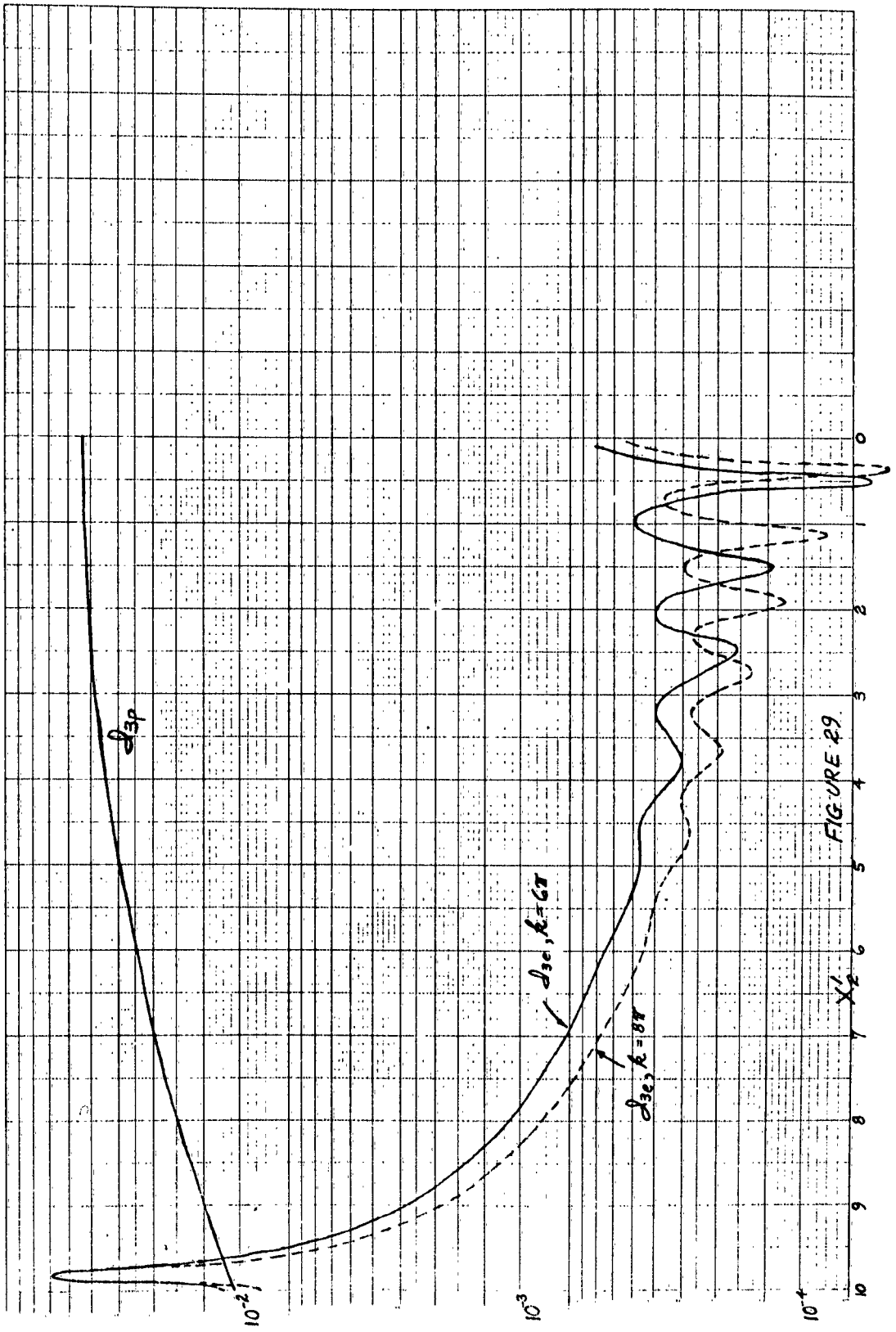

FIGURE 29

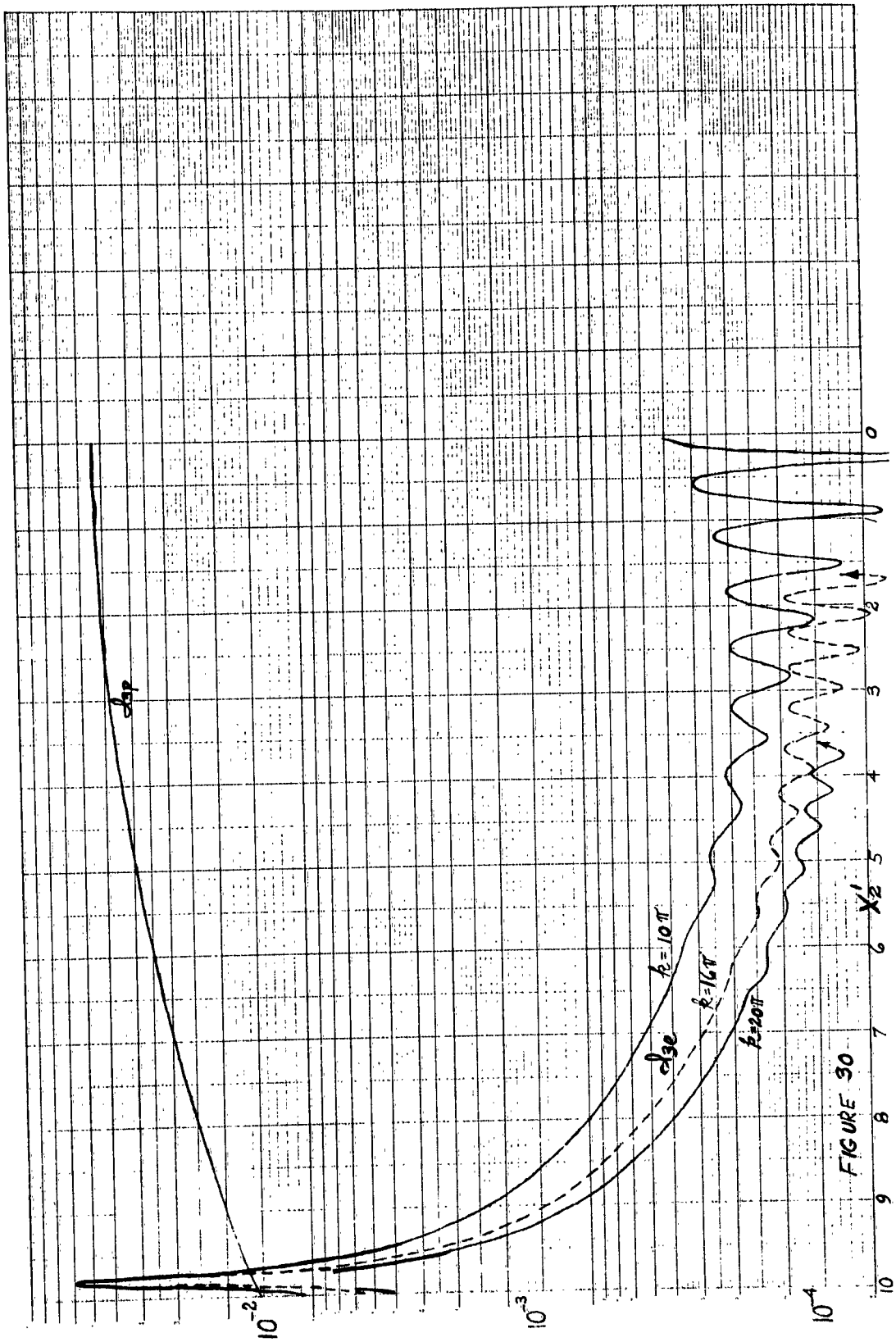

FIGURE 30

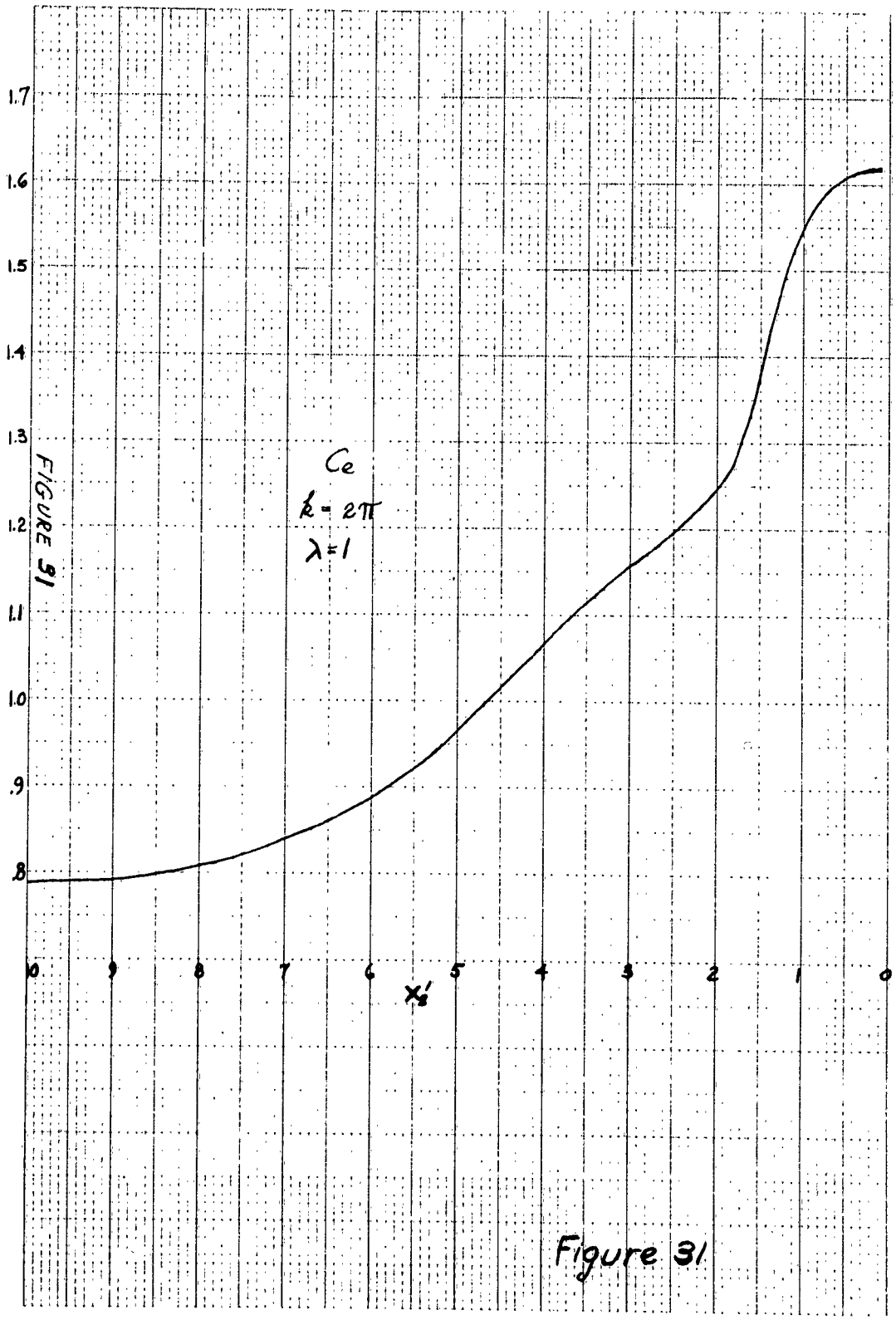

Figure 31

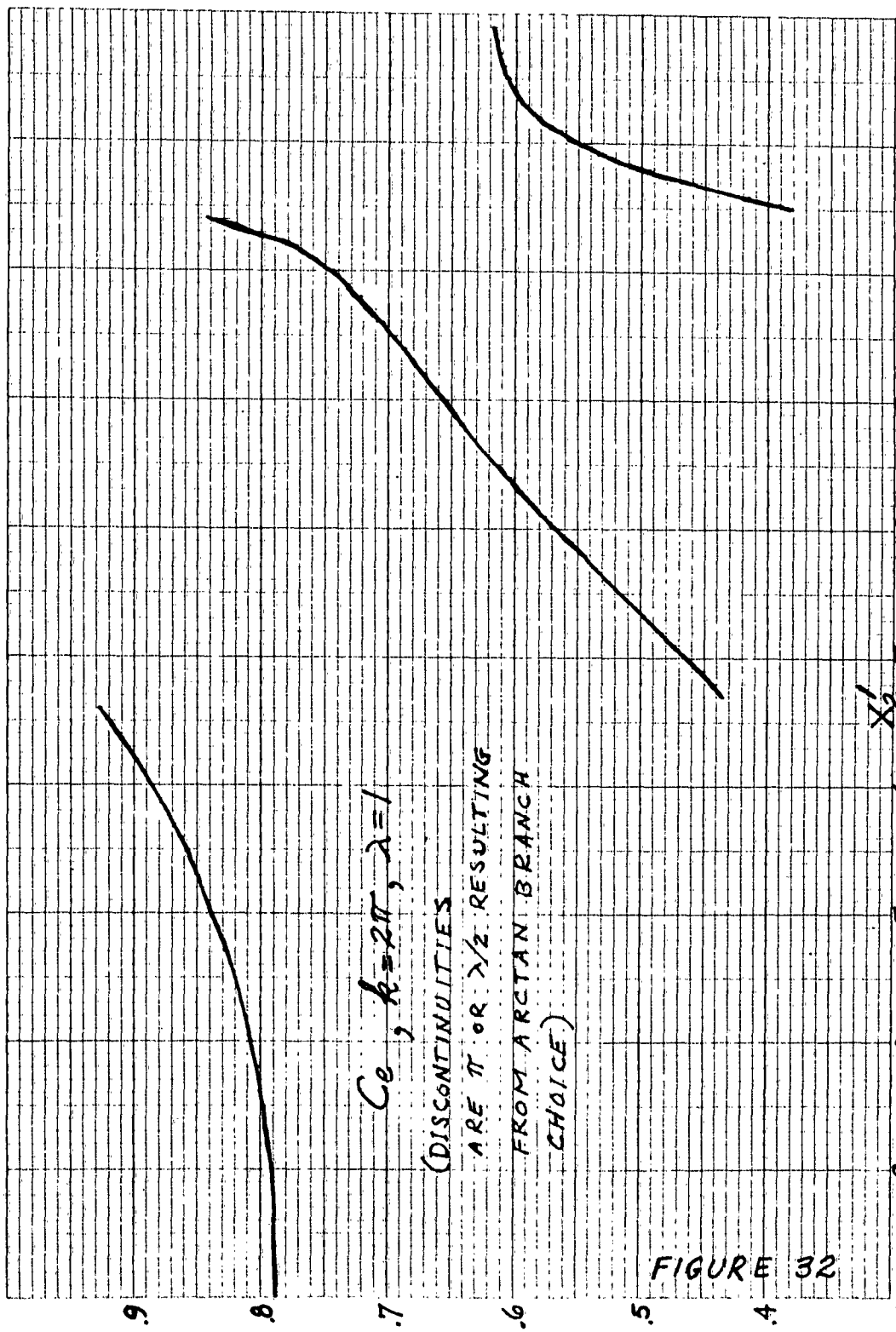
Ce , k=2π, λ=1
(DISCONTINUITIES
ARE π OR λ/2 RESULTING
FROM ARCTAN BRANCH
CHOICE)
X2'
.9
.8
.7
.6
.5
.4
0
1
2
3
4
5
6
7
8
9
10

FIGURE 32

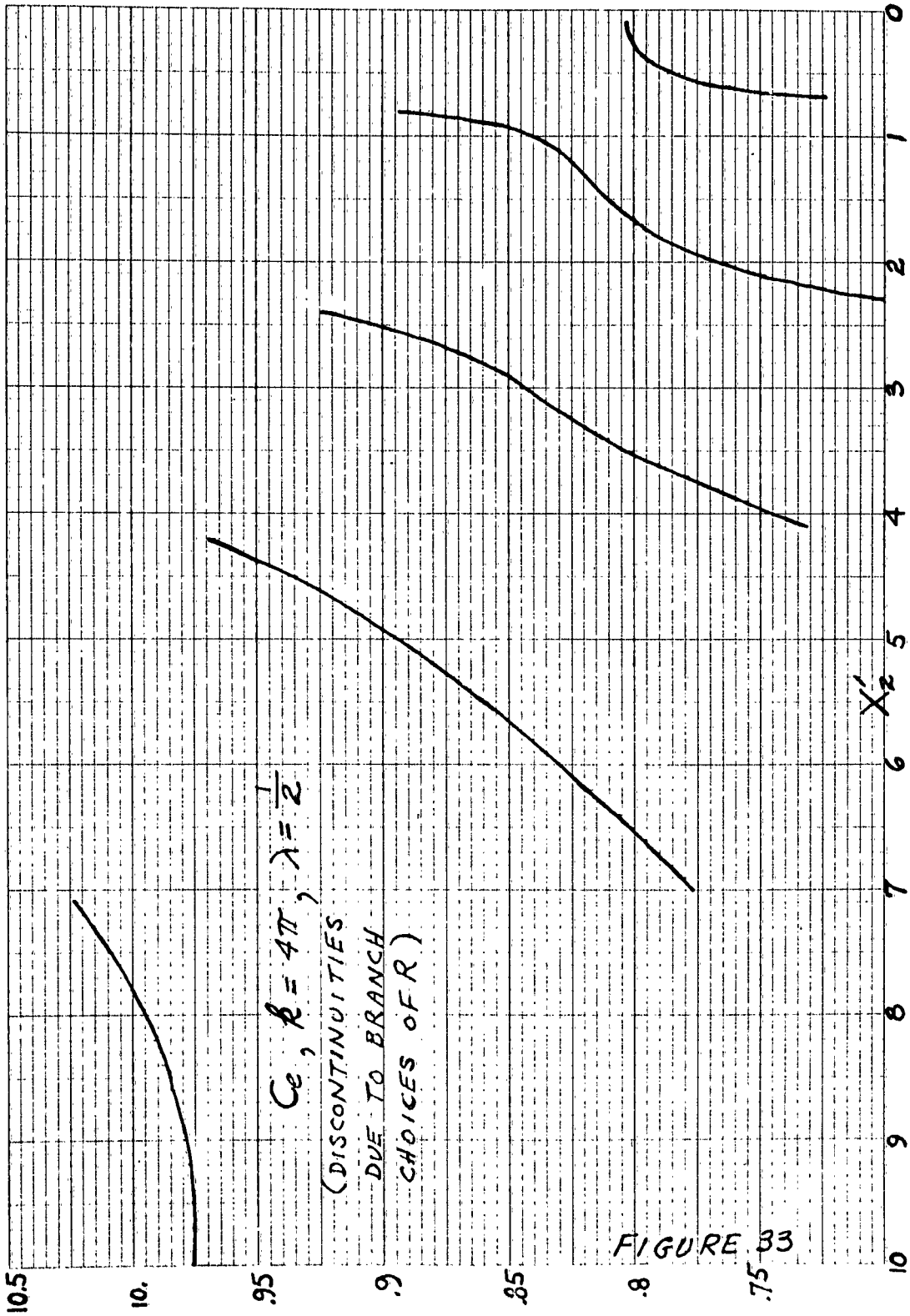
10.5
10.
.95
.9
.85
.8
.75
0
1
2
3
4
5
6
7
8
9
10
X_2'
$C_e, \beta = 4\pi, \lambda = \frac{1}{2}$
(DISCONTINUITIES
DUE TO BRANCH
CHOICES OF R)

FIGURE 33

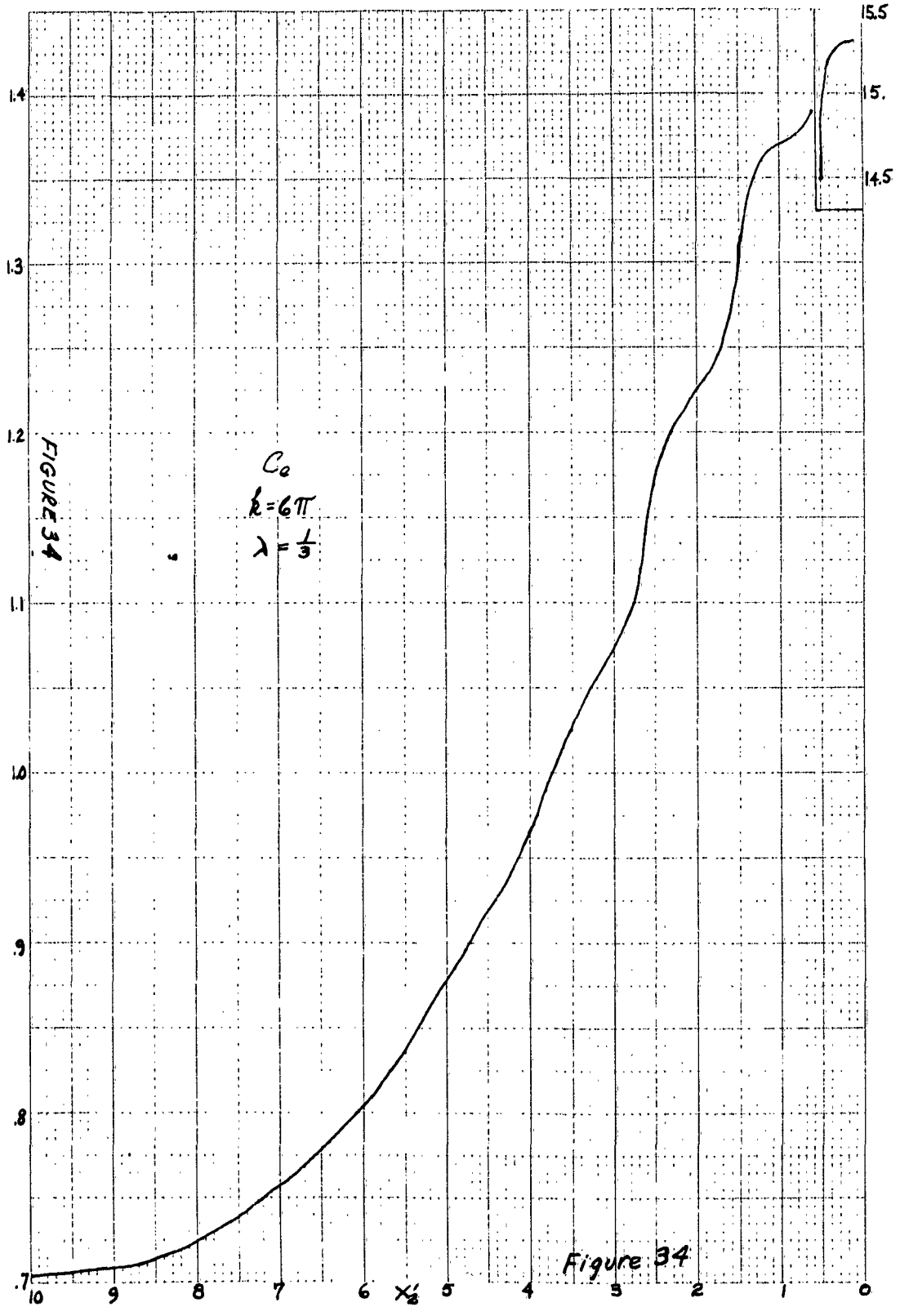
15.5
15.
14.5
1.4
1.3
1.2
1.1
1.0
.9
.8
.7
FIGURE 34
C_e
$k = 6\pi$
$\lambda = \frac{1}{3}$
10
9
8
7
6
X_2'
5
4
3
2
1
0

Figure 34

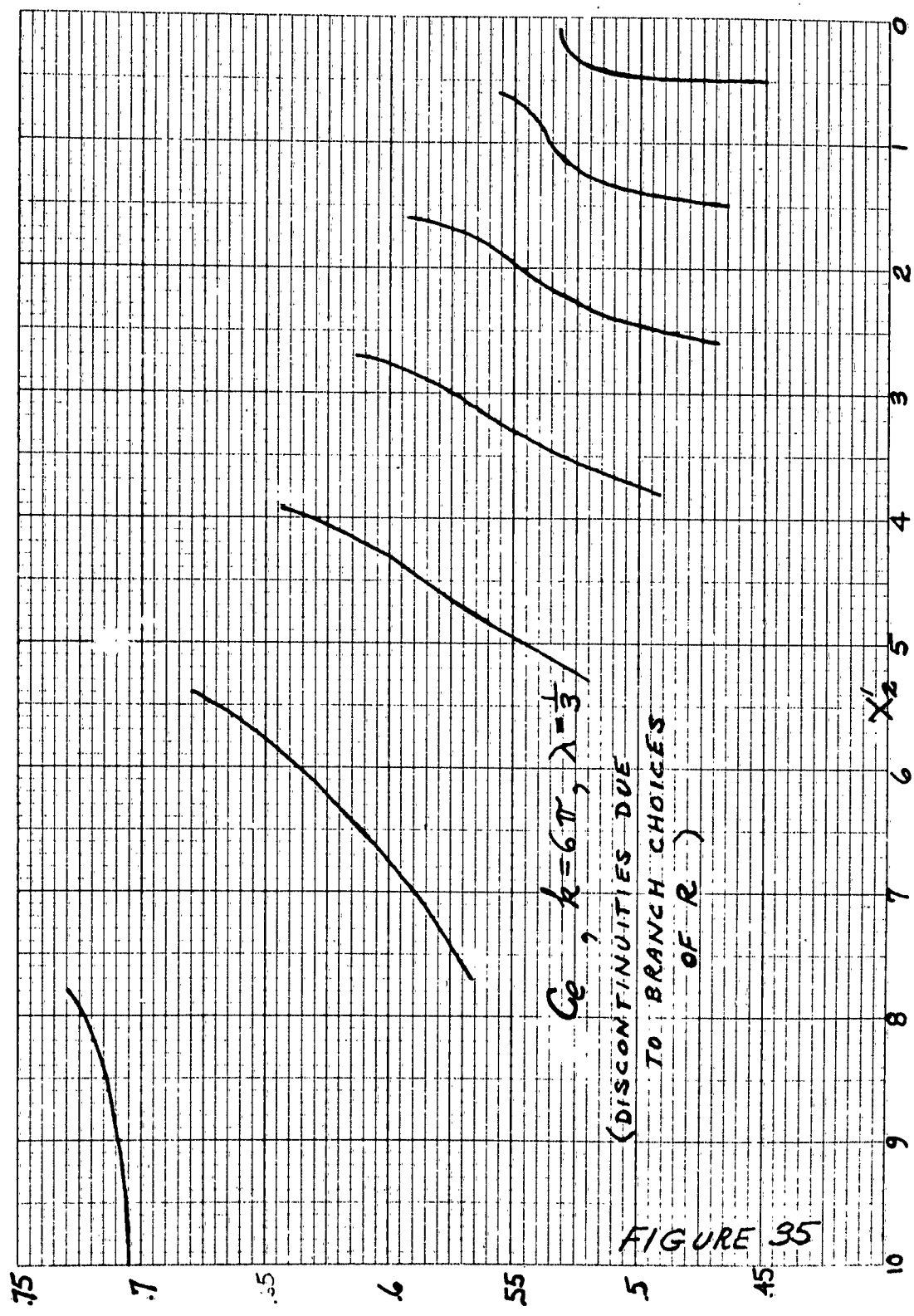
.75
.7
.65
.6
.55
.5
.45
0
1
2
3
4
5
6
7
8
9
10
X_2'
C_e ? $k=6\pi$, $\lambda=\frac{1}{3}$
(DISCONTINUITIES DUE TO BRANCH CHOICES OF R)

FIGURE 35

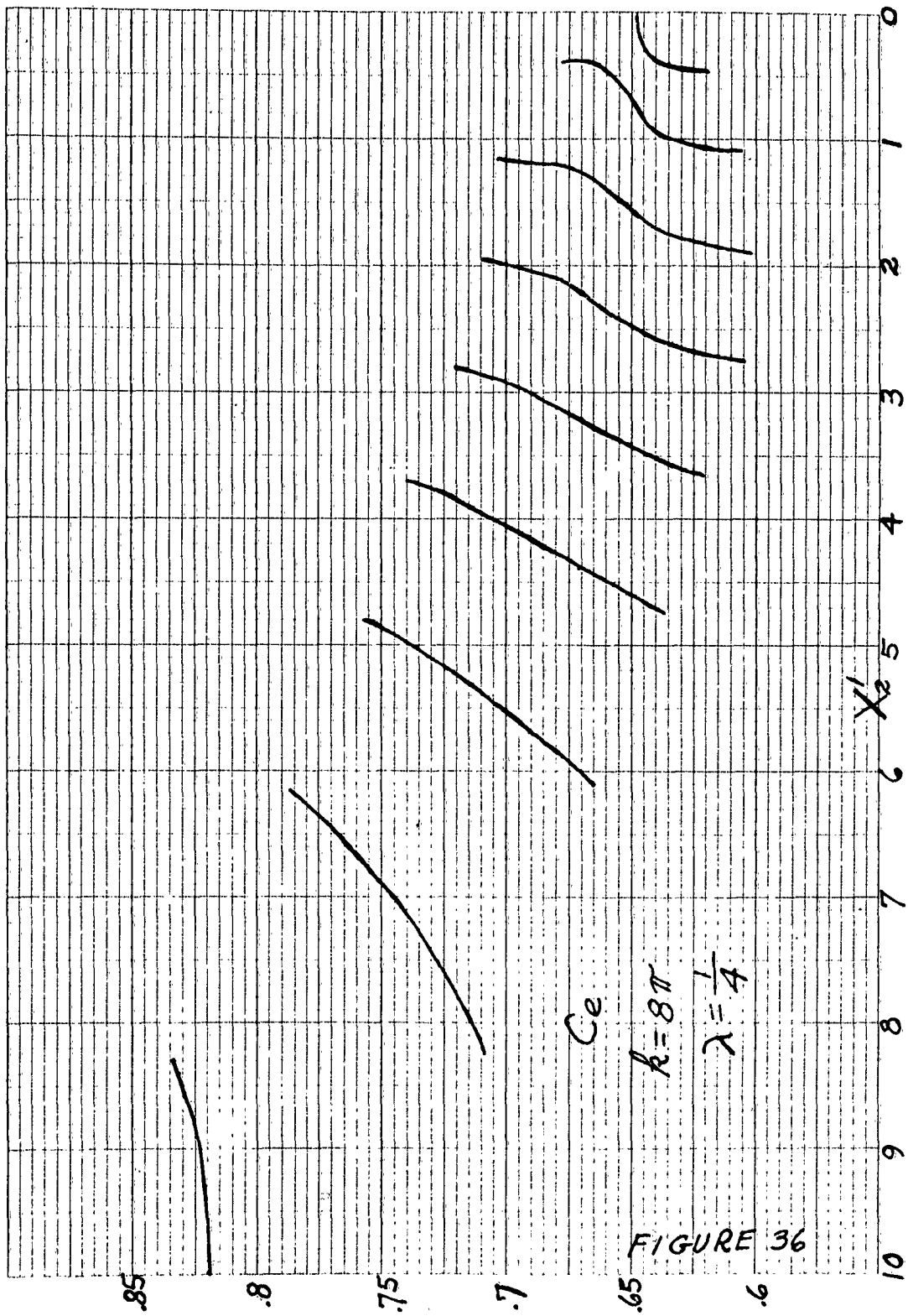

FIGURE 36

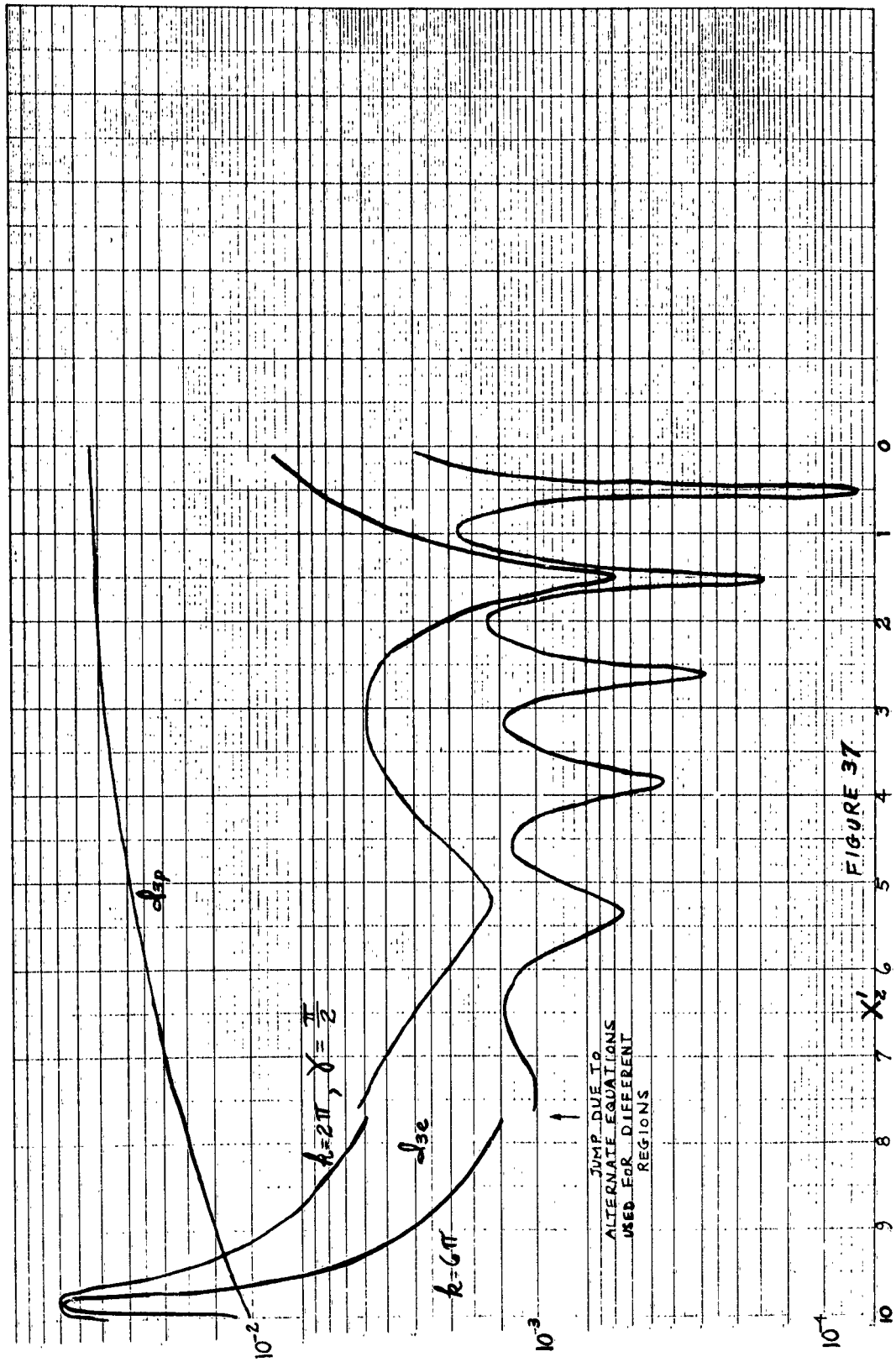
δ_{3p}
$k=2\pi$, $\gamma=\frac{\pi}{2}$
δ_{3e}
$k=6\pi$
10^{-2}
10^{-3}
10^{-4}
JUMP DUE TO ALTERNATE EQUATIONS USED FOR DIFFERENT REGIONS
0 1 2 3 4 5 6 7 8 9 10
X'_2

FIGURE 37

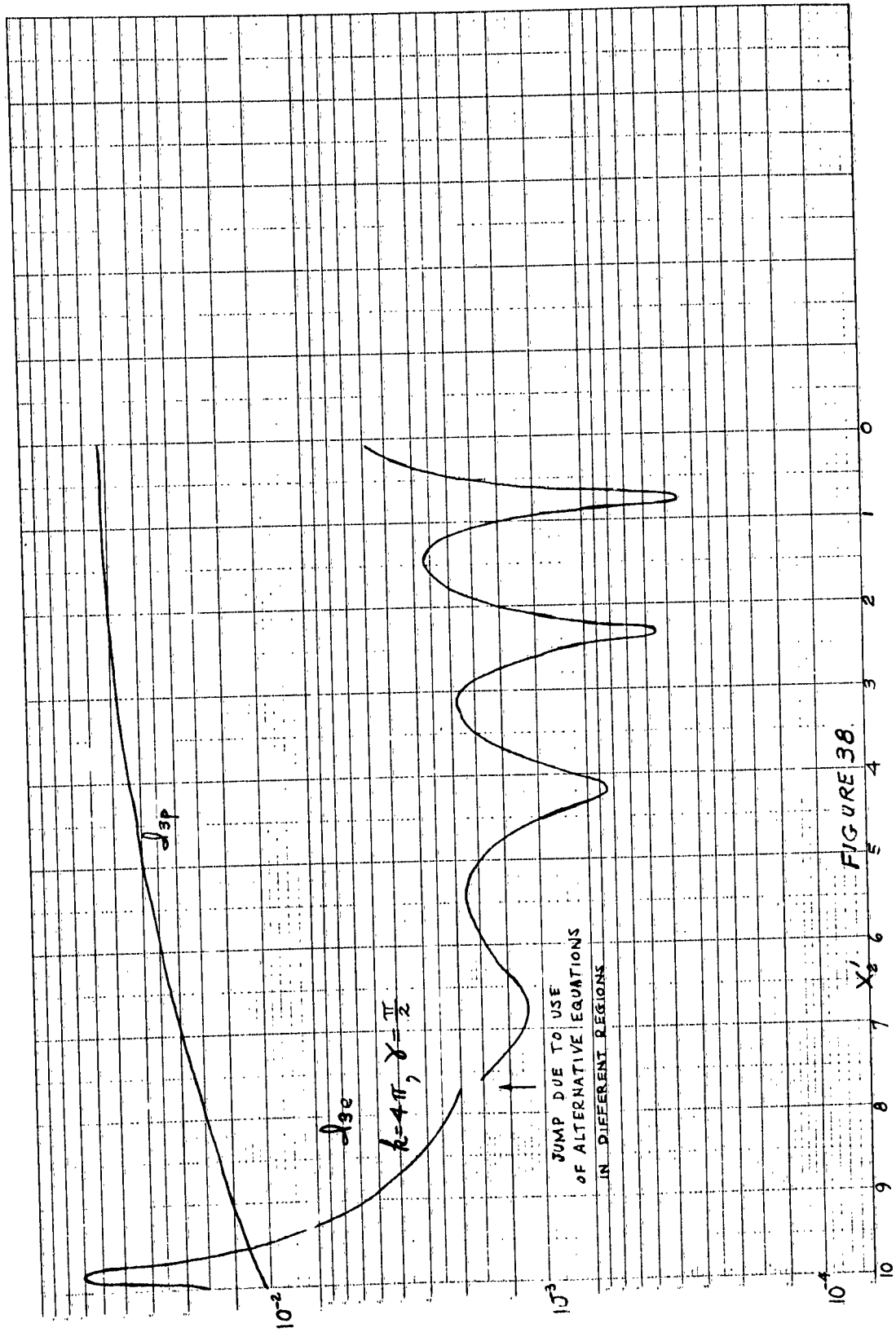
J_{3P}
J_{3e}
$k=4\pi,\ \gamma=\frac{\pi}{2}$
JUMP DUE TO USE
OF ALTERNATIVE EQUATIONS
IN DIFFERENT REGIONS
10^{-2}
10^{-3}
10^{-4}
0
1
2
3
4
5
6
7
8
9
10
X_2'

FIGURE 38.

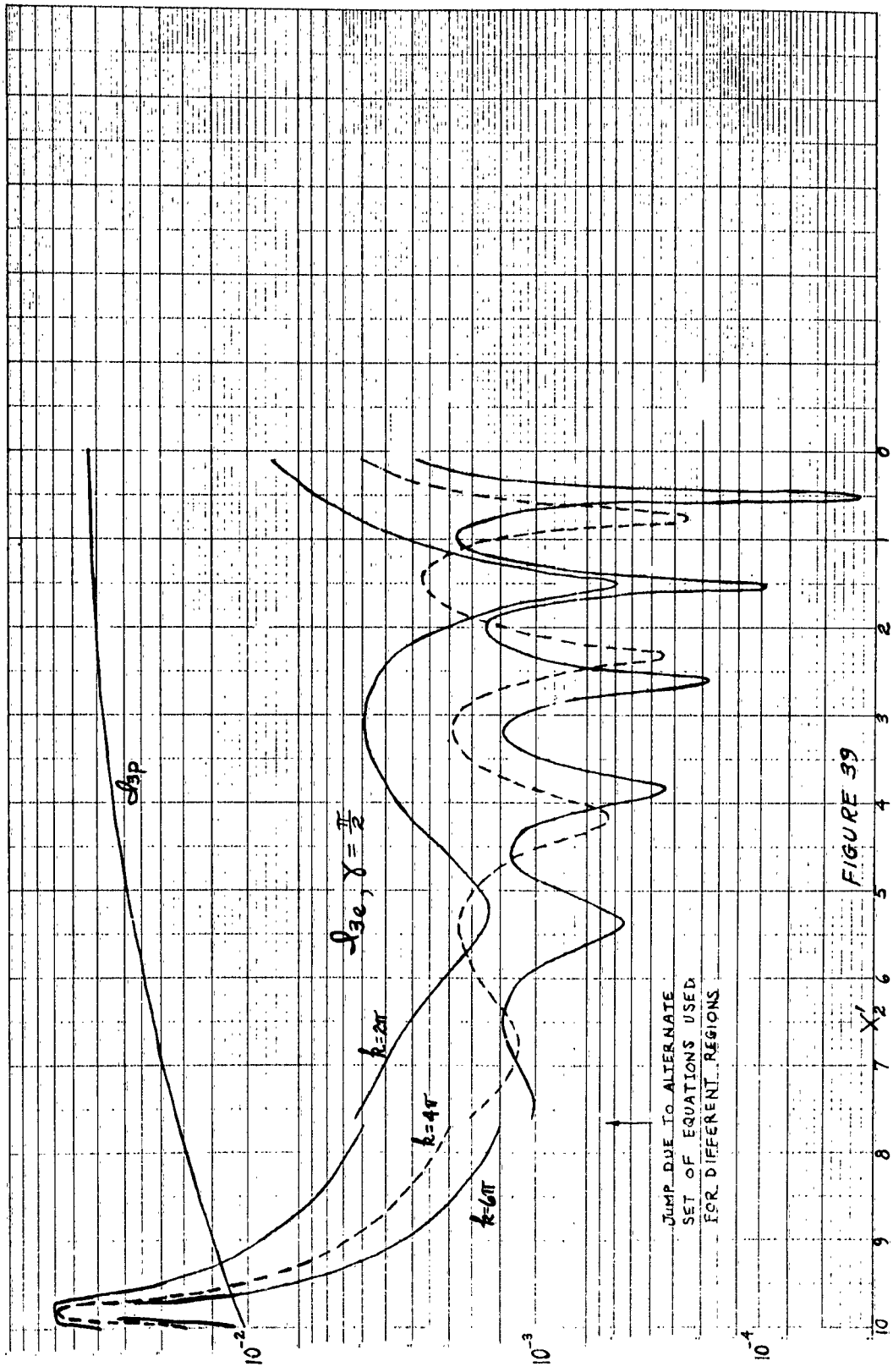
β_{3p}
$\beta_{3e}, \gamma = \frac{\pi}{2}$
k=2π
k=4π
k=6π
10^{-2}
10^{-3}
10^{-4}
0
1
2
3
4
5
6
7
8
9
10
X_2'
JUMP DUE TO ALTERNATE
SET OF EQUATIONS USED
FOR DIFFERENT REGIONS

FIGURE 39

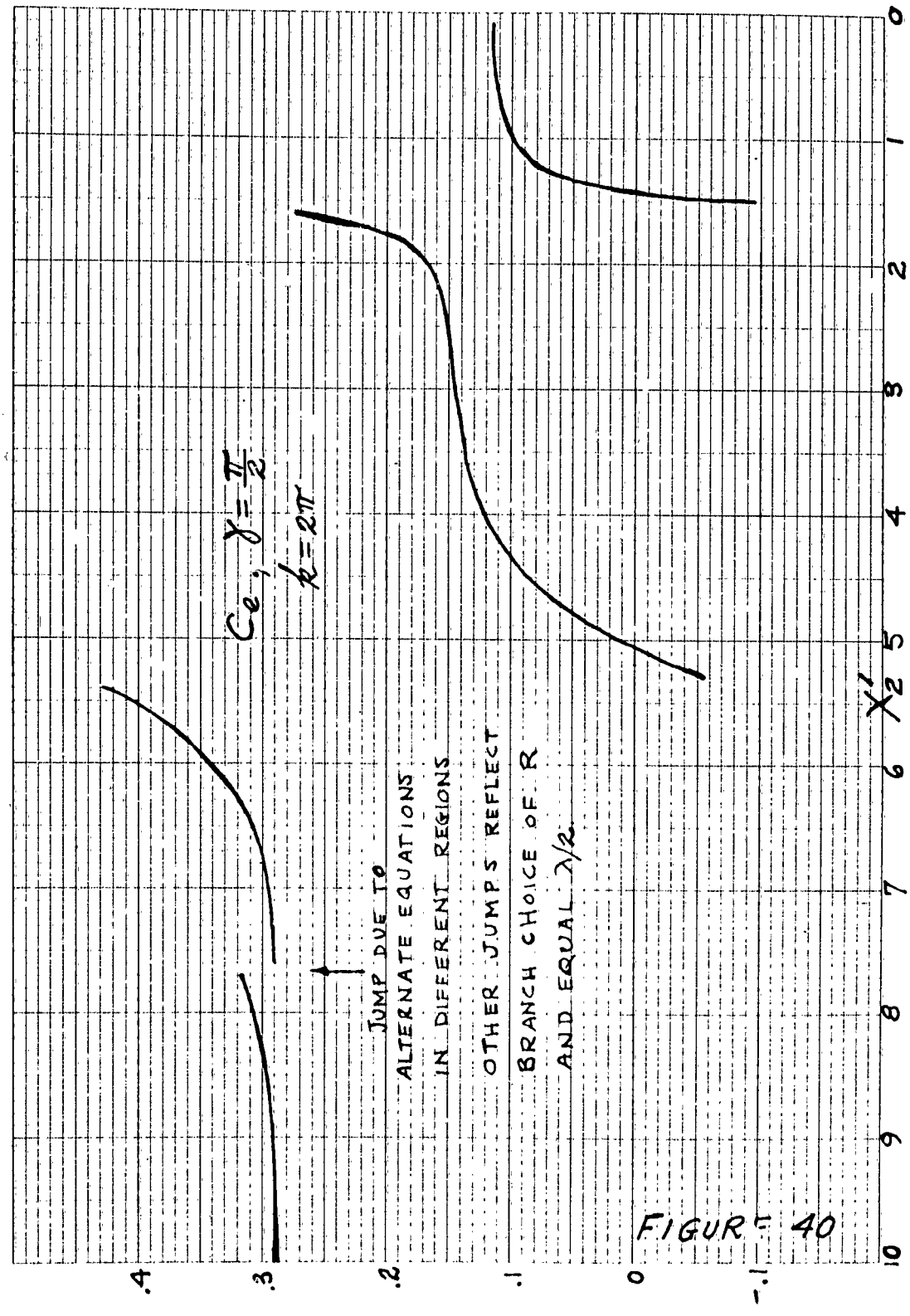
C_e, $\gamma = \frac{\pi}{2}$
$k = 2\pi$
JUMP DUE TO
ALTERNATE EQUATIONS
IN DIFFERENT REGIONS
OTHER JUMPS REFLECT
BRANCH CHOICE OF R
AND EQUAL $\lambda/2$.
.4
.3
.2
.1
0
-.1
0
1
2
3
4
5
6
7
8
9
10
X_2'

FIGURE 40

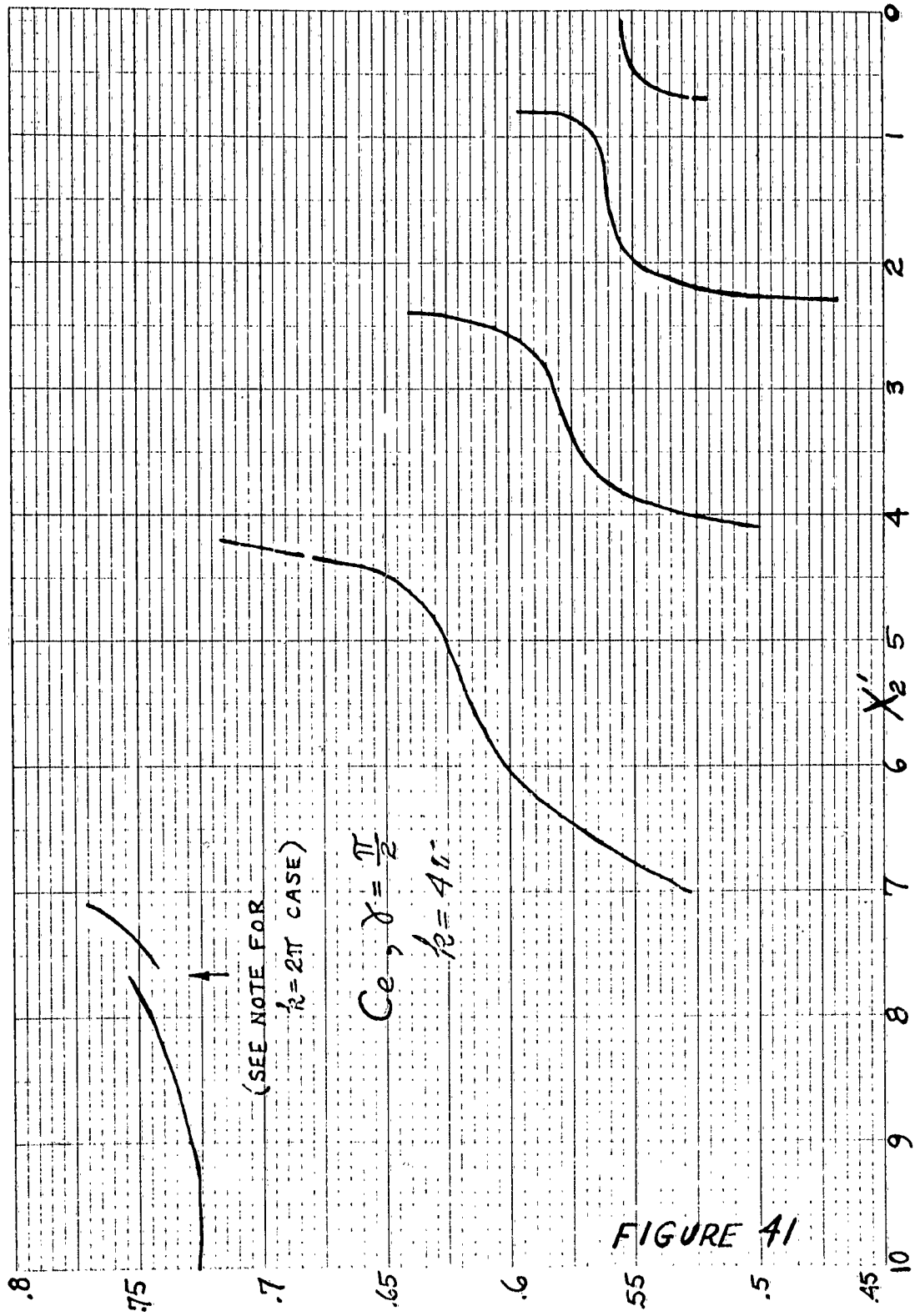
.8
.75
.7
.65
.6
.55
.5
.45
0
1
2
3
4
5
6
7
8
9
10
X_2'
(SEE NOTE FOR $\lambda = 2\pi$ CASE)
C_e, $\gamma = \frac{\pi}{2}$
$\lambda_2 = 4\pi$

FIGURE 41

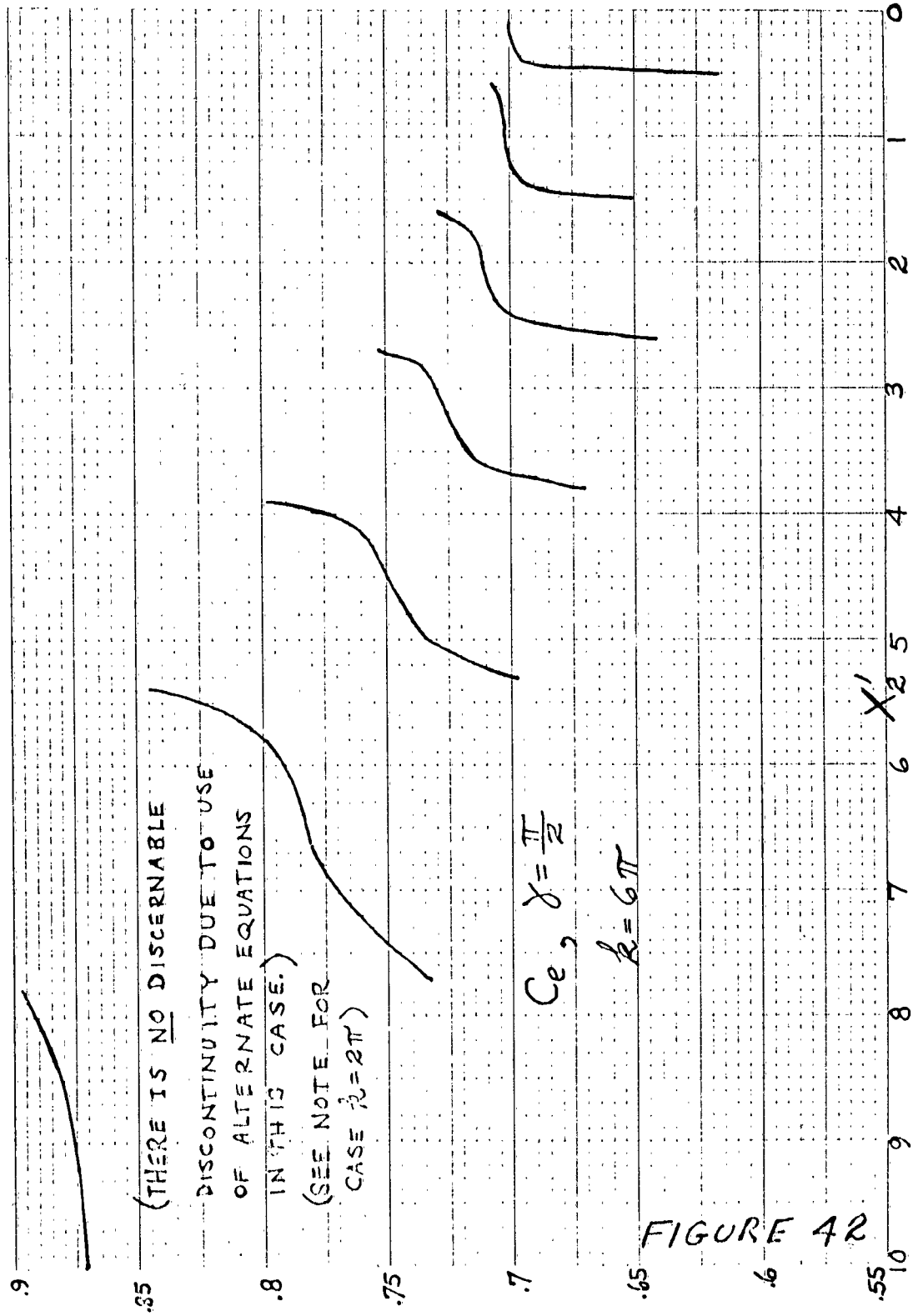
.9
.85
.8
.75
.7
.65
.6
.55
0
1
2
3
4
5
6
7
8
9
10
X'2
(THERE IS NO DISCERNABLE
DISCONTINUITY DUE TO USE
OF ALTERNATE EQUATIONS
IN THIS CASE.)
(SEE NOTE FOR
CASE λ=2π)
Ce, γ=π/2
λ=6π

FIGURE 42

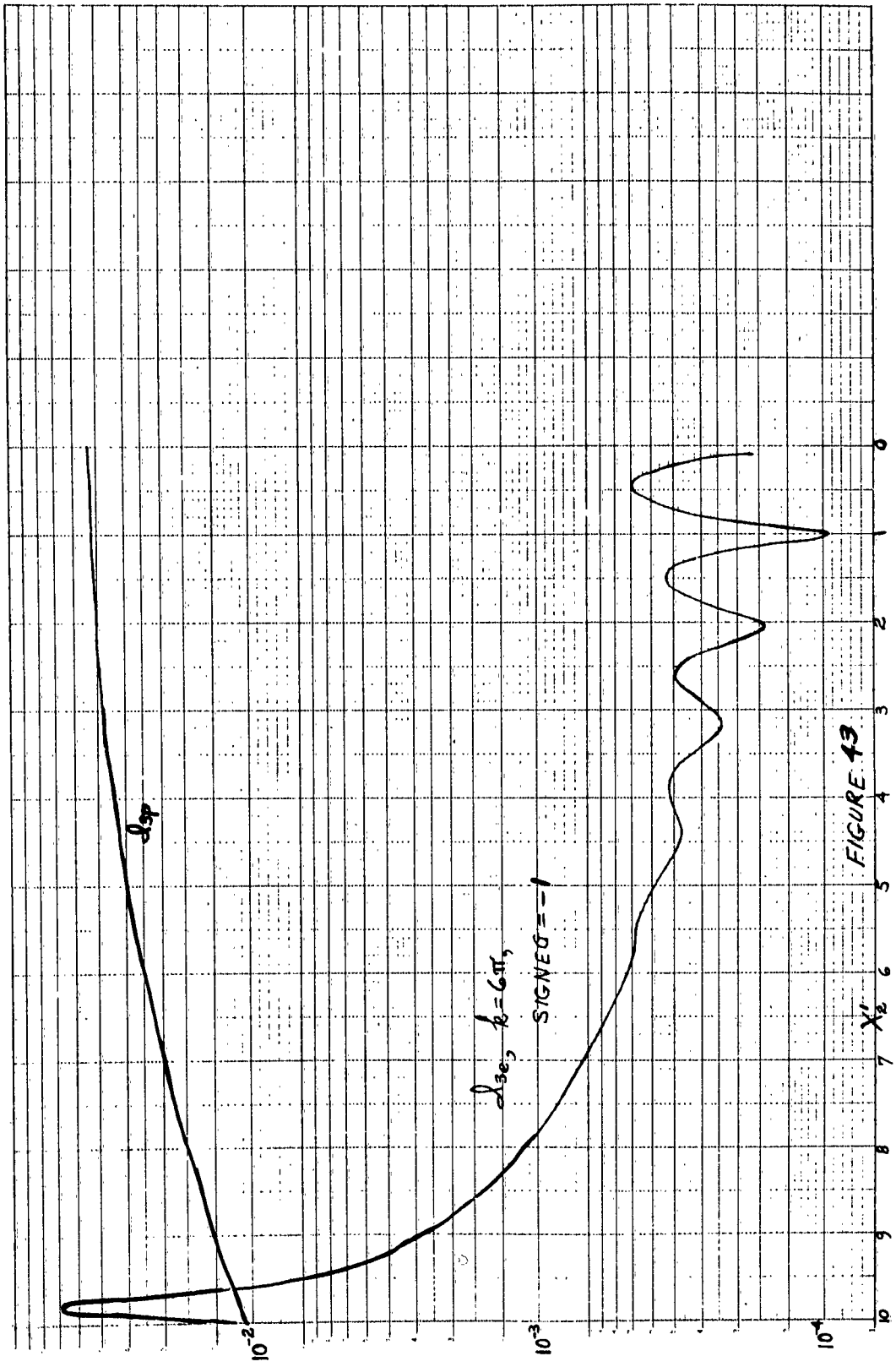

FIGURE 13

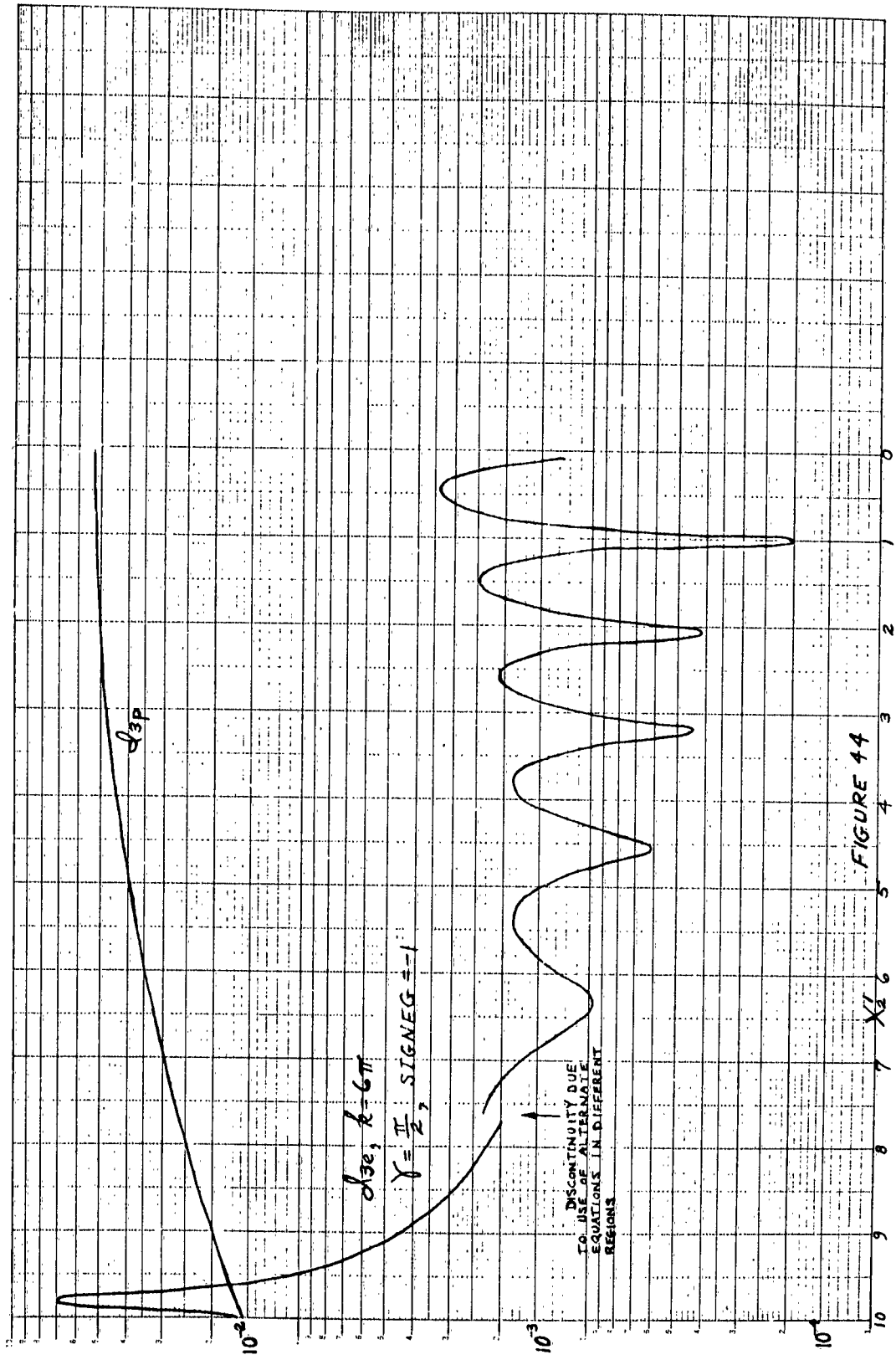
δ_{3P}
δ_{3E}; $k = 6\pi$
$\gamma = \frac{\pi}{2}$, SIGNEG = -1
DISCONTINUITY DUE TO USE OF ALTERNATE EQUATIONS IN DIFFERENT REGIONS
10^{-2}
10^{-3}
10^{-4}
X'_2
0
1
2
3
4
5
6
7
8
9
10

FIGURE 44

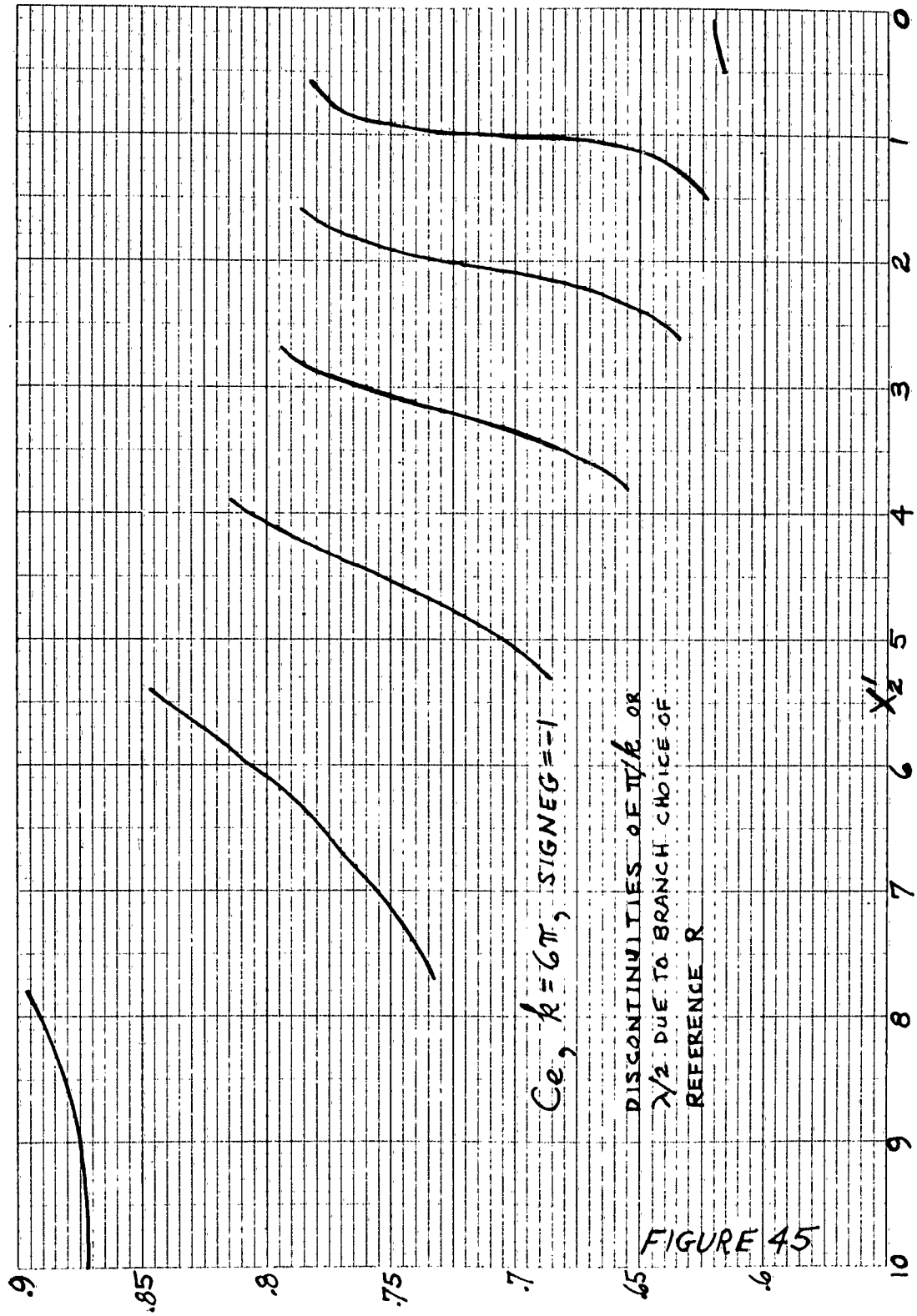
.9
.85
.8
.75
.7
.65
.6
0
1
2
3
4
5
6
7
8
9
10
X2
Ce, k = 6π, SIGNEG = -1
DISCONTINUITIES OF π/k OR
λ/2 DUE TO BRANCH CHOICE OF
REFERENCE R

FIGURE 45

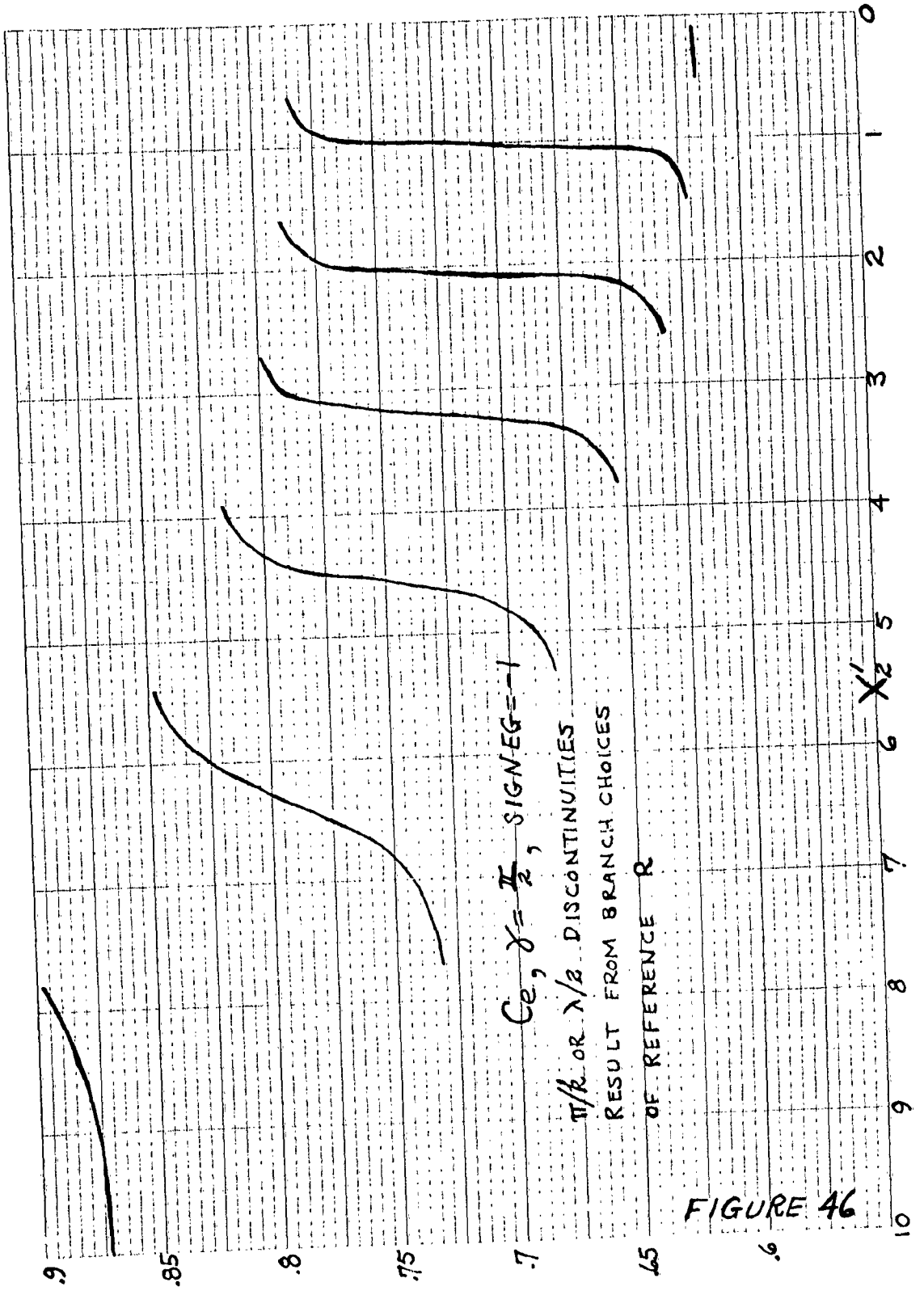
.9
.85
.8
.75
.7
.65
.6
0
1
2
3
4
5
6
7
8
9
10
X_2'
C_2, $\gamma = \frac{\pi}{2}$, SIGN-EG=-1
π/k OR $\lambda/2$ DISCONTINUITIES
RESULT FROM BRANCH CHOICES
OF REFERENCE R

FIGURE 46

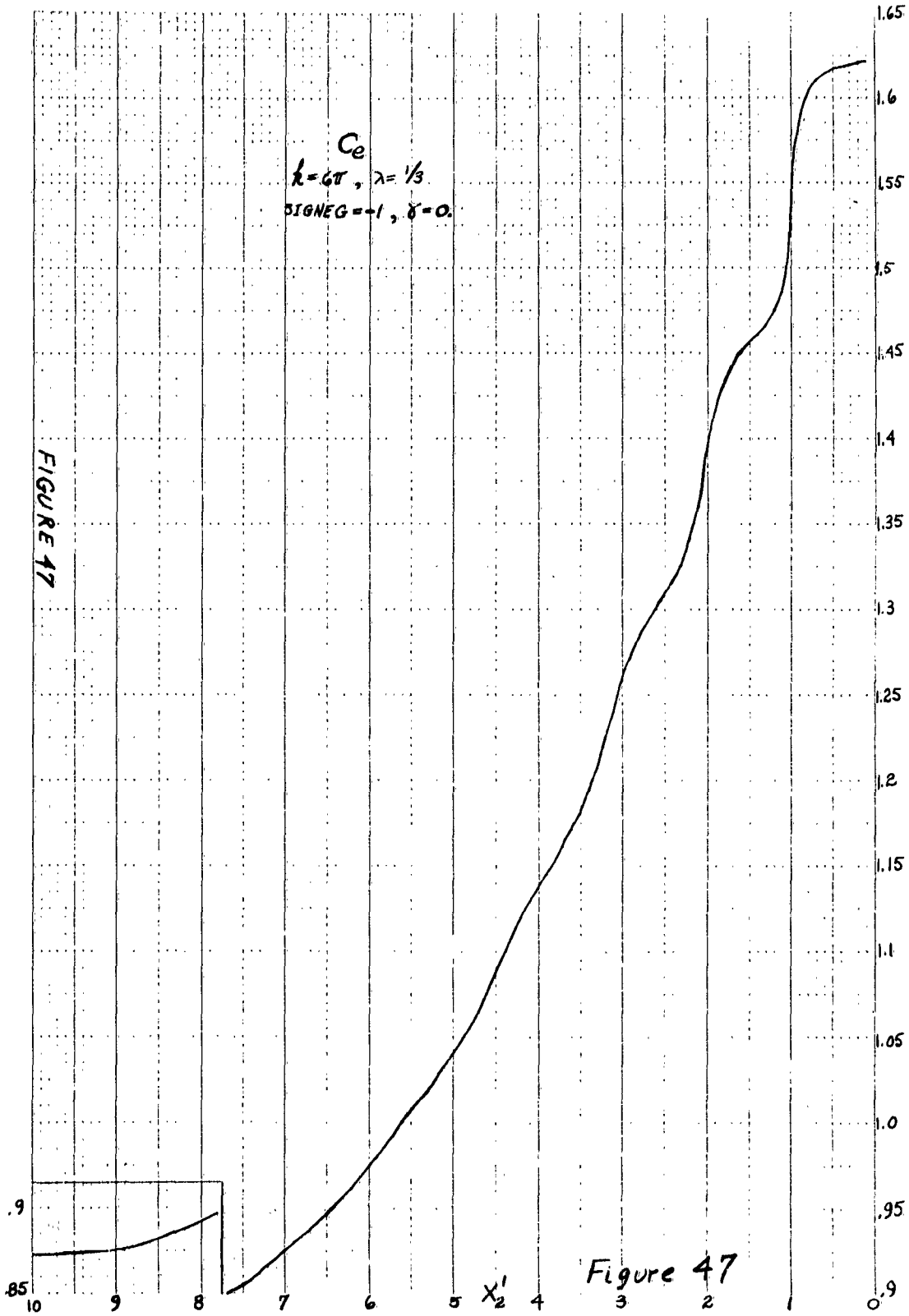
Ce
k=6π, λ=1/3
SIGNEG=-1, δ=0.
FIGURE 47
1.65
1.6
1.55
1.5
1.45
1.4
1.35
1.3
1.25
1.2
1.15
1.1
1.05
1.0
.95
.9
.9
.85
10
9
8
7
6
5
X'2
4
3
2
1
0

Figure 47

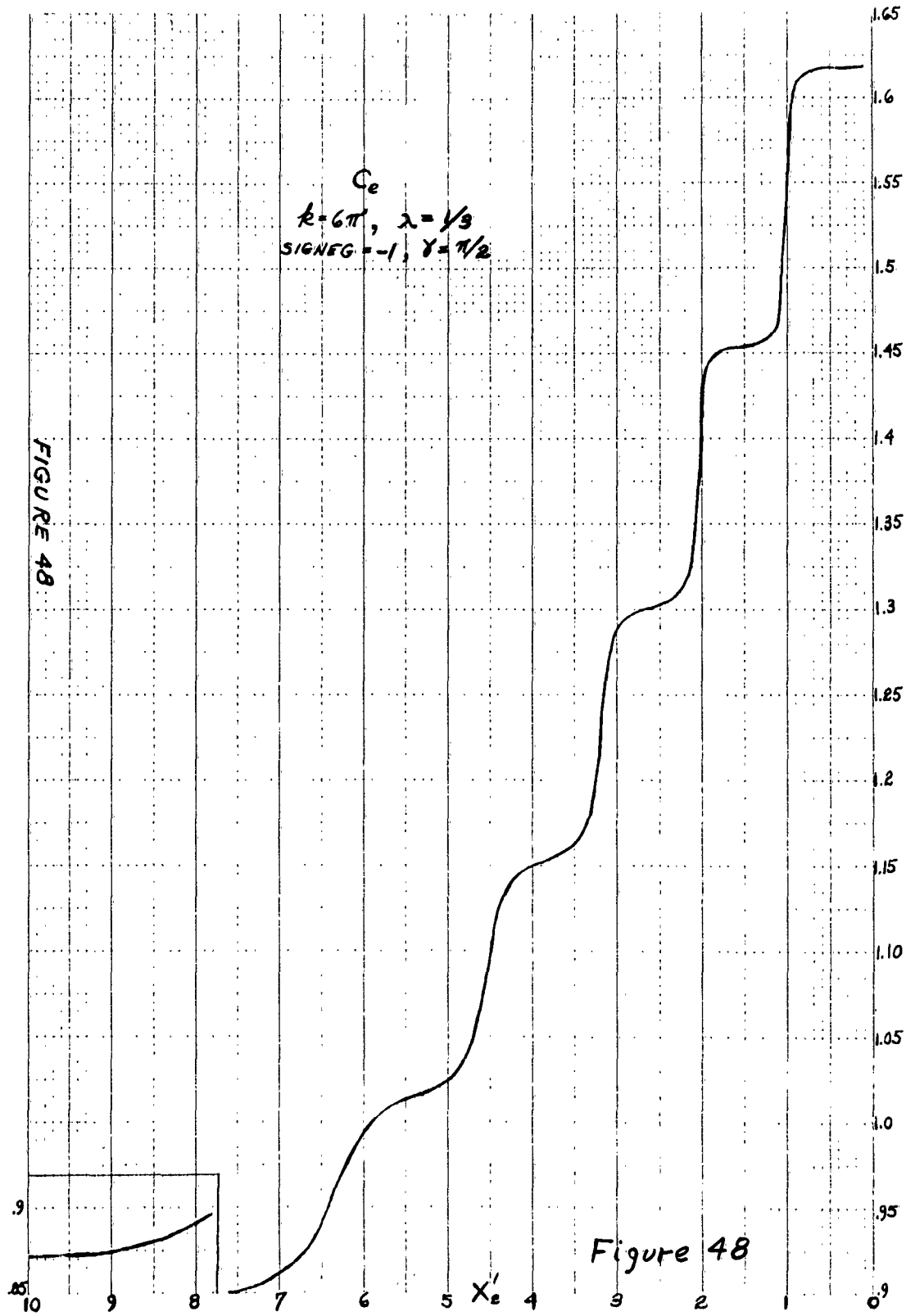
C_e
$k = 6\pi$, $\lambda = 1/3$
SIGNEG = -1, $\gamma = \pi/2$
FIGURE 48
1.65
1.6
1.55
1.5
1.45
1.4
1.35
1.3
1.25
1.2
1.15
1.10
1.05
1.0
.95
.9
.85
10
9
8
7
6
5
X'_e
4
3
2
1
0

Figure 48

CHAPTER 4

ON THE POSSIBILITY OF EXTENDING THE SYNTHESIS METHOD TO INCLUDE THE EDGE DIFFRACTED FIELD

I. Introduction

The discussion and computations presented in Chapter 3 illustrated the importance of the effect of the edge diffracted field upon the aperture distribution. The synthesis method developed in Chapter 1 showed how a specified aperture amplitude and phase distribution may be obtained by shaping the reflectors' cross-sections when the diffracted field is not included. It would be ideal if we could extend the synthesis method of Chapter 1 so as to include the edge diffracted field's contribution to the aperture distribution. In this chapter we will discuss an attempt at finding such a solution which proved unsuccessful. The method for obtaining a solution which was attempted appears to be a powerful approach to the problem despite the lack of success found in using it. The inadequacy of this approach was by no means proven so it seems worthwhile to present the technique for the record.

The use of the edge source on the sub-reflector for obtaining the diffracted field is an excellent choice for several reasons. Besides providing an accurate result for the diffracted field of small sub-reflectors as was discussed in Chapter 3, the edge diffracted field is independent of the reflector cross-section and depends only upon the boundary conditions such as were stated in the synthesis method of Chapter 1. These conditions are the position of the edge and the slope of the edge which are determined by X_{1m}, X_{2m}, $\alpha(\theta_{1m})$, and $\beta(\theta_{1m})$.

Hence the diffracted field is a fixed field distribution which illuminates only the main reflector. Since it does not depend upon $Y_1(X_1)$ as a Kirchhoff integration would, it lends itself to an extension of the synthesis method of Chapter 1.

It is not at all clear, however, whether a solution exists to this problem. Unfortunately, this problem will remain unresolved in this work, although it is the feeling of the author that the results found in this chapter imply, by no means prove, that a solution does not exist under any conditions except that $J_e = 0$.

It is well known[1] that an arbitrary phase and amplitude cannot be specified in the aperture of a single reflector system for an arbitrary source illumination. Referring to Figure 1, we see that I_{3p} and C_p must be controlled by shaping both $Y_1(X_1)$ and $Y_2(X_2)$ in order that upon complex addition to I_{3e} and C_e, a specified amplitude and phase, I_{3a} and C, will result in the aperture. From an iterative point of view, whenever I_{3p} and C_p are altered to compensate for I_{3e} and C_e, the change in $Y_1(X_1)$ and $Y_2(X_2)$ also alters I_{3e} and C_e. It is not clear then whether an iteration would converge. The results of Chapter 5 indicate that such an iteration would not converge, although by no means conclusively. If a solution does not exist of course such an iteration would not converge. The inverse is not necessarily true, however, since the problem, mathematically, is not a linear one. If J_e were very large, it is clear that a solution would not exist. The dominance of I_{3e} over I_{3p} would preclude the possibility of correction

of I_{3e} by adjustment of I_{3p}. On the other hand, even when I_{3e} is very much less than I_{3p}, it is not clear whether or not a solution exists.

The above method of reasoning was inconclusive so that a more formal or mathematical approach to the problem is necessary. Before actually attempting the solution mathematically, let us see from Figure 2 how the various laws and principles relevant to the problem fit together. A normal congruence for the rays and wavefronts is defined for the primary and edge sources when C_{po} and C_{eo} are specified. We know that this normal congruence is maintained upon successive reflections if the appropriate optical principles are applied. Application of Snell's law at reflector #1 insures a normal congruence for the I_2 waves incident upon reflector #2. Now the theorum of Malus applied for C_p and C_e in the aperture insures a normal congruence for the waves and rays reflected from the main reflector. Hence it would appear that Snell's law applied at the main reflector would be redundant. However, the two energy conservation equations taken together with those principles already stated do not define a unique solution to the problem for $Y_1(X_1)$ and $Y_2(X_2)$. Since C_p and C_e are not known (and neither are $C_p' = dC_p/dX_2'$ nor $C_e' = dC_e/dX_2'$), then it may be true that inclusion of Snell's law at the main reflector is not redundant. Inclusion of both these principles as independent conditions would mean that the problem is overstated; that is, there is no solution. On the other hand, since C and I_{3a} are given functions, it may be that one of the two Snell's law applications is necessary, whereas the other is redundant. This reasoning is certainly inconclusive, but unfortunately,

that is the state of this attempt to an exact solution to this problem. A reasonably satisfactory approximate solution to this problem is obtained in Chapter 5. The remainder of this chapter is devoted to explicitely formulating the above ideas mathematically.

II. Equations for the Attempted Exact Solution

The mathemtaical formulation of the problem described in Section I above will be performed briefly in this section. We will attempt to arrive at a set of six simultaneous first order differential equations with the dependences indicated below:

$$\gamma_2' = f_{\gamma 2}(\gamma_2, C_p, C_e; X_2') \quad (1)$$

$$\theta_1' = f_{\theta_1}(\theta_1, C_p, C_e; X_2') \quad (2)$$

} From Energy Conservation

$$C_p' = f_{Cp}(C_p, \theta_1, Y_1, Y_2; X_2') \quad (3)$$

$$C_e' = f_{Ce}(C_e, \gamma_2; X_2') \quad (4)$$

} From Theorum of Malus

$$Y_1' = f_{Y_1}(\theta_1, C_e, C_p, Y_1, Y_2; X_2') \quad (5)$$

$$Y_2' = f_{Y_2}(\theta_1, C_e, C_p, Y_1, Y_2; X_2') \quad (6)$$

} From Snell's Law

These equations, as shown, form a complete interdependent set. The primed variables denote total differentiation with respect to X_2' except in the case of X_2'. The total derivative of X_2 with respect to X_2' will always be denoted as dX_2/dX_2'. Rather arbitrarily, all the variables may be considered dependent variables with X_2' the independent variable. The remaining variables of significance in the problem can

be found from those in (1) through (6) with the following dependence:

$$X_3 = X_3(C_e, \gamma_2; X_2') \tag{7}$$

$$Y_3 = Y_3(C_e, \gamma_2; X_2') \tag{8}$$

$$X_2 = X_2(C_p, \theta_1, Y_1, Y_2; X_2') \tag{9}$$

$$X_1 = X_1(\theta_1, Y_1) \tag{10}$$

As we derive the explicite forms of the above equations, we will point out the deficiencies in the formulation.

The energy conservation equations leading to (1) and (2) are

$$\gamma_2' = \left[I_{3e} \Big/ J_e(\gamma_2) \right] \left(X_2' \Big/ \sin \gamma_2 \right) \tag{11}$$

and

$$\theta_1' = \left[I_{3p} \Big/ I_1(\theta_1) \right] \left(X_2' \Big/ \sin \theta_1 \right) \tag{12}$$

The quantities I_{3e} and I_{3p} can be expressed in forms of the specified aperture distribution amplitude, I_{3a}, and phase, C, as will be done shortly.

From expression of the theorum of Malus at the aperture we obtain

$$C_p' = \sin \theta_3 = (X_2' - X_2) \Big/ \sqrt{(X_2' - X_2)^2 + Y_2^2} \tag{13}$$

and

$$C'_e = \sin \gamma_3 = (X'_2 - X_3) \Big/ \sqrt{(X'_2 - X_3)^2 + Y_3^2} \qquad (14)$$

which will lead to equations (3) and (4).

Snell's law for each reflector and each ray system is expressed as

$$Y'_1 = \tan \frac{1}{2}\left[\theta_1 - \theta_2\right] X'_1 = \tan \frac{1}{2}\left[\theta_1 - \arctan\left(\frac{X_2 - X_1}{Y_2 - Y_1}\right)\right] X'_1, \qquad (15)$$

$$Y'_2 = -\tan \frac{1}{2}\left[\theta_2 - \theta_3\right]\frac{dX_2}{dX'_2} = -\tan \frac{1}{2}\left[\arctan\left(\frac{X_2 - X_1}{Y_2 - Y_1}\right) - \arctan\left(\frac{X'_2 - X_2}{Y_2}\right)\right]\frac{dX_2}{dX'_2}, \qquad (16)$$

and

$$Y'_3 = -\tan \frac{1}{2}\left[\gamma_2 - \gamma_3\right] X'_3 = -\tan \frac{1}{2}\left[\arctan\left(\frac{X_3}{Y_3 + d_e}\right) - \arctan\left(\frac{X'_2 - X_3}{Y_3}\right)\right] X'_3 . \qquad (17)$$

Equations (15) and (16) lead to equations (5) and (6). It is here that the difficulties or unresolved portions of the problem exist. First of all, as will be seen shortly, it turns out that equation (17) is not necessary to arrive at the formulation expressed by equations (1) through (10). This may be explained by stating that equation (4) or (14) for the Theorum of Malus makes (17) redundant. In this case, however, we would expect that (16) would also be redundant with (3)

or (13). However, it is not clear that (1) through (6) are not a complete set of differential equations with a unique solution unless (6) or (16) is included. Excluding (6) leads to the conclusion that $Y_2(X_2')$ is arbitrary. It is conceivable that this is the case, and that the Cauchy-Lipschitz conditions (see Appendix I) are not satisfied except for certain $Y_2(X_2')$ and in some cases for no function $Y_2(X_2')$. This last conclusion is the only one which appears consistent with all the results obtained. It is however very unsatisfactory from an engineering point of view since appropriate choices of $Y_2(X_2')$ are too difficult to find and their existence is not certain in any specific case. The general complexity of the equations precluded the possibility of applying the Cauchy-Lipschitz conditions in any useful way. In addition, as the results in Chapter 3 have shown, we frequently find $I_{3e} \gtrsim I_{3p}$ for some X_2' and may expect that very often a solution will not exist in practical cases. The formulation is however uncertain and the possibility remains that a solution does not exist even when $I_{3e} \ll I_{3p}$.

Continuing the formulation, we find for the unknown path lengths or phases at the aperture for each source, the primary and edge sources, that

$$C_p = (\beta - Y_1)/\cos\theta_1 + \sqrt{(X_2 - X_1)^2 + (\nu + Y_2 - Y_1)^2} + \sqrt{(X_2' - X_2)^2 + Y_2^2} + C_{po}(\epsilon_1) \tag{18}$$

where

$$X_1 = (\beta - Y_1)\tan\theta_1, \tag{19}$$

and

$$C_e = (Y_3 + d_e(\gamma_2))/\cos\gamma_2 + \sqrt{(X_2' - X_3)^2 + Y_3^2} + C_{eo}(\gamma_2) \tag{20}$$

where

$$X_3 = (Y_3 + d_e(\gamma_2))\tan\gamma_2. \tag{21}$$

The inclusion of C_{po} and C_{eo} in these expressions defines the primary and edge source rays and wavefronts to be a normally congruent system.

If we let $\mathcal{J}^2(X_2') = I_{3a}$, $\mathcal{J}_{3p}^2 = I_{3p}$, and $\mathcal{J}_{3e}^2 = I_{3e}$, then we can add the two fields in the aperture by complex addition,

$$\mathcal{J}\exp(kc) = \mathcal{J}_{3p}\exp(kC_p) + \mathcal{J}_{3e}\exp(kC_e), \text{ and find that}$$

$$I_{3p} = I_{3a}(X_2') \frac{\sin^2 k(C(X_2') - C_e)}{\sin^2 k(C_p - C_e)} \tag{22}$$

and

$$I_{3e} = I_{3a}(X_2') \frac{\sin^2 k(C(X_2') - C_p)}{\sin^2 k(C_p - C_e)} \tag{23}$$

We will now outline the substitutions that are necessary to arrive at equations (1) through (10) from (11) through (23) and in addition point out some of the difficulties. In the following we read "(11) + (23) ⟹ "as" equations (11) and (23) imply." The plus sign does not necessarily indicate summation. The reductions follow:

$$\left[(11) + (23) \Longrightarrow (1)\right] \tag{24}$$

$$\left[(12) + (22) \Longrightarrow (2)\right] \tag{25}$$

$$\left[(18) + (19) \Longrightarrow (9)\right] \tag{26}$$

$$\left[(20) + (21) \Longrightarrow (7)\right] \tag{27}$$

$$\left[(20) + (21) \Longrightarrow (8)\right] \tag{28}$$

$$\left[(26) + (13) \Longrightarrow (3)\right] \tag{29}$$

$$\left[(27) + (28) + (14) \Longrightarrow (4)\right] \tag{30}$$

$$\left[(25) + (19) \Longrightarrow X_1' = \frac{\partial X_1}{\partial \theta_1} f_{\theta 1} + \frac{\partial X_1}{\partial Y_1} Y_1'\right] \tag{31}$$

$$\left[(15) + (19) + (26) + (31) \Longrightarrow (5)\right] \tag{32}$$

$$\left[(26) + (29) + (25) + (32) \Longrightarrow dX_2 \Big/ dX_2' = \frac{\partial X_2}{\partial C_p} C_p' + \frac{\partial X_2}{\partial \theta_1} \theta_1' + \frac{\partial X_2}{\partial Y_1} Y_1' + \frac{\partial X_2}{\partial X_2'} + \frac{\partial X_2}{\partial Y_2} Y_2'\right] \tag{33}$$

and

$$\left[(16) + (19) + (26) + (33) \Longrightarrow (6)\right] . \tag{34}$$

With the exception of (33) and (34), no difficulty with the above substitutions occurs and they lead directly to explicite forms of (1) through (5). Upon substituting (33) in the expression for Y_2', equation (16), and solving for Y_2' as directed in (34) we find that Y_2' is identically zero. Such a result does not make physical sense and no alternative or method for finding a usable explicite form of (6) has been found. It is possible that this result is due to a redundancy of Snell's law and the Theory of Malus as discussed earlier. In this case we are left with the indefinite results and conclusions drawn earlier. We will therefore conclude the discussion of this attempt at an exact solution by outlining more clearly the derivations indicated in (34).

By performing the operations indicated in (34) we obtain

$$Y_2' = -\tan\left(\frac{\theta_2 - \theta_3}{2}\right)\frac{\left[\frac{\partial X_2}{\partial C_p} C_p' + \frac{\partial X_2}{\partial X_2'} + \theta_1' \frac{\partial X_2}{\partial \theta_1} + Y_1' \frac{\partial X_2}{\partial Y_1}\right]}{\left[1 + \tan\left(\frac{\theta_2 - \theta_3}{2}\right) \frac{\partial X_2}{\partial Y_2}\right]} \tag{35}$$

We then obtain equation (9) from (18) and (19) as directed by (26). Differentiating (9) then gives the partial derivatives necessary for for evaluating (35).

Consider the denominator of (35) first. Evaluating $\frac{\partial X_2}{\partial Y_2}$ we get

$$\frac{\partial X_2}{\partial Y_2} = - \frac{(\cos \theta_2 + \cos \theta_3)}{(\sin \theta_2 - \sin \theta_3)} \tag{36}$$

We find therefore, upon expanding $\tan\left(\frac{\theta_2 - \theta_3}{2}\right)$, that

$$\left[1 + \tan\left(\frac{\theta_2 - \theta_3}{2}\right) \frac{\partial X_2}{\partial Y_2}\right] = 1 - \left(\frac{\sin(\theta_2 - \theta_3)}{1 + \cos(\theta_2 - \theta_3)}\right) \cdot \left(\frac{\cos\theta_2 + \cos\theta_3}{\sin\theta_2 - \sin\theta_3}\right) \tag{37}$$

and that therefore the denominator of (35) goes to zero if either $\theta_2 = 0$ or $\theta_3 = 0$. We will find however, that the bracketed terms in the numerator vanish for all θ_2 and θ_3.

From equation (13) we have that

$$C_p' = \sin \theta_3.$$

Differentiating (9) gives

$$\frac{\partial X_2}{\partial C_p} = 1 \Big/ (\sin \theta_2 - \sin \theta_3) \tag{38}$$

and

$$\frac{\partial X_2}{\partial X_2'} = -\sin \theta_3 \Big/ (\sin \theta_2 - \sin \theta_3), \tag{39}$$

so that

$$\frac{\partial X_2}{\partial C_p} C_p' + \frac{\partial X_2}{\partial X_2'} \equiv 0.$$

This leaves (35) as

$$Y_2' = -\tan\left(\frac{\theta_2 - \theta_3}{2}\right) \frac{\left[\theta_1' \frac{\partial X_2}{\partial \theta_1} + Y_1' \frac{\partial X_2}{\partial Y_1}\right]}{\left[1 + \tan\left(\frac{\theta_2 - \theta_3}{2}\right) \frac{\partial X_2}{\partial Y_2}\right]} \tag{40}$$

With considerable algebraic effort for the case wherein

$$\frac{d\beta}{d\theta_1} = 0 \quad \text{and} \quad \frac{dC_{po}}{d\theta_1} = 0,$$

the case of a fixed center of phase for the primary source, we can show that

$$\theta_1' \frac{\partial X_2}{\partial \theta_1} + Y_1' \frac{\partial X_2}{\partial Y_1} \equiv 0$$

for all values of the variables. Now $\frac{d\beta}{d\theta_1}$ and $\frac{dC_{po}}{d\theta_1}$ are not independent if a normally congruent ray and wavefront system is defined for the primary source. It is presumed, although not shown, that the same result would be obtained with $\frac{d\beta}{d\theta_1} \neq 0$ and $\frac{dC_{po}}{d\theta_1} \neq 0$. The case when these quantities are zero is, however, by far the most important practical case. Differentiation of (9) gives

$$\frac{\partial X_2}{\partial \theta_1} = -\left[\frac{d\mathcal{C}}{d\theta_1} \sec\theta_1 + (\mathcal{B} - Y_1)\sec\theta_1 \tan\theta_1 - \left(\sin\theta_2 \frac{d\mathcal{B}}{d\theta_1}\right)\right. \tag{41}$$

$$\left.\cdot\left(\tan\theta_1\right) - (\mathcal{B} - Y_1)\sin\theta_2 \sec^2\theta_1 + \frac{dC_{po}}{d\theta_1}\right] \Big/ (\sin\theta_2 - \sin\theta_3),$$

and

$$\frac{\partial X_2}{\partial Y_1} = \left[\sec\theta_1 - \sin\theta_2\tan\theta_1 + \cos\theta_2\right] \Big/ (\sin\theta_2 - \sin\theta_3). \tag{42}$$

These equations together with (40) may be used to verify the above assertions. In order to complete the result, the explicite form of θ_1' and Y_1' must first be obtained by carrying out the substitutions indicated in (25) and (32).

If the difficulties indicated in the above derivations could be overcome this method for obtaining an exact solution would be very powerful since, for one reason, the six simultaneous first order differential equations (1) through (6) are readily solved by the high speed computors available today. However, since in this work the problem of the edge source diffracted field has been defined and a partial correction obtained (see Chapter 5) no further effort for an exact solution will be made.

CHAPTER 4

REFERENCES

1. S. Silver, 'Microwave Antenna Theory and Design", McGraw -Hill Book Company, N.Y., N.Y., 1949, Chapter 13.

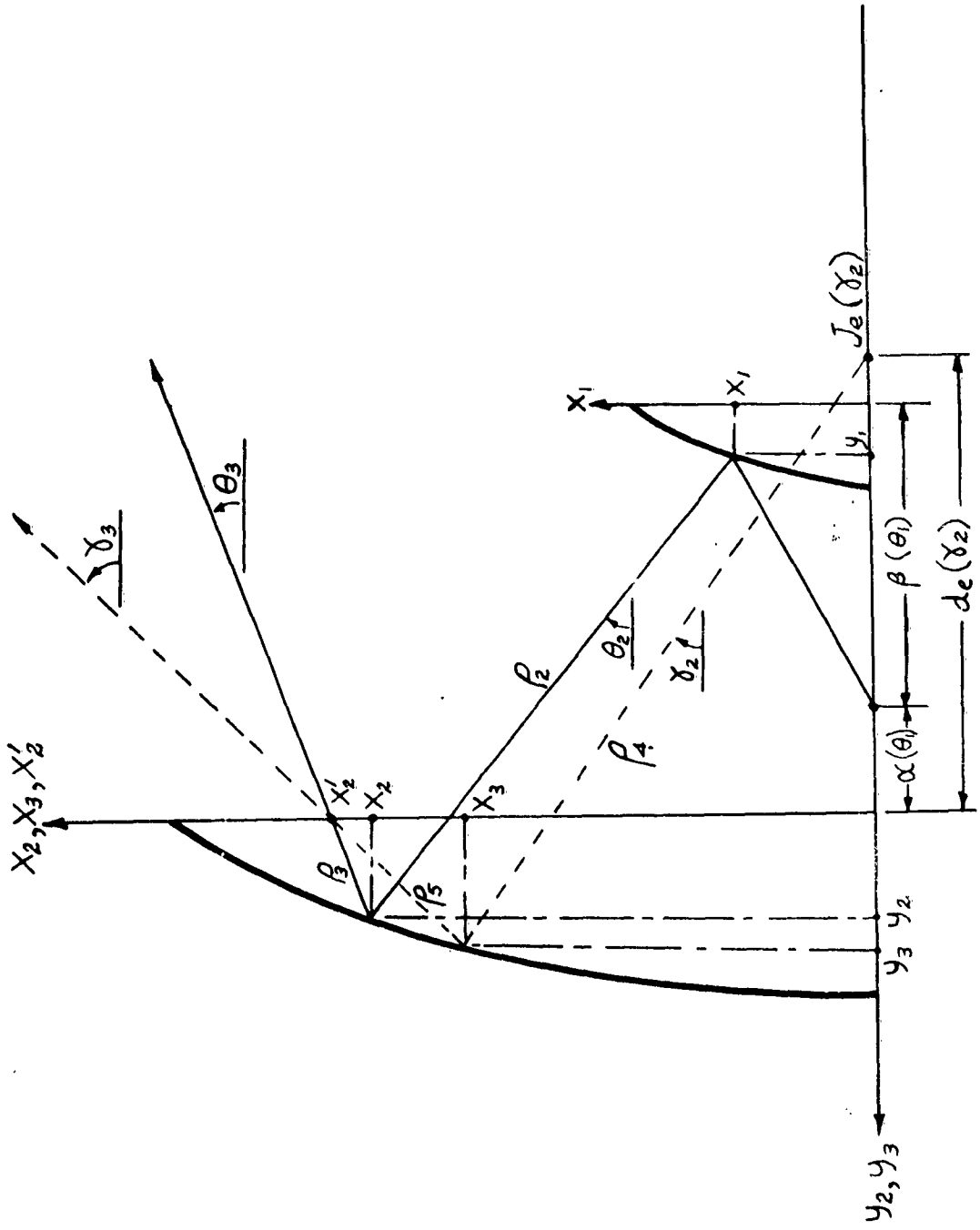
x_2, x_3, x_2'
γ_3
θ_3
β_3
x_2'
x_2
x_3
β_3
ρ_2
θ_2'
γ_2'
ρ_4
x_1
x_1
y_1
$J_e(\gamma_2)$
$\beta(\theta_1)$
$d_e(\gamma_2)$
$\alpha(\theta_1)$
y_3 y_2
y_2, y_3

Figure 1

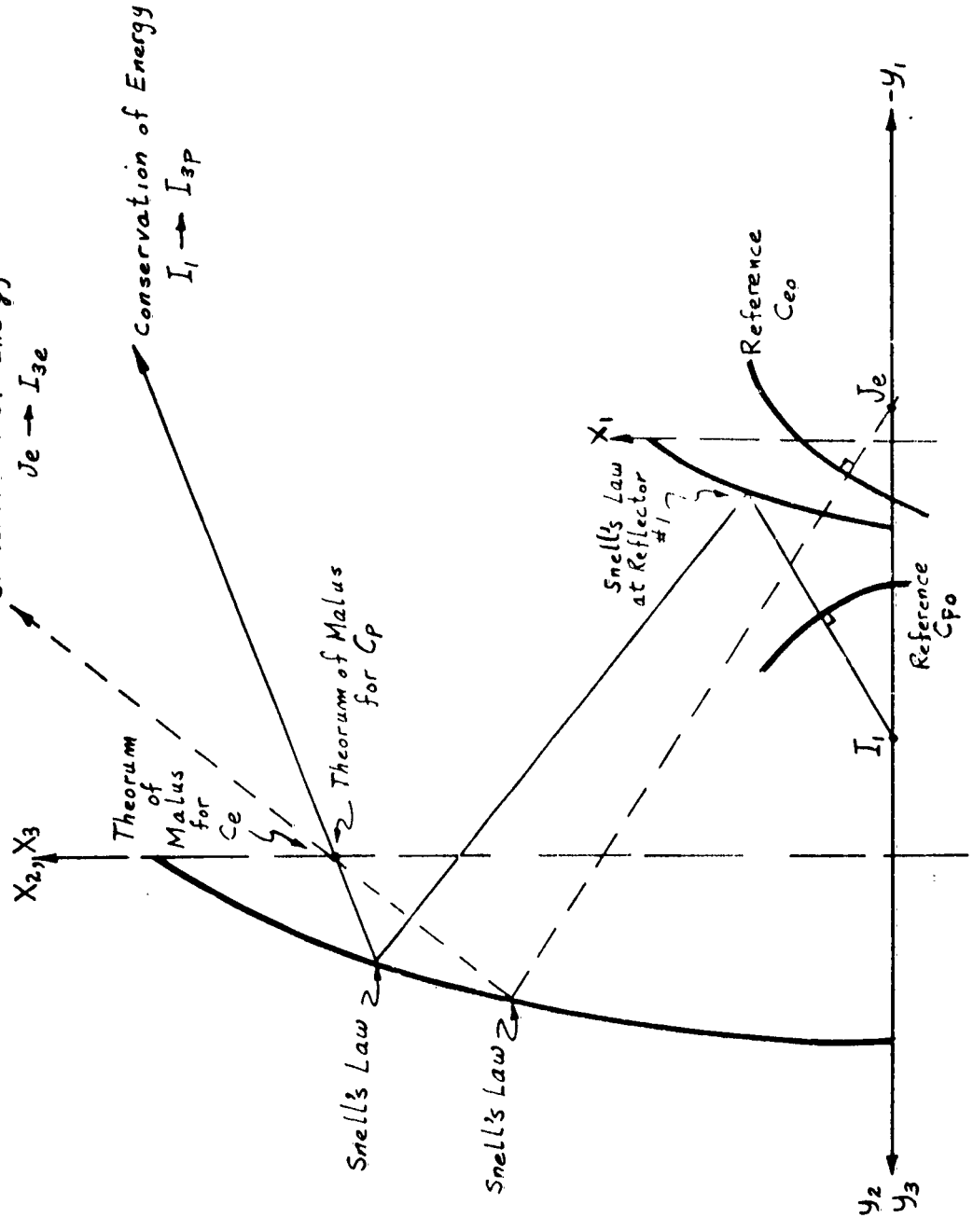
Conservation of Energy
Je → I3e
Conservation of Energy
I1 → I3P
Theorum of Malus for Ce
Theorum of Malus for Cp
Snell's Law 2
Snell's Law 2
Snell's Law at Reflector #1
Reference Ceo
Reference Cpo
Je
I1
X2, X3
X1
-y1
y2 y3

Figure 2.

CHAPTER 5

CORRECTING THE EDGE DIFFRACTED FIELD BY APPLICATION OF THE SYNTHESIS METHOD

I. Introduction

The effect of the aperture edge field and its significance was discussed in detail in Chapter 3. As was evident from the results of Chapter 3, the shadow boundary lobe could be reduced to a negligible width by increasing the size of the subreflector in wavelengths. This approach, however, merely substitutes aperture blockage for the aperture edge field effect. To date this has been the standard approach to this problem. In this chapter, we shall show that much of the deleterious effect of the shadow boundary lobe can be reduced by application of the synthesis method developed in Chapter 1.

It was asserted in Chapter 3 that the most significant aspect of the shadow boundary lobe effect was the fact that it causes the total field in the aperture in the region of the lobe to be 180° out of phase with the rest of the approximately uniformly phased aperture. Computations will be presented later to verify this assertion. The results obtained in this chapter by repeated application of the synthesis method is that the shadow boundary lobe phase can be made very nearly uniform with the phase of the geometrical optics field over the entire aperture. Hence, even though essentially no correction of the amplitude of this lobe was obtainable, it is possible to substantially increase the gain and efficiency of the antenna by this method. As mentioned in Chapter 3, this correction could potentially increase the effective aperture area

by the order of 30% for a 2λ diameter subreflector and on the order of 10% for a 6λ diameter subreflector.

The method used for correcting the shadow boundary lobe is by no means limited to the degree of success so far obtained and discussed above. While a 100% correction of this effect does not seem possible, substantial correction of both the amplitude and phase does appear possible by continued judicious application of the technique.

The method to be used for correction is essentially an iterative approach to the solution with only one iteration taken. It will be clear from the computed results presented later that repeated application or iteration of this method shows no promise of uniform convergence, or at least rapid convergence. This is to be expected, since it appears very likely that an exact solution does not exist in any case. The phasor diagram (a) illustrates how the subreflector edge field adds to the geometrical optics field to give the total field amplitude $\mathcal{J}_{eR}$ and phase C_1. (C_1 will be denoted as the total phase of the resultant field and normalized to a length approximately equal to that of C_p. We designate C_R as the unnormalized phase. Hence we get $C_R/k < 2\pi$ and $\tan k C_1 = \tan k C_R$). This phasor diagram applies to a specific value of x_2' in the aperture. If we presume that $\mathcal{J}_{3e}$ and C_e will remain essentially unchanged upon a small deformation of the reflector shapes, then we may apply the synthesis method of Chapter 1 to obtain an aperture distribution given by $\mathcal{J}$ and C as indicated in the phasor diagram (b). If $\mathcal{J}_{3e}$ and C_e actually did remain unchanged for this aperture point, x_2', then we would expect to obtain the original geometric optics field $\mathcal{J}_{3p}$ and C_p

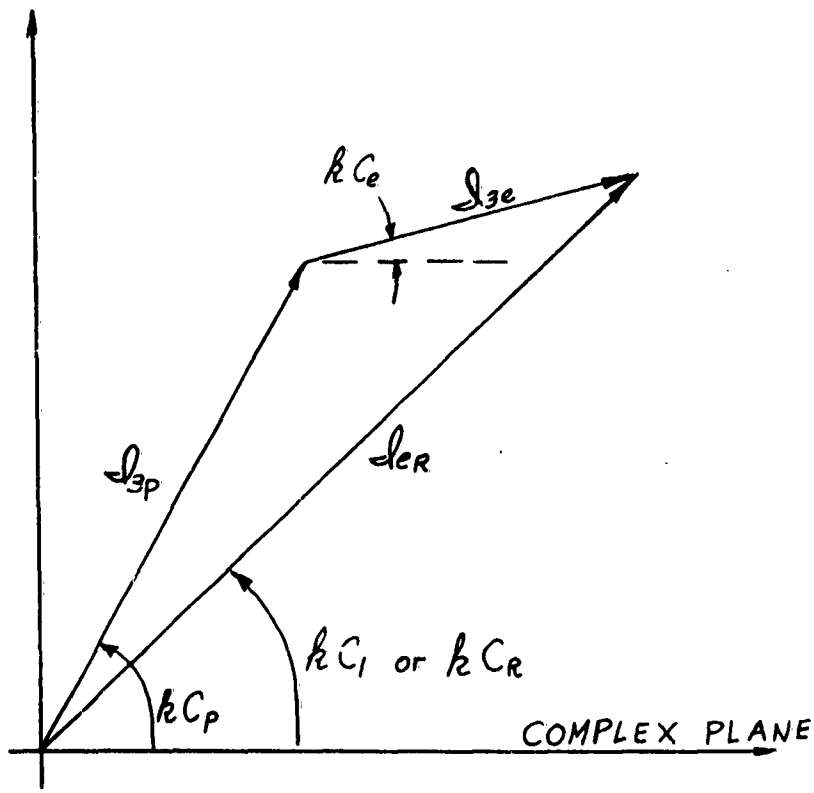

(a)

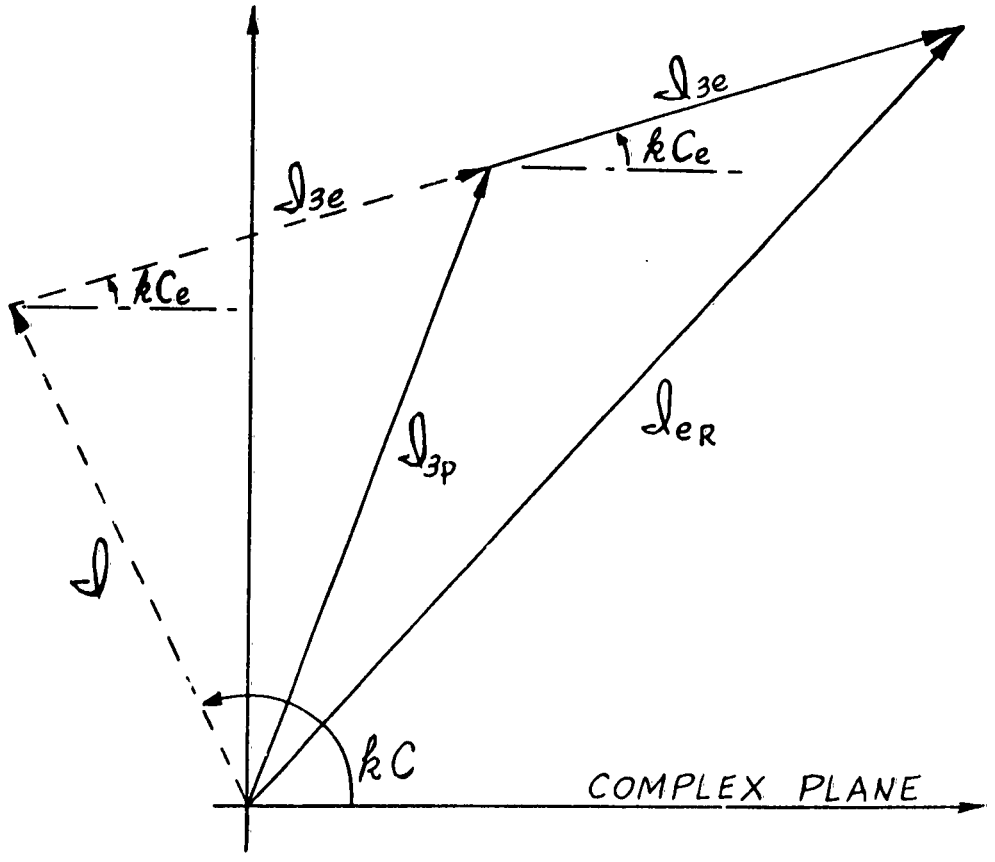
$\mathcal{I}_{3e}$
kC_e
$\mathcal{I}_{3e}$
kC_e
$\mathcal{I}_{3p}$
$\mathcal{I}_{eR}$
$\mathcal{I}$
kC
COMPLEX PLANE

(b)

at this point. We will define the original geometric optics field as the "desired" distribution we would like to obtain finally.

Upon synthesizing for $\mathcal{J}(x'_2)$ and $C(x'_2)$ we change the reflector shapes from $y_1(x_1)$ and $y_2(x_2)$ to the new shapes $y_{1n}(x_{1n})$ and $y_{2n}(x_{2n})$ and as a consequence, the new edge diffracted field in the aperture, $\mathcal{J}_{3en}$ and C_{en}, is not equal to the former edge field. As might be expected, we find in general that the correction method is most sensitive to the changes in C_e to C_{en}. This will be evident in the computed results presented later. However, it is precisely for this reason that the correction obtained with the total resultant phase distribution, C_2, is very satisfactory even when the resultant amplitude distribution, $\mathcal{J}_{RSL}$, is not substantially changed. This may be seen from a phasor diagram wherein $\mathcal{J}_{3e}$ is approximately equal to $\mathcal{J}_{3en}$, but wherein C_e and C_{en} may be greatly different. For a very large range of C_{en} we will find a good phase correction even when a poor amplitude correction results. This is illustrated in the phasor diagram (c) wherein the phasor $\mathcal{J}_{3en}$ connected to $\mathcal{J}$ is allowed to swing over a wide arc of a circle. The resultant phasor, regardless of the amplitude, ends up with a substantially corrected phase. The computed results presented later will illustrate this effect.

There is no reason why we must start the synthesis for $y_{2n}(x_{2n})$ and $y_{1n}(x_{1n})$ with the same boundary conditions from which $y_2(x_2)$ was computed. It is, in fact, desirable to adjust the boundary conditions so that $C_e \sim C_{en}$ near the shadow boundary lobe, namely at $x'_2 = x_{2m}$. An adjustment of x_{2n} by a fraction of a wavelength makes it possible to obtain C_e and C_p equal to the extent that

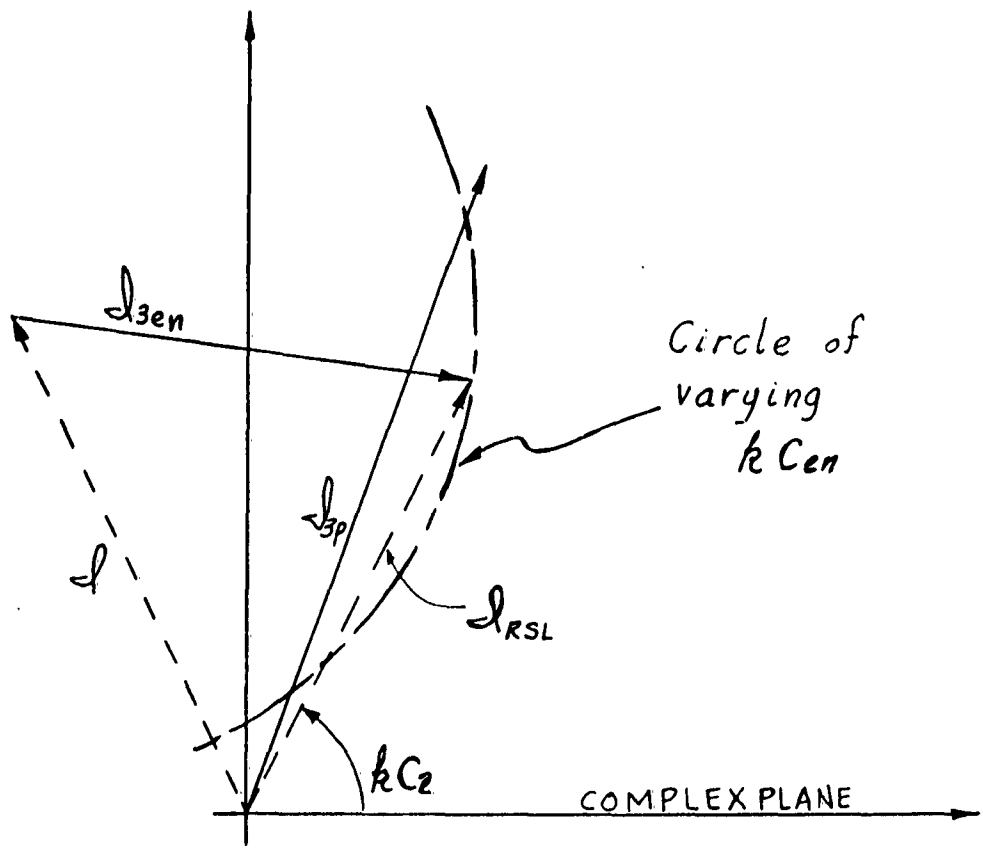
ℓ_{3en}
Circle of
varying
$k\,C_{en}$
ℓ_{3p}
ℓ
ℓ_{RSL}
kC_2
COMPLEX PLANE

(c)

$\tan k C_e \approx \tan k C_p$ (i.e., $k C_e + n\pi \approx k C_p$). Since x_{2m} is always very large in wavelengths, this alteration of x_{2m} can have no significant effect on the general properties of the antenna aside from the fact that since $k C_e + n\pi \approx k C_p$ we will find that $\tan k C_{en} \approx \tan k C_e \approx \tan k C_p$. Hence, in the vicinity of the shadow boundary lobe, we can insure that a point, specifically the boundary point, will have $C_e \approx C_{en}$ (or just as well, $k C_e \approx k C_{e\eta} + \pi$ if desired). This particular adjustment does not, unfortunately, lead to any substantial correction of the shadow boundary lobe in amplitude. It merely causes the shadow boundary lobe to remain in essentially the same position in the aperture before and after correction. In other words, this change in boundary condition causes the new main reflector shape to be less altered in shape in the vicinity of the shadow boundary lobe. This adjustment of the boundary does lead, on the other hand, to a substantially improved phase correction, as will be seen later.

For the purposes of correction in this chapter, we will choose the parabola-hyperbola system used in Chapter 3 for analysis purposes. Hence $y_2(x_2)$ and $y_1(x_1)$ will be respectively a parabola and hyperbola. We will, however, alter somewhat what we consider to be standard input parameters or boundary conditions. The change will be in the value of x_{2m} chosen. As Standard Set No. 2 input parameters, we will choose the following:

---

* n is any integer, usually positive, since usually $C_p > C_e$.

STANDARD SET NO. 2 PARAMETERS

Same as Standard Set No. 1 except that:

x_{2m} = Maximum value indicated on Graphs.

OPTION = -1 is the standard option indicating that x_{2m} for the new reflectors is computed so that $k C_e \approx k C_{en}$ at $x_2' = x_{2m}$. If x_{2m} is not chosen this way, then an OPTION = +1 will be indicated where appropriate.

As indicated in Chapter 3 also, the above Standard Set No. 2 parameters may be assumed in any discussion or graphical illustration unless some modification is specifically mentioned.

As was mentioned earlier, an improved correction of the shadow boundary lobe may be possible if the amplitude and phase, $\mathcal{J}$ and C, which are synthesized by the method of Chapter 1, are altered somewhat in anticipation of the fact that the altered reflector shapes will make $\mathcal{J}_{3en}$ and C_{en} different than $\mathcal{J}_{3e}$ and C_e. Such a change in and C should be made judiciously after a careful investigation. This change is not attempted here. Inadvertantly, however, in the process of making machine computations, the value of C was changed, in other words this phasor was rotated in a manner described later in this chapter. The results of these computations are presented, since it is interesting that although the specific values of the computed variables is, of course, different than the case with $\mathcal{J}_{exp}(kC)$ not rotated, the results are in all qualitative aspects the same as before rotation. Computed results that are illustrated in the figures of this chapter will

be denoted by ROT on graphs if such a rotation was made.

Before presenting the computed results, we will develop the mathematics of the correction procedure. Several approximations which afford a simplification in numerical computations are indicated in this development.

II. Application of the Synthesis Method

Before we actually apply the synthesis method to correct the edge field, we will compute the total field amplitude, phase, and phase derivative in the aperture.

The relative phase, C_R, of the total uncorrected aperture distribution is easily found as

$$C_R = \frac{1}{k} \arctan \left[\frac{\sin k C_p + \left(\frac{\partial 3e}{\partial 3p}\right) \sin k C_e}{\cos k C_p + \left(\frac{\partial 3e}{\partial 3p}\right) \cos k C_e} \right] \qquad (1)$$

It is convenient for purposes of comparison and computation to add an integral number of half wavelengths to C_R so that C_R is approximately equal to

$$C_{pm} \equiv C_p(x'_{2m}) = C_p \, . \qquad (2)$$

We define this "normalized" phase as C_1 and find its value by

$$C_1 = C_R + C_{pm} - 1/k \arctan \left(\tan (k C_{pm})\right) \, . \qquad (3)$$

The last two terms on the right hand side of (3) add up to an integral

number of half wavelengths and thus provide the "normalization" that is sought.

Now the rotation of C_1, which was discussed in the introduction and is indicated in the figures by the designation ROT, was made by choosing, inadvertently,

$$C_1 = C_R + C_{pm} - 1/k \arctan (k\ C_{pm}) . \tag{3a}$$

The amplitude of the total field is found as

$$I_{eR} = I_{3p} + 2\sqrt{I_{3p} \cdot I_{3e}}\ \cos (k\left[C_p - C_e\right]) + I_{3e} . \tag{4}$$

These formulas are easily derived from the phasor diagrams presented earlier. Note that we continue the convention that

$$I_{eR} = \mathcal{J}^2_{eR}\ ,\quad I_{RSL} = \mathcal{J}^2_{RSL},\quad I_{3p} = \mathcal{J}^2_{3p}\ ,\quad I_{3e} = \mathcal{J}^2_{3e}\ ,\ \text{etc.}\ .$$

In order to obtain C and $\mathcal{J}$, the phase and amplitude for which we will synthesize new reflector shapes, we either let $C_e \rightarrow C_e + \pi/k$ or $\mathcal{J}_{3e} \rightarrow -\mathcal{J}_{3e}$, with the result that this <u>negative</u> edge field added to the geometrical optics field gives for the phase

$$C = 1/k \arctan \left[\frac{\sin k\ C_p - (\frac{\mathcal{J}_{3e}}{\mathcal{J}_{3p}}) \sin k\ C_e}{\cos k\ C_p - (\frac{\mathcal{J}_{3e}}{\mathcal{J}_{3p}}) \cos k\ C_e}\right] + C_{pm} \tag{5}$$

$$- 1/k \arctan (\tan k\ C_{pm}),$$

and for the amplitude

$$I = I_{3p} - 2\sqrt{I_{3p} \cdot I_{3e}}\ \cos (k\left[C_p - C_e\right]) + I_{3e} . \tag{6}$$

Note that the value of C must be normalized by the addition of

$$C_{pm} - 1/k \arctan (\tan k C_{pm})$$

in order that the synthesis yield a usable result. Note also that when $\tan k C_e = \tan k C_p$ then $\sin k C_p = \pm \sin k C_e$ and $\cos k C_p = \pm \cos k C_e$ and equation (5) reduces to

$$C = C_{pm} . \tag{7}$$

This holds true for the standard OPTION = -1 when $\tan k C_p = \tan k C_e$ at $x_2' = x_{2m}$.

In order to actually carry out the synthesis we still need the derivative function

$$\frac{dC}{dx_2'} = \frac{dC}{dx_2}$$

where the value x_2 in the above derivative is that point in the aperture which is designated in the uniform phase case as $x_2 = x_2'$. A different value of x_2 exists for the generally non-uniform phase distribution C but is not needed in the derviations we shall consider. This may be made somewhat clearer by the diagram below (d) wherein the ray passing normally through the aperture belongs to C_p for which $x_2 = x_2'$ and the ray passing obliquely through the aperture belongs to C and has the same x_2' value but is incident upon the main reflector at a point different in value than x_2'.

As an approximation in obtaining $\frac{dC}{dx_2}$ we will assume that

$$\frac{d\vartheta_{3p}}{dx_2} \ll \frac{d\vartheta_{3e}}{dx_2} .$$

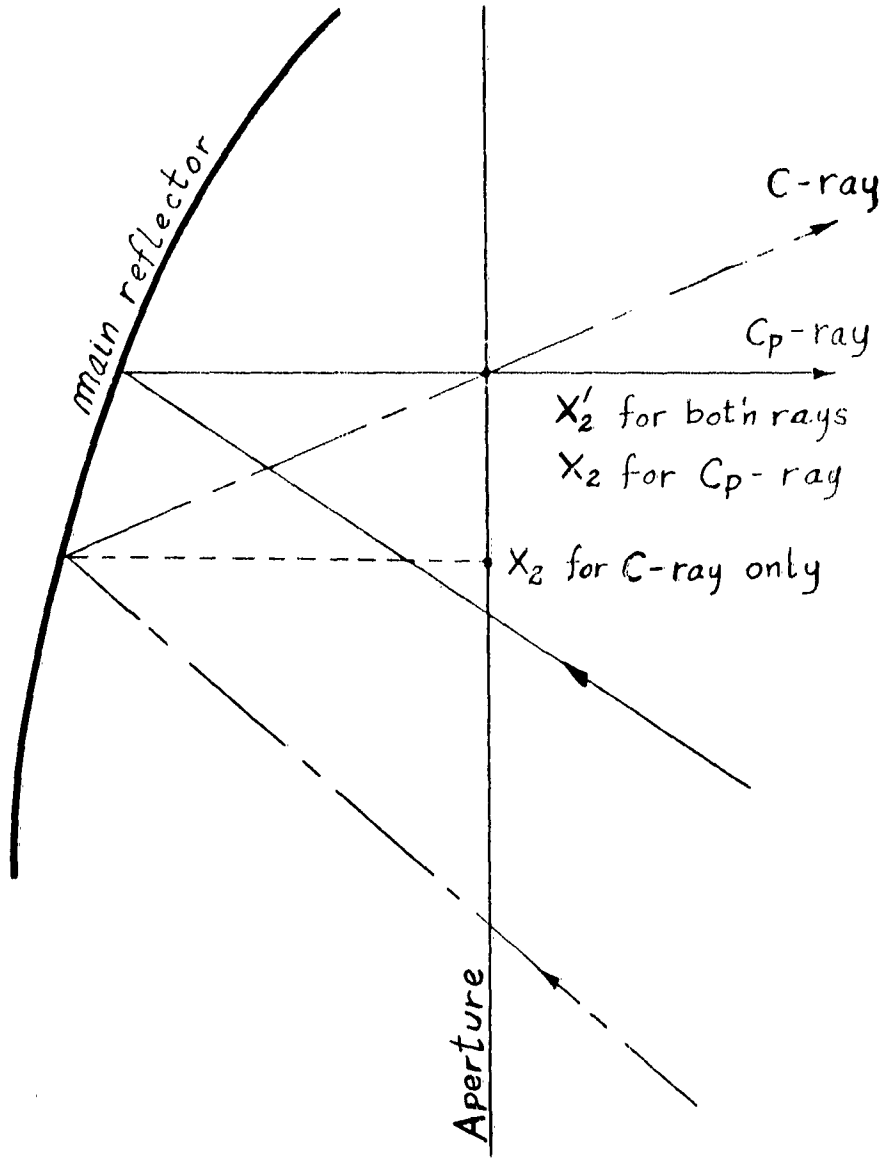
main reflector
C-ray
C_p-ray
X_2' for both rays
X_2 for C_p-ray
X_2 for C-ray only
Aperture

(d)

From the results illustrated in chapter three it is evident that $\mathfrak{J}_{3p}$ (or I_{3p}) is a very smooth function in comparison with $\mathfrak{J}_{3e}$ (or I_{3e}).

This is especially true when $\mathfrak{J}_{3e}$ is large or on the order of $\mathfrak{J}_{3p}$. When $\mathfrak{J}_{3e} \ll \mathfrak{J}_{3p}$ the approximation is not as good but it also is not necessary here since no correction is needed. Hence we may state that

$$\frac{d}{dx_2}\left(\frac{\mathfrak{J}_{3e}}{\mathfrak{J}_{3p}}\right) = \frac{1}{\mathfrak{J}_{3p}} \quad \frac{d\mathfrak{J}_{3e}}{d x_2} = \frac{1}{2\left(\frac{\mathfrak{J}_{3e}}{\mathfrak{J}_{3p}}\right)} \quad \frac{d I_{3e}}{d x_2} \quad . \tag{8}$$

In practice, one of the most important cases to which this correction may be applied is, incidently, the case wherein $\mathfrak{J}_{3p}$ = constant and $d\mathfrak{J}_{3p} / d x_2 = 0$. In the present case we have, identically, that

$$\frac{dC_p}{d x_2} = 0 \quad . \tag{9}$$

We now must evaluate $\frac{dI_{3e}}{d x_2}$ explicitly in order to obtain $\frac{dC}{d x_2}$. Referring to equation (90) of chapter three, we obtain

$$\frac{dI_{3e}}{d x_2} = I_{3e}\left[\frac{dJ'_e}{d x_2} - \left(\frac{d^2 x_2}{d\Gamma_2 \, d x_2}\right) \cdot \frac{1}{\left(\frac{d x_2}{d\Gamma_2}\right)} + \frac{ctn\Gamma_2}{\left(\frac{d x_2}{d\Gamma_2}\right)} - \frac{1}{x_2}\right] , \tag{10}$$

where $\left(\frac{d x_2}{d\Gamma_2}\right)$ is defined by equation (87) in chapter three. From equation (39) of chapter three we obtain by differentiation

$$\frac{dJ'_e}{d\Gamma_2} = \frac{1}{4\pi}\left[G_e^2\ I_{lm}\ G_{lm}^2\right]\cdot$$

$$\cdot\left[Y_1\cdot Y_1'\cos^2\xi + Y_2\ Y_2'\ \sin^2\xi + Y_2^2\ Y_1^2\ \sin\xi\ \cos\xi\cdot\xi'\right] \tag{11}$$

The remaining terms in (11) are defined in chapter three.

In order to obtain $\frac{d_2 x_2}{d\Gamma_2\, d x_2}$ we differentiate $\left(\frac{d x_2}{d\Gamma_2}\right)$ and get

$$\left.\begin{aligned}
\frac{d^2 x_2}{d\Gamma_2\, d x_2} &= \left(\frac{d^2 x_3}{d\Gamma_2\, d x_2}\right) + \left(\frac{d^2 y_3}{d x_3\, d x_2}\right)\left(\frac{d x_3}{d\Gamma_2}\right)\ \tan\gamma_3 \\
&+\left(\frac{d y_3}{d x_3}\right)\left(\frac{d^2 x_3}{d\Gamma_2\, dx_2}\right)\tan\gamma_3 + \left(\frac{dy_3}{dx_3}\right)\left(\frac{dx_3}{d\Gamma_2}\right)\sec^2\gamma_3\left(\frac{d\gamma_3}{dx_2}\right) \\
&+\left(\frac{dy_3}{dx_2}\right)\left(\frac{d\gamma_3}{d\Gamma_2}\right)\sec^2\gamma_3 + y_3\ \frac{d^2\gamma_3}{d\Gamma_2\, dx_2}\ \sec^2\gamma_3 \\
&+ 2y_3\left(\frac{d\gamma_3}{d\Gamma_2}\right)\ \sec^2\gamma_3\ \tan\gamma_3\ \left(\frac{d\gamma_3}{dx_2}\right).
\end{aligned}\right\} \tag{12}$$

Most of the quantities in equation (12) are defined already in chapter three. That is, in chapter three we have γ_3 defined by (85), y_3 by (80), $\frac{dy_3}{dx_3}$ by (81), $\frac{d\gamma_3}{d\Gamma_2}$ by (88), and $\frac{dx_3}{d\Gamma_2}$ by (89). The remaining new differentials are readily found in terms of those already defined. We have

$$\frac{d\gamma_3}{dx_2} = \left(\frac{d\gamma_3}{d\Gamma_2}\right) \Big/ \left(\frac{dx_2}{d\Gamma_2}\right) \tag{13}$$

directly. By differentiating $\left(\frac{d\gamma_3}{d\Gamma_2}\right)$ we get

$$\frac{d^2\gamma_3}{d\Gamma_2\, dx_2} = -\frac{d^2 x_3}{d\Gamma_2\, dx_2}\cos^2\left(\frac{\Gamma_2 - \gamma_3}{2}\right)\frac{1}{f_2} + \left.\frac{1}{f_2}\;\frac{dx_3}{d\Gamma_2}\cos\left(\frac{\Gamma_2 - \gamma_3}{2}\right)\sin\left(\frac{\Gamma_2 - \gamma_3}{2}\right)\left\{\frac{1}{\frac{d\Gamma_2}{dx_2}} - \frac{d\gamma_3}{dx_2}\right\}\right\} \quad (14)$$

where f_2 is the main reflector focal length derived in Chapter 3. Differentiating $\left(dy_3/dx_3\right)$ we get

$$\frac{d^2 y_3}{dx_3\, d\Gamma_2} = -\frac{1}{2 f_2}\left(\frac{dx_3}{dx_2}\right) \quad (15)$$

where

$$\frac{dx_3}{dx_2} = \left(\frac{dx_3}{d\Gamma_2}\right)\left(\frac{dx_2}{d\Gamma_2}\right) \quad (16)$$

From (16) we get

$$\frac{dy_3}{dx_2} = \left(\frac{dy_3}{dx_3}\right)\cdot\left(\frac{dx_3}{dx_2}\right) . \quad (17)$$

The final remaining derivative is obtained by differentiating $\left(dx_3 \,/\, d\Gamma_2\right)$ with the result that

$$\frac{d^2 x_3}{d\Gamma_2\, dx_2} = \left(\frac{dx_3}{d\Gamma_2}\right)\operatorname{ctn}\Gamma_2\left[\sin^2\Gamma_2\left(\frac{dx_3}{d\Gamma_2}\right)^2 - 2\right] . \quad (18)$$

With the above derivatives defining $\left(\frac{dI_{3e}}{dx_2}\right)$ completely and $\left(dC_e \,/\, dx_2\right)$ already defined in Chapter 3 by equation (94) we can obtain $\left(dC/dx_2\right)$. For notational convenience we define first

$$kQ = kC - kC_{pm} + \arctan\,(\tan\,(kCpm)\,), \tag{19}$$

$$D_{nc} = \cos k C_p - \left(\frac{\vartheta_{3e}}{\vartheta_{3p}}\right) \cos k C_e\,, \tag{20}$$

and

$$D_{3p} = \frac{d}{dx_2} \left(\frac{\vartheta_{3e}}{\vartheta_{3p}}\right) \tag{21}$$

from equation (8) above. We find then for (dC/dx_2):

$$\frac{dC}{dx_2} = \left[\frac{\cos^2 kQ}{k\,D_{nc}^2}\right] \cdot \left[D_{nc} \cdot \left\{- D_{3p} \sin k C_e - \left(\frac{\vartheta_{3e}}{\vartheta_{3p}}\right) k \frac{d C_e}{dx_2} \cos k C_e\right\} - \left\{\sin k C_p - \left(\frac{\vartheta_{3e}}{\vartheta_{3p}}\right) \sin k C_e\right\} \cdot \left\{\left(\frac{\vartheta_{3e}}{\vartheta_{3p}}\right) k \frac{d C_e}{dx_2} \sin k C_e - D_{3p} \cos k C_e\right\}\right]. \tag{22}$$

We are now in a position to use the results of Chapter 1 and synthesize new reflector cross-sections $y_{2n}\,(x_{2n})$ and $y_{1n}\,(x_{1n})$. The variables in the new dual reflector system will be subscripted by the letter n with the exception of x_2'. This variable remains the same, by definition, in both systems. Hence a reference to a point x_2' in the aperture applies to both reflector systems. The diagram below (e) illustrates that the primary source rays for each reflector system have been chosen to cross in the aperture. This is convenient for comparison of the results when they are tabulated and in programming for machine computations.

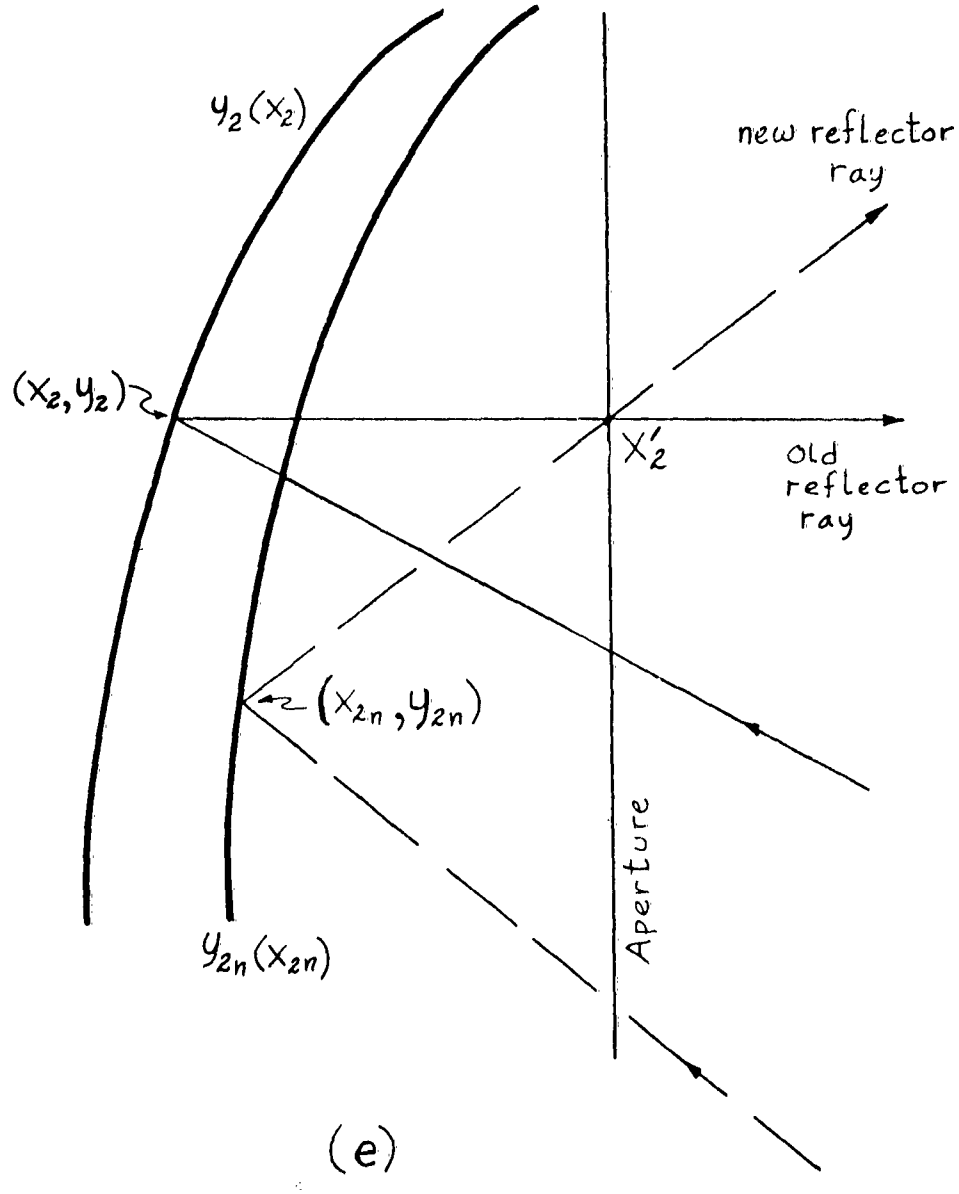
$y_2(x_2)$
new reflector ray
(x_2, y_2)
x'_2
old reflector ray
(x_{2n}, y_{2n})
Aperture
$y_{2n}(x_{2n})$

(e)

The boundary conditions for the new two first order differential equations, θ'_{1n} and y'_{1n}, will remain unchanged, that is:

$$\theta_{1\,max} = (\text{initial } \theta_1) = \arctan\,(x_{1\,max}/\beta) \tag{23}$$

and

$$y_{1\,max} = (\text{initial } y_1) = 0. \tag{24}$$

These are the conditions which would have been used if the parabola-hyperbola system ($y_2\,(x_2)$ and $y_1\,(x_1)$) had been derived by means of the synthesis method of Chapter 1. The boundary conditions are consistent with Standard Set 2 parameters.

The two simultaneous first order differential equations for the new reflector system are

$$\theta'_{1n} = \left(\frac{I}{I_1(\theta_{1n})}\right) \left(\frac{x'_2}{\sin\theta_{1n}}\right) \tag{25}$$

and

$$y'_{1n} = \frac{(\beta - y_{1n})\,\sec^2\theta_{1n}\,.\,\tan\left(\frac{\theta_{1n} - \theta_{2n}}{2}\right)\,.\,\theta'_{1n}}{1 + \tan\theta_{1n}\,.\,\tan\left(\frac{\theta_{1n} - \theta_{2n}}{2}\right)}\,. \tag{26}$$

where the pertinent variables for the system are defined as set forth in Chapter 1:

$$x_{1n} = (\beta - y_{1n})\tan\,\theta_{1n}\,, \tag{27}$$

$$B = C - (\beta - y_{1n})\sec\theta_{1n}\,, \tag{28}$$

$$x_{2n} = x_2' + \left(\frac{1}{2}\right) \frac{\left[(x_{1n} - x_2')^2 + (\gamma - y_{1n})^2 - B^2\right]}{\left[(x_{1n} - x_2') + \frac{1}{\left(\frac{dC}{dx_2}\right)}\left\{(\gamma - y_{1n})\sqrt{1 - \left(\frac{dC}{dx_2}\right)^2} + B\right\}\right]}, \tag{29}$$

$$y_{2n} = -\left(\frac{1}{2}\right) \frac{\left[(x_{1n} - x_2')^2 + (\gamma - y_{1n})^2 - B^2\right]}{\left[(\gamma - y_{1n}) + \frac{\left(\frac{dC}{dx_2}\right)(x_{1n} - x_2') + B}{\sqrt{1 - \left(\frac{dC}{dx_2}\right)^2}}\right]}, \tag{30}$$

$$\theta_{2n} = \arctan\left(\frac{x_{2n} - x_{1n}}{\gamma + y_{2n} - y_{1n}}\right), \tag{31}$$

$$\theta_{3n} = \arcsin\left(\frac{dC}{dx_2}\right), \tag{32}$$

and

$$\frac{d\,y_{2n}}{d\,x_{2n}} = -\tan\left(\frac{\theta_{2n} - \theta_{3n}}{2}\right). \tag{33}$$

The value of $\left(\frac{d\,y_{2n}}{d\,x_{2n}}\right)$ is not necessary for integrating (25) and (26) but will be used to find C_{en} and subsequently I_{RSL}.

The values of C_{en}, I_{3en}, and I_{RSL} will not be computed at x_2' but at a different point in the aperture defined as x_{2n}'. This is done for computational convenience. Although in principle we could compute these variables at x_2' and not define x_{2n}', this would involve a considerably more complicated computer program. Furthermore we find, upon making the computations, that $x_2' \sim x_{2n}'$ and in the region of the shadow boundary lobe the difference between x_2' and x_{2n}' is negligible. The value of x_{2n}' is defined by

$$x'_{2n} = x_{2n} + y_{2n} \tan(\gamma_{3n}) \tag{34}$$

where

$$\gamma_{3n} = \Gamma_{2n} + 2 \arctan\left(\frac{dy_{3n}}{dx_{3n}}\right), \tag{35}$$

$$\Gamma_{2n} = \arctan\left(x_{3n} / (y_{3n} + \nu)\right), \tag{36}$$

and

$$\left.\begin{aligned} x_{3n} &= x_{2n} \\ y_{3n} &= y_{2n} \\ \frac{dy_{3n}}{dx_{3n}} &= \frac{dy_{2n}}{dx_{2n}} \end{aligned}\right\} \tag{37}$$

The edge source ray making an angle Γ_{2n} with the y_2 and y_1 axes is thus seen to intersect y_{2n} (x_{2n}) at the point (x_{2n}, y_{2n}). Since $\Gamma_{2n} \neq \theta_{2n}$, then the reflected ray intersects the aperture not at x'_2 but at the newly defined point x'_{2n}. These rays are illustrated in the diagram below (f).

In order to compute C_{en} at x'_{2n} we first compute ρ_{4n} and ρ_{5n} to that point and find

$$\rho_{4n} = \sqrt{x_{3n}^2 + (\nu + y_{3n})^2} \tag{38}$$

and

$$\rho_{5n} = y_{3n} / \cos \gamma_{3n}. \tag{39}$$

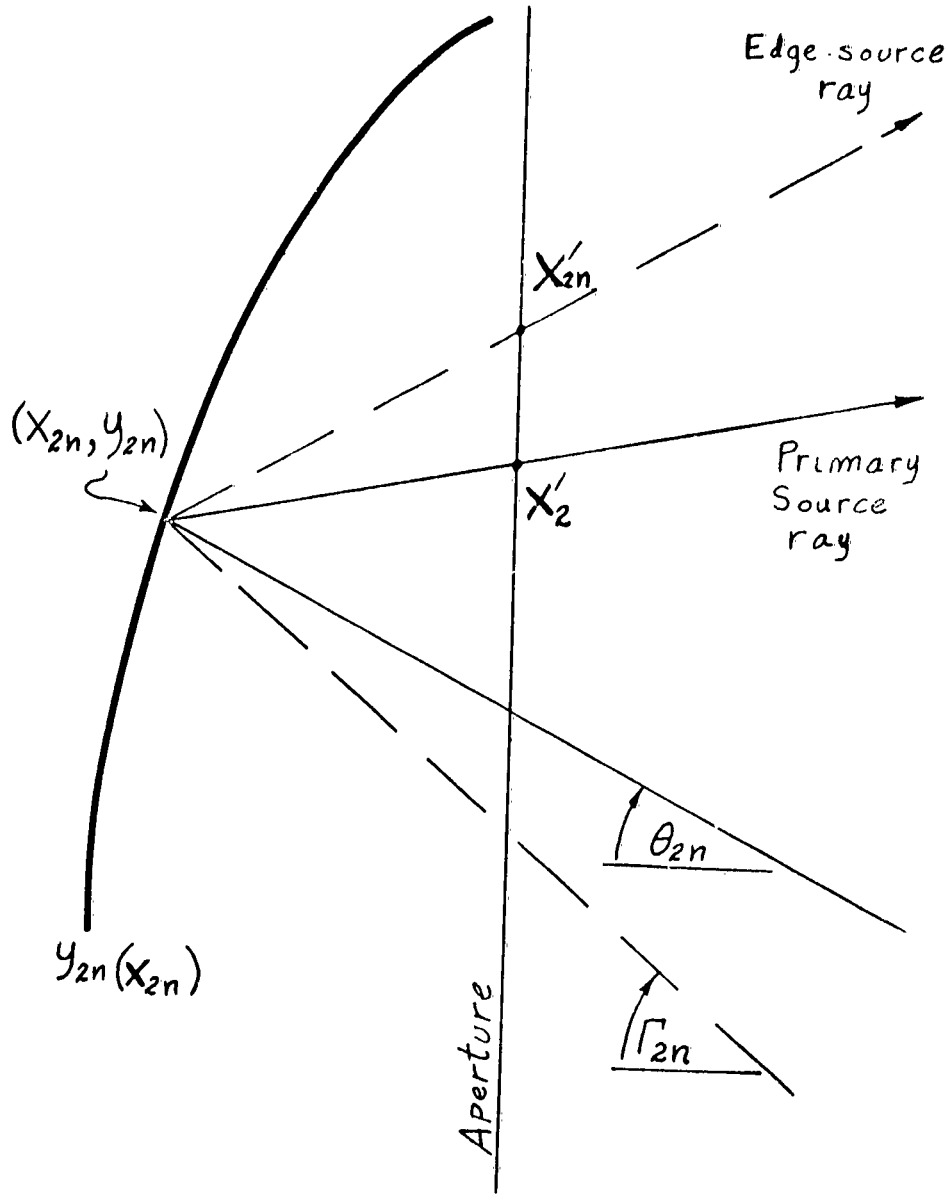
Edge-source ray
X'_{2n}
(X_{2n}, y_{2n})
Primary Source ray
X'_2
θ_{2n}
$y_{2n}(x_{2n})$
Γ_{2n}
Aperture

(f)

We find R_n, the reference phase (or C_{eon}) by using Γ_{2n} from (36) and the results of Chapter 3 (equation (41) in that chapter). With these values we obtain

$$C_{en} = \rho_{4n} + \rho_{5n} - R_n \tag{40}$$

or alternatively (since $\gamma_{2n} \rightarrow \Gamma_{2n}$ as explained in Chapter 3)

$$C_{en} = \rho_{4n} + \rho_{5n} + C_{eon}.$$

From equation (39) of Chapter 3 we obtain the value of J'_{en} (Γ_{2n}). In order to obtain I_{3en} from the energy conservation equation

$$I_{3en} = J'_{en} \left[\frac{\sin(\Gamma_{2n})}{x'_{2n}} \right] \frac{1}{\left(\frac{d\, x'_{2n}}{d\, \Gamma_{2n}} \right)} . \tag{41}$$

we must first find $\left(\frac{d\, x'_{2n}}{d\, \Gamma_{2n}} \right)$. The value of this derivative is found numerically from

$$\frac{d\, x'_{2n}}{d\, \Gamma_{2n}} \approx \left(\frac{x'_{2nLS} - x'_{2n}}{\Gamma_{2nLS} - \Gamma_{2n}} \right) \tag{42}$$

where x'_{2nLS} and Γ_{2nLS} are points adjacent to x'_{2n} and Γ_{2n}. For the purposes of the computations made in this report, the interval $x'_{2n} - x'_{2nLS}$ was almost a constant 0.05 (note that x'_2 and not x'_{2n} is the independent variable; the equivalent interval was precisely 0.05 for x'_2). Since Γ_{2n} was an almost linearly varying function of x'_2 also, the approximation for $(d\, x'_{2n} / d\, \Gamma_{2n})$ and consequently I_{3en} was very good.

If, as explained earlier, we assume that $x_2' \sim x_{2n}'$, we can calculate I_{RSL} directly. Actually this assumption is not necessary for finding I_{RSL} at x_2' but it is very convenient for machine computations. Since this approximation was made in the computational results that will be presented shortly, we make the approximation in these derivations also. The approximation is excellent in the vicinity of the shadow boundary lobe which is most important. With this approximation we assume that I, I_{3en}, C, and C_{en} are all computed at the same point instead of at the different points x_2' and x_{2n}'. We find therefore, for I_{RSL} that

$$I_{RSL} = I + 2\sqrt{I \cdot I_{3en}} \cos k (C - C_{en}) + I_{3en}. \tag{43}$$

With the same assumptions made in the last paragraph we can compute the normalized phase of I_{RSL}, C_2, which is found as

$$\left.\begin{aligned} C_2 = \left(\frac{1}{k}\right) \arctan \left[\frac{\sin k C + \frac{\mathcal{J}_{3en}}{\mathcal{J}} \sin k C_{en}}{\cos k C + \frac{\mathcal{J}_{3en}}{\mathcal{J}} \cos k C_{en}}\right] \\ + C_{pm} - \left(\frac{1}{k}\right) \arctan (\tan (k C_{pm})). \end{aligned}\right\} \tag{44}$$

Equation (44) completes the derivations necessary for an evaluation of this method for correcting the aperture edge field effect. It might be pointed out, in addition, that the syntheses indicated above and presented in the next section are more general illustrations of the synthesis method than was presented in Chapter 1. Neither the phase, C, nor the amplitude $\mathcal{J}$, are linear for these cases.

III. Computer Edge Field Correction Results

Extensive computations were made to test the aperture edge field correction technique discussed and derived in Sections I and II. The results of these computations are illustrated in Figures 1 through 47 of this chapter. For the most part the results depicted in the figures are self explanatory when taken together with the discussion in Section I. Hence this section will be devoted to merely pointing out some of the more significant aspects of the results and just how the figures are organized.

Figures 1 through 23 use the value for C_1 given by equation (3). In other words, they do not have $\vartheta \exp(kC)$ rotated in the complex plane. Figures 24 through 47 depict the "rotated" results and have the ROT designation noted in the figures. The amount of rotation, incidentally, will be different for each case of different k.

Figures 1 through 23 consist of four complete correction attempts for the three frequencies $k = 2\pi$, 4π, and 6π. These lower frequencies are the most significant from the point of view that an edge field correction is necessary for these small sub-reflector diameters if they are to be of practical value Note that a frequency of $k = n\pi$ implies a sub-reflector diameter of n wavelengths since $x_{1m} = 1.0$. For the frequency $k = 2\pi$, a case with the option value +1 in addition to the case with the standard option value -1 (Standard Set 2 parameters; see Section I of this chapter) is illustrated. The differences between the results obtained with each option value is very much the same for all k. Figures 22 and 23 illustrate the shape of the sub-reflector before and after

correction, $y_1(x_1)$ and $y_{1n}(x_{1n})$, for rather large k values, $k = 16\pi$ and 32π. The convergence of $y_{1n}(x_{1n}) \rightarrow y_1(x_1)$ should be noted.

Figures 24 through 47 consist of four complete cases with k equal to 32π, 2π, 6π, and 16π. For $k = 6\pi$ there are two cases illustrated with option = +1 in one case and option = -1 in the other case. Figure 47, for frequency $k = 32\pi$, illustrates $y_1(x_1)$ and $y_{1n}(x_{1n})$ for this high frequency. The results for the rotated cases (ROT = designation on Figures 24 through 47) are qualitatively the same as those for the non-rotated cases. This result is of some significance and is the primary reason for presenting these figures in this work.

In each case the following curves are illustrated:

C_e and C_{en} versus x_2' ;

ϑ_{3p}, ϑ_{3e}, ϑ_{3en} versus x_2' ;

C_1, C_2, C_p versus x_2' ;

ϑ_{3p}, ϑ_{er}, ϑ_{RSL} versus x_2' ;

and $y_2(x_2)$, $y_{2n}(x_{2n})$; $y_1(x_1)$, $y_{1n}(x_{1n})$.

In each case the independent variable x_2' varies from $x_2' = x_{2m}$ to $x_2' \sim 6$. This range covers the significant portion of the edge field contribution to the aperture. The value of x_{2m} is approximately equal to 10, but of course varies with k for the standard option value -1.

The polarization case $\gamma = 0$ was the only case treated herein. No change of any qualitative significance is expected for the $\gamma = \frac{\pi}{2}$ case. However it may be expected that the correction in reflector shapes will be different for this polarization if the same correction technique is applied. When the primary pattern has vector symmetry (polarization angle with the sub-reflector edge independent of rotation angle) then this presents no problem. The very significant case of circular polarization is such a case with vector symmetry. Otherwise some average correction or possibly a simultaneous correction must be searched for.

In all cases the degree of equality occurring simultaneously between C_e and C_{en} and also between ϑ_{3e} and ϑ_{3en} is a measure of the correction obtainable. Although general agreement between ϑ_{3e} and ϑ_{3en} was obtained the correlation between C_e and C_{en} was poor. This was expected since the amplitude is more sensitive to changes in the second derivative of the reflector contour and the phases, C_e and C_{en}, are sensitive to both position and slope of the reflectors.

The correlation between ϑ_{3e} and ϑ_{3en} was actually very poor for the option = +1 as is clearly evident from Figure 2. When the value of x_{2m} is adjusted so that $\tan k C_p \approx \tan k C_e$ at $x_2' = x_{2m}$, the condition when option = -1, then very good correlation between ϑ_{3e} and ϑ_{3en} is obtained. The improvement is evident from a comparison of Figure 7 results with those of Figure 2.

The change in option choice does not affect the agreement between C_e and C_{en} except near $x_2' = x_{2m}$ where, as discussed in Section I, a close agreement is expected. This change does however result in a considerable improvement of the total phase distribution C_2, as shown in Figure 8. The value of C_2 obtained when option = +1, Figure 3, is not nearly as uniform as that shown in Figure 8 when option = -1.

The improvement in total phase for all value of k as illustrated in Figures 8, 13, and 19 is actually excellent. The resulting phase, C_2, for the new dual reflector system is essentially uniform for most practical considerations. The phase, C_1, before correction is generally of the order of 180° out of phase with the remainder of the aperture in the vicinity of the shadow boundary lobe. This is true for all value of k considered. As evidenced by the amplitudes $\mathcal{J}_{er}$ and $\mathcal{J}_{3p}$ shown in Figures 4, 9, 14, and 20, a substantial amount of energy is radiated out of phase with the rest of the aperture from the shadow boundary lobe region. Although the final amplitude, $\mathcal{J}_{RSL}$, is not substantially different than the uncorrected amplitude, $\mathcal{J}_{er}$, the phase correction is sufficient to alter the efficiency of the antenna substantially as was discussed earlier. Actually, in the particular cases studied here, the distribution $\mathcal{J}_{RSL}$ is considerably more uniform than either $\mathcal{J}_{er}$ or $\mathcal{J}_{3p}$ and would result in improved gain for this antenna. The reason that an improvement in phase, C_1 to C_2, was obtained while no improvement in amplitude, $\mathcal{J}_{er}$ to $\mathcal{J}_{RSL}$, was found was explained qualitatively in Section I.

The reflector shapes before and after correction are illustrated in Figures 5, 10, 15, 16, 21, and 22. Of particular interest in the cases of the main reflector correction is the small change near $x_2' \sim x_{2m}$ for the option = -1 and the large change when option = +1. Compare Figures 5 and 10 for this effect.

Two factors are worthy of notice in the sub-reflector correction. For smaller k it will be noticed that the corrected sub-reflector, $y_{1n}(x_{1n})$, is contoured so that a great deal of reflected energy is directed towards the upper portion of the main reflector. This is to help correct the large shadow boundary lobe in this region of the main reflector. Notice that a much larger segment of the sub-reflector illuminates the same portion of the main reflector after correction. This effect decreases uniformly as k increases, as is evident from the $k = 16\pi$ and 32π cases, Figures 21 and 22.

In Figure 5 a primary ray trajectory was traced as it was reflected from the sub-reflector and main reflector. The ray trajectory was constructed from numerical data obtained with the machine computed results and it is seen that Snell's law is satisfied at each new reflector.

All the cases discussed above were also analyzed for the case wherein $\mathcal{G}$ is rotated (designated by ROT on the graphs) and these results are similarly illustrated in Figures 24 through 47. The above discussion applies equally to these results in every qualitative respect. While these results may discourage somewhat the hope that a judicious variation of the parameters will lead to both an amplitude and phase

correction, such a parameter study does seem worthwhile since the improvement in antenna performance could be substantial if the study is successful.

Various discontinuities and other minor irregularities on the graphs are explained by accompanying notes for the most part. It is worth noting that these computations taxed almost the complete storage capacity of the IBM 7090 at Berkeley and were very time consuming and hence costly to obtain Computation of all the variables in Section II and those of Chapter 3 where necessary for one value of x_2' consumed approximately fifteen seconds of computer time. Hence relatively minor inaccuracies may be expected due to the computer in addition to the approximations made in the course of the derivations.

The above inaccuracies may give rise to the result that $\mathcal{D}_{RSL}$ does not appear to converge to $\mathcal{D}_{3p}$ for very small ϑ_{3en}, whereas $\mathcal{D}_{er}$ does converge (comparatively) to $\mathcal{D}_{3p}$ for small ϑ_{3e}. This may be due to the accuracy obtained or to the possibility that no exact solution exists. If an exact solution does not exist, then an iterative solution of this type will never converge precisely.

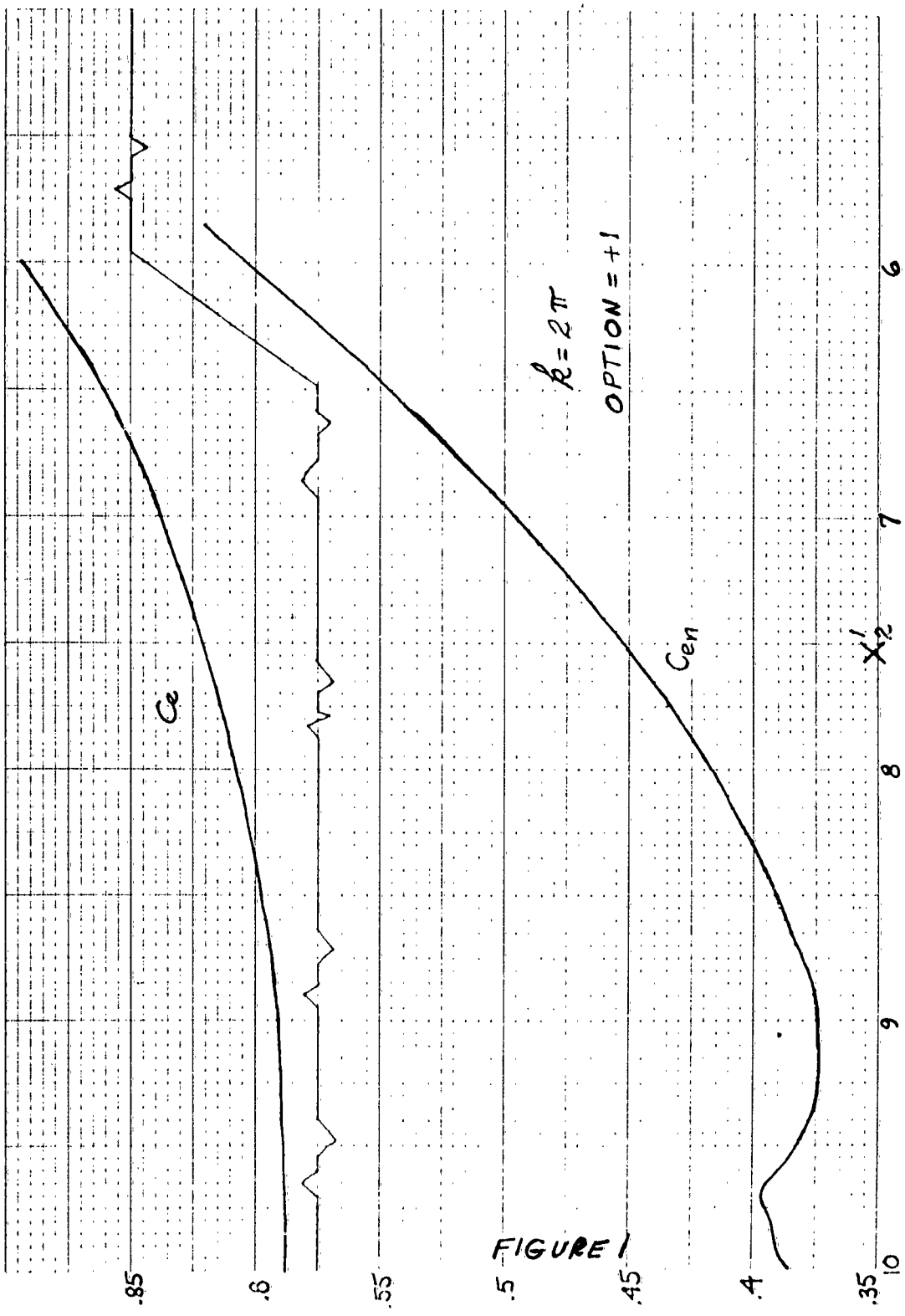

FIGURE 1

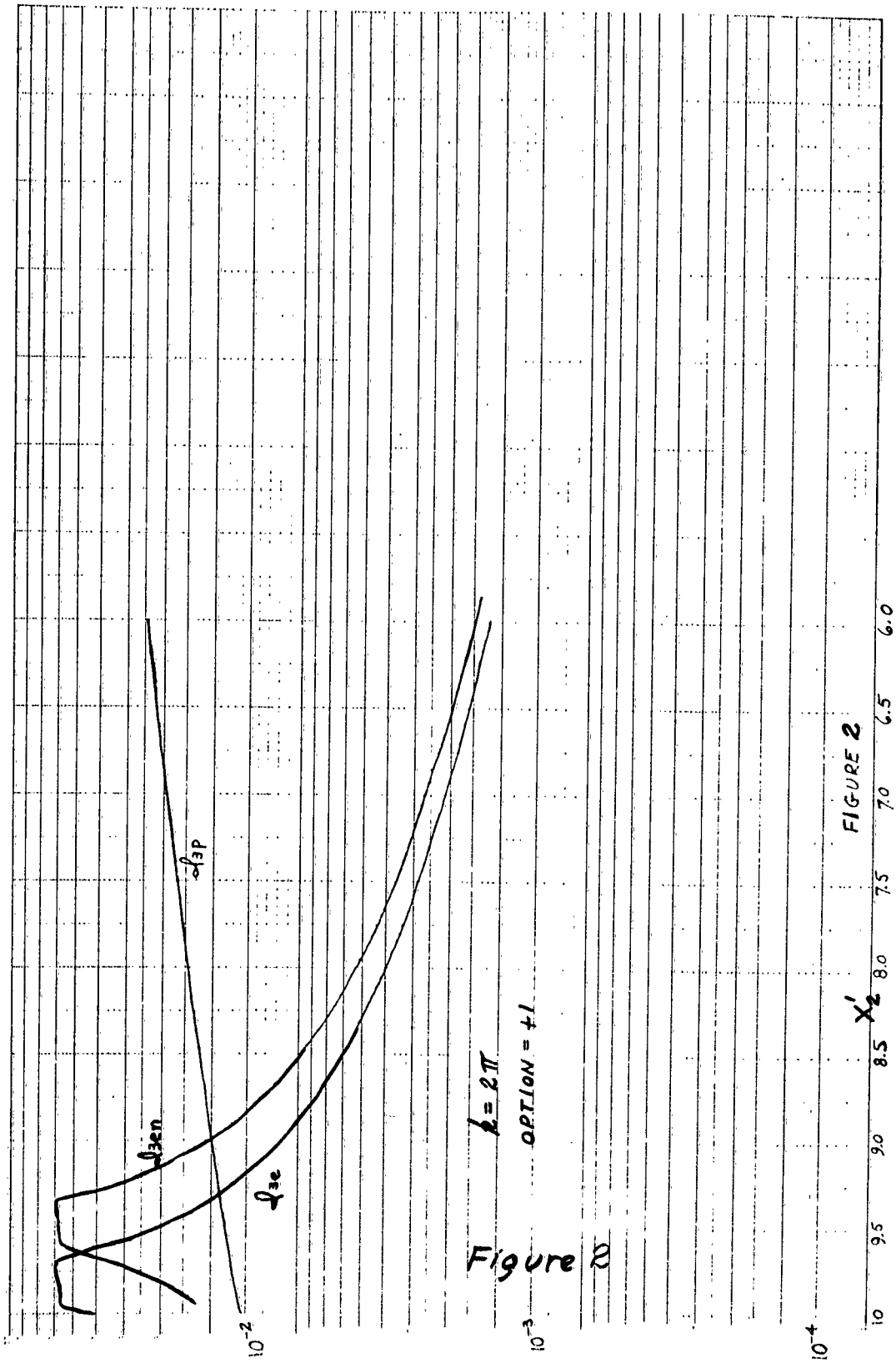

Figure 2

FIGURE 2

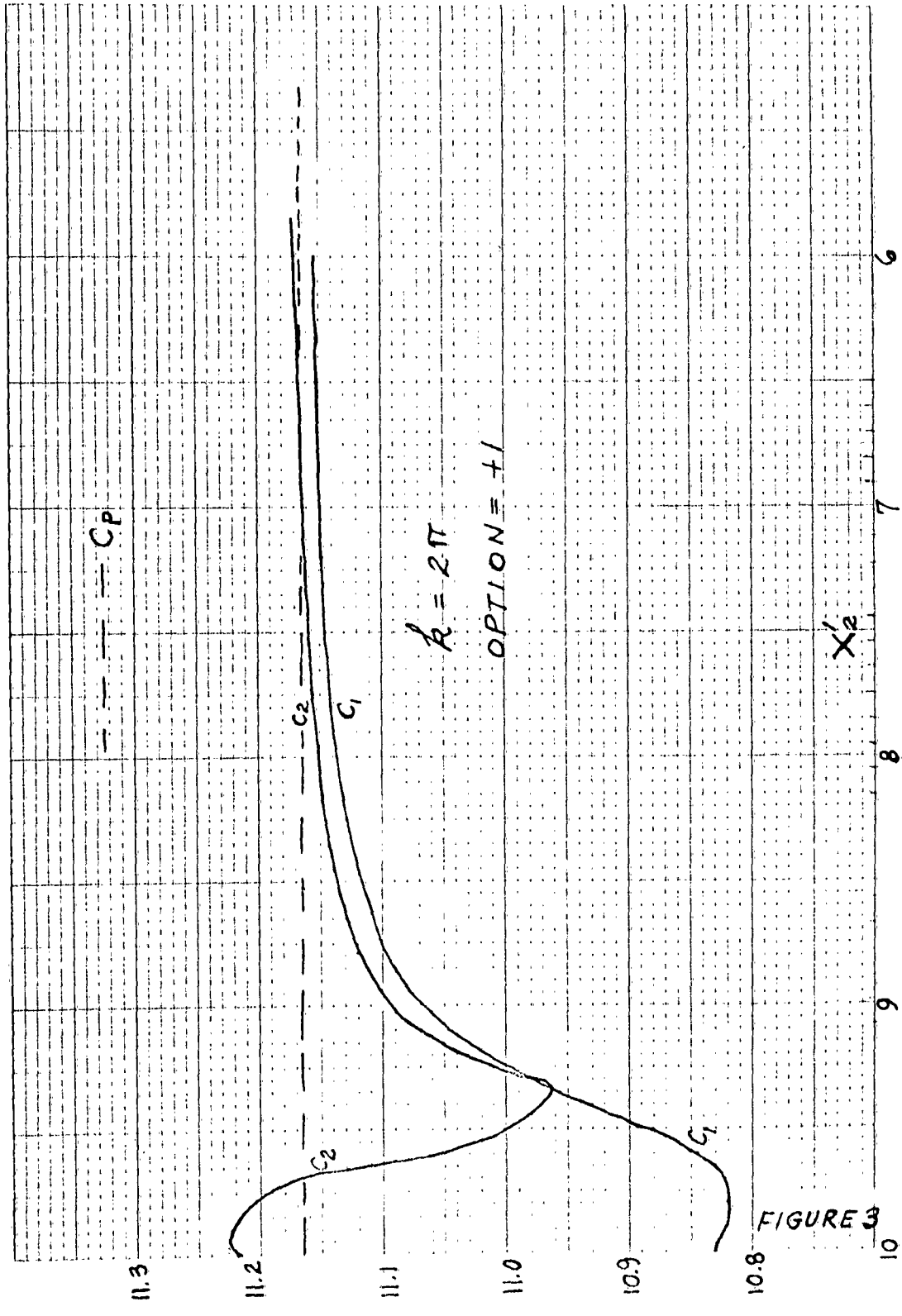

FIGURE 3

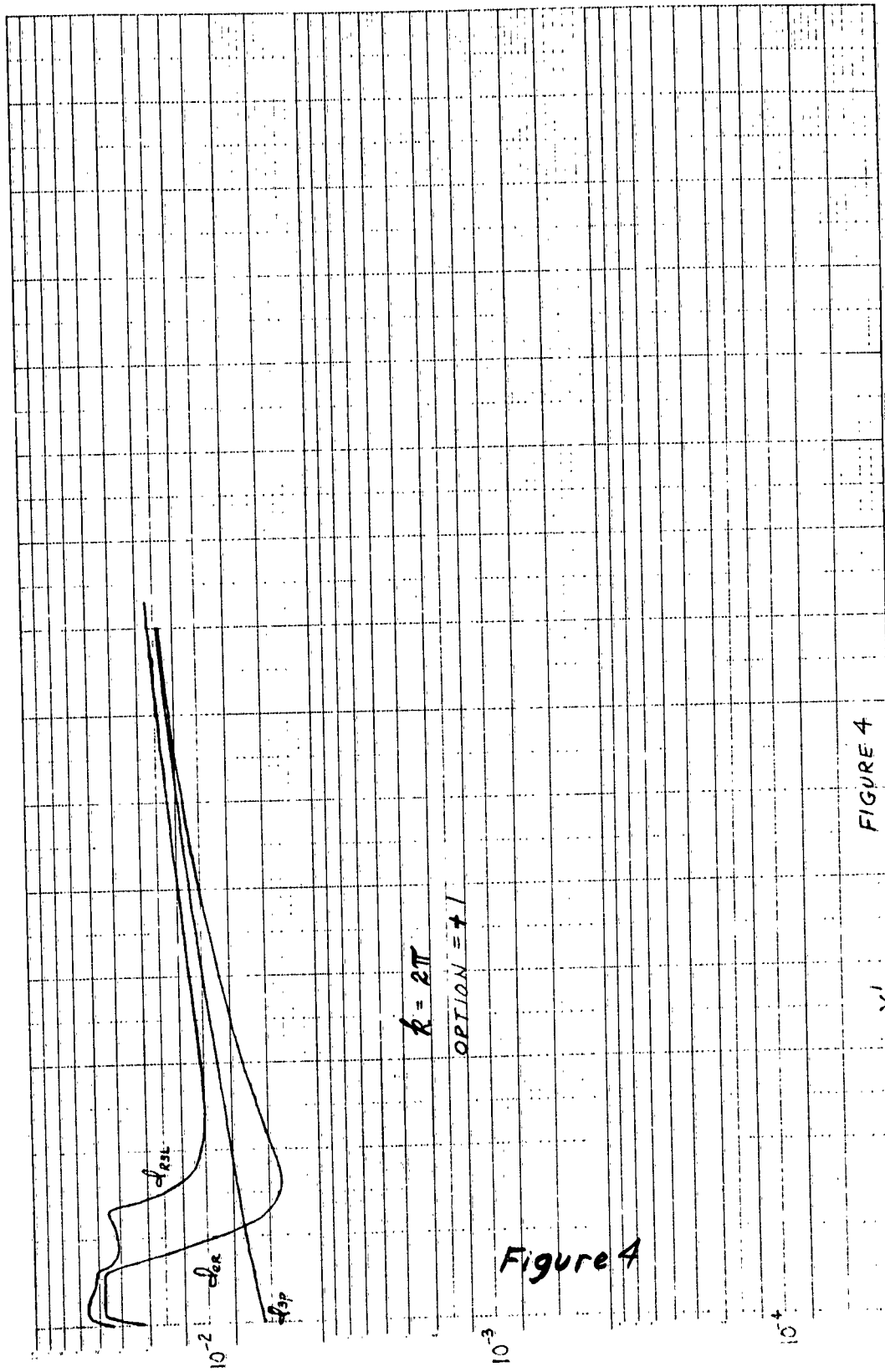

Figure 4

FIGURE 4

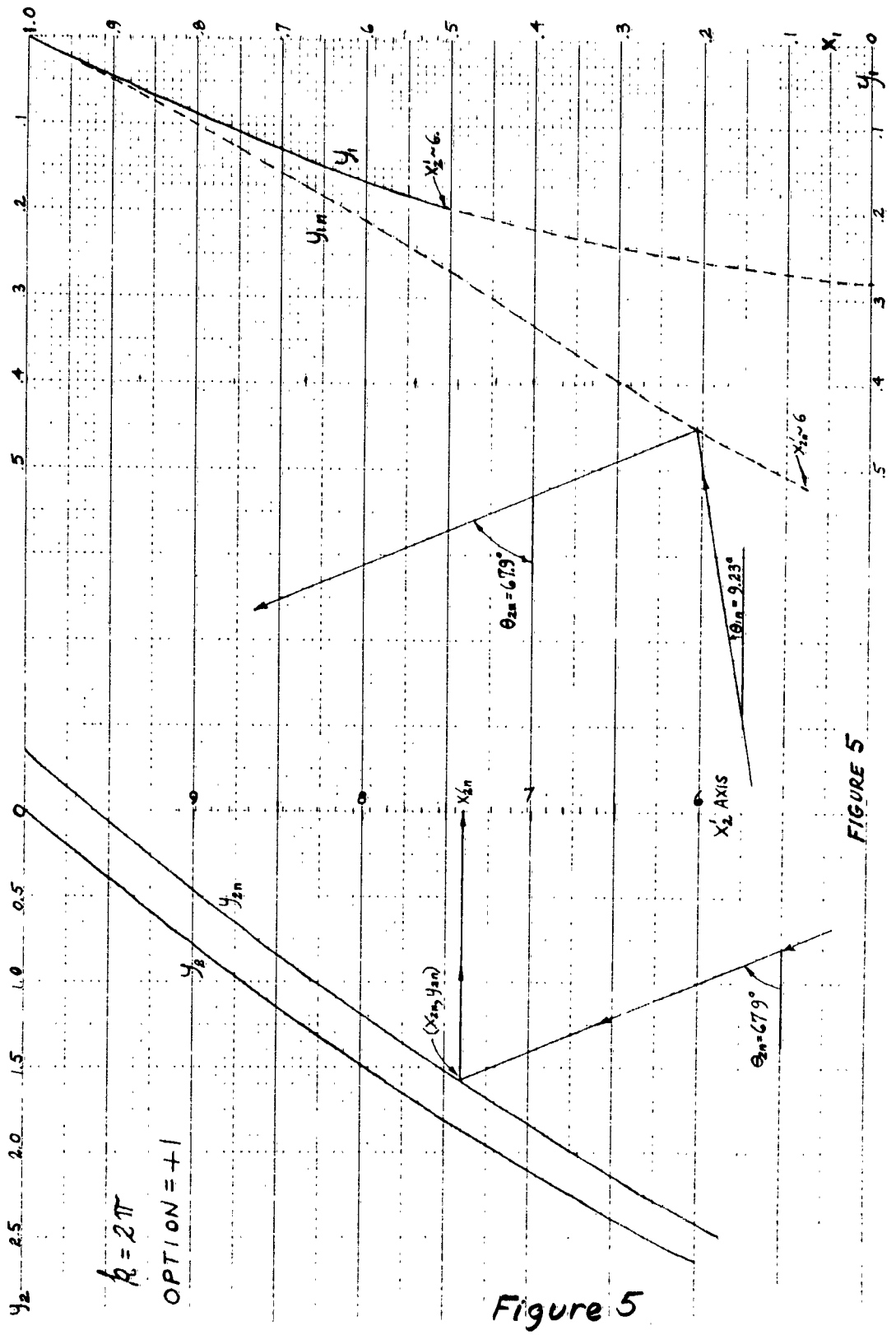

Figure 5

FIGURE 5

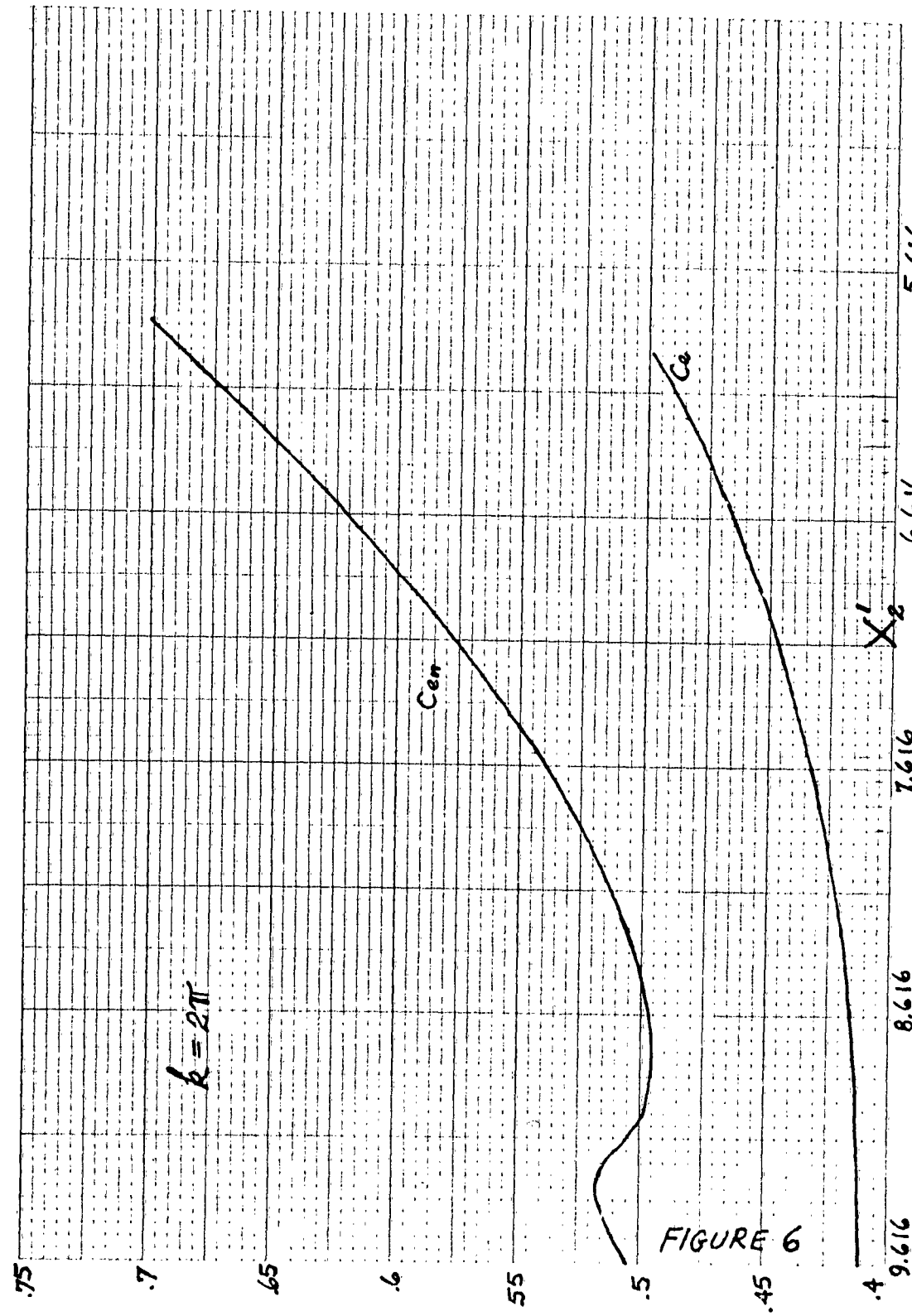

FIGURE 6

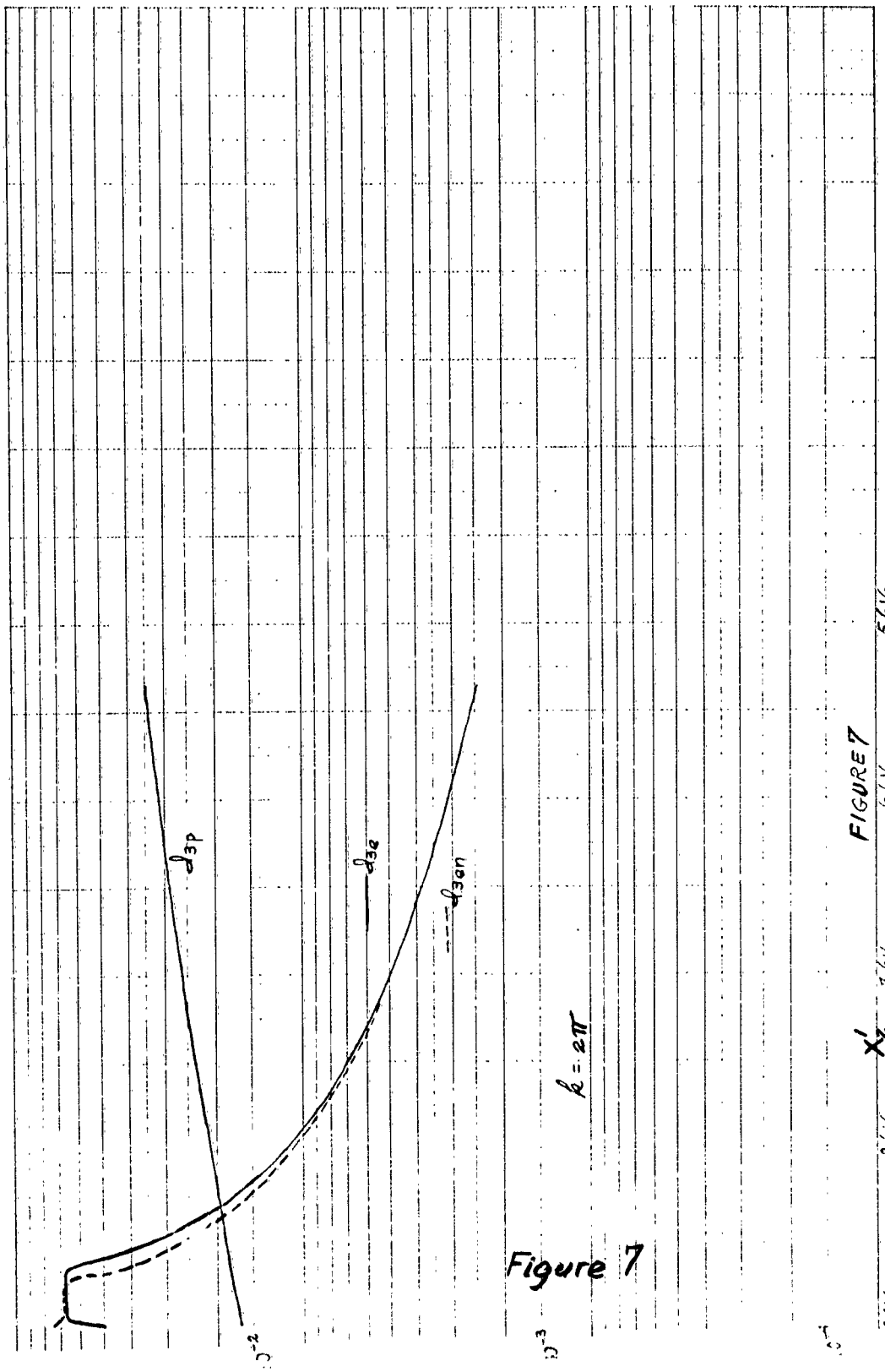
J_{3P}
J_{3a}
J_{3an}
$k = 2\pi$
X'_2
FIGURE 7
Figure 7

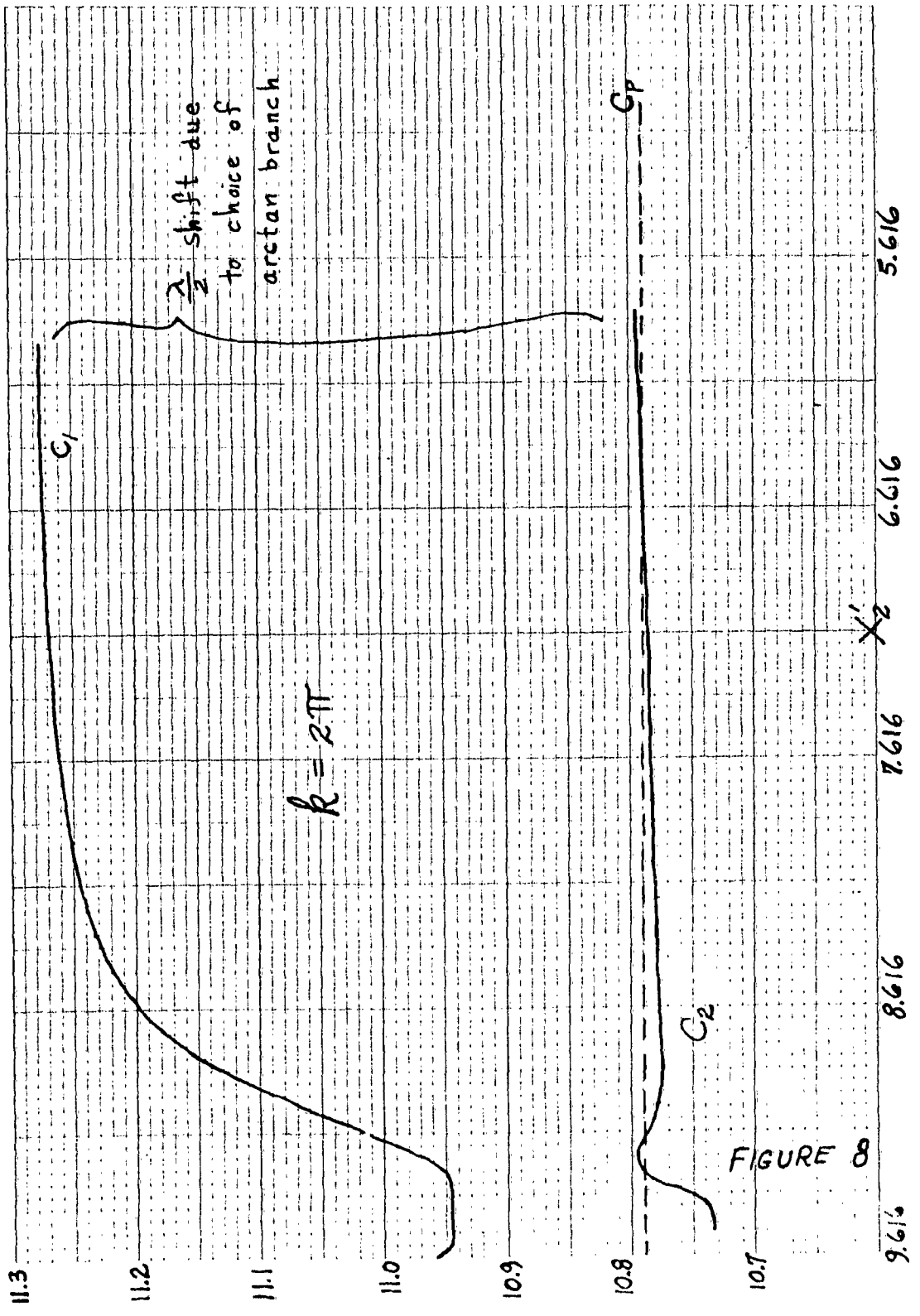
11.3
11.2
11.1
11.0
10.9
10.8
10.7
9.616
8.616
7.616
6.616
5.616
X'2
C1
C2
CP
λ/2 shift due to choice of arctan branch
R=2π

FIGURE 8

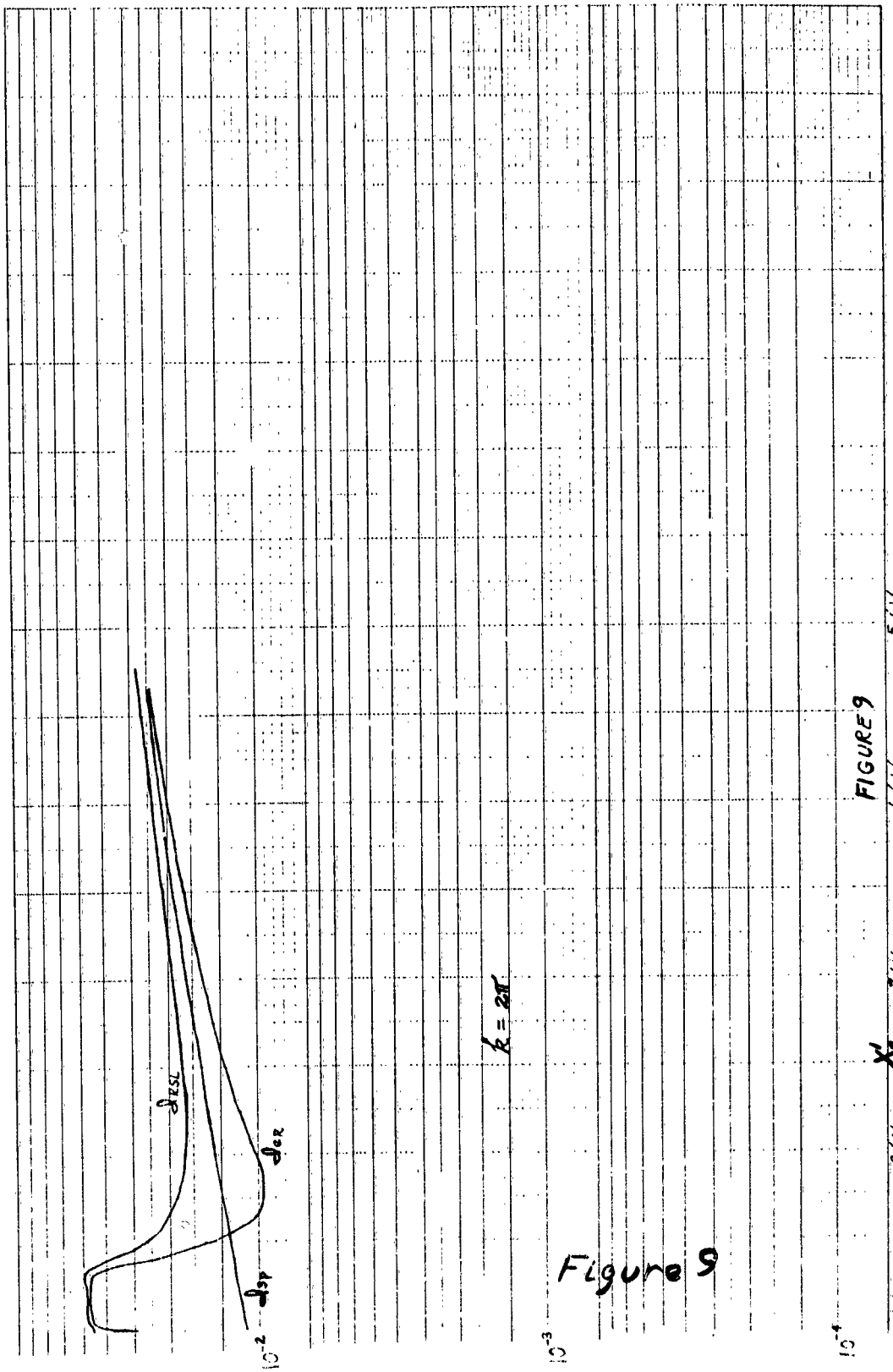

FIGURE 9

Figure 9

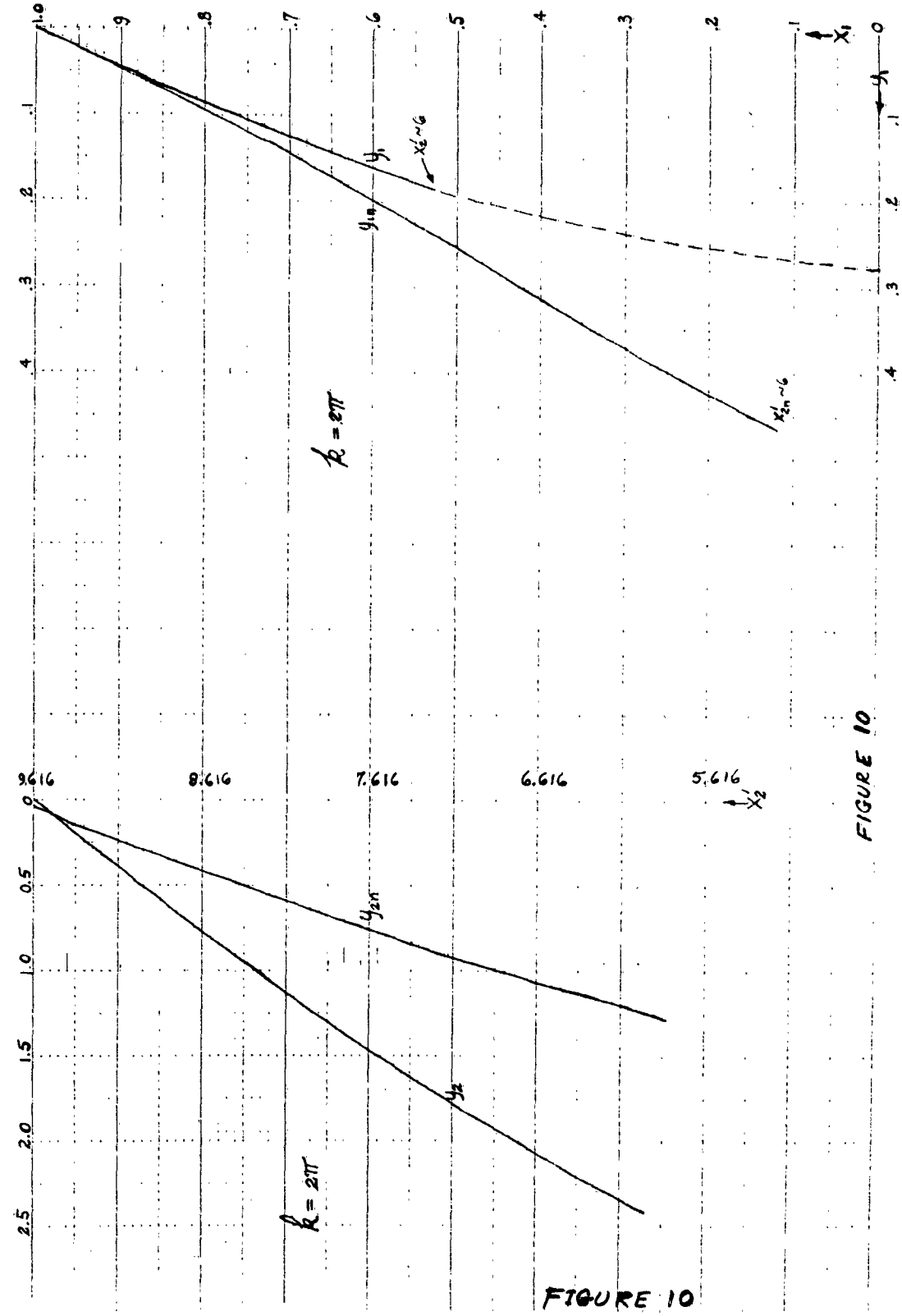

FIGURE 10

FIGURE 10

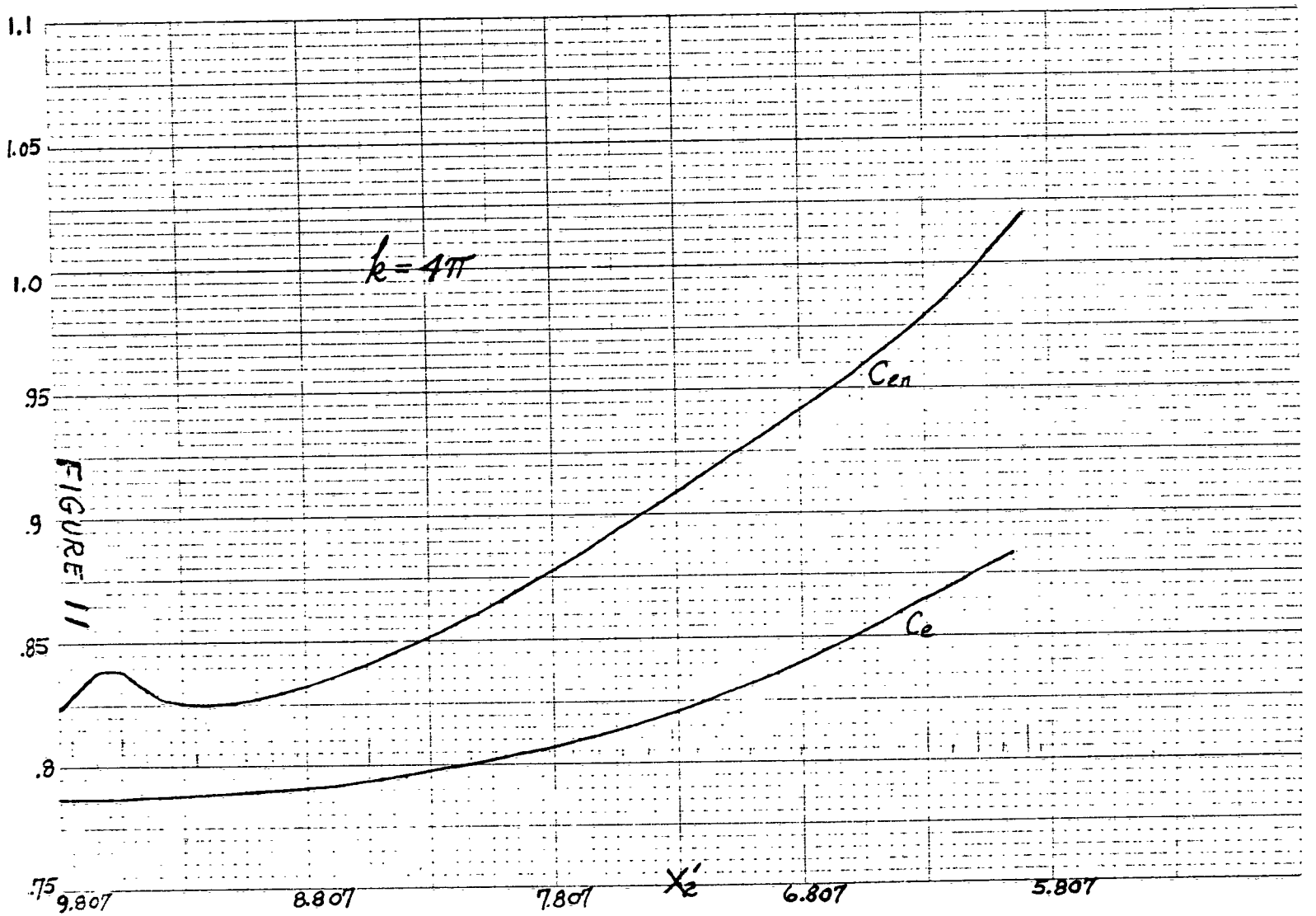

FIGURE 11

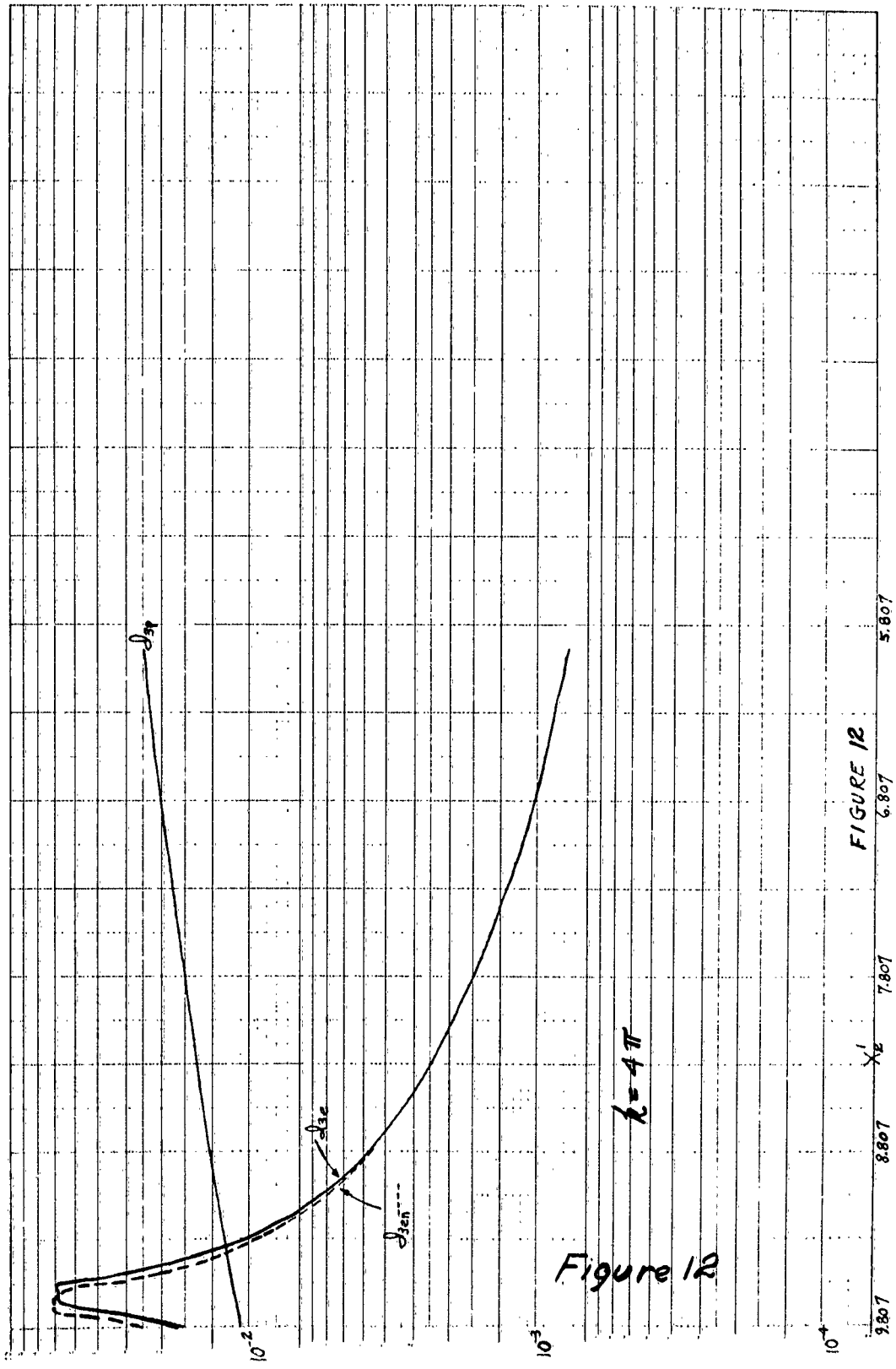
J_{3T}
J_{3E}
J_{3EN}
10^{-2}
10^{-3}
10^{-4}
9.807
8.807
7.807
6.807
5.807
X_2
FIGURE 12
$k = 4\pi$

Figure 12

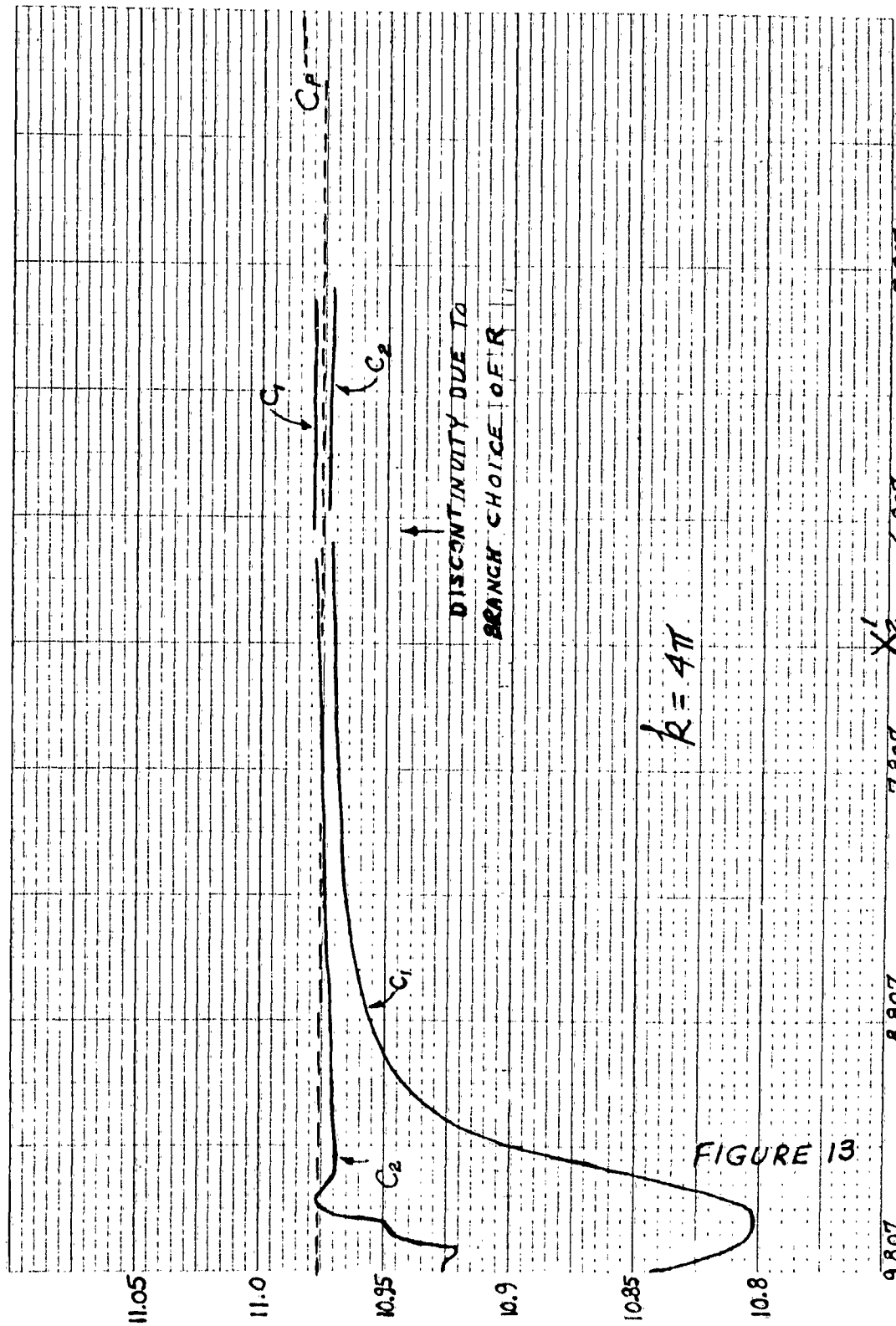
11.05
11.0
10.95
10.9
10.85
10.8
9.807
8.807
7.807
6.807
5.807
X_2'
C_P
C_1
C_2
C_1
C_2
DISCONTINUITY DUE TO
BRANCH CHOICE OF R
$R = 4\pi$

FIGURE 13

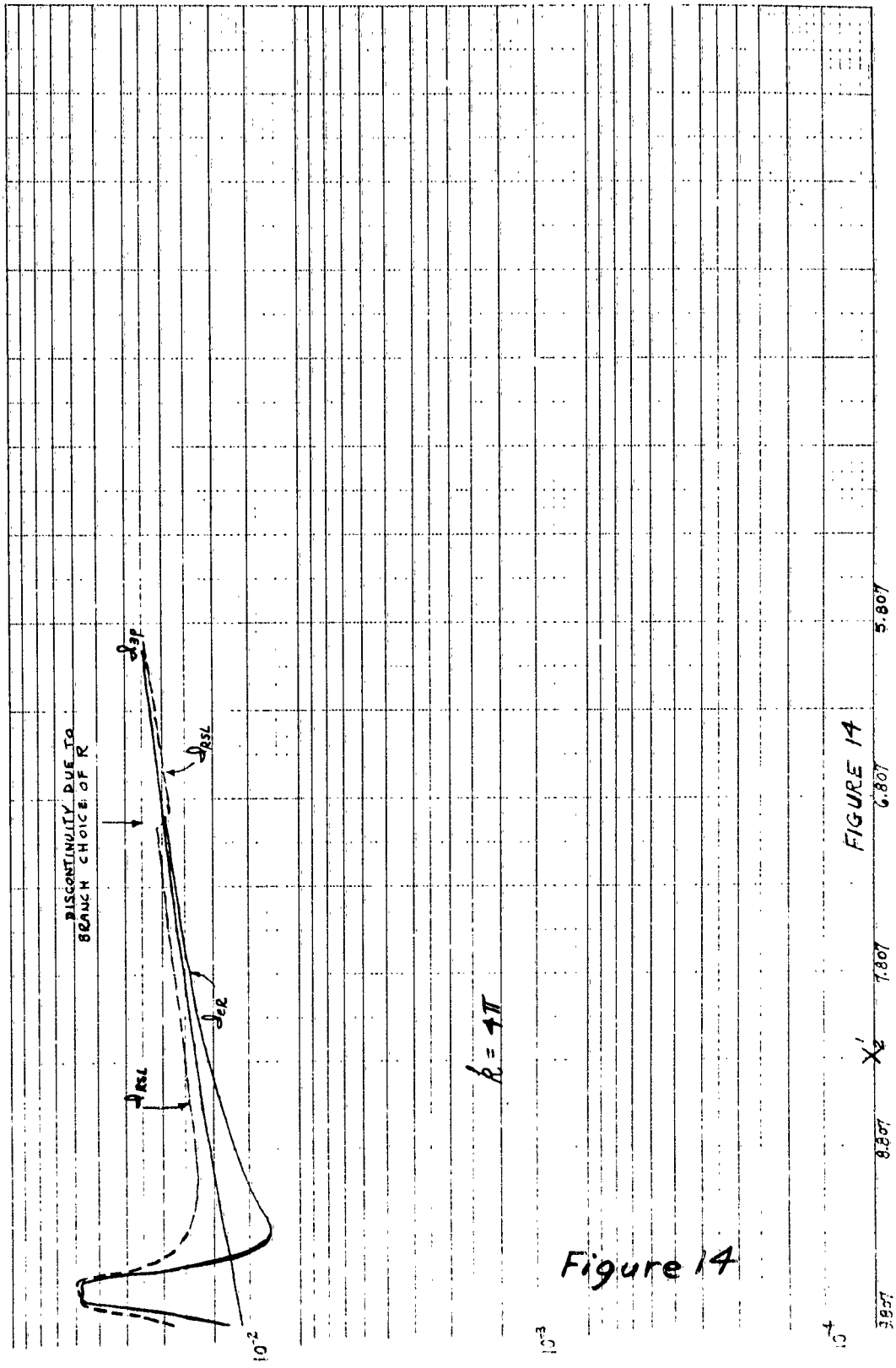
DISCONTINUITY DUE TO
BRANCH CHOICE OF R
δ_{RSL}
δ_{e2}
δ_{RSL}
δ_{e2}
10^{-2}
10^{-3}
10^{-4}
$k = 1T$
8.80T
7.80T
6.80T
5.80T
X_2'
FIGURE 14

Figure 14

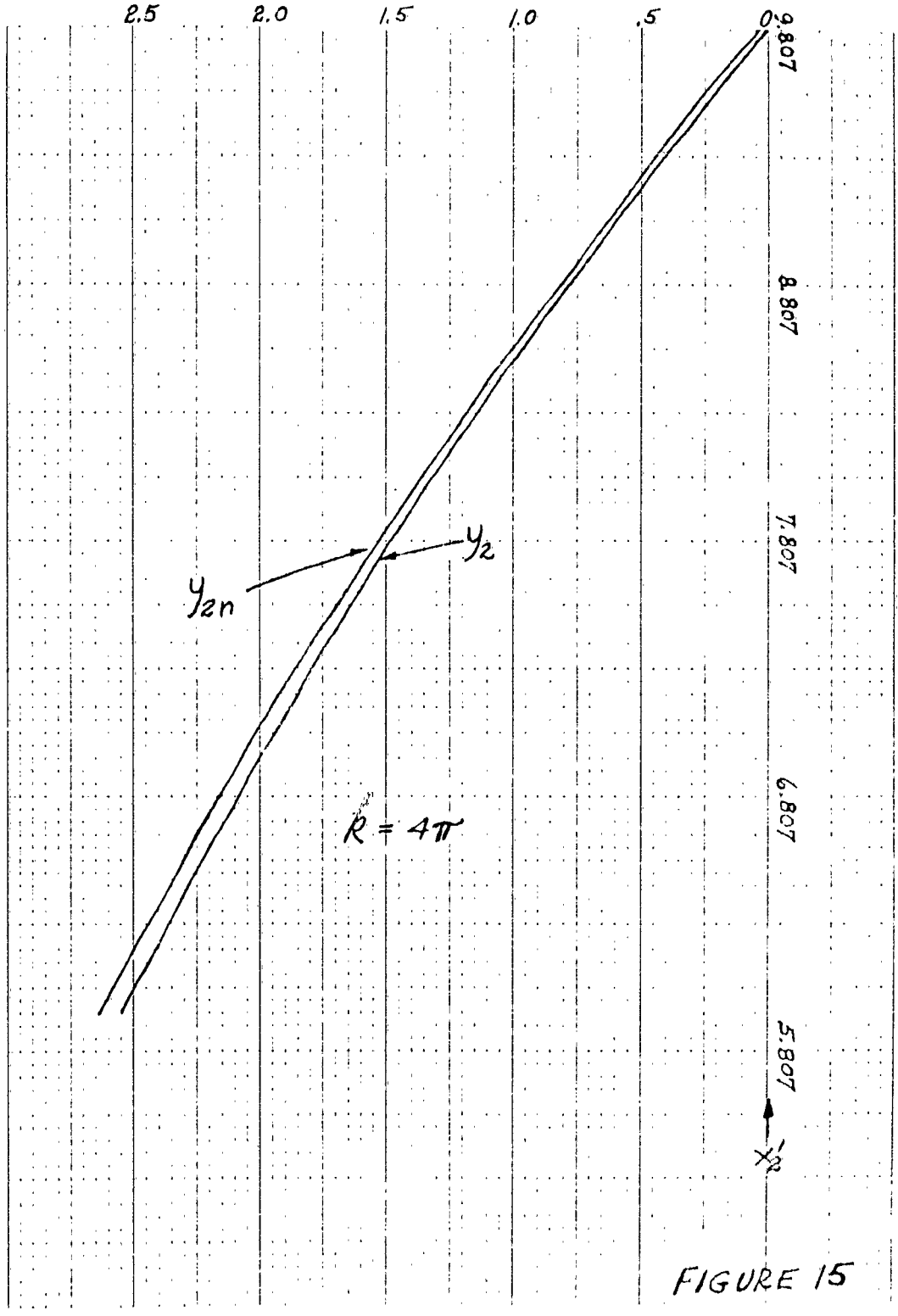

FIGURE 15

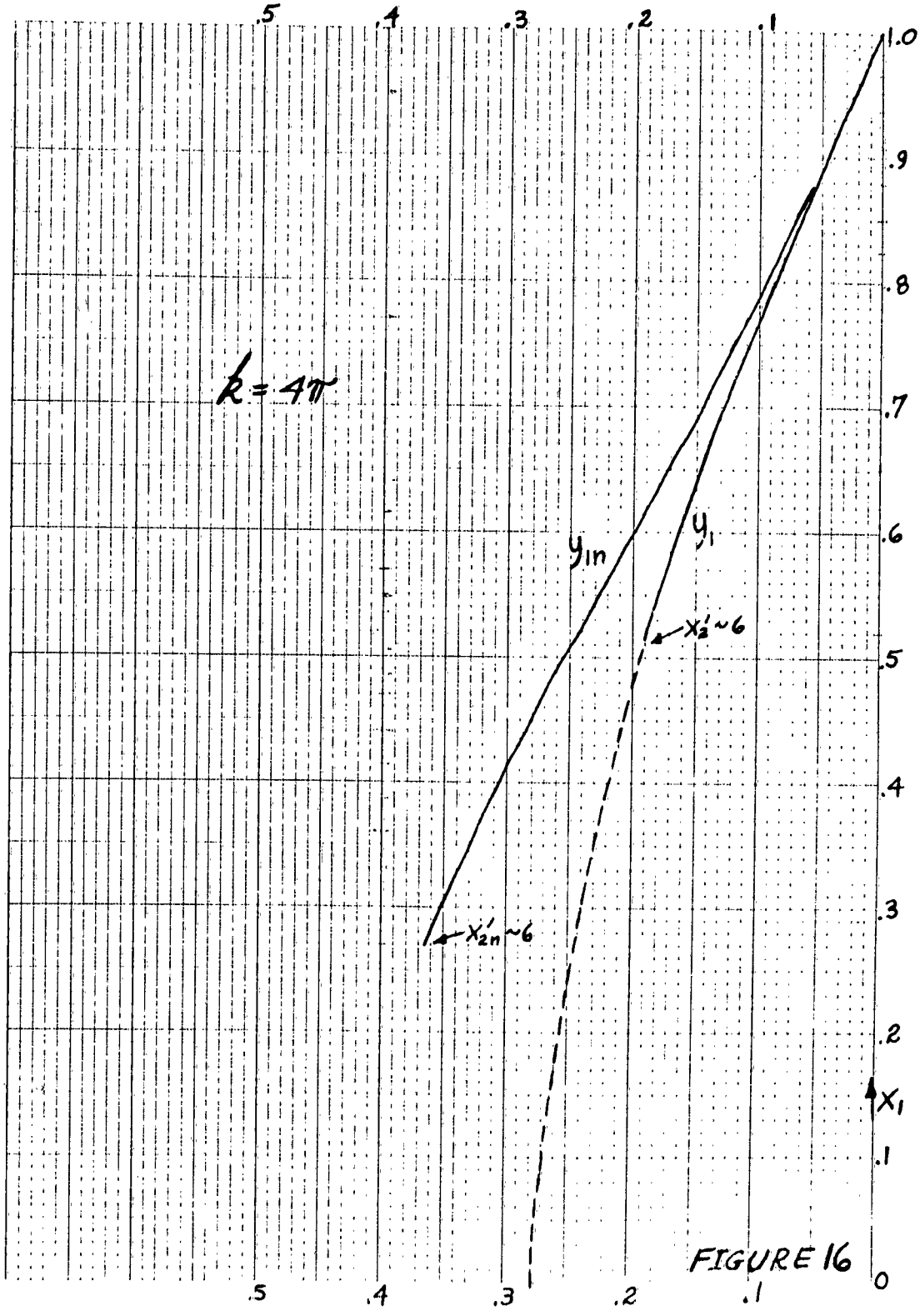

FIGURE 16

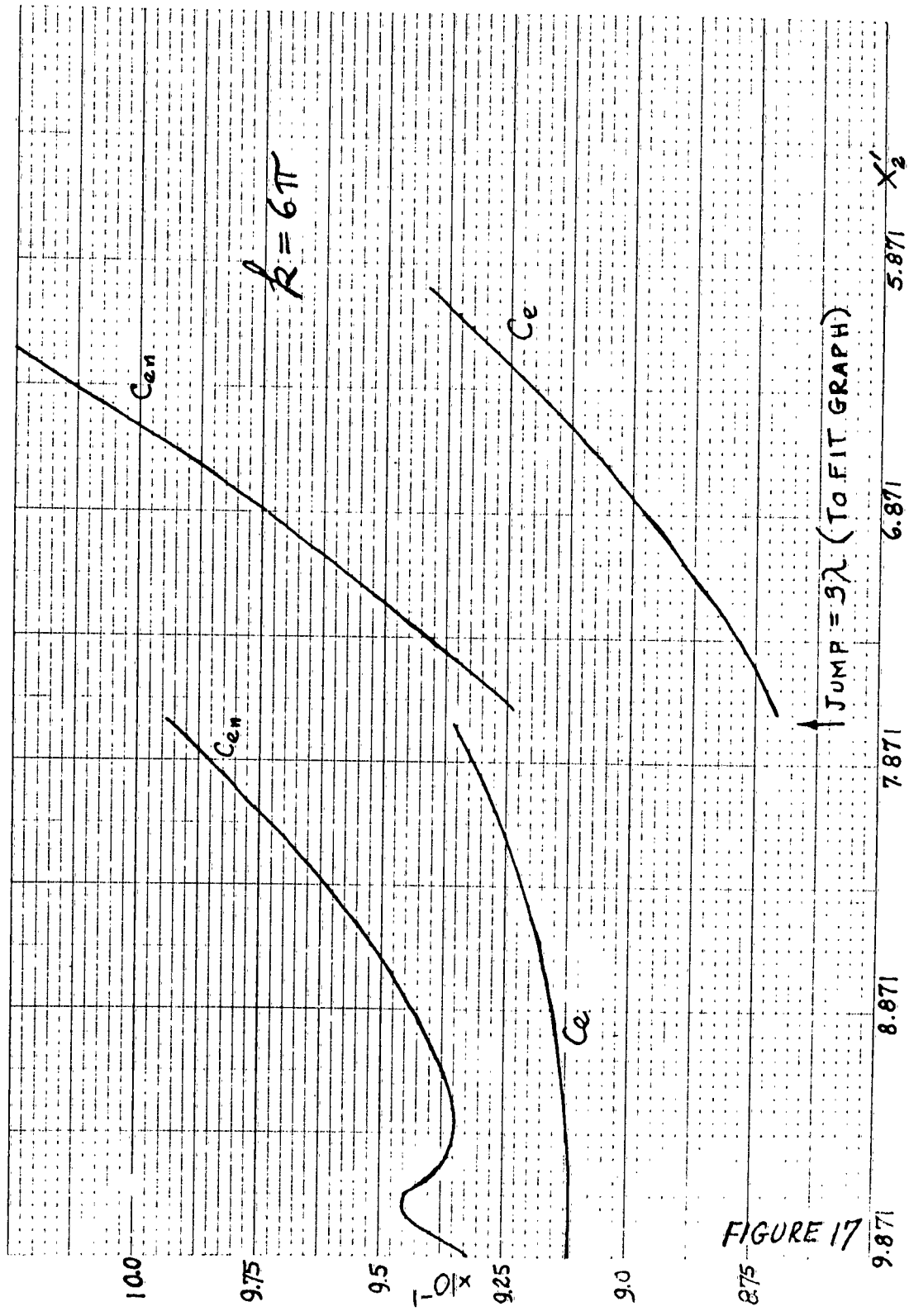
$R = 6\pi$
C_{en}
C_{en}
C_e
C_e
JUMP = 3λ (TO FIT GRAPH)
10.0
9.75
9.5
9.25
9.0
8.75
$\frac{1}{x} - 0$
5.871
6.871
7.871
8.871
9.871
x_2'

FIGURE 17

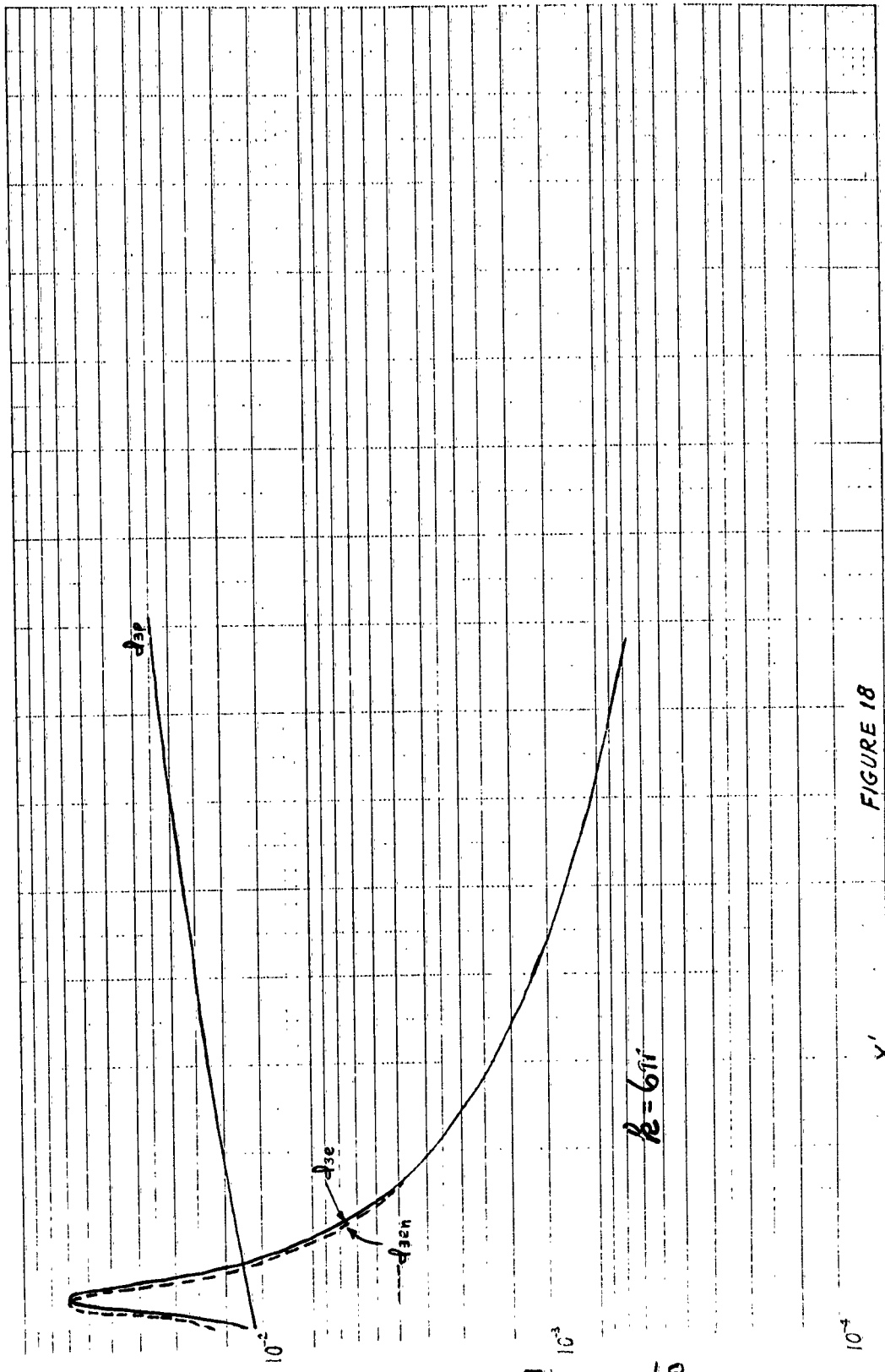

Figure 18

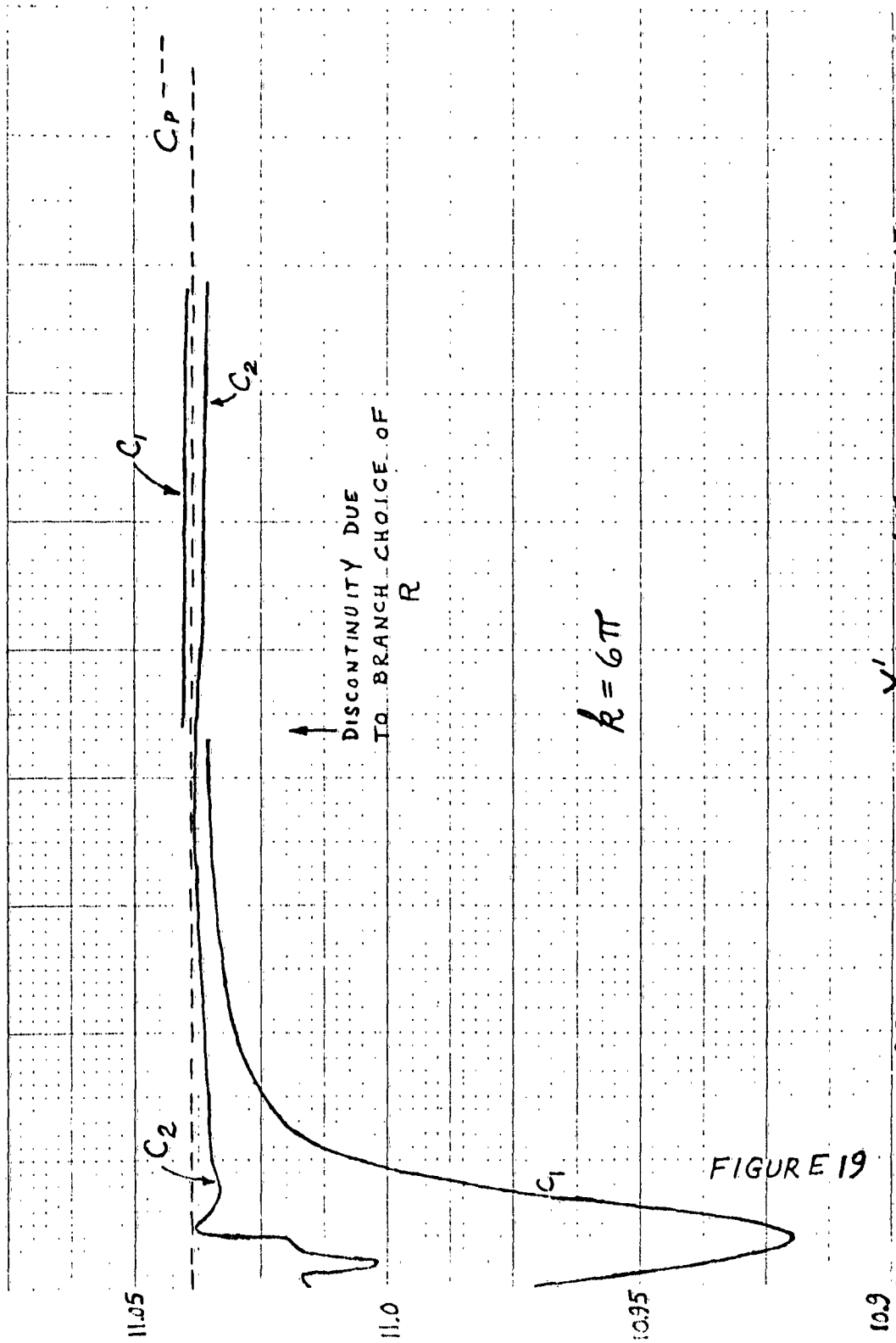
C_P
C_1
C_2
C_2
C_1
DISCONTINUITY DUE
TO BRANCH CHOICE OF
R
$k = 6\pi$
11.05
11.0
10.35
10.3
9.871
8.871
7.871
X_2'
6.871
5.871

FIGURE 19

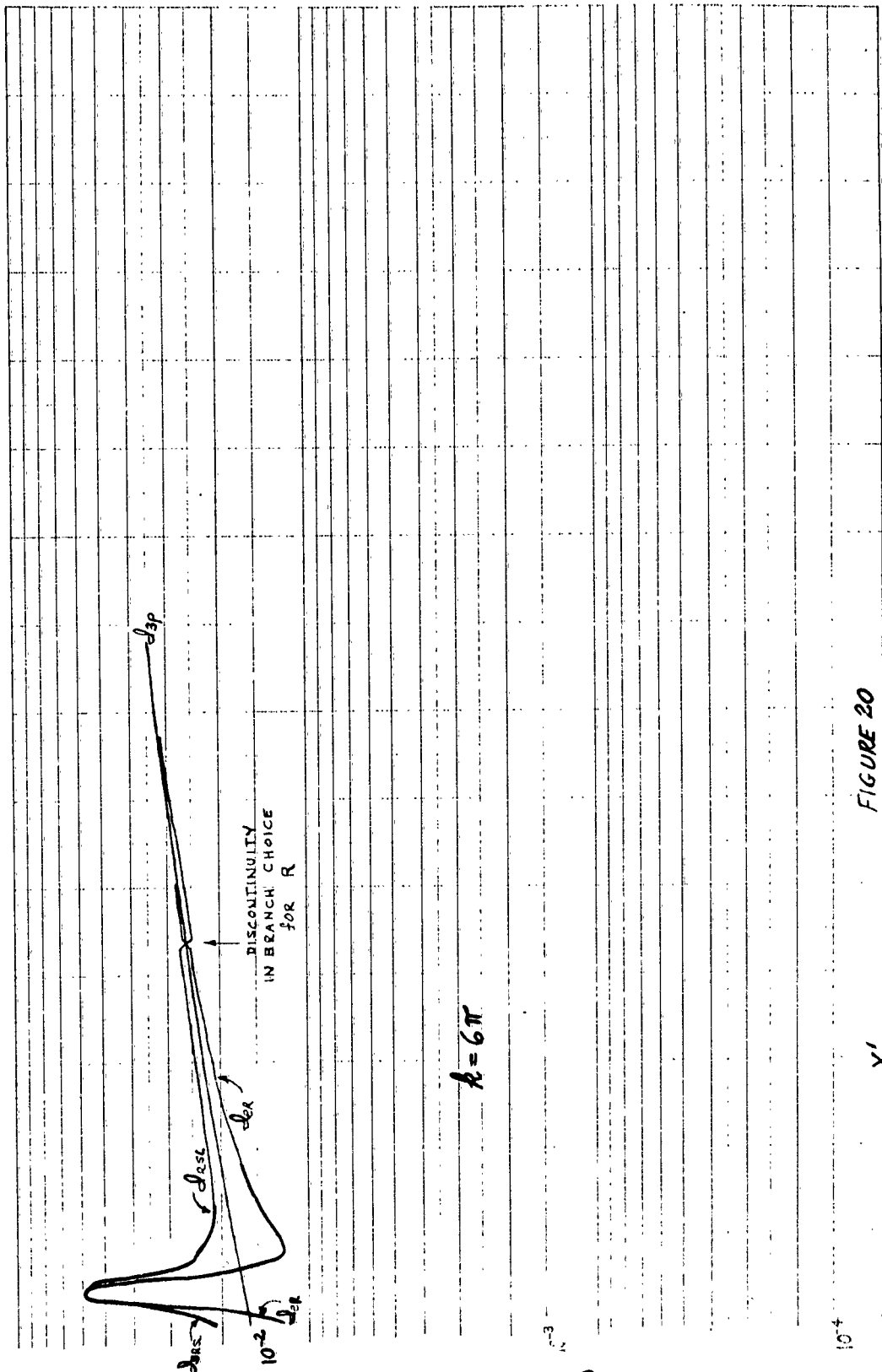
DISCONTINUITY
IN BRANCH CHOICE
FOR R
$k = 6\pi$
10^{-2}
10^{-3}
10^{-4}
3.871
8.871
7.871
6.871
5.871
X_2'
FIGURE 20

Figure 20

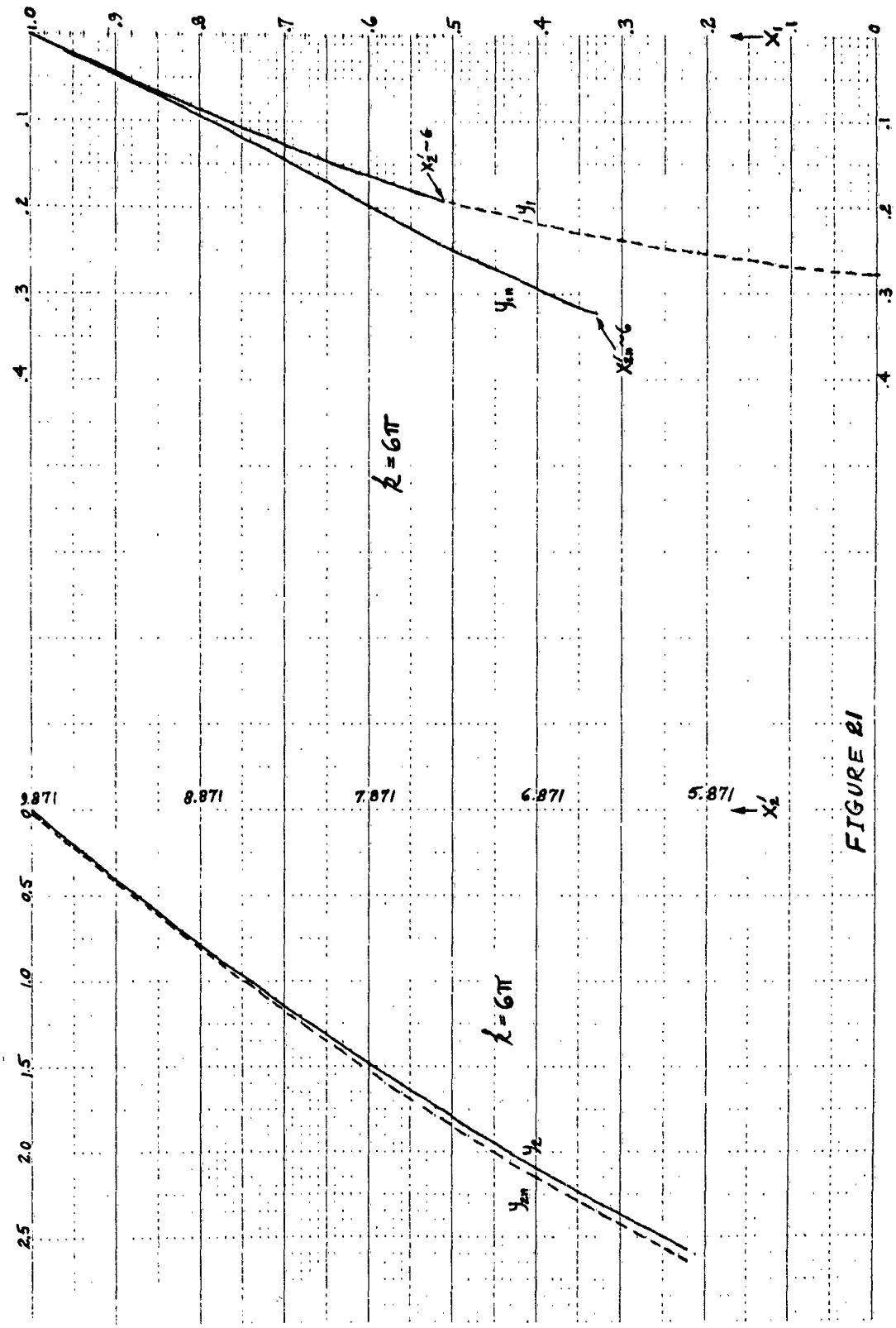
1.0
.9
.8
.7
.6
.5
.4
.3
.2
.1
0
x_1
$x_2'=6$
y_1
y_{1n}
$x_{2n}=6$
$\lambda=6\pi$
9.871
8.871
7.871
6.871
5.871
x_2'
FIGURE 21
0.5
1.0
1.5
2.0
2.5
$\lambda=6\pi$
y_2
y_{2n}

Figure 21

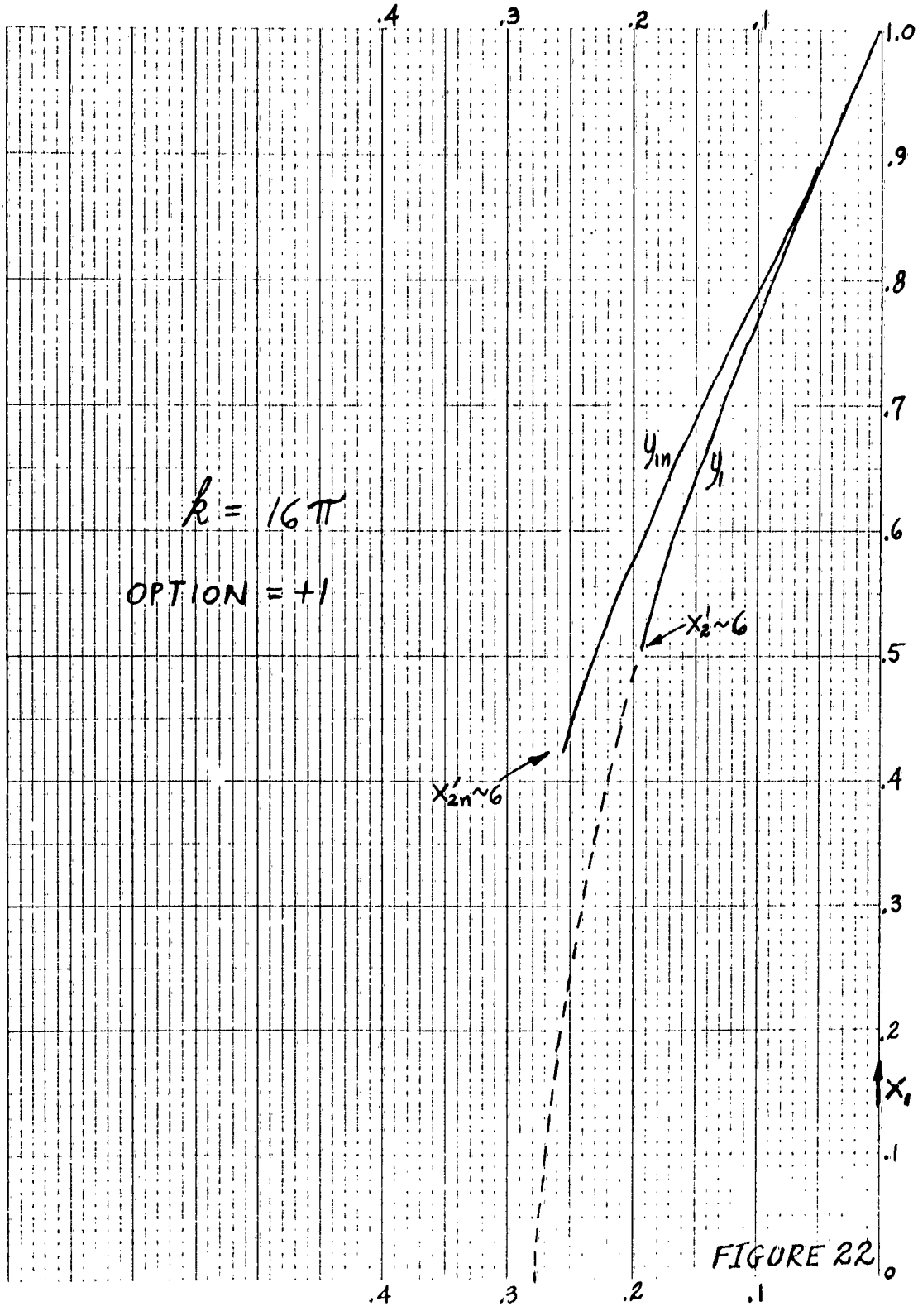

FIGURE 22

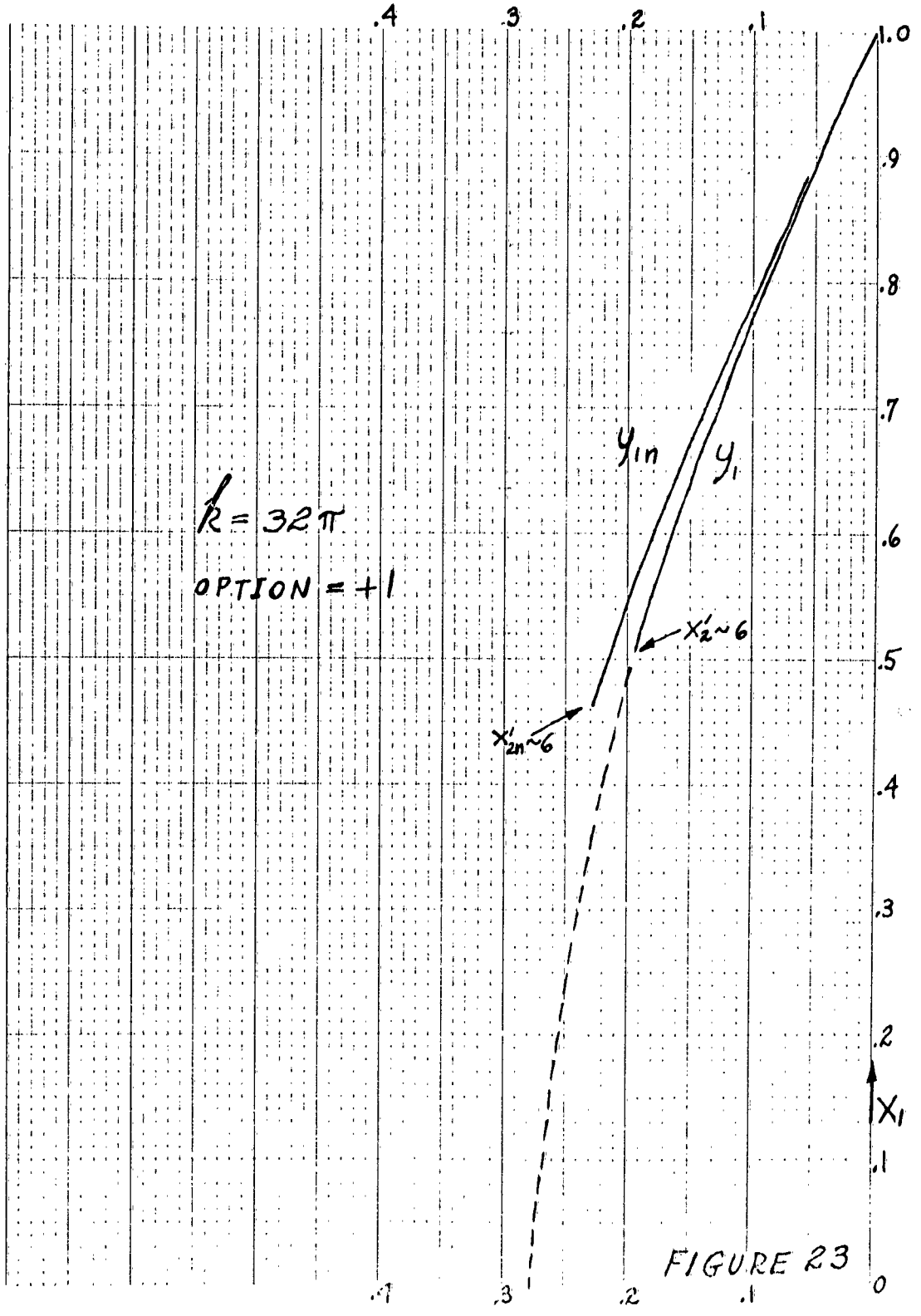

FIGURE 23

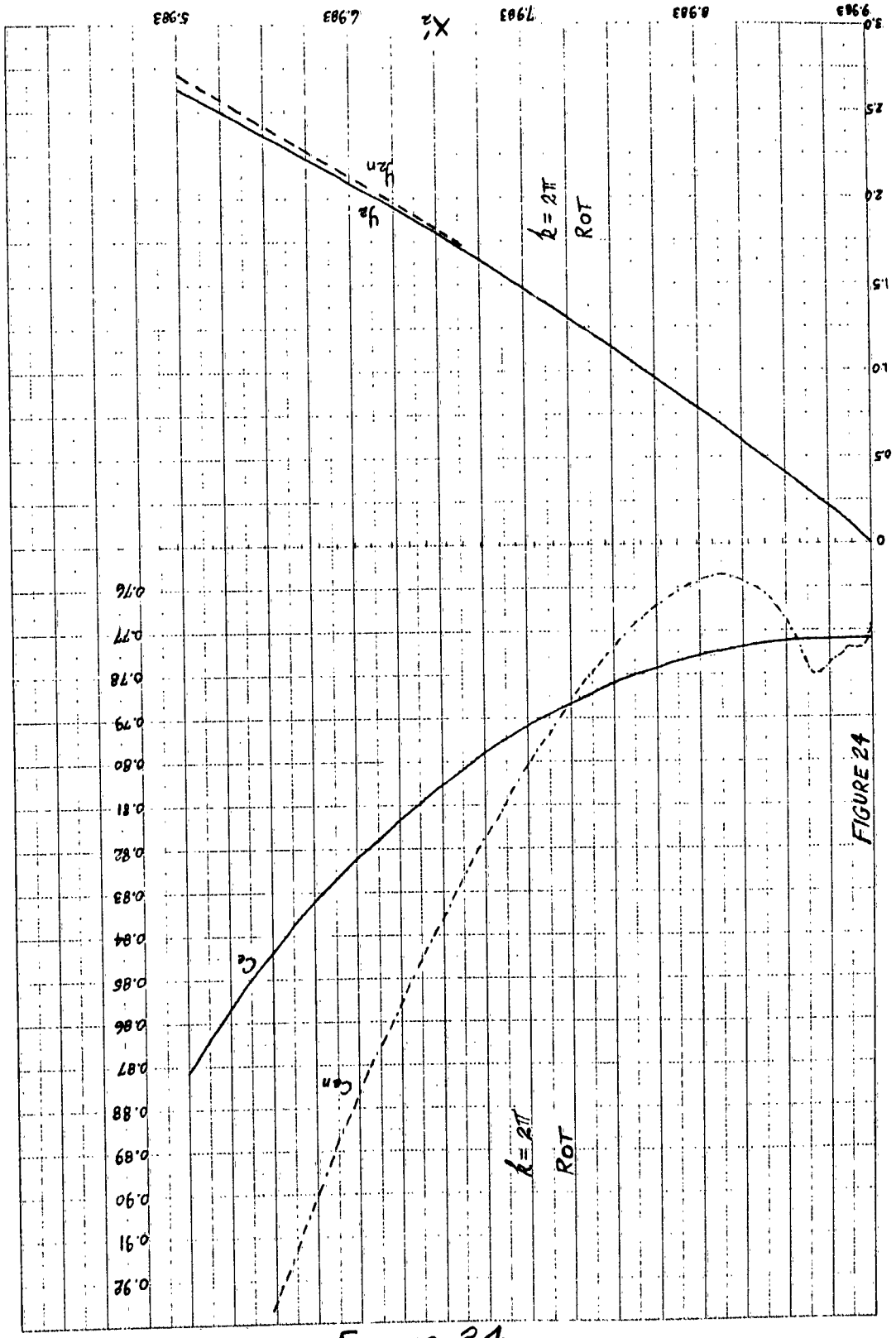
X'2
5.983
6.983
7.983
8.983
9.983
3.0
2.5
2.0
1.5
1.0
0.5
0
μ_{2n}
μ_2
$k = 2\pi$
ROT
C_n
C_2
$k = 2\pi$
ROT
0.76
0.77
0.78
0.79
0.80
0.81
0.82
0.83
0.84
0.86
0.86
0.87
0.88
0.89
0.90
0.91
0.92
FIGURE 24

Figure 24

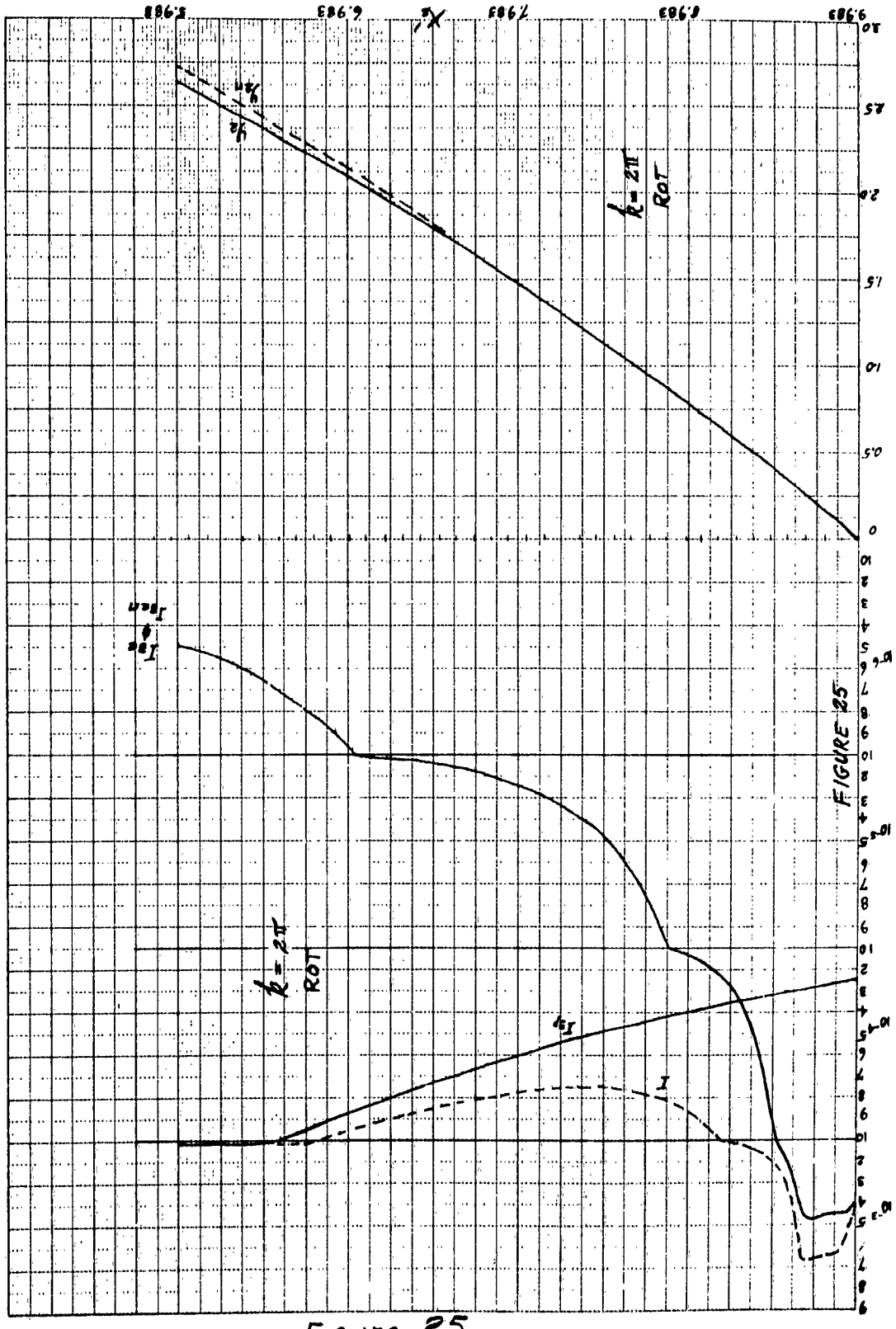

Figure 25

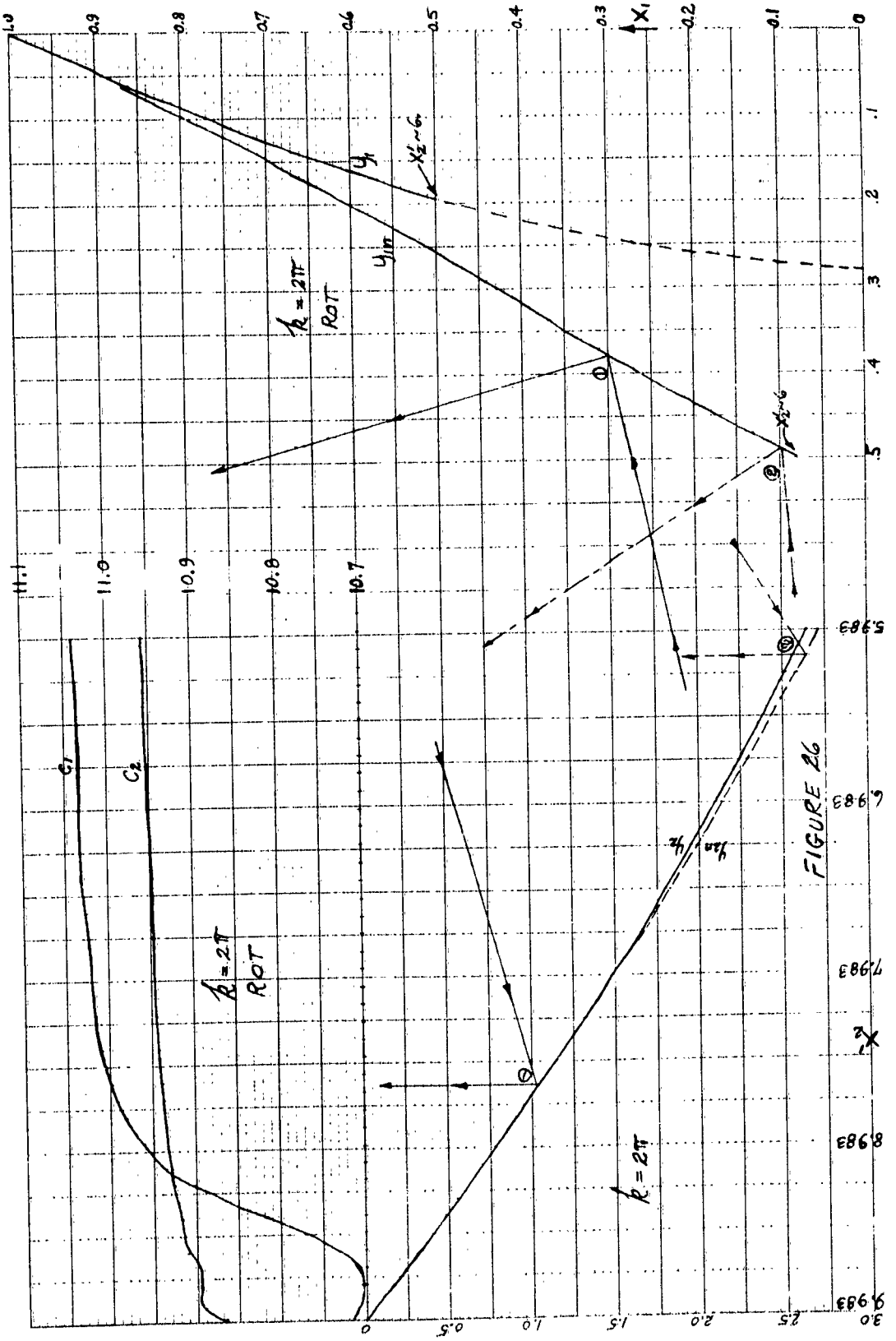
FIGURE 26
C_1
C_2
$k = 2\pi$ ROT
$k = 2\pi$ ROT
$k = 2\pi$
y_{in}
y_{an}
X_1
X_2
$X_2' \sim 6$
11.1
11.0
10.9
10.8
10.7
1.0
0.9
0.8
0.7
0.6
0.5
0.4
0.3
0.2
0.1
0
.1
.2
.3
.4
.5
5.983
6.983
7.983
8.983
9.983
0
0.5
1.0
1.5
2.0
2.5
3.0

Figure 26

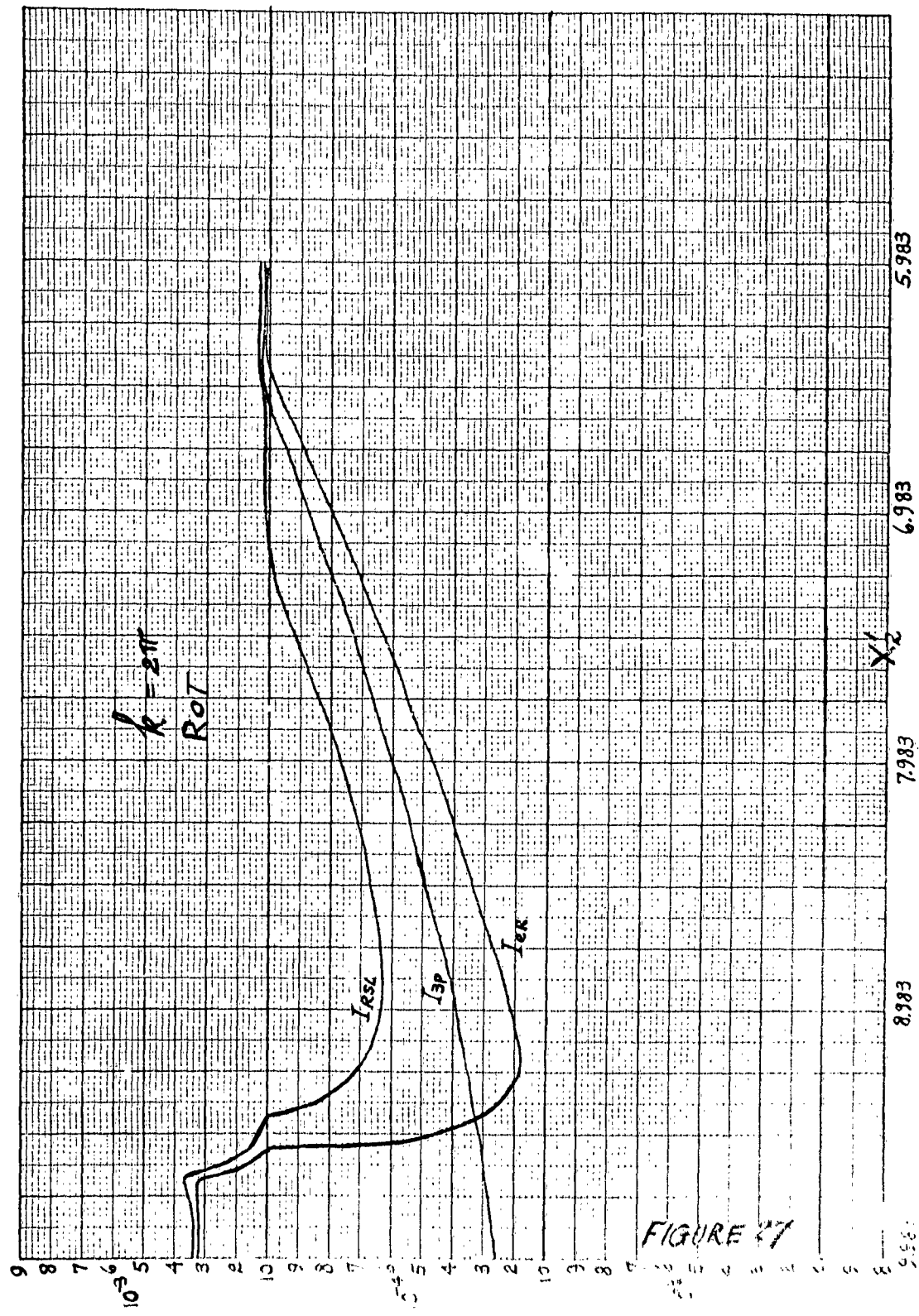

FIGURE 27

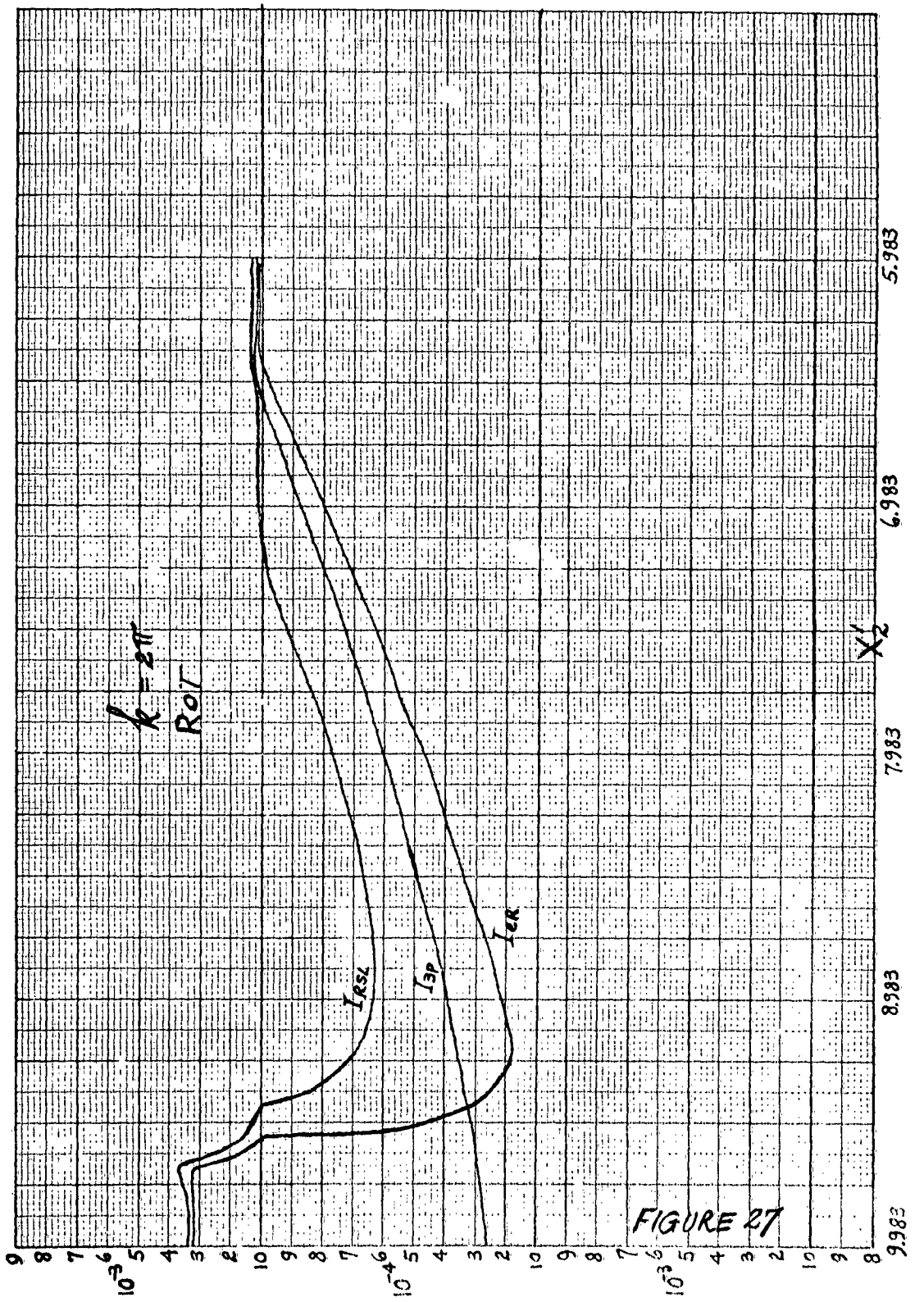

FIGURE 27

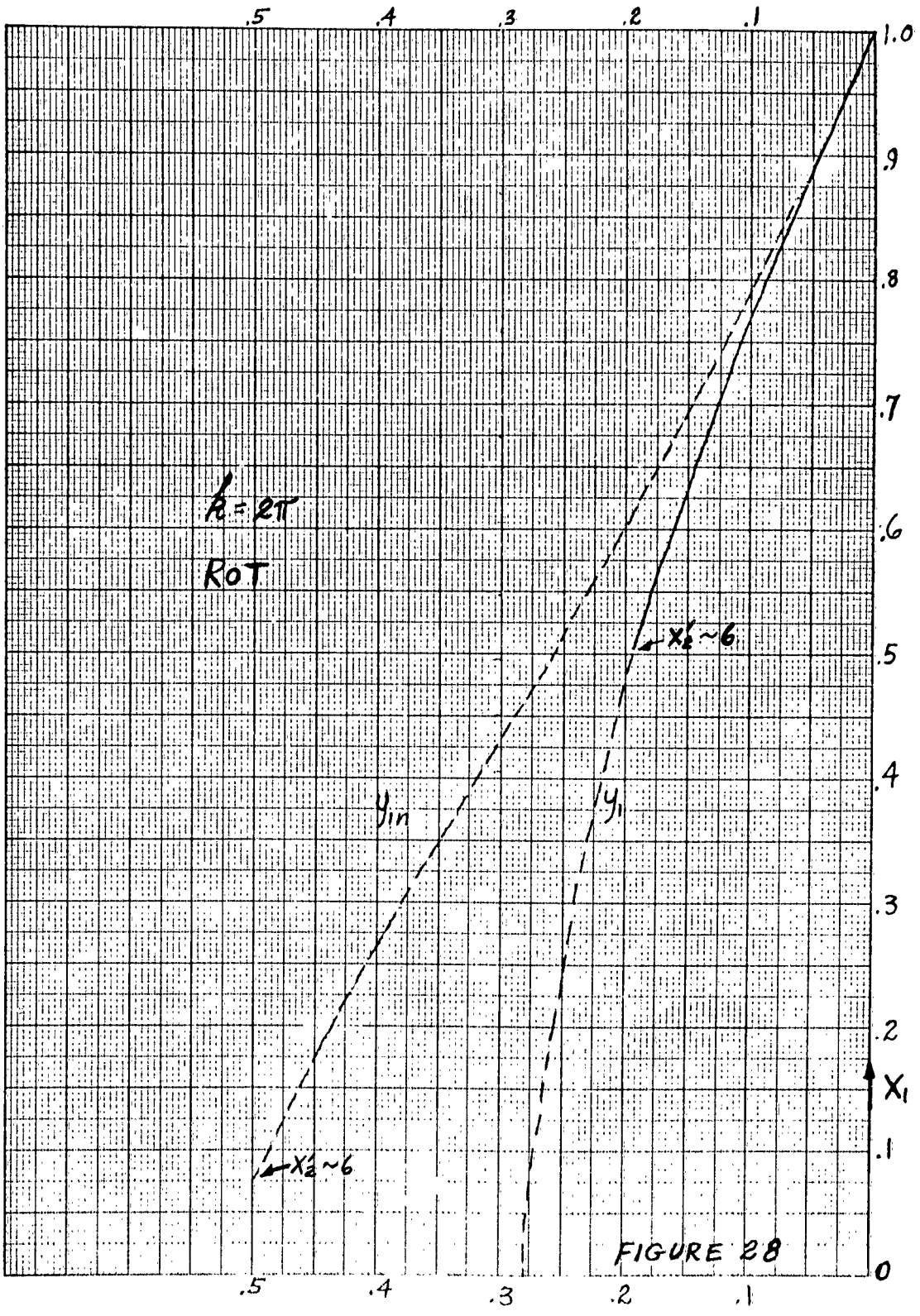

FIGURE 28

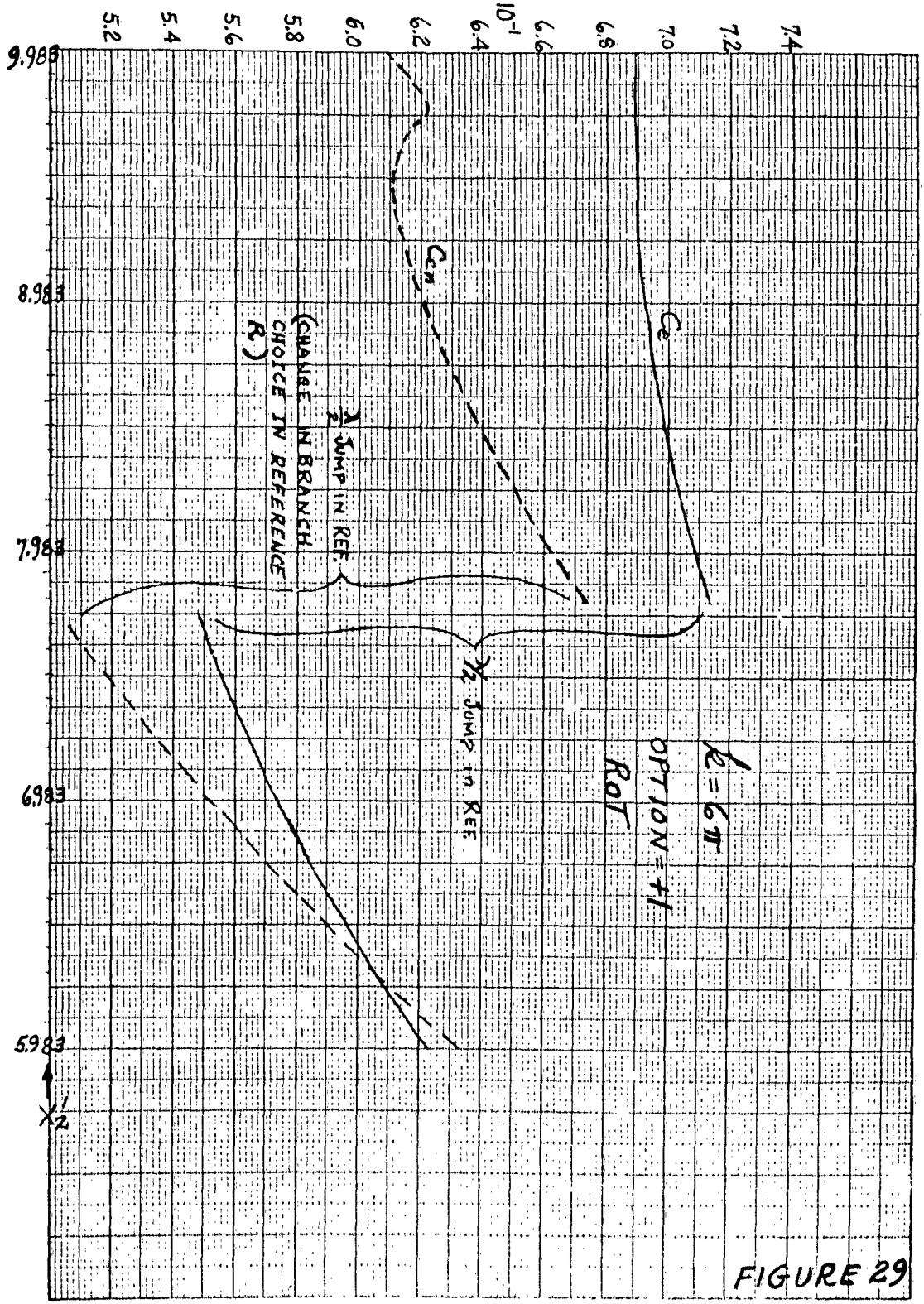
9.983
8.983
7.983
6.983
5.983
5.2
5.4
5.6
5.8
6.0
6.2
6.4
10⁻¹
6.6
6.8
7.0
7.2
7.4
Ce
Cen
λ/2 JUMP IN REF.
(CHANGE IN BRANCH CHOICE IN REFERENCE R.)
λ/2 JUMP IN REF.
k = 6π
OPTION = +1
ROT
X'2
X2

FIGURE 29

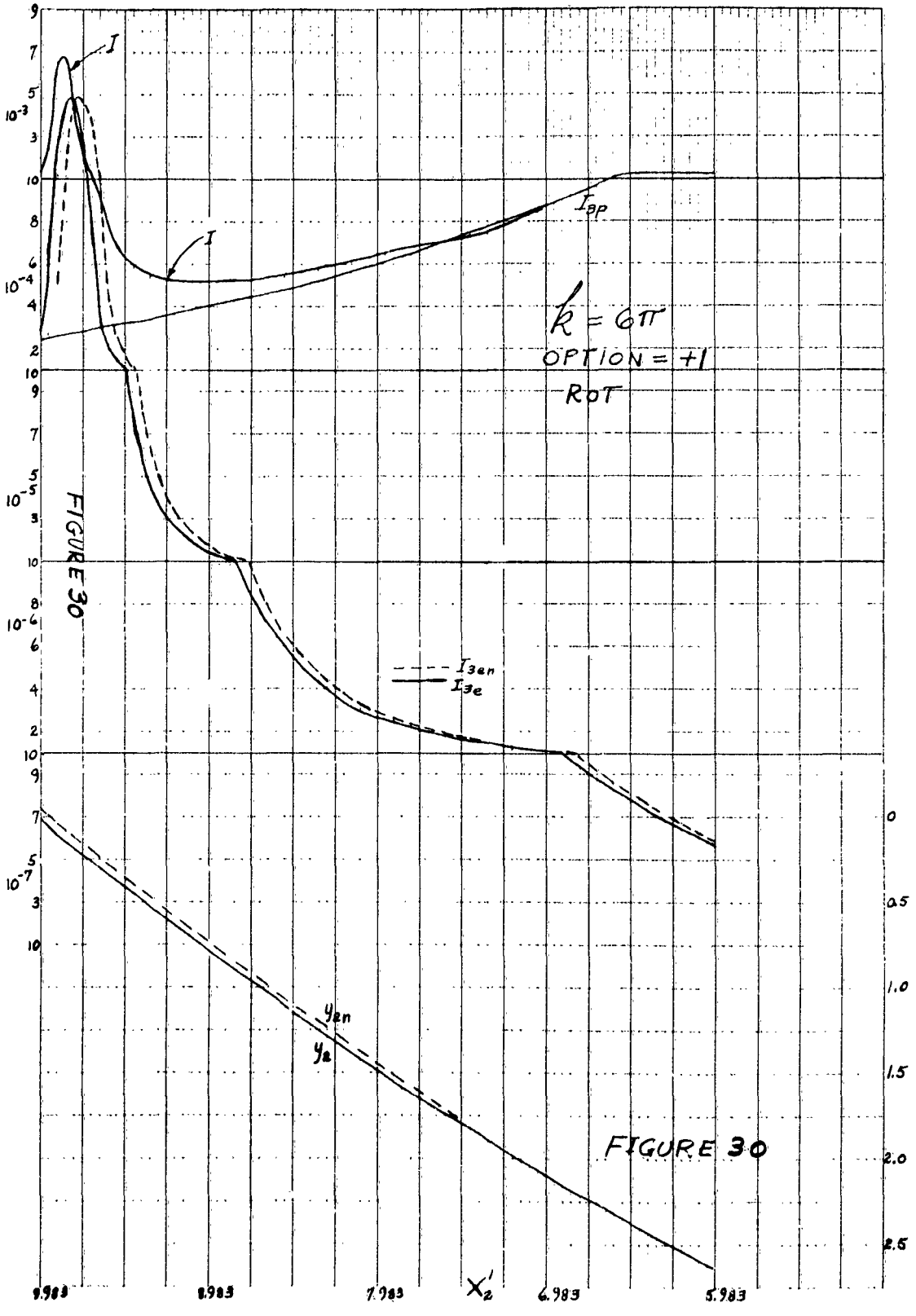

FIGURE 30

FIGURE 30

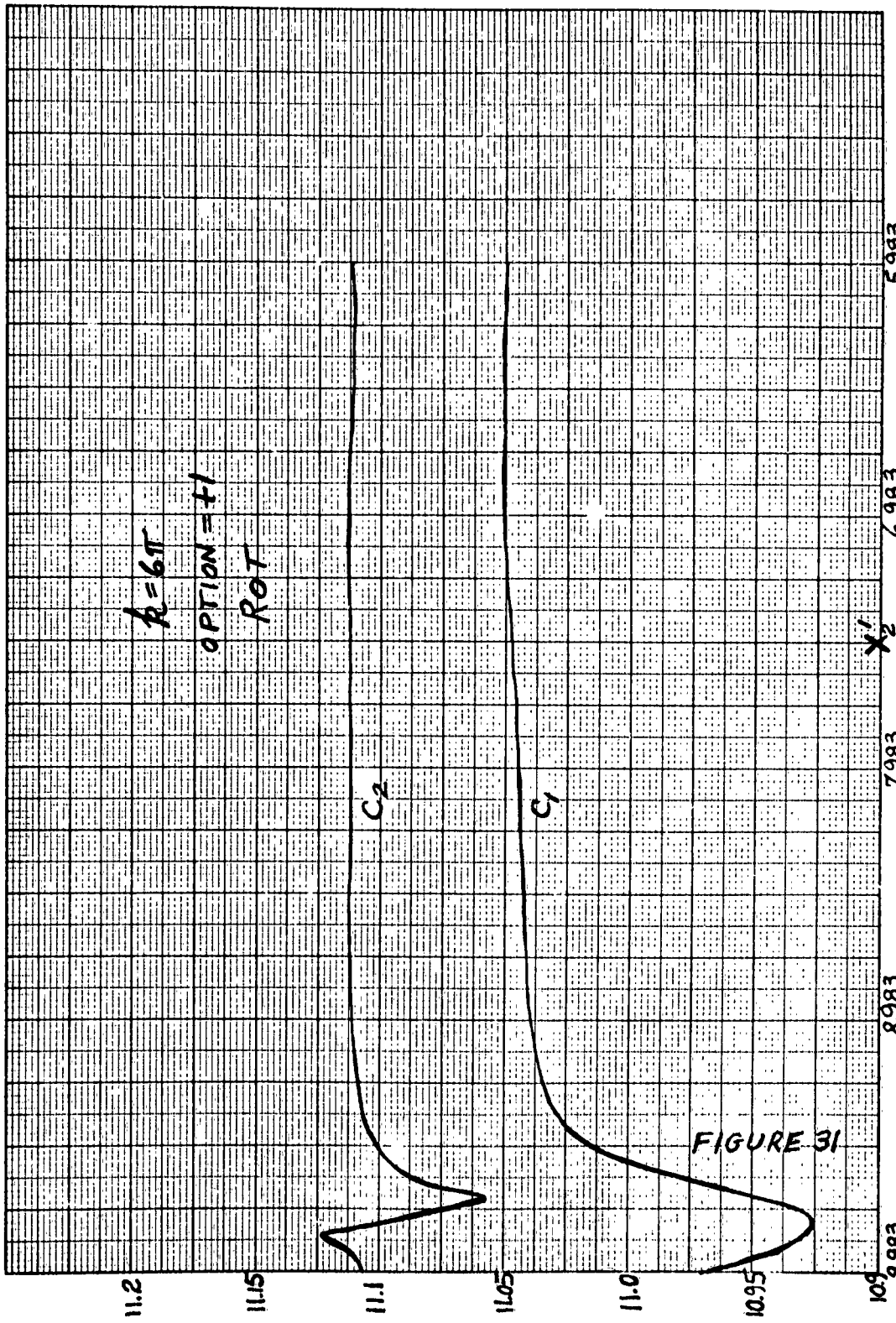
h=6π
OPTION=+1
ROT
C2
C1
X'2
5.983
6.983
7.983
8.983
9.983
11.2
11.15
11.1
11.05
11.0
10.95
10.9

FIGURE 31

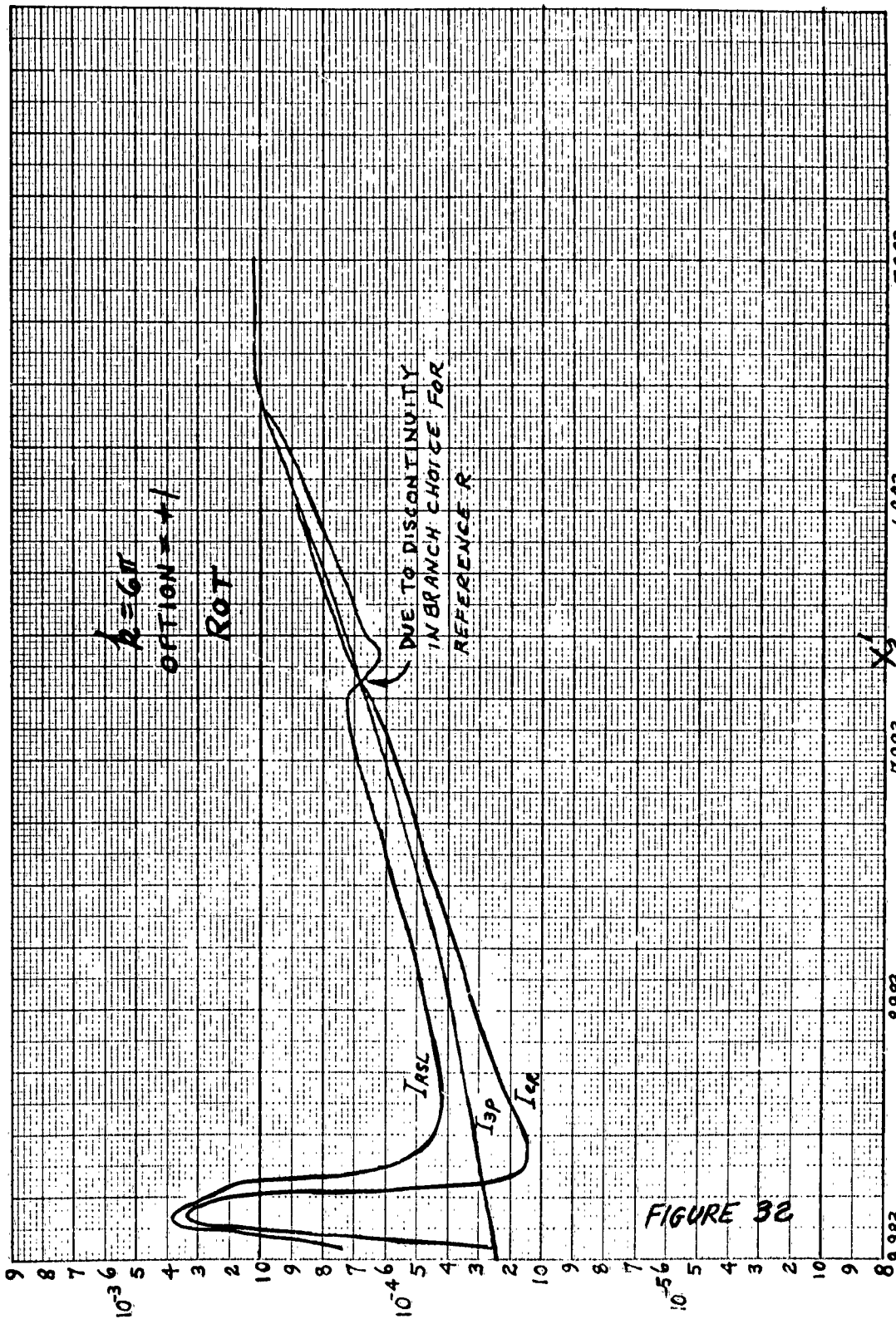
h=6M
OPTION=+1
ROT
DUE TO DISCONTINUITY
IN BRANCH CHOICE FOR
REFERENCE R
I_{ASL}
I_{3P}
I_{4P}
10^{-3}
10^{-4}
10^{-5}
5.983
6.983
7.983
8.983
9.983
X_2
X_1

FIGURE 32

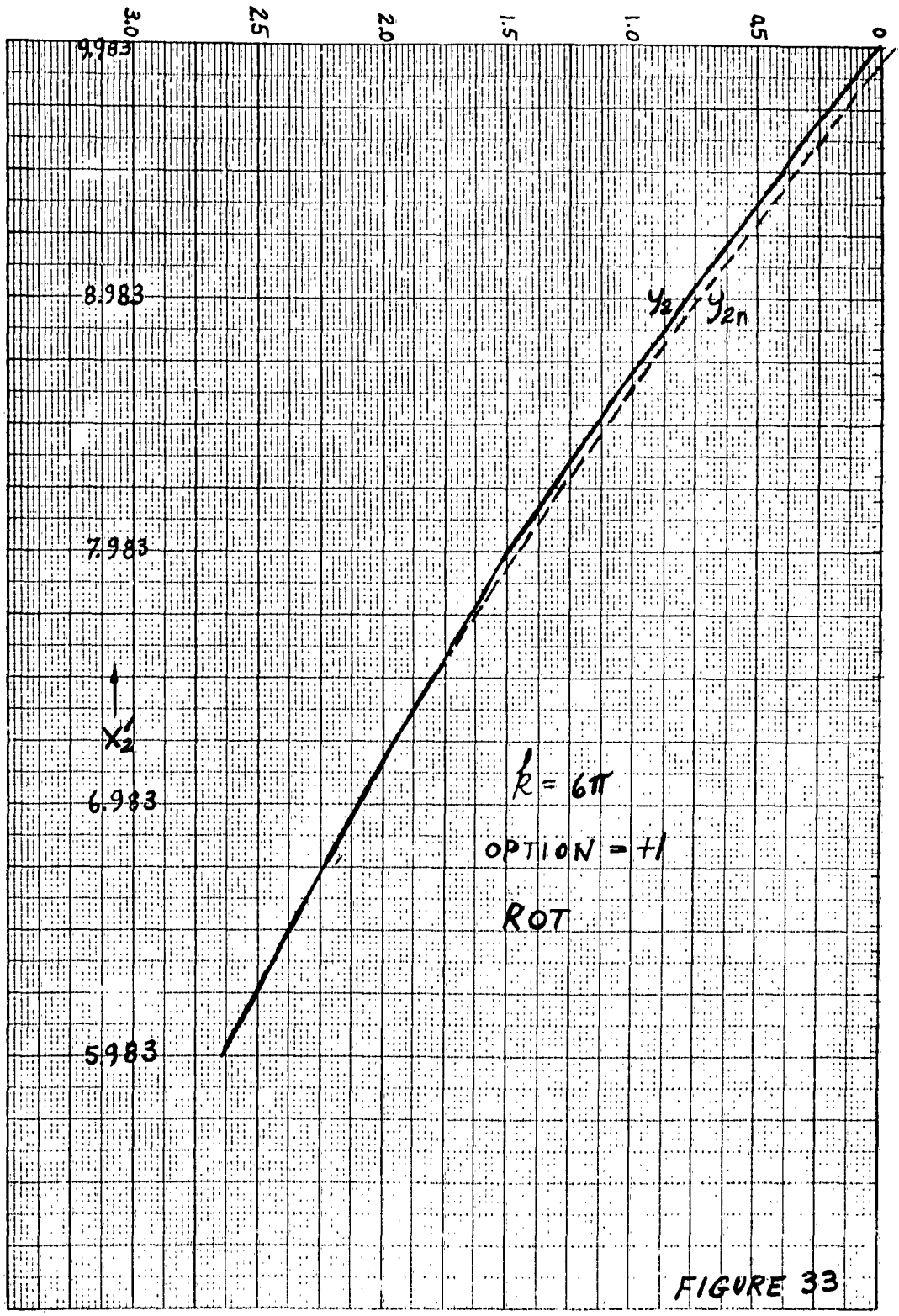
3.0
2.5
2.0
1.5
1.0
.5
0
9.983
8.983
7.983
6.983
5.983
X_2'
y_2
y_{2n}
$k = 6\pi$
OPTION = +1
ROT

FIGURE 33

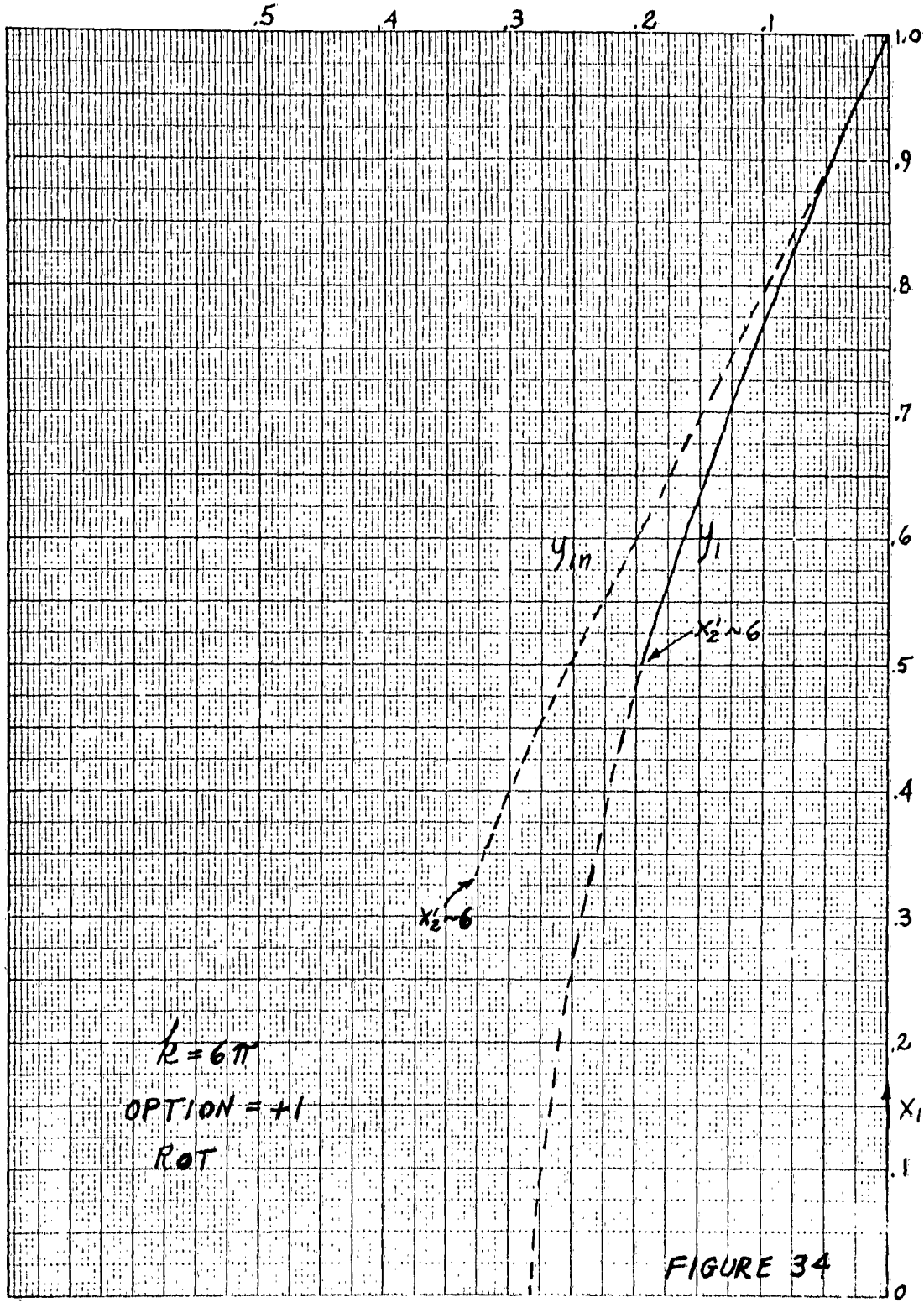

FIGURE 34

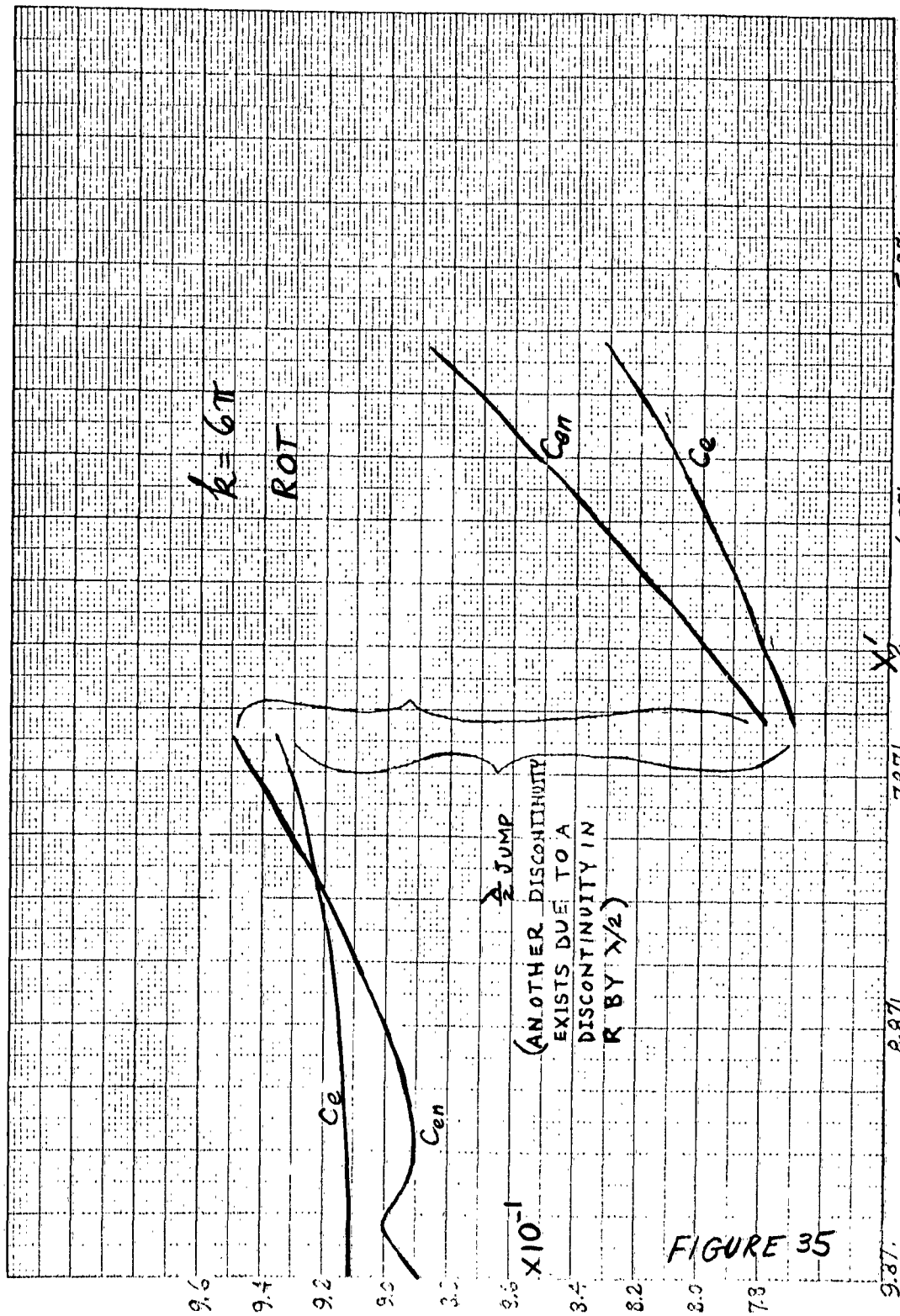
k = 6π
ROT
Ce
Cen
Cen
Ce
½ JUMP
(ANOTHER DISCONTINUITY EXISTS DUE TO A DISCONTINUITY IN R BY λ/2)
X10⁻¹
X'2
5.871
6.871
7.871
8.871
9.87
9.6
9.4
9.2
9.0
3.6
3.4
8.2
8.0
7.8

FIGURE 35

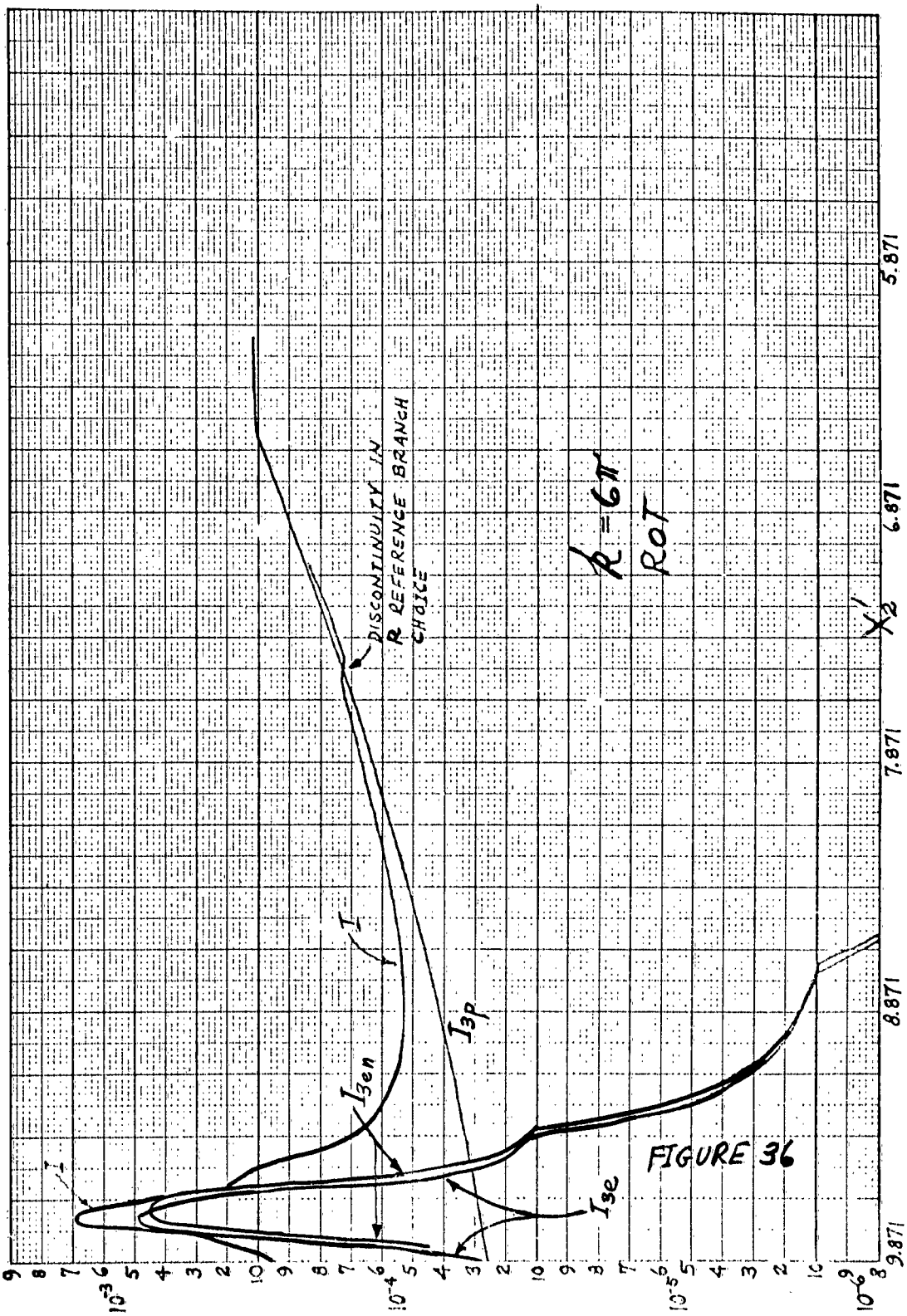
DISCONTINUITY IN
R REFERENCE BRANCH
CHOICE
I_{3en}
I_{3p}
I_{3e}
$R = 6\pi$
ROT
X_2'
5.871
6.871
7.871
8.871
9.871

FIGURE 36

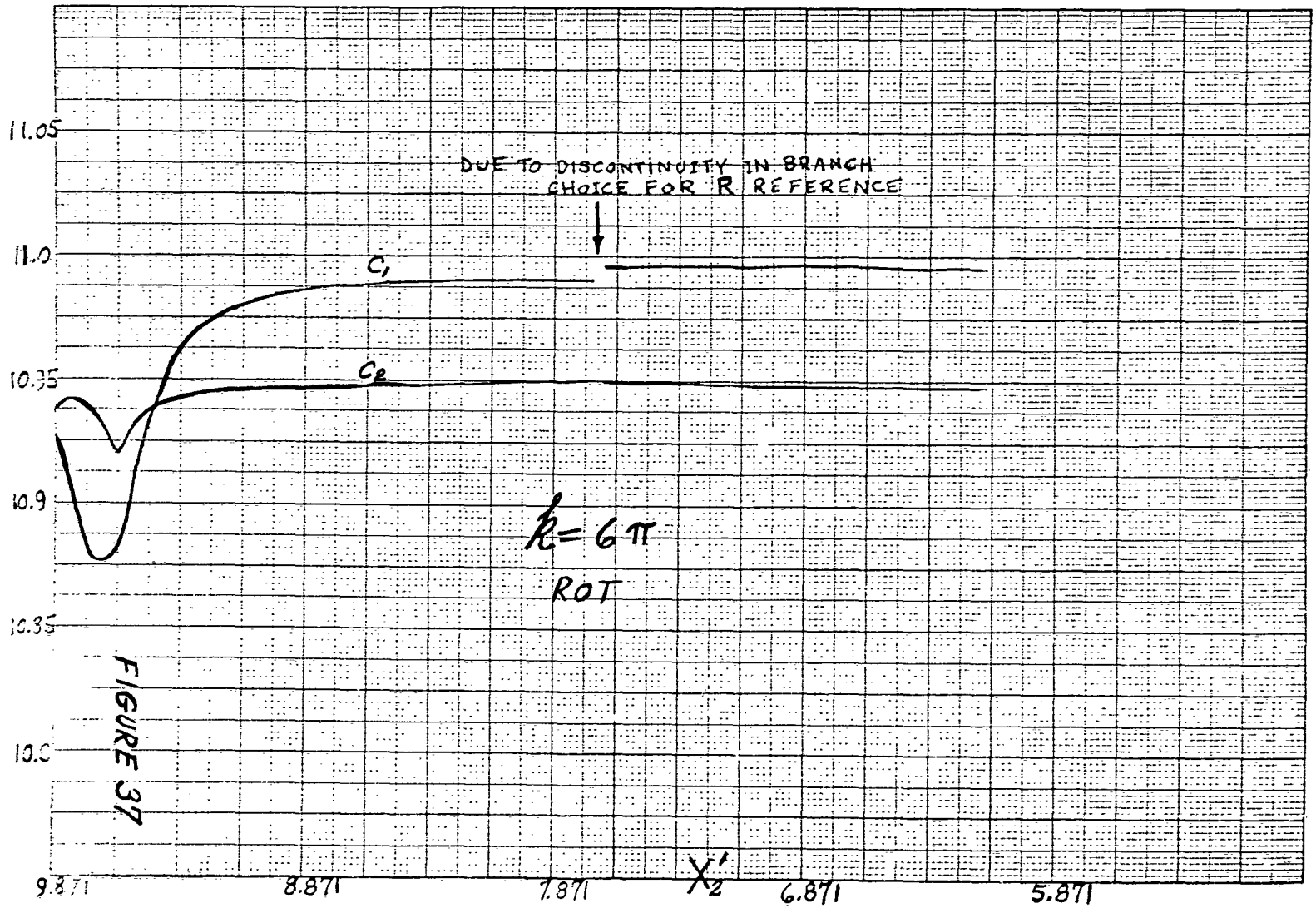
11.05
11.0
10.35
10.9
10.35
10.0
DUE TO DISCONTINUITY IN BRANCH CHOICE FOR R REFERENCE
C1
C2
k=6π
ROT
9.871
8.871
7.871
X'2
6.871
5.871

FIGURE 37

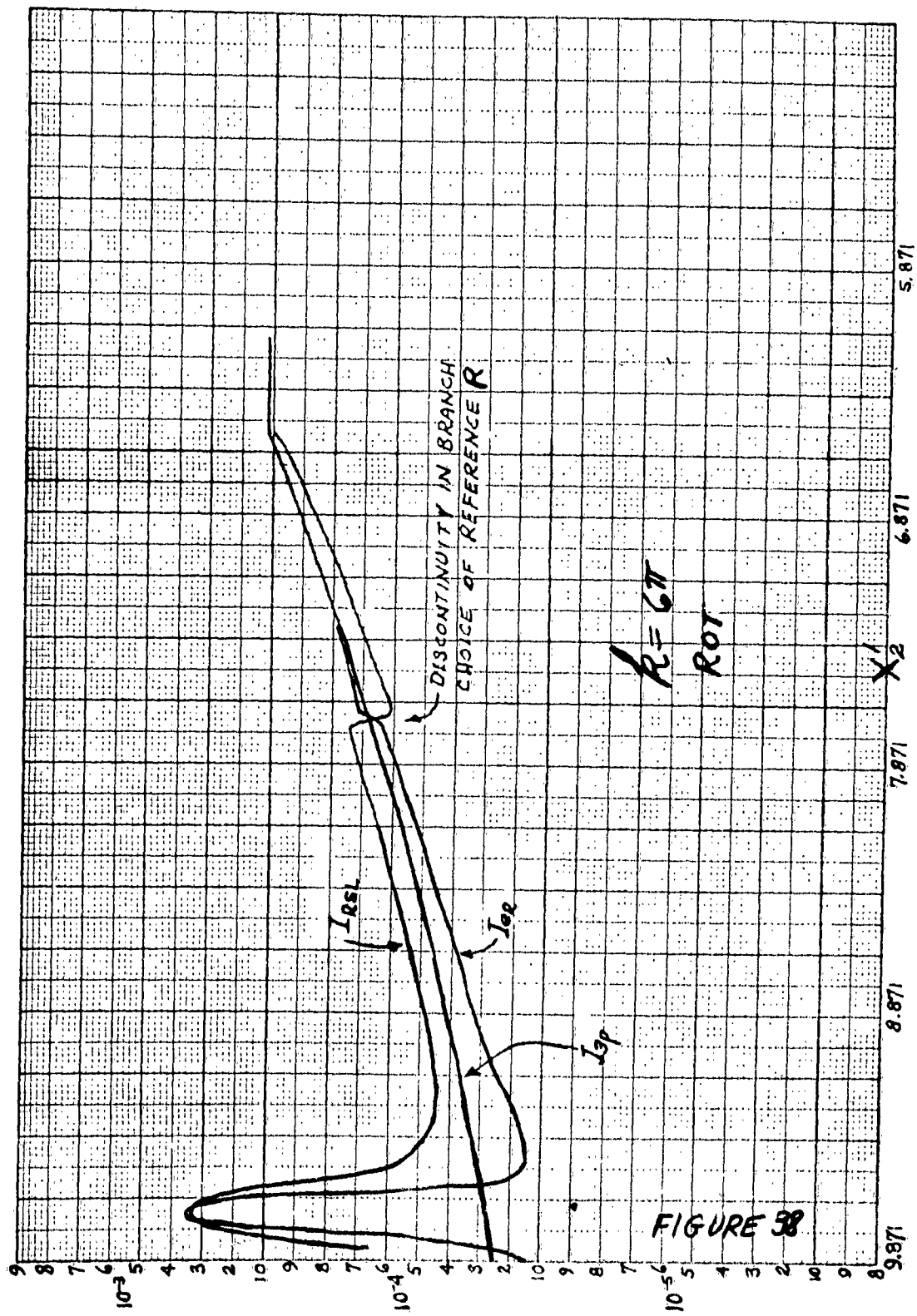
DISCONTINUITY IN BRANCH
CHOICE OF REFERENCE R
I_{RSL}
I_{SR}
I_{SP}
$R = 6\pi$
ROT
X_1
X_2
5.871
6.871
7.871
8.871
9.871
10^{-3}
10^{-4}
10^{-5}

FIGURE 38

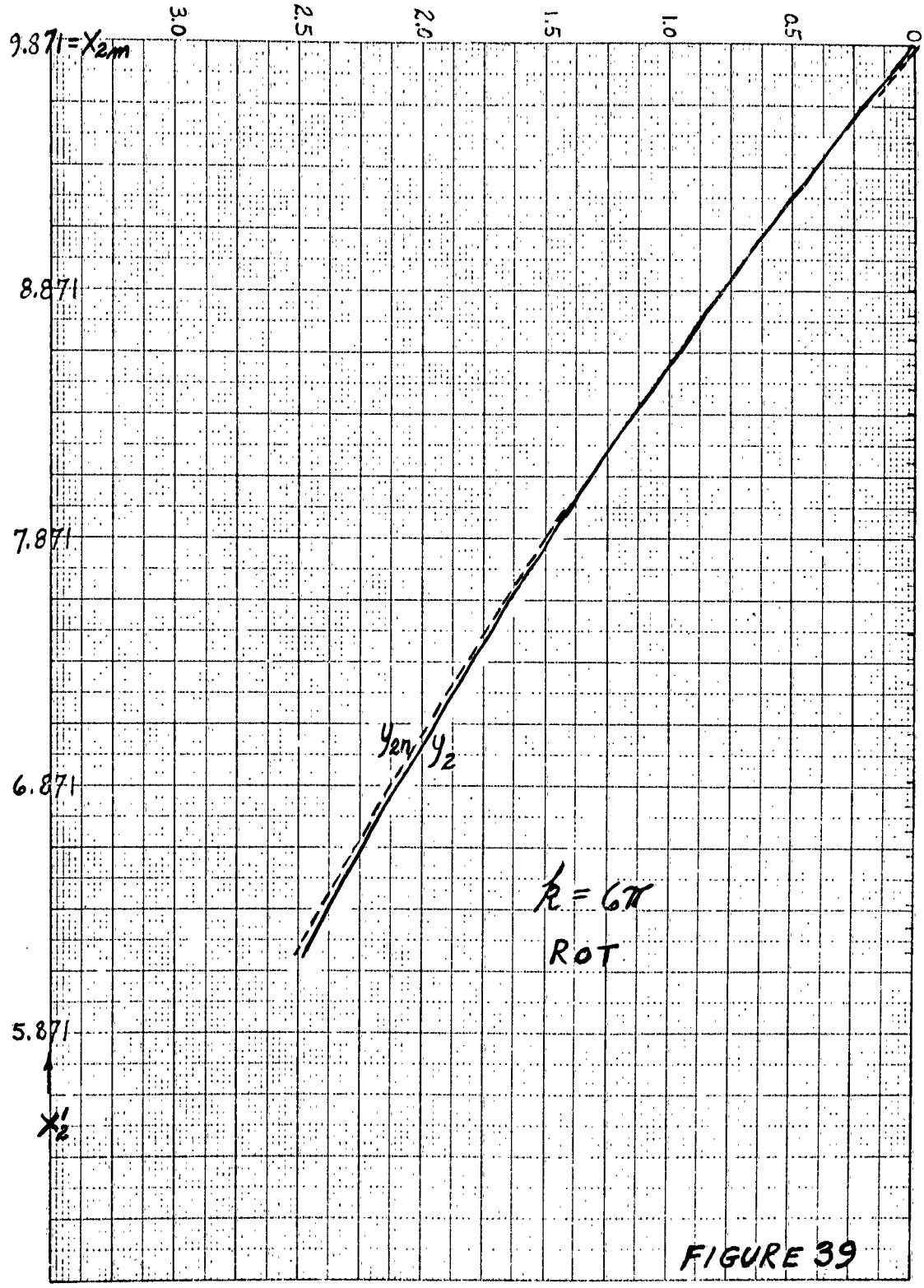

FIGURE 39

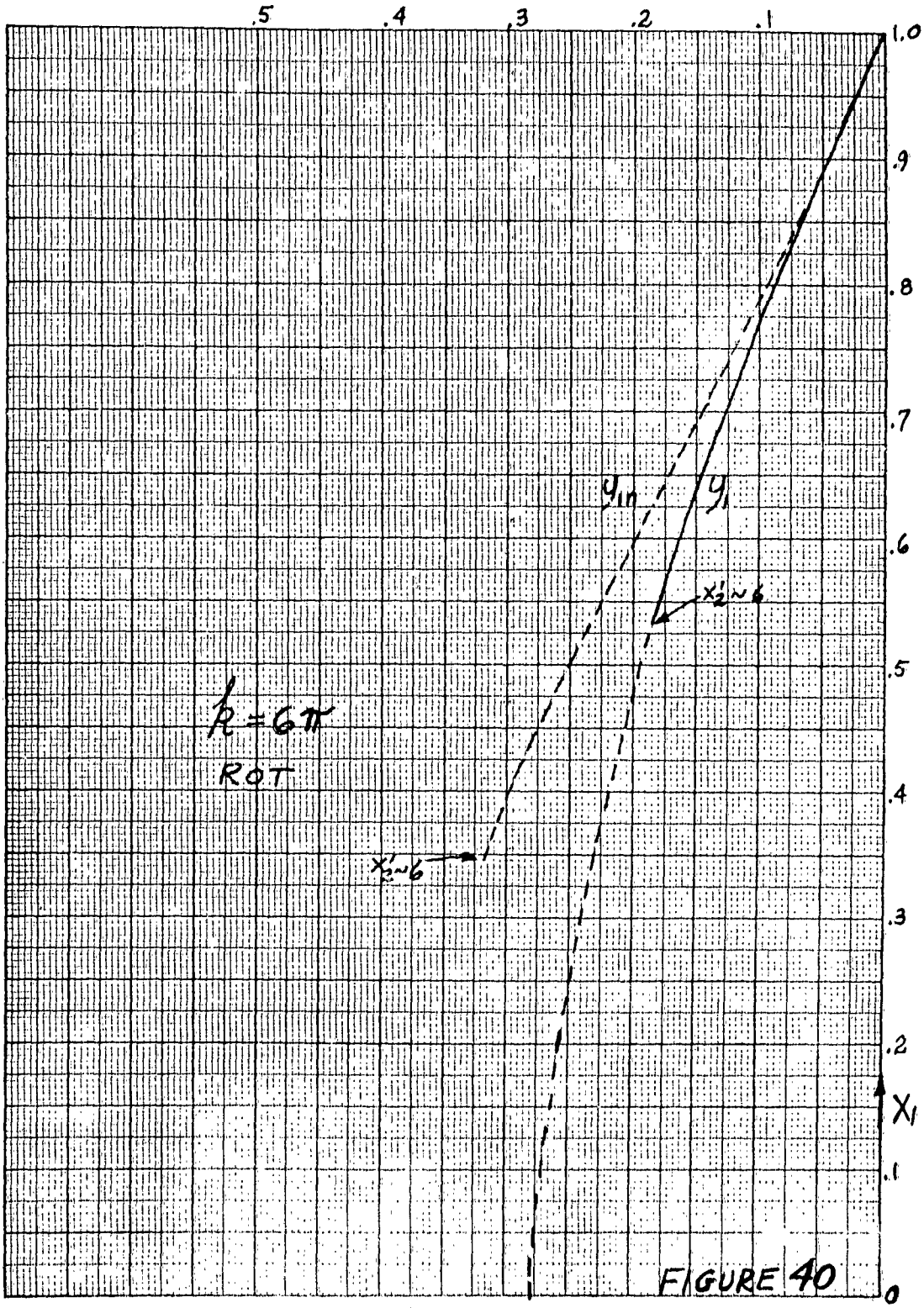

FIGURE 40

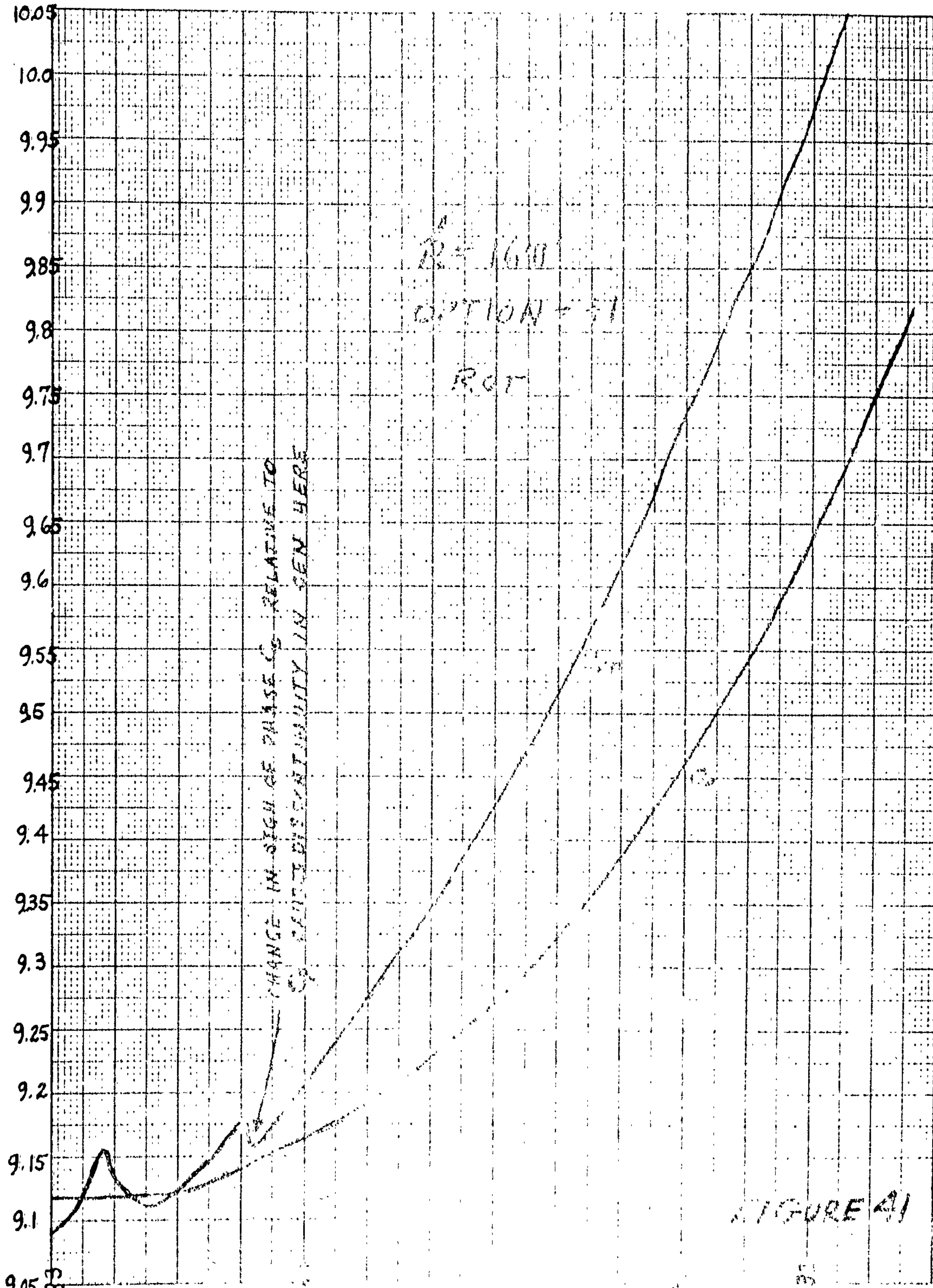

10.05
10.0
9.95
9.9
9.85
9.8
9.75
9.7
9.65
9.6
9.55
9.5
9.45
9.4
9.35
9.3
9.25
9.2
9.15
9.1
9.05
CHANGE IN SIGN OF PHASE C_5 RELATIVE TO C_3 DISCONTINUITY IN SEN HERE
OPTION

FIGURE 41

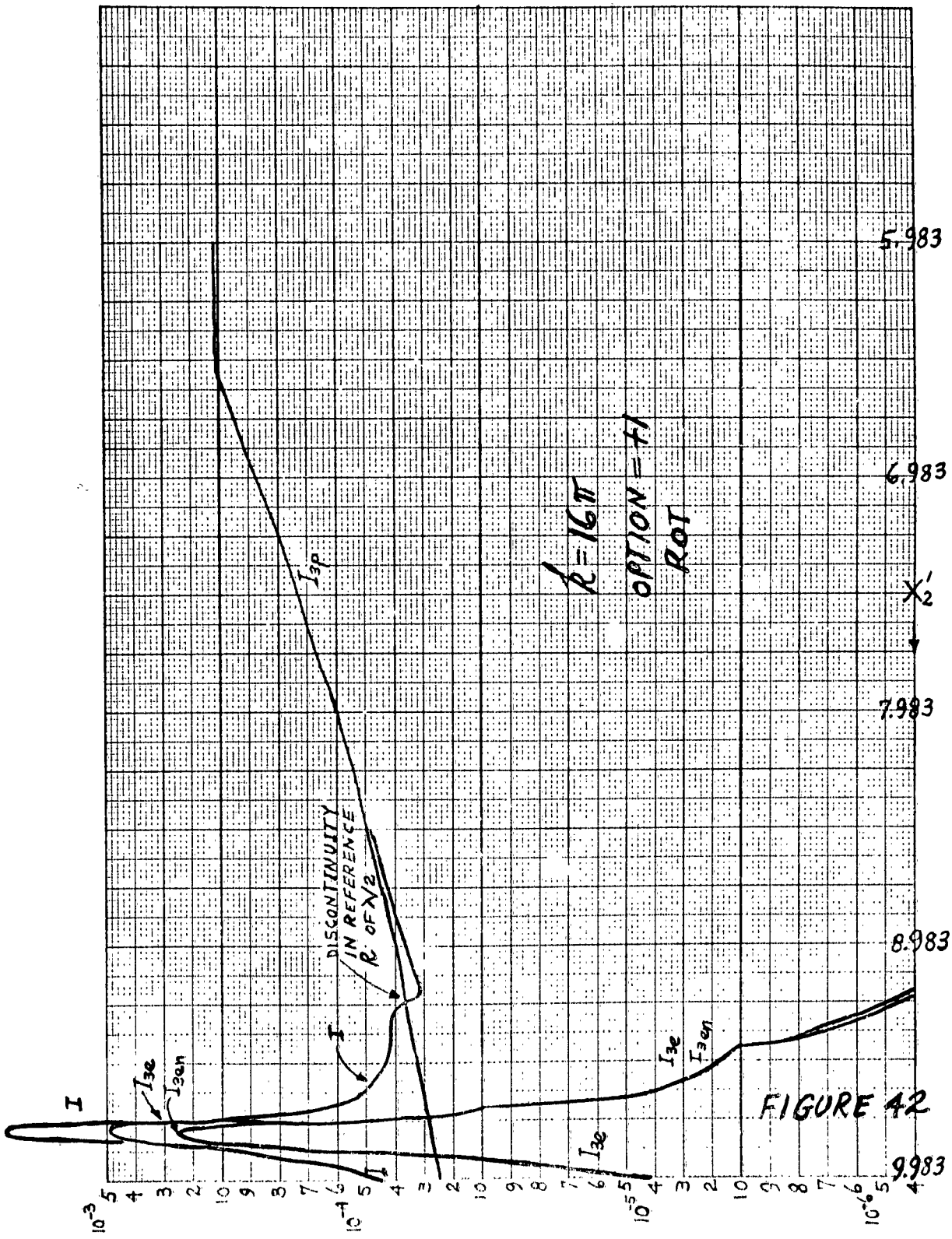
I
I_{3e}
I_{3an}
I_{3p}
DISCONTINUITY IN REFERENCE R OF λ/2
I_{3e}
I_{3an}
I_{3e}
10^{-3}
10^{-4}
10^{-5}
10^{-6}
5.983
6.983
X_2'
7.983
8.983
9.983
$k = 16\pi$
OPTION = 41
ROT

FIGURE 42

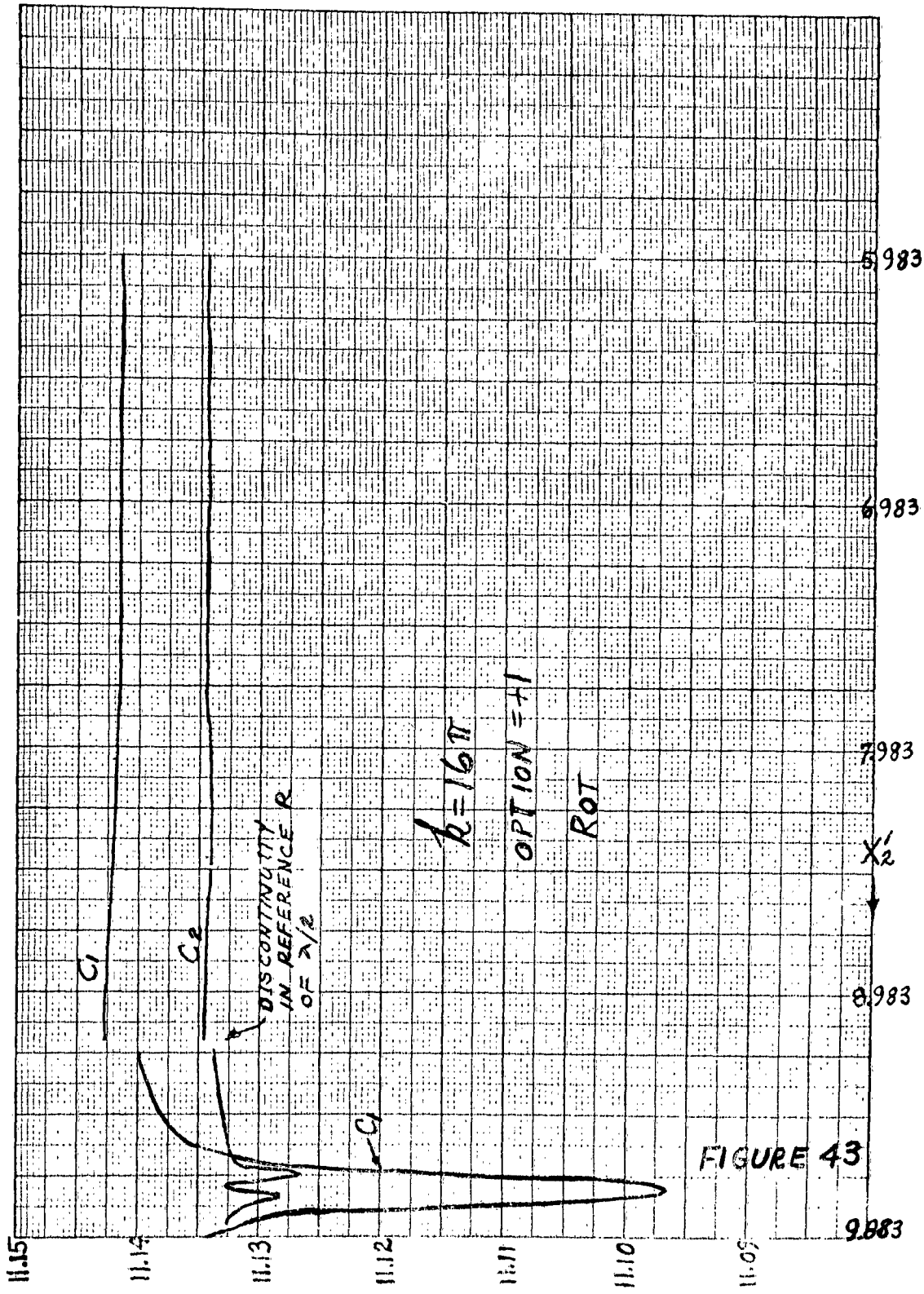
C1
C2
DISCONTINUITY IN REFERENCE R OF λ/2
C1
h=16 π
OPTION =+1
ROT
X'2
5.983
6.983
7.983
8.983
9.983
11.15
11.14
11.13
11.12
11.11
11.10
11.09

FIGURE 43

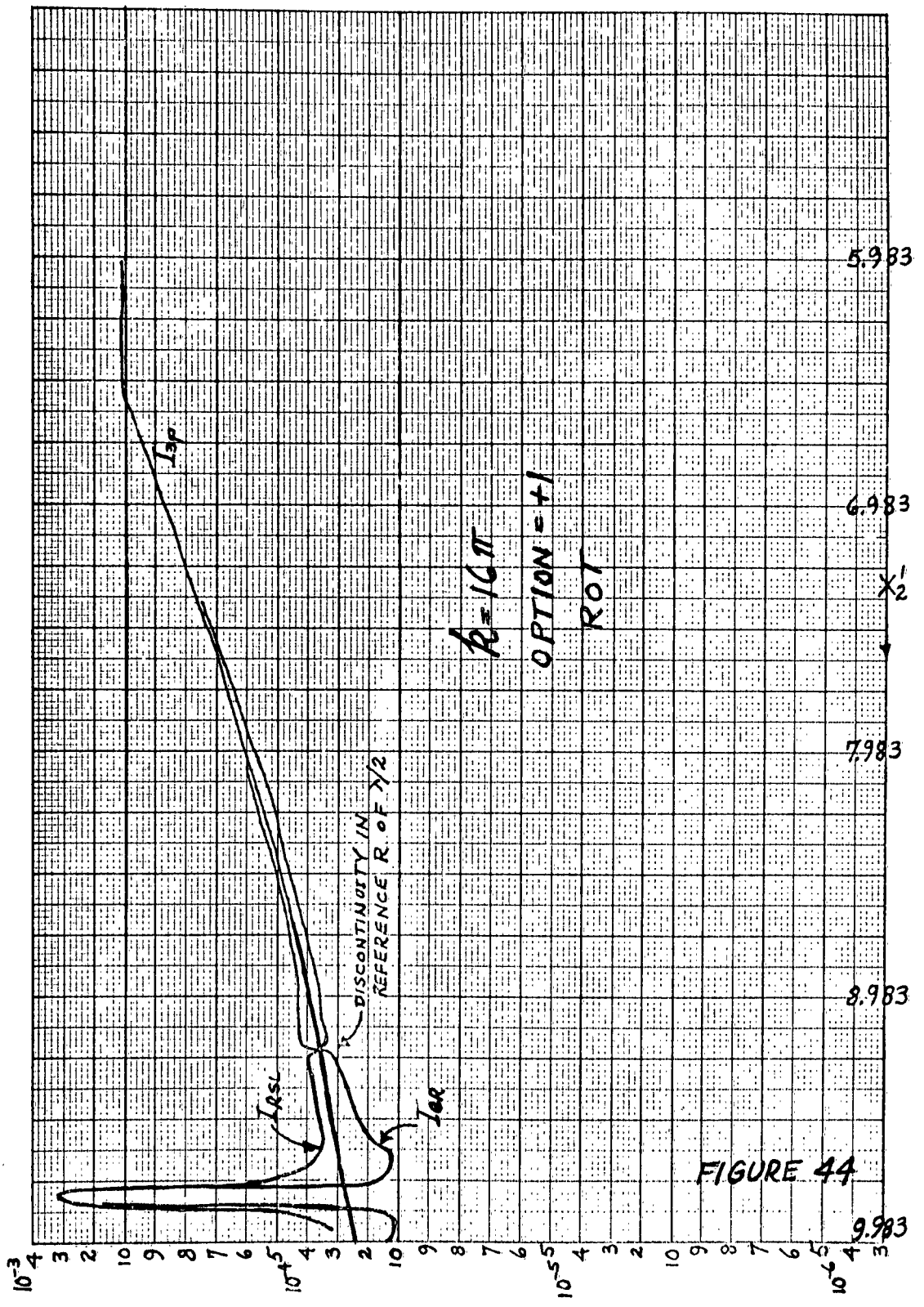
I_{3P}
I_{RSL}
I_{AR}
DISCONTINUITY IN R. OF $\chi/2$
REFERENCE
$R = 16\pi$
OPTION = +1
ROT
5.983
6.983
X'_2
7.983
8.983
9.983
10^{-3}
10^{-4}
10^{-5}
10^{-6}

FIGURE 44

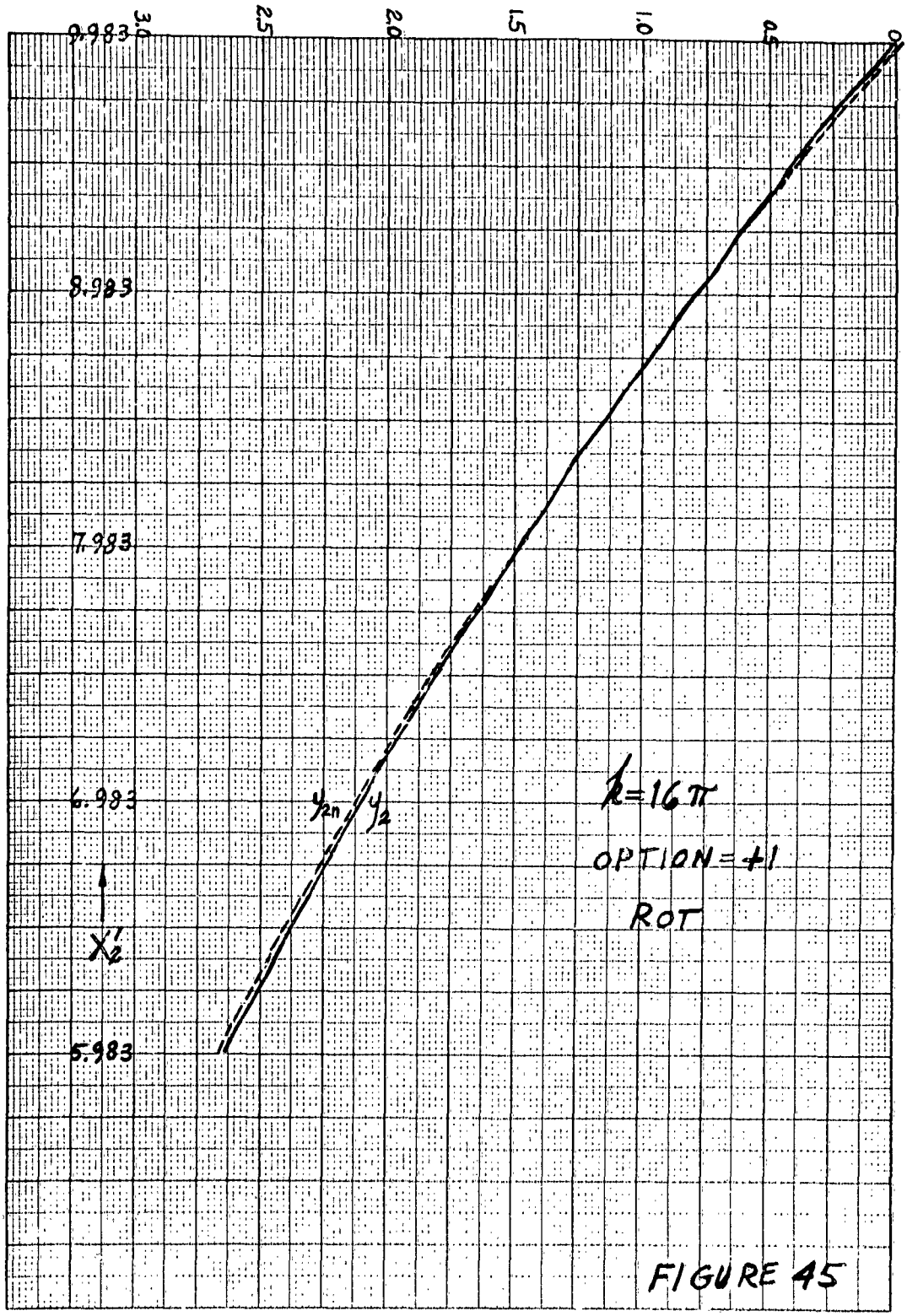
9.983
8.983
7.983
6.983
5.983
3.0
2.5
2.0
1.5
1.0
0.5
0
y_{2n}
y_2
X_2'
$k=16\pi$
OPTION=+1
ROT

FIGURE 45

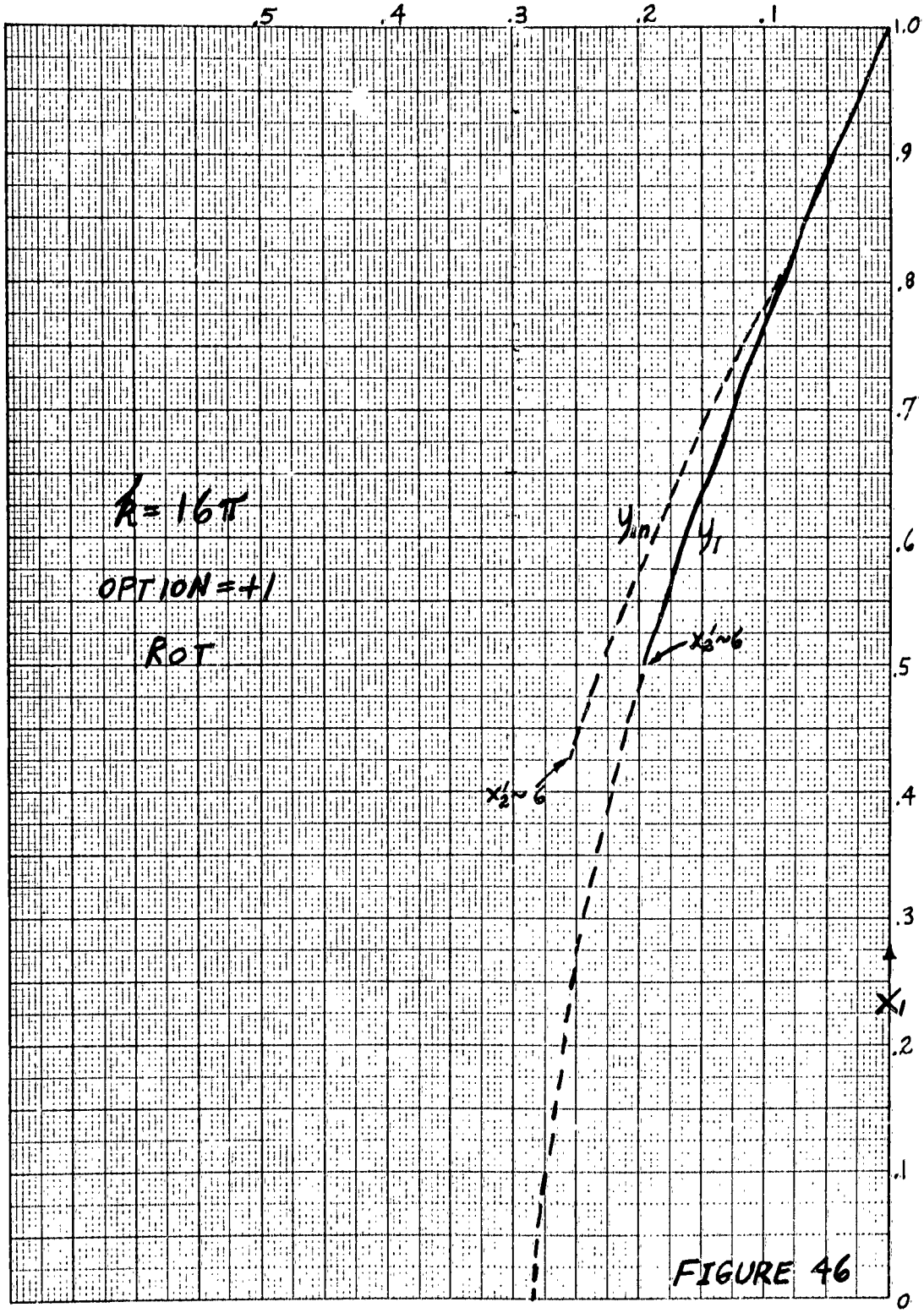
.5
.4
.3
.2
.1
1.0
.9
.8
.7
.6
.5
.4
.3
.2
.1
0
R = 16π
OPTION = +1
ROT
y_{in}
y_1
$x_2' \sim 6$
$x_2' \sim 6$
x_1

FIGURE 46

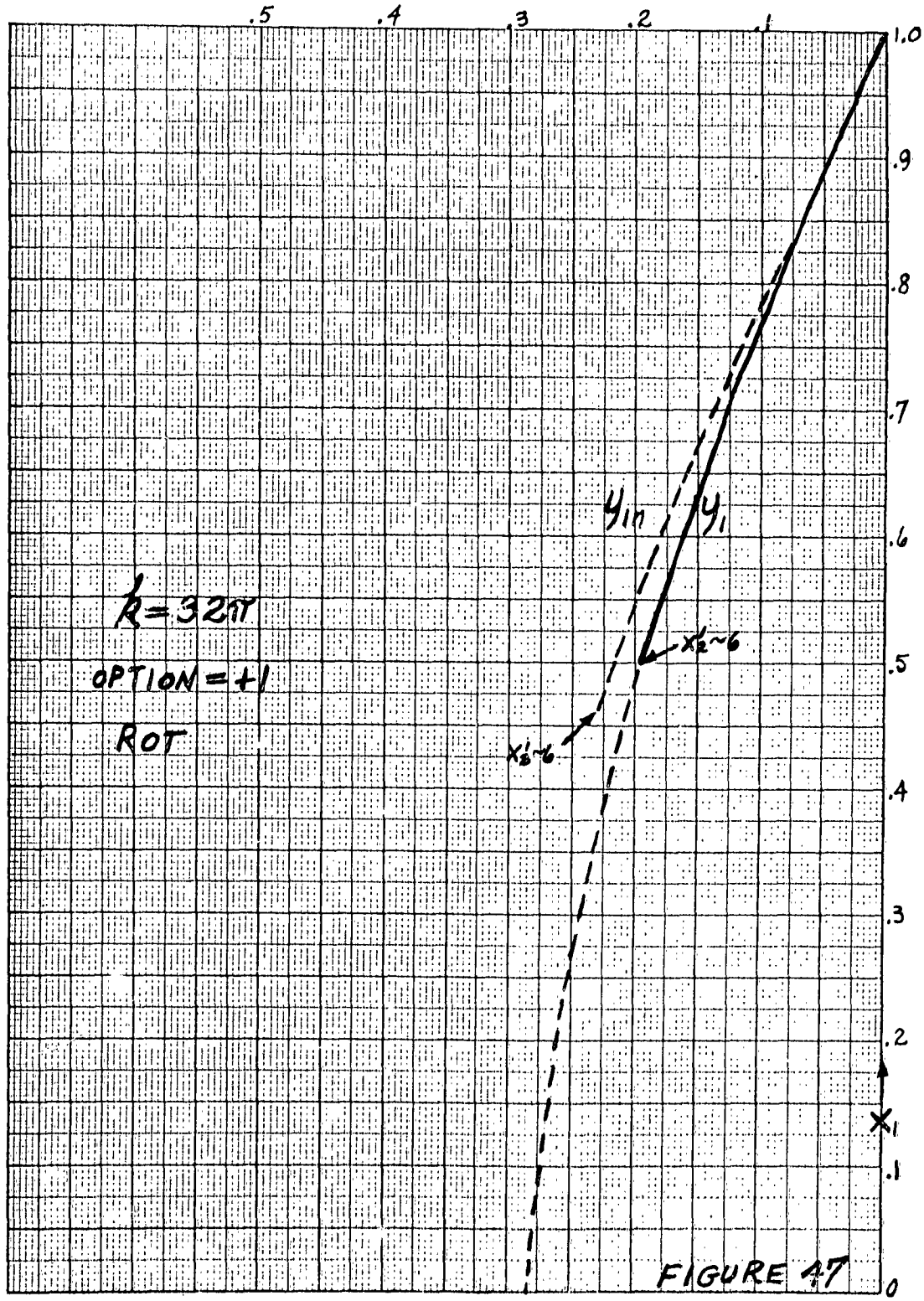
.5
.4
.3
.2
.1
1.0
.9
.8
.7
.6
.5
.4
.3
.2
.1
0
y_{in}
y_1
$x_2 \sim 6$
$x_2 \sim 6$
x_1
K=32π
OPTION=+1
ROT

FIGURE 47

Acknowledgement

The author wishes to express his sincere appreciation to Professor William J. Welch of the University of California at Berkeley for his very helpful assistance, guidance, and encouragement in this work.

APPENDIX I

EXISTENCE, UNIQUENESS AND BOUNDS

With the functions

$$\left.\begin{aligned} \frac{dy_1}{dx_1} &= f_1(x_1, y_1) = \tan\left(\frac{\theta_1 - \theta_2}{2}\right) \\ \text{and} \quad \frac{dy_2}{dx_2} &= f_2(x_2, y_2) = -\tan\left(\frac{\theta_2 - \theta_3}{2}\right) \end{aligned}\right\} \tag{1}$$

determined for each reflector, it is important to know whether a solution to these equations subject to the appropriate boundary conditions exists, and if so, what the maximum possible value of $|y|$ is for each solution, particularly the solution for $y_2(x_2)$.

The Cauchy-Lipschitz method [1] for integrating (1) provides a useful way to determine bounds to the solution. Briefly, the method approximately integrates (1) by the Riemann sum

$$y_n = \sum_{i=0}^{n-1} f(x_i, y_i)\, \Delta x_i ,$$

where $n\Delta x_i = x$ and Δx_i is < 0 when the solution is developed from x_{max}, and also provides the necessary and sufficient conditions for the limit ($n \to \infty$) to exist. If the limit exists, then the solution exists. The conditions for existence also provide a means for determining an upper bound for $|y|$.

---

1. H. T. Davis, "Introduction to Non-Linear Differential and Integral Equations", pp. 88-93, U.S. Atomic Energy Commission; September 1960

The Cauchy-Lipschitz conditions state that:

1. $f(x, y)$ must be uniformly continuous. That is

$$|f(x, y) - f(x + h, y)| < \epsilon \text{ when } h < \delta \text{ for all } \delta > 0.$$

2. $f(x, y)$ must satisfy the Lipschitz condition. That is, there exists a number K such that

$$|f(x, y) - f(x, y + h)| < K\ h \text{ for all } h > 0.$$

3. $|f(x, y)|$ must have a maximum M, in a rectangular region in the (x, y) plane defined by $x_{2_{max}} - x_{2_{min}}$; $+b$; $-b$; such that

$$M\ x_{max} < b \tag{2}$$

In (2) and what follows, the value of x_{min} will be taken as zero for convenience.

The first two conditions will usually be satisfied since $f(x, y)$ will, in general, be single-valued, continuous and have continuous derivatives in practical problems. This is assured by making appropriate choices of any branches of $f(x, y)$ if such exist. The distributions $I_1(\theta_1)$ and $I_{3p}(x_2')$ may be discontinuous even though equation (1) remains analytic. In other words, if discontinuities in $I_1(\theta_1)$ are reflected in $I_{3p}(x_2')$ then the reflectors may be continuous.

Satisfaction of the last condition also provides an upper bound for $|y|$ which is equal to b. In this case, the solution is constrained

to lie in the shaded triangular region depicted in Figure 1.

If $f(x,y)$ can be found in explicit form and can be readily manipulated, then the value of M and a bound for $|y|$ can be found directly from $f(x,y)$. Furthermore, a lower bound for the radius of curvature of the reflectors can be found directly by maximizing $\frac{df}{dx}$ in $\mathcal{R}$.

If $f(x,y)$ cannot be found explicitly or in sufficiently simple form, then absolute bounds $|y_1|_b$ and $|y_2|_b$ for $|y_1|$ and $|y_2|$ can be found from equation (1) and the boundary conditions. Although $|y_1|_b$ and $|y_2|_b$ may be considerably higher than $|y_1|_{max}$ and $|y_2|_{max}$, respectively, their finite values are proof of the existance of a solution.

Absolute bounds for $|y_1|$ and $|y_2|$ will be found for two cases of the boundary conditions:

a. $x_{2max} > 0$ (leads to solutions similar to the Cassegrainian type)

and b.

$x_{2max} < 0$ (a negative maximum is implied and leads to solutions similar to the Gregorian type).

For convenience, it will be assumed that $\theta_{3\,min} = \theta_{1\,min} = 0$. Since $\theta_{3\,max}$* and $\theta_{1\,max}$ are usually given boundary conditions,

---

* Since $\theta_3 = \arcsin(dCp/dx_2')$ and $Cp(x_2')$ is given, then $\theta_3(x_2')$ is known and so are $\theta_{3\,min}$ and $\theta_{3\,max}$.

it is clear from equation (1) that it is sufficient to determine an absolute upper bound for $|\theta_2|$, θ_{2b}, in order to determine $\left|\frac{dy_1}{dx_1}\right|_b$ and $\left|\frac{dy_2}{dx_2}\right|_b$.

It is also assumed that α and β are given boundary conditions (note that they may be negative or positive).

The appropriate geometry for case (a) is depicted in Figure 2. Only the end points of the reflectors are depicted. An extreme ray trajectory is depicted from the phase center of $I_1(\theta_1)$ to the point $(y_2 = 0, \; x_2 = x_{2\,max})$. The value for θ_{2b} is found as

$$\theta_{2b} = \arctan\left(\frac{x_{2\,max}}{\alpha}\right) \text{ for } x_{2max} > 0 \tag{3}$$

which leads to a value for $|y_1|_b$ as

$$|y_1|_b = x_{1\,max} \tan 1/2 \left\{\arctan\left(\frac{x_{2\,max}}{\alpha}\right)\right\} \text{ so long as}$$

$$\theta_{2b} \gtrless \theta_{1\,max} \text{ and with } x_{2\,max} > 0 \; . \tag{4}$$

If θ_{2b} is less than $\theta_{1\,max}$ then $\theta_{1\,max}$ may be substituted for θ_{2b} in (4). The value for $|y_2|_b$ is found as either

$$|y_2|_b = x_{2\,max} \tan \frac{1}{2}\left\{\arctan\left(\frac{x_{2\,max}}{\alpha}\right)\right\} \text{ for } \theta_{2b} \geq \theta_{3\,max}$$

$$\text{with } x_{2\,max} > 0 \tag{5}$$

or

$$|y_2|_b = x_{2\,max} \tan \frac{1}{2}\left\{\theta_{3\,max}\right\} \text{ for } \theta_{3\,max} \geq \theta_{2b}$$

$$\text{with } x_{2\,max} > 0 \tag{6}$$

There are two possible geometries for case (b) which are depicted in Figures 3a and 3b. The geometry in Figure 3a leads to a value for θ_{2b} as

$$\theta_{2b} = \arctan\left(\frac{|x_{2\,max}|}{\alpha}\right) \text{ with } x_{2\,max} < 0, \tag{7}$$

and the geometry in Figure 3b leads to

$$\theta_{2b} = \arctan\left(\frac{|x_{2\,max}| + x_{1\,max}}{\alpha + \beta}\right) \text{ with } x_{2\,max} < 0 \tag{8}$$

The appropriate value of θ_{2b}, as given by (7) or (8), is used to find $|y_1|_b$ and $|y_2|_b$. Since θ_1 and θ_2 always have opposite signs in this case, the value for $|y_1|_b$ is found as

$$|y_1|_b = x_{1\,max} \tan\left(\frac{\theta_{2b} + \theta_{1\,max}}{2}\right) \text{ with } x_{2\,max} < 0 \tag{9}$$

Since the signs of θ_2 and θ_3 remain the same for this case, as for case (a), the value of $|y_2|_b$ is found as either

$$|y_2|_b = |x_{2\,max}| \tan\left(\frac{\theta_{2b}}{2}\right) \text{ for } \theta_{2b} > |\theta_{3\,max}|$$

$$\text{and with } x_{2\,max} < 0 \tag{10}$$

or

$$|y_2|_b = |x_{2\,max}| \tan\left(\frac{|\theta_{3\,max}|}{2}\right) \text{ for } |\theta_{3\,max}| > \theta_{2b}$$

$$\text{with } x_{2\,max} > 0 \tag{11}$$

A somewhat improved estimate of an upper bound for $|y|$ can be obtained if the assumption is made that the sign of $\frac{d^2y}{dx^2}$ does not change over the reflector. This assumption is usually valid for reasonably smooth $I_{3p}(x_2')$ and $I_1(\theta_1)$. For example, it is true for all Cassegrain parabola-hyperbola and Gregorian parabola-ellipse designs. It is also true in the computed designs shown in Chapter 1. If the assumption is not valid, that is $\frac{d^2y}{dx^2}$ does reverse sign for a small interval of $x_{max} - x_{min}$, then the proposed estimate for an upper bound to $|y|$ may be in error, but may nevertheless be a closer estimate to the true value $|y_{max}|$ than the absolute bounds previously considered.

If the second derivatives

$$\frac{d^2y_1}{dx_1^2} = \left(\frac{1}{2}\sec^2\left\{\frac{\theta_1 - \theta_2}{2}\right\}\right)\left(\frac{d\theta_1 - d\theta_2}{dx_1}\right)$$

and

$$\frac{d^2y_2}{dx_2^2} = \left(-\frac{1}{2}\sec^2\left\{\frac{\theta_2 - \theta_3}{2}\right\}\right)\left(\frac{d\theta_2 - d\theta_3}{dx_2}\right)$$

do not change sign then this implies, for most cases, that $(d\theta_1 - d\theta_2)$ and $(d\theta_2 - d\theta_3)$ do not change sign. In this circumstance, the differences of the angles,

$$(\theta_{1\,max} - \theta_{2ba})$$

and

$$(\theta_{2ba} - \theta_{3\,max})$$

will, in general, be the maximum differences. The value θ_{2ba} is an improved estimate of an upper bound for $|\theta_2|$ which will be found for cases (a) and (b).

For case (a), $x_{2\,max} > 0$, an approximate upper bound for $|\theta_2|$, θ_{2ba}, can be obtained by using the value depicted in Figure 4. This value is given by

$$\theta_{2ba} = \arctan\left(\frac{x_{2\,max} - x_{1\,max}}{\alpha + \beta}\right) \quad \text{for } x_{2\,max} > 0 \tag{12}$$

The corresponding approximate upper bounds for $|y_{1\,max}|$ and $|y_{2\,max}|$, $|y_1|_{ba}$ and $|y_2|_{ba}$, are then given by

$$|y_1|_{ba} = x_{1\,max}\left|\tan\left(\frac{\theta_{2ba} - \theta_{1\,max}}{2}\right)\right| \text{for } x_{2\,max} > 0 \tag{13}$$

and

$$|y_2|_{ba} = x_{2\max} \left| \tan\left(\frac{\theta_{2ba} - \theta_{3\max}}{2}\right)\right| \quad \text{for } x_{2\max} > 0 \qquad (14)$$

For this case, (a), the assumption has been made that

$$\frac{d^2 y_1}{dx_1^2} < 0 \text{ for all } x_1.$$

For case (b), $x_{2\max} < 0$, the assumption is that $\frac{d^2 y_1}{dx_1^2} > 0$ for all x_1. The approximate upper bound for $|\theta_2|$, θ_{2ba}, is found from Figure 3b, irrespective of the position of the focal point F. The value of θ_{2ba} is the same as that given for θ_{2b} by equation (9) since θ_1 and θ_2 have opposite signs in this case. It should be added that the geometry of Figure 3b occurs less frequently than that of Figure 3a in practice so that the improved bounds for $|y_1|_{\max}$ are usually different than the absolute bounds. The signs of θ_2 and θ_3 both change in this case, (b), so that the improved bound for $|y_2|_{\max}$ is given by

$$|y_2|_{ba} = |x_{2\max}| \cdot \left| \tan\left(\frac{\theta_{2ba} - |\theta_{3\max}|}{2}\right)\right| \qquad (15)$$

for $x_{2\max} < 0$.

Some computed bounds which are applicable to the numerical solutions shown in Chapter 1 (Figures 5 and 6) are presented in the table below. The values of these bounds would justify a computation and are valuable for that purpose.

CASE	TRUE $\lvert Y_2 \rvert_{max}$	$\lvert Y_2 \rvert_b$	$\lvert Y_2 \rvert_{ba}$
Convex	0.4237	1	0.84
Concave	0.4162	1	0.84

CASE	TRUE $\lvert Y_1 \rvert_{max}$	$\lvert Y_1 \rvert_b$	$\lvert Y_1 \rvert_{ba}$
Convex	0.0387	0.1	0.0466
Concave	0.0674	0.173	0.146

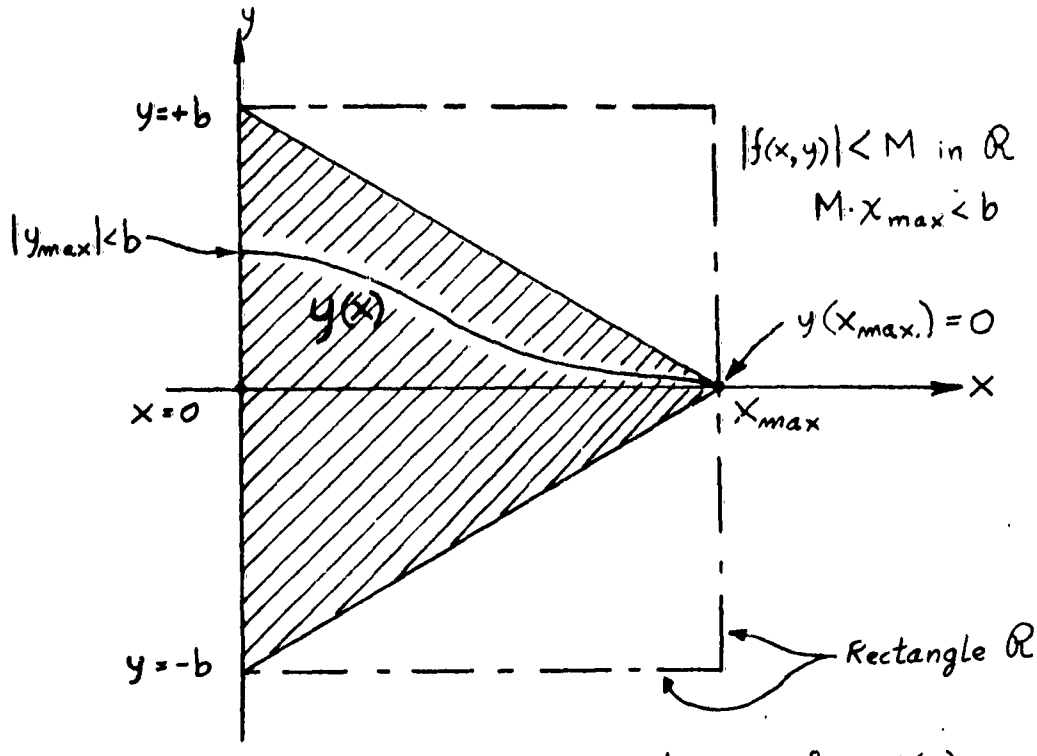

Fig. 1. Existence and bound for $y(x)$

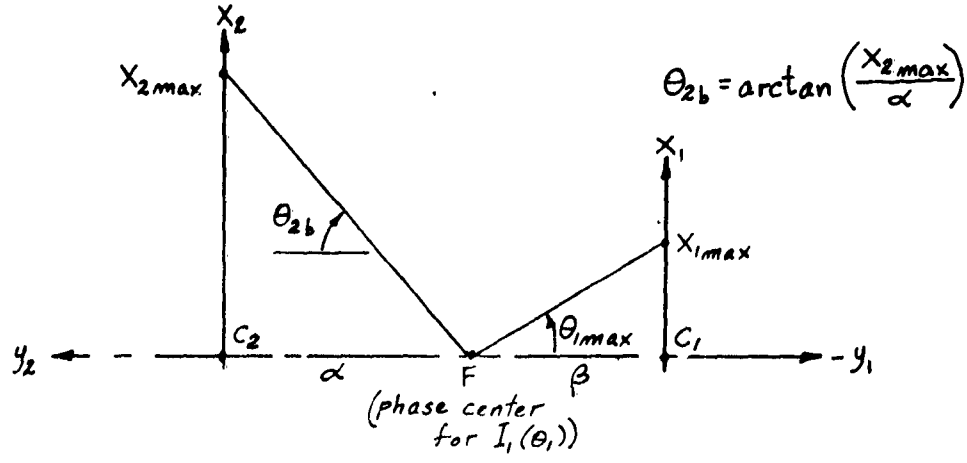

Fig. 2. Case (a), $(x_{2max} > 0)$, Cassegrainian Type, Absolute bound for $|\theta_2|$.

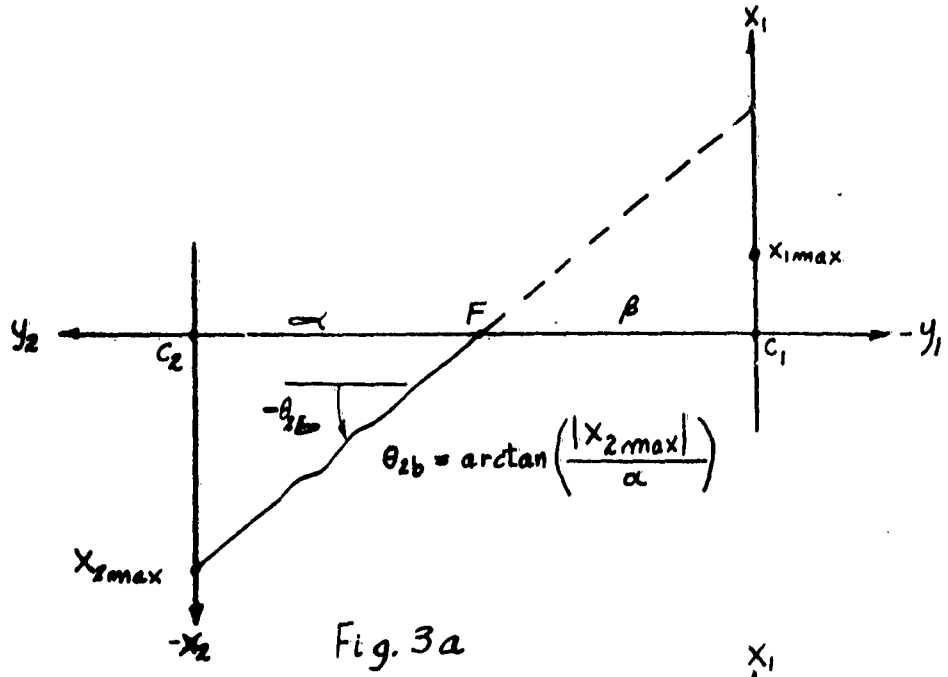

Fig. 3a

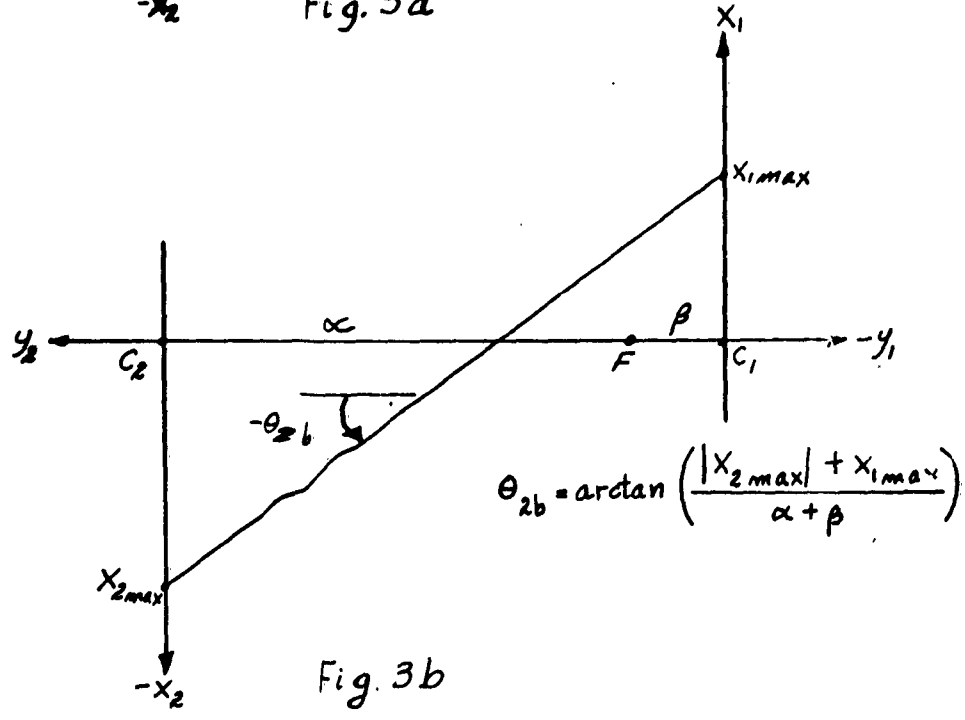

Fig. 3b

Fig. 3. Case (b), ($X_{2max} < 0$), Gregorian type, Absolute bound for $|\theta_2|$.

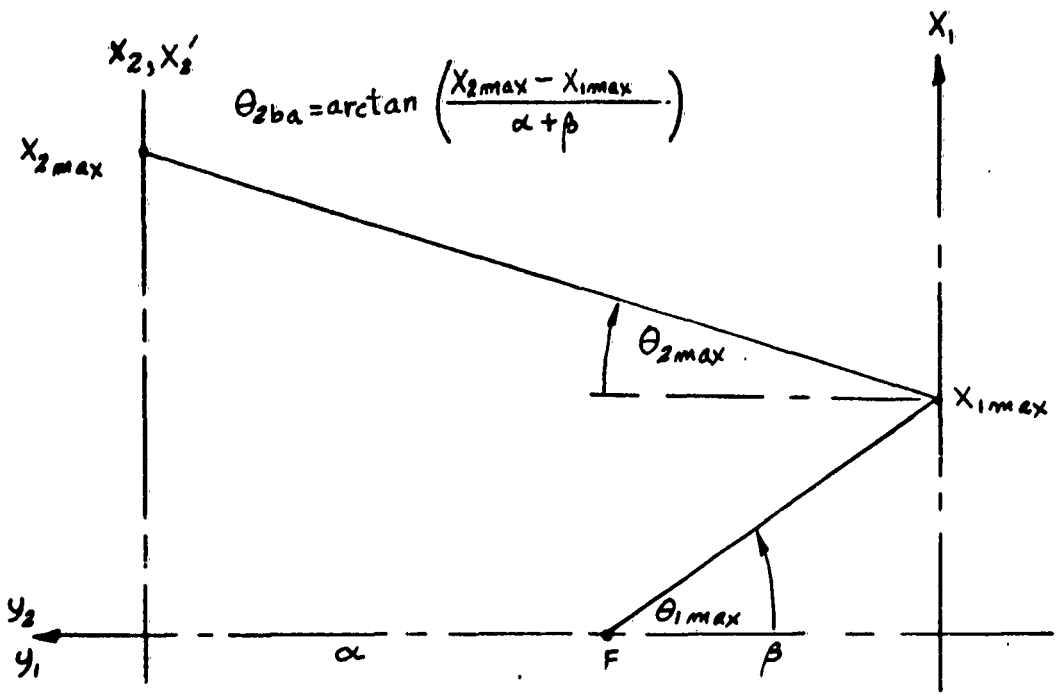

Fig. 4. Case (a), ($X_{2max} > 0$); Approximate $|y_{max}|$

APPENDIX II

ON THE AXIAL CAUSTIC OF THE EDGE FIELD FOR SURFACES OF REVOLUTION

In this appendix we shall justify the use of the factor G_{Ae} which is the Gaussian curvature of the field wavefront in the axial case. We will also justify the fact that a very accurate approximation of the field near the caustic is not necessary, since only a very small solid angle is subtended in this region.

1. The Factor G_{Ae}

In equation (6) of Chapter 3, the amplitude of the field U_e varies as $1/\sqrt{kr}$. This is typical for the far zone of any cylindrical field, when r is the distance from the source to the field point. Energy is thus conserved in any angular sector per unit length along the cylindrical axis. For the edge field the caustic or source point is the edge itself, and as seen in the diagram (a), the normal area subtended by a tube of rays from the caustic depends on the value of kr. Alternatively, the ratio of areas is given by kr_2/kr_1 for areas No. 1 and No. 2 in the diagram. The curvature of the wavefronts is proportional to kr. We thus define G_{Ae} for the cylindrical case as

$$G_{Ae} = 1/\sqrt{kr} \quad .$$

When the edge is part of a circular curve as in the axially symmetric case, the ratio of two areas subtended by a tube of rays through which

a constant rate of energy flow passes is proportional to r^2 in the far zone except near the caustic axis. Consider the diagram (b) for this case. The ratio of areas now obtained is

$$(k r_2)\left|k r_2 \sin \Gamma_2 + k x_{1m}\right| / (k r_1)\left|k r_1 \sin \Gamma_2 + k x_{1m}\right| \quad .$$

In this case the curvature of the wavefronts is defined as the Gaussian curvature which is

$$G_{Ae} = 1 \Big/ \sqrt{k r \left|k r \sin \Gamma_2 + k x_{1m}\right|} \quad .$$

For the bottom edge when Γ_2 is still in the same direction, we have

$$G_{Ae} = 1 \Big/ \sqrt{k r \left|k r \sin \Gamma_2 - k x_{1m}\right|} \quad .$$

We assume, therefore, that for the curved edges of the axially symmetric case, the angular dependence of the edge field is identical to that of the straight edge case (cylindrical case) except as modified by the Gaussian curvature given above. This assumption is the same as that employed by Keller for diffraction from a flat aperture with excellent results obtained in that case.

At $\phi = \pi - \alpha^1$ we have defined $G_{Ae}^{-1}(\rho_{2m}) = \sqrt{k^2 \rho_{2m}^2 \sin\left|\theta_{2m}\right|}$ for the axial case, where $\Gamma_{2m} \approx \theta_{2m}$. We should note that Γ_{2m} is only proximately θ_{2m} to within the accuracy of the far field approximation. This is explained as follows. We define Γ_{2m} not as the angle Γ_2 when the edge ray intercepts the edge of the large reflector, but rather the value of Γ_2 when γ_2 intercepts the edge

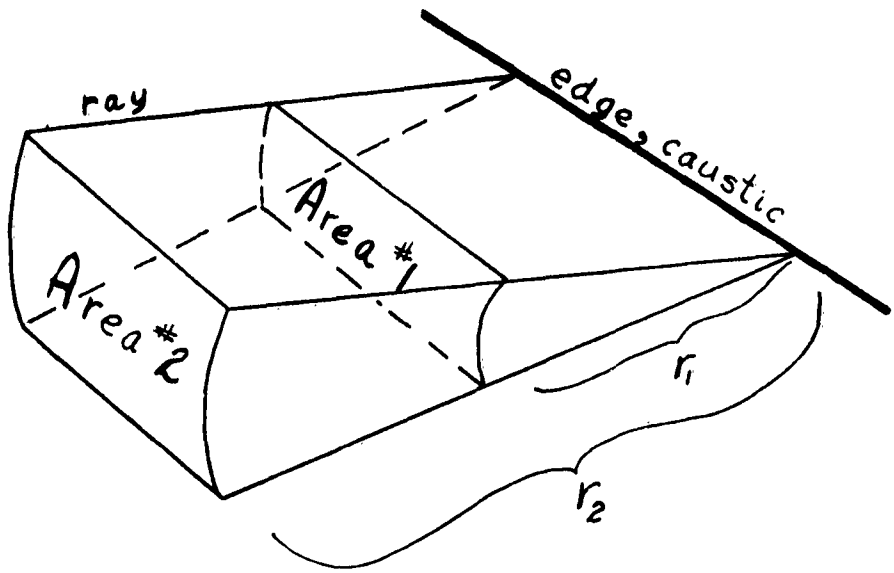
ray
edge, caustic
Area #1
Area #2
r_1
r_2

(a)

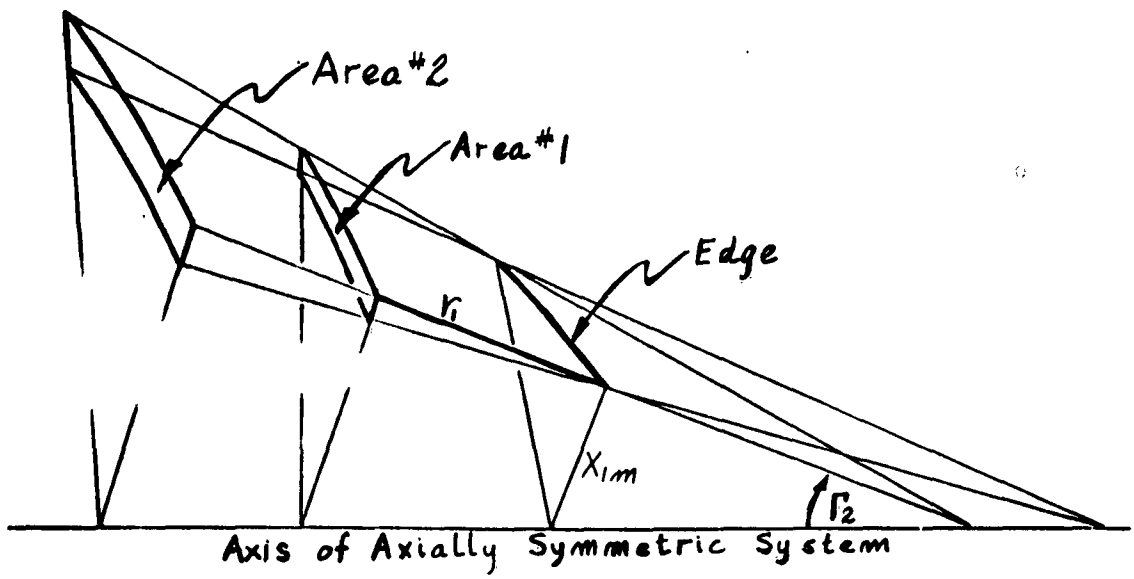
Area#2
Area#1
Edge
r_1
x_{1m}
r_2
Axis of Axially Symmetric System

(b)

of the large reflector. Hence, $\Gamma_2 = \Gamma_{2m}$ when $\gamma_2 = \gamma_{2m}$ (γ_2 being the angle the normal to the total edge diffracted field wavefront makes with the y_1 axis). While this distinction is really not very important to the theory of the analysis and negligible when the far field approximations are excellent, it nevertheless is important when numerical computations are made, especially by machine computors. The machine will not overlook a small difference between the true far field and approximate far field and may not complete the calculation. Hence, the difference between the defined Γ_{2m} and θ_{2m} must be considered carefully.

2. The Caustic Axis of the Axially Symmetric Case

In general, for the far field we will have $r >> x_{1m}$ for the edge fields. Hence, G_{Ae} reduces to the same expression for the top and bottom edges

$$G_{Ae}^{-1} = k r \sin^{1/2} |\Gamma_2|$$

providing that Γ_2 is not small. This assumption is valid so long as

$$\sin |\Gamma_2| >> \left| \frac{x_{1m}}{r} \right| .$$

When Γ_2 is small, we take as an approximation for the above inequality the value for r given by $r_c = \rho_{2m}$*. This is a rough approximation for the distance from the edge to reflector No. 2, when Γ_2 is small. A more accurate approximation will not be of great value as we

---

* More suitable choices for r_c can be made for specific problems.

shall show shortly. On this basis we take for the value of G_{Ae}:

$$G_{Ae}^{-1} = kr\sqrt{\left|\sin \Gamma_2 \pm \frac{x_{1m}}{r_c}\right|} \quad .$$

When $\Gamma_2 > 0$ and near zero, we will obtain an infinity from G_{Ae} due to the bottom edge. To eliminate this, we make the further approximation that

$$G_{Ae}^{-1} = kr\sqrt{\sin\left|\Gamma_2\right| + \frac{x_{1m}}{r_c}}$$

for <u>both</u> edges.

At $\Gamma_2 = 0$, this value for G_{Ae} is correct for both edges. For

$$\sin\left|\Gamma_2\right| >> \left|\frac{x_{1m}}{r_c}\right|$$

this value is again correct for both edges. Hence, it is only for a small angular sector in Γ_2 and a very small solid angle that the last given value for G_{Ae} is in error. In the case of vector symmetry for the axial system, we have $\Lambda_e = 0$ (equation(13)) on axis ($\Gamma_2 = 0$) and the total energy in this small solid angle will be very small as compared with the surface reflected primary field in this same region. Even when $\Lambda_e \neq 0$ as when we "average" an incident linearly polarized primary field, the net energy in this solid angle is still small and the value for G_{Ae} at the center ($\Gamma_2 = 0$) is fairly accurate.

As an example, let us define Γ_{2R} as that angle at which

$$\sin \left|\Gamma_{2R}\right| \lesssim (10) \cdot \left|\frac{x_{1m}}{r_c}\right| \quad .$$

The total solid angle subtended by the range ($0 \leq \left|\Gamma_2\right| \leq \left|\Gamma_{2R}\right|$) is very small for $\left|x_{1m}/r_c\right| \ll 1$. The percentage solid angle in this range of the total 4π steradians is

$$\left(\frac{1 - \cos \Gamma_{2R}}{2}\right) \quad x \quad 100\%$$

Hence if Γ_{2R} were as large as 20 degrees, the percentage solid angle would be only 6%. The percentage solid angle of that subtended by reflector No. 2 is much larger, however, but $\Gamma_{2R} = 20°$ is very large also. For $\Gamma_{2R} \approx 5°$, the subtended solid angle is only 0.2%.

The above numbers indicate that a precise correction for the fields on the caustic is not necessary and will not alter the final results in any significant way. Hence a reasonable approximation from a computational point of view was chosen.